

Women in molecular mechanisms of aging research

Edited by

Consuelo Borrás and Aurélie Ledreux

Published in

Frontiers in Aging



FRONTIERS EBOOK COPYRIGHT STATEMENT

The copyright in the text of individual articles in this ebook is the property of their respective authors or their respective institutions or funders. The copyright in graphics and images within each article may be subject to copyright of other parties. In both cases this is subject to a license granted to Frontiers.

The compilation of articles constituting this ebook is the property of Frontiers.

Each article within this ebook, and the ebook itself, are published under the most recent version of the Creative Commons CC-BY licence. The version current at the date of publication of this ebook is CC-BY 4.0. If the CC-BY licence is updated, the licence granted by Frontiers is automatically updated to the new version.

When exercising any right under the CC-BY licence, Frontiers must be attributed as the original publisher of the article or ebook, as applicable.

Authors have the responsibility of ensuring that any graphics or other materials which are the property of others may be included in the CC-BY licence, but this should be checked before relying on the CC-BY licence to reproduce those materials. Any copyright notices relating to those materials must be complied with.

Copyright and source acknowledgement notices may not be removed and must be displayed in any copy, derivative work or partial copy which includes the elements in question.

All copyright, and all rights therein, are protected by national and international copyright laws. The above represents a summary only. For further information please read Frontiers' Conditions for Website Use and Copyright Statement, and the applicable CC-BY licence.

ISSN 1664-8714
ISBN 978-2-8325-5647-4
DOI 10.3389/978-2-8325-5647-4

About Frontiers

Frontiers is more than just an open access publisher of scholarly articles: it is a pioneering approach to the world of academia, radically improving the way scholarly research is managed. The grand vision of Frontiers is a world where all people have an equal opportunity to seek, share and generate knowledge. Frontiers provides immediate and permanent online open access to all its publications, but this alone is not enough to realize our grand goals.

Frontiers journal series

The Frontiers journal series is a multi-tier and interdisciplinary set of open-access, online journals, promising a paradigm shift from the current review, selection and dissemination processes in academic publishing. All Frontiers journals are driven by researchers for researchers; therefore, they constitute a service to the scholarly community. At the same time, the *Frontiers journal series* operates on a revolutionary invention, the tiered publishing system, initially addressing specific communities of scholars, and gradually climbing up to broader public understanding, thus serving the interests of the lay society, too.

Dedication to quality

Each Frontiers article is a landmark of the highest quality, thanks to genuinely collaborative interactions between authors and review editors, who include some of the world's best academicians. Research must be certified by peers before entering a stream of knowledge that may eventually reach the public - and shape society; therefore, Frontiers only applies the most rigorous and unbiased reviews. Frontiers revolutionizes research publishing by freely delivering the most outstanding research, evaluated with no bias from both the academic and social point of view. By applying the most advanced information technologies, Frontiers is catapulting scholarly publishing into a new generation.

What are Frontiers Research Topics?

Frontiers Research Topics are very popular trademarks of the *Frontiers journals series*: they are collections of at least ten articles, all centered on a particular subject. With their unique mix of varied contributions from Original Research to Review Articles, Frontiers Research Topics unify the most influential researchers, the latest key findings and historical advances in a hot research area.

Find out more on how to host your own Frontiers Research Topic or contribute to one as an author by contacting the Frontiers editorial office: frontiersin.org/about/contact

Women in molecular mechanisms of aging research

Topic editors

Consuelo Borras — University of Valencia, Spain

Aurélie Ledreux — University of Colorado Anschutz Medical Campus, United States

Citation

Borras, C., Ledreux, A., eds. (2024). *Women in molecular mechanisms of aging research*. Lausanne: Frontiers Media SA. doi: 10.3389/978-2-8325-5647-4

Table of contents

- 04 **Editorial: Women in molecular mechanisms of aging**
Aurélie Ledreux and Consuelo Borrás
- 06 **Survival-Span Method: How to Qualitatively Estimate Lifespan to Improve the Study of Aging, and not Disease, in Aging Studies**
Julia Adelöf, Jaime M. Ross, Madeleine Zetterberg and Malin Hernebring
- 13 **Progerin-Induced Impairment in Wound Healing and Proliferation in Vascular Endothelial Cells**
Yizhi Jiang and Julie Y. Ji
- 25 **The *C. elegans* Observatory: High-throughput exploration of behavioral aging**
Rex A. Kerr, Antoine E. Roux, Jérôme Goudeau and Cynthia Kenyon
- 49 **Systematic estimation of biological age of *in vitro* cell culture systems by an age-associated marker panel**
Christiane Hartmann, Luise Herling, Alexander Hartmann, Verena Köckritz, Georg Fuellen, Michael Walter and Andreas Hermann
- 64 **Quantitative nanohistology of aging dermal collagen**
Sophia Huang, Adam Strange, Anna Maeve, Samera Siddiqui, Phillipe Bastien, Sebastian Aguayo, Mina Vaez, Hubert Montagu-Pollock, Marion Ghibaudo, Anne Potter, Herve Paeon and Laurent Bozec
- 74 **Simufilam suppresses overactive mTOR and restores its sensitivity to insulin in Alzheimer's disease patient lymphocytes**
Hoau-Yan Wang, Zhe Pei, Kuo-Chieh Lee, Boris Nikolov, Tamara Doehner, John Puente, Nadav Friedmann and Lindsay H. Burns
- 89 **Expression of concern: Simufilam suppresses overactive mTOR and restores its sensitivity to insulin in Alzheimer's disease patient lymphocytes**
Frontiers Editorial Office
- 90 **Change in circulating klotho in response to weight loss, with and without exercise, in adults with overweight or obesity**
Katherine A. Collins, Fabrisia Ambrosio, Renee J. Rogers, Wei Lang, Eric B. Schelbert, Kelliann K. Davis and John M. Jakicic



OPEN ACCESS

EDITED AND REVIEWED BY

Laura Haynes,
University of Connecticut, United States

*CORRESPONDENCE

Aurélie Ledreux,
✉ aurelie.ledreux@cuanschutz.edu

RECEIVED 26 July 2024

ACCEPTED 29 July 2024

PUBLISHED 05 August 2024

CITATION

Ledreux A and Borrás C (2024) Editorial: Women in molecular mechanisms of aging.
Front. Aging 5:1471233.
doi: 10.3389/fragi.2024.1471233

COPYRIGHT

© 2024 Ledreux and Borrás. This is an open-access article distributed under the terms of the [Creative Commons Attribution License \(CC BY\)](#). The use, distribution or reproduction in other forums is permitted, provided the original author(s) and the copyright owner(s) are credited and that the original publication in this journal is cited, in accordance with accepted academic practice. No use, distribution or reproduction is permitted which does not comply with these terms.

Editorial: Women in molecular mechanisms of aging

Aurélie Ledreux^{1*} and Consuelo Borrás²

¹Department of Neurosurgery, School of Medicine, University of Colorado Anschutz Medical Campus, Aurora, CO, United States, ²MiniAging Research Group, Department of Physiology, Faculty of Medicine, University of Valencia, Valencia, Spain

KEYWORDS

aging, lifespan, *C. elegans*, Klotho, vascular aging, mTOR, nanohistology

Editorial on the Research Topic

Women in molecular mechanisms of aging

This *Women in molecular mechanisms of aging* Research Topic highlights research studies and methods focused on aging. This Research Topic includes 7 articles, spanning various areas of aging research but with a common goal of deepening the current understanding of mechanisms and pathways involved in aging. From *in vitro* studies (Hartmann et al.; Wang et al.; Jiang and Ji; Huang et al.), to a novel *C. elegans* Observatory (Kerr et al.), or a clinical study (Collins et al.) and a research method study proposing a novel way to estimate lifespan (Adelöf et al.).

Lifespan analyses are important in determining the effect of a gene or the efficacy of a drug intervention and other therapeutic approaches to elucidate the underlying molecular mechanisms of aging. Adelöf et al. propose a novel method to better estimate lifespan in aging studies. The aging process strongly intertwines with disease onset and progression, which can complicate the rigorous interpretation of aging mechanisms since diseased animals are often excluded in traditional methods to estimate lifespan. The “survival-span method” proposed by this team of women scientists integrates the effect of decreased health by including euthanized “diseased” animals together with animals that died from “natural causes.” This is significant for aging studies since the exclusion of diseased animals from a lifespan analysis can decrease the power of the study and might provide misleading data on actual genes or pathways involved in aging (Adelöf et al.).

While various cellular systems have been implicated in regulating aging, it remains unclear how these processes cause the aging process to unfold. *C. elegans* short lifespan and ease of genetic manipulation has made it a premier model organism for aging studies, leading to the identification of hundreds of genes that modulate lifespan. Kerr et al. from Calico Life Science have created an automated system for monitoring the behavior of group-housed *C. elegans* throughout their lifespans. The *C. elegans* Observatory makes it possible to study known and to-be-discovered lifespan genes that influence how animals age in a high-throughput yet approachable manner, opening the avenue for a deeper exploration of aging trajectories.

In vitro studies have yielded a great deal of knowledge on aging processes. Yet, comparison between studies is rendered challenging not only by the use of different cell lines but is also hampered by the lack of a uniform panel of age markers. Hartmann et al. from Rostock University Medical Center in Germany highlight the heterogeneity of single markers and the flaws of using individual marker expression. Instead, they designed a panel of markers that are sensitive to various aging conditions and can be used to assess different

aspects of aging. They propose an “AgeScore” including primary aging markers as well as antagonist aging markers that can be used in any *in vitro* cell culture system to estimate the biological age of cells in culture.

The skin is a complex and multi-layered connective tissue and illustrates the naturally occurring changes associated with age, resulting from both chronological and environmental factors. Huang et al. used Atomic-Force Microscopy (AFM) quantitative nanohistology to gain a better understanding of the phenotypic diversity of collagen across age at the nanoscale level. Their study provides new insights into the structural and functional properties of the skin and could drive a new field of quantitative nanohistology.

The mammalian target of rapamycin (mTOR) is a critical protein kinase that regulates cell growth and metabolism, and overactive mTOR has been implicated in cancer, aging, and neurodegeneration. Wang et al. investigated the mechanisms by which simufilam, a small oral molecule drug candidate for Alzheimer’s disease (AD) can reduce mTOR activity in the lymphocytes of people with AD who participated in a phase 2 clinical trial of simufilam.

Klotho is another protein that has been associated with healthy aging, shown to promote longevity and provide cardiovascular and neuroprotective effects. Obesity and overweight can accelerate aging mechanisms through, e.g., increased oxidative stress and inflammation or DNA damage. Blood levels of Klotho are lower in obese individuals, highlighting the accelerated aging process at play. Collins et al. from Duke Molecular Physiology Institute found that, in middle-aged obese people who underwent weight loss treatment (diet) associated or not with physical activity, Klotho levels increased significantly in participants with weight loss $\geq 10\%$ compared to 5% across 12 months. These findings suggest that weight loss is favorably associated with changes in Klotho concentrations, potentially counteracting the accelerated aging effects of obesity.

Vascular aging is considered a prominent factor in the global prevalence of cardiovascular diseases. Jiang and Ji from the Department of Biomedical Engineering at Purdue Indiana University investigated the role of progerin in wound healing and proliferation of endothelial cells (EC) submitted to shear stress. Progerin, a mutant truncated form of lamin A, is involved in

Hutchinson-Gilford progeria syndrome, but it has also been detected in healthy donor cells. Progerin activates a proinflammatory response in vascular cells and accelerates senescence, suggesting a role for progerin in vascular aging. Steady laminar flow, by regulating EC proliferation and remodeling processes, can protect against atherosclerosis. The study by Jiang and Ji showed that progerin-expressing ECs exposed to physiological levels of laminar shear stress exhibit delayed wound healing, which might affect atherosclerosis in older individuals.

Author contributions

AL: Writing—original draft. CB: Writing—review and editing.

Funding

The author(s) declare that no financial support was received for the research, authorship, and/or publication of this article.

Conflict of interest

The authors declare that the research was conducted in the absence of any commercial or financial relationships that could be construed as a potential conflict of interest.

The author(s) declared that they were an editorial board member of Frontiers, at the time of submission. This had no impact on the peer review process and the final decision.

Publisher’s note

All claims expressed in this article are solely those of the authors and do not necessarily represent those of their affiliated organizations, or those of the publisher, the editors and the reviewers. Any product that may be evaluated in this article, or claim that may be made by its manufacturer, is not guaranteed or endorsed by the publisher.



Survival-Span Method: How to Qualitatively Estimate Lifespan to Improve the Study of Aging, and not Disease, in Aging Studies

Julia Adelöf^{1*}, Jaime M. Ross^{2,3*}, Madeleine Zetterberg^{1,4} and Malin Hernebring^{1,4}

¹Department of Clinical Neuroscience, Institute of Neuroscience and Physiology, Sahlgrenska Academy at the University of Gothenburg, Gothenburg, Sweden, ²Department of Biomedical and Pharmaceutical Sciences, College of Pharmacy, George & Anne Ryan Institute for Neuroscience, University of Rhode Island, Kingston, RI, United States, ³Department of Neuroscience, Biomedicum, Karolinska Institutet, Stockholm, Sweden, ⁴Department of Ophthalmology, Region Västra Götaland, Sahlgrenska University Hospital, Mölndal, Sweden

OPEN ACCESS

Edited by:

Richard C. Slow,
King's College London,
United Kingdom

Reviewed by:

Evandro Fei Fang,
University of Oslo, Norway
Alejandro Ocampo,
University of Lausanne, Switzerland

*Correspondence:

Julia Adelöf
julia.adelof@gu.se
Jaime M. Ross
jaime_ross@uri.edu

Specialty section:

This article was submitted to
Molecular Mechanisms of Aging,
a section of the journal
Frontiers in Aging

Received: 14 June 2021

Accepted: 22 November 2021

Published: 14 December 2021

Citation:

Adelöf J, Ross JM, Zetterberg M and
Hernebring M (2021) Survival-Span
Method: How to Qualitatively Estimate
Lifespan to Improve the Study of
Aging, and not Disease, in
Aging Studies.
Front. Aging 2:724794.
doi: 10.3389/fragi.2021.724794

Lifespan analyses are important for advancing our understanding of the aging process. There are two major issues in performing lifespan studies: 1) late-stage animal lifespan analysis may include animals with non-terminal, yet advanced illnesses, which can pronounce indirect processes of aging rather than the aging process *per se* and 2) they often involves challenging welfare considerations. Herein, we present an option to the traditional way of performing lifespan studies by using a novel method that generates high-quality data and allows for the inclusion of excluded animals, even animals removed at early signs of disease. This Survival-span method is designed to be feasibly done with simple means by any researcher and strives to improve the quality of aging studies and increase animal welfare.

Keywords: aging, lifespan, survival analysis, animal research, 3R

INTRODUCTION

Aging is a complex process that affects virtually all organisms and tissues, and is a major risk factor for developing diseased states, such as forms of cancer, cardiovascular diseases, and neurodegenerative diseases. Thus, a better understanding of the mechanisms of aging is of major importance for most, if not all, medical fields (Harman, 1991; Niccoli and Partridge, 2012). Aging studies in animal models are complex, expensive, and require optimal study design and execution in order to obtain useful data to draw reliable conclusions. Determining lifespan is an important analysis used in conducting aging studies and aids in identifying the molecular mechanisms that control the pace of aging, including drug intervention, the effect of a gene, as well as lifestyle factors such as diet (caloric restriction, high-fat diet etc.) and exercise. However, experiments that monitor and test animals until advanced age, such as lifespan and behavioral studies, are challenging to execute due to the fact that the aging process strongly correlates with disease onset and progression. Thus, it is often the case that studies of aging also include diseased animals, and analyses on these animals consequently investigate both aging and disease, which in turn could introduce subject variation and conceal mechanistic changes brought about by the aging process *per se*. This is particularly important in homogenous cohorts, for example inbred mice, that are more prone to develop specific diseases due to homozygosity rather than heterogeneous populations such as humans. Thus, by excluding animals that show overt signs of decreased

health, variance within the remaining cohort is less likely due to an effect of illness or disease. Although necropsies can provide clarity as to the health state of an animal, insights from this postmortem approach cannot be applied *ex post facto*. This quandary has led the quest for better discernment between aging versus disease. From a study design perspective, however, the removal of diseased animals from a lifespan analysis can be problematic because it: 1) selects for some aged animals, and not all aged animals, 2) decreases the power of the study, and 3) might provide misleading data on actual aging.

In a previously published behavioral aging study, we devised a novel method that can be used for lifespan analysis, herein coined “Survival-span method”. This method allows for the inclusion of euthanized animals together with animals that died from “natural causes” (Adelöf et al., 2019). The Survival-span method generates high-quality data on survival using the entire data set and without reducing the number of animals, skewing results, or compromising animal welfare. Our approach involves creating a range between minimum and maximum survival curves by categorizing removed animals differently in the Kaplan-Meier survival analysis. The minimum survival curve is generated by labelling the removed animals similarly to animals that died from “natural causes”, which creates an underestimation of natural lifespan since those animals would have lived longer, although diseased, if not removed. The maximum survival curve is then generated when the removed animals are instead “censored” (i.e., a statistically unknown fate when removed from the study), which generates an overestimation of lifespan since it considers these animals as merely removed from the study at a given time. The actual lifespan lies in the span between these two survival curves.

The Survival-span method was first performed using hybrid mice in our previous study, though this method is applicable to all animal lifespan analyses. The interval of median lifespan in our C57BL/6N×BALB/c F2 male hybrids was very similar (789 ± 130 compared to $742\text{--}826$ days) to the four-way cross UM-HET3 male mice (offspring of BALB/cByJ×C57BL/6J F1 females and C3H/HeJ×DBA/2J F1 males), and was slightly lower in females (801 ± 88 compared to $832\text{--}891$ days; Strong et al., 2013; Adelöf et al., 2019). In comparison to inbred mice, the Survival-span of the C57BL/6N×BALB/c F2 hybrids surpassed that of short-lived BALB/c, but did not attain the longevity of the long-lived C57BL/6J mice, using data from the Aging Phenome Project (711/901 days for males and 771/866 days for females; Yuan et al., 2009; Adelöf et al., 2019). The Survival-span method was also recently applied in understanding the effect of overexpressing the proteasome activator PA28αβ (Adelöf et al., 2021).

Lifespan analyses are important in determining the effect of a gene as well as efficacy of drug interventions and other therapeutic approaches to elucidate the underlying molecular mechanisms of aging. Herein, we present a step-by-step description of how to generate lifespan analyses applying the Survival-span method. Using the Survival-span method allows for the inclusion of all animals in the study while removing those

with advanced diseased states and provides distinction between animals that present healthy from those with decreased health. Additionally, the Survival-span method decreases the introduction of sample variance due to disease-associated alterations that could confound behavioral/biochemical analyses of the aging process and creates results that are comparable to other aging studies. Lastly, this method improves animal welfare and facilitates institutional compliance while performing lifespan analyses, even under more rigorous animal guidelines.

MATERIAL AND EQUIPMENT

The requirements to perform this method are a spreadsheet program (e.g., Microsoft Excel) and a statistical program (e.g., SPSS, SAS, Prism) in which Kaplan-Meier survival analysis can be done. The Kaplan-Meier nonparametric test revolutionized survival analyses when presented in 1958 because it allowed, for the first time, the inclusion of incomplete observations in survival statistics. To correctly run the Kaplan-Meier analysis, specific criteria (statistically coined “assumptions”) regarding the dataset need to be acquired as indicated below (Kaplan and Meier, 1958).

- 1) The time until observation for each subject must be clearly defined and precisely measured. Having a clear starting point is optimal to reduce the risk of left-censoring, which can skew results. For example, if survival time of a specific subject group is studied, left-censoring can be a result of inclusion criteria dependent on vague diagnosis, making the actual starting point difficult to obtain. In lifespan studies, left-censoring is not an issue if the animal’s exact birth date is used.
- 2) Every observation must fit into one of the two different states: “event” or “censored”. In lifespan studies, the observation is animal fate and can be either “event” (death) or “censored” (removed from study).
- 3) The two states should be independent of each other and subjects should not be categorized as “censored” if the risk of an “event” occurring is increased. The Kaplan-Meier analysis assumes that censored data behaves as uncensored data beyond the time of censoring and if the prognosis of censored subjects relates to the event, this introduces a bias. However, in aging studies this assumption is difficult to adhere to since diseased subjects have an increased risk of dying and should not be either censored or removed from the study. The Survival-span method addresses this bias by including both possible fates and not selecting one fate above the other. Using both possible fates results in two lifespan calculations, one being an underestimation and the other an overestimation of an animal’s “true” lifespan.

To evaluate if the survival curves of experimental groups are significantly different, there are a variety of statistical tests that can be applied. The most commonly used is the log-rank (Mantel-Cox) test, but depending on the dataset other tests may be more appropriate. The log-rank test is nonparametric and calculates

TABLE 1 | Date of birth log.

Animal number	Date of birth	Days from birth to start of the study
350	April 28, 2020	−3
357	May 1, 2020	0
366	May 4, 2020	+3
...		

the chi-square (χ^2) for each group for each event time and summarizes the results. Similar to the Kaplan-Meier test assumptions, the log-rank test requires that the comparison groups include similar degrees of censoring and that survival probability is the same regardless of when subjects were included in the study. The log-rank test should not be used on datasets with overlapping survival curves (Mantel, 1966; Cox, 1972; Peto and Peto, 1972; Bland and Altman, 2004). In contrast to the log-rank test, which weighs all calculations equally, the Wilcoxon (also called Breslow, Gehan) test weighs early events heavier than late ones and may be a preferred test to use when the initial phase is of particular importance and censoring is scarce (Breslow 1974).

METHODS

To perform the Survival-span method, follow these instructions. Steps 1–3 are done in a spreadsheet (e.g., Excel), and steps 4–5 in a statistical program (e.g., SPSS, SAS, Graphpad Prism).

- 1) Procedure: For each subject, log the date of birth and the number of days the birth date differs from the start of the study, as shown in **Table 1**. Number the days of the study, as shown in **Table 2**.

Rationale: To adhere to the assumption of exactness of time until an event is recorded, it is important to log the date of birth and days of lifespan. At the time of starting a lifespan study, animals typically would not be born on the same day. Thus, one should register each animal's date of birth and the number of days differing for all animals to obtain a precise time until fate. In addition, a reference calendar for days of the lifespan study should be created. This enables knowing the exact study day for each animal.

- 2) Procedure: Monitor animals on a regular basis and remove animals with significantly decreased health.

Rationale: Follow the animal research permit of the study per institutional guidelines. If using mice, animals should be checked at least twice per week when less than 24 months of age, and daily when older than 24 months of age. Symptoms indicating significant decreased health in mice may include, for example: hunched shoulders, shabby fur, rapid decrease in activity, decreased eating/drinking, tumors.

TABLE 2 | Day of study log.

Date	Study day
May 30, 2020	30
May 31, 2020	31
June 1, 2020	32
June 2, 2020	33
...	

- 3) Procedure: Log the fate of each animal in the lifespan study. Code animals that died from “natural causes” with “1” for both minimum and maximum survival boxes. Euthanized animals are coded with “1” in the minimum survival log and with “0” in the maximum survival log, as shown in **Table 3**.

Rationale: To prepare data for statistical analysis, the fates need to be converted into “1” and “0” so that statistical programs can run the Kaplan-Meier analysis. In the Kaplan-Meier analysis “1” signifies an event and “0” signifies censored subject. It is the coding of the euthanized subjects that differs in the two lifespan curves.

- 4) Procedure: Transfer **Table 3** data (use columns: Lifespan for each animal with both Minimum and Maximum Survival Codes) to an appropriate statistical program where Kaplan-Meier analysis can be performed. Set Lifespan as time (X-variable) and Minimum and Maximum survival as two separate columns or groups (Y-variables), as shown in **Table 4**.

Rationale: Enables a statistical program to run the Kaplan-Meier analysis.

- 5) Procedure: Run the statistical analyses and obtain results.

Rationale: The Kaplan-Meier Survival analysis will generate data of survival (e.g., median, standard deviation of the median, % survival, # of subjects for each fate) and graphs for visualization of lifespan (see **Figure 1**). Some statistical programs also report estimates of the mean survival; however, this should be analyzed with caution since it does not take the censored subjects into account and may be misleading.

In addition to the median (50%) survival, it can be helpful to estimate additional survival times (e.g., 25%, 75%) in order to compare the lifespan data with other aging studies. These additional survival percentages can be extrapolated from the Kaplan-Meier analysis and visualized as shown in **Figure 2** and presented in **Table 5**.

RESULTS

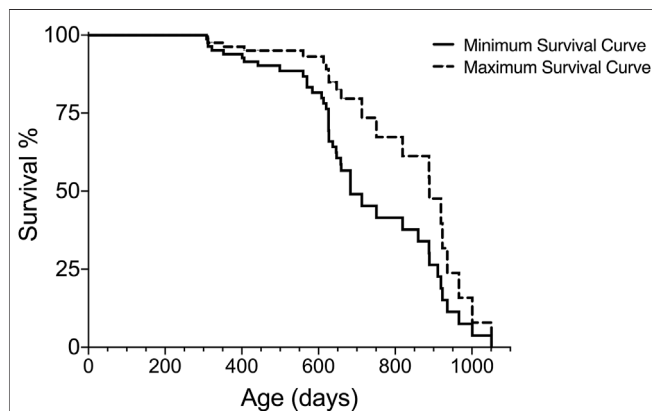
In traditionally conducted lifespan studies, the strategy to generate a lifespan with the closest proximity to the exact

TABLE 3 | Generation of minimum and maximum survival codes.

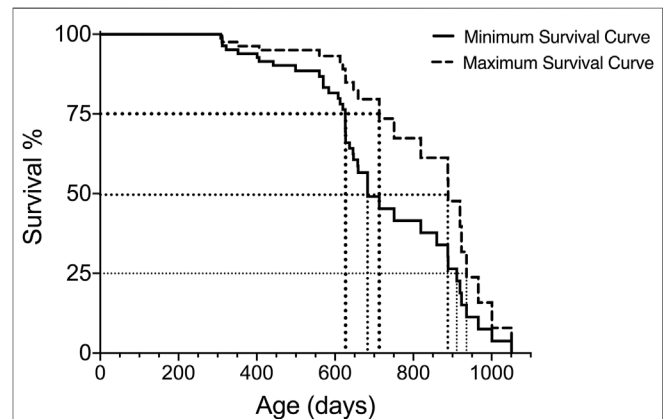
Animal number	Birth date difference (birth date –study start date)	Study day of fate	Lifespan (study days –birth date difference)	Fate	Minimum survival code 1= all deaths	Maximum survival code
						1= natural
						0= euthanized
366	+3	903	900	Natural	1	1
357	0	957	957	Euthanized	1	0
350	–3	957	960	Natural	1	1
...						

TABLE 4 | Data transfered into a statistical program.

Days of lifespan (X)	Minimum survival (Y ₁)	Maximum survival (Y ₂)
900	1	1
957	1	0
960	1	1
...		

**FIGURE 1** | Graphical readout of minimum and maximum survival curves generated with Kaplan-Meier analysis for one group of subjects.

lifespan is to, ideally, not interfere with the fate of subjects, but this may introduce variations due to disease and may not be compatible with ethical considerations of animal welfare. During aging, variation in cohorts of animals can increase; however, the removal of animals with evident signs of decreased health assists in decreasing some of the variation introduced by the reduced health state. Using the Survival-span method, all animals are included in the lifespan analyses regardless of when they might be removed due to decreased health. In **Figure 3**, we compare the lifespan curves using the Survival-span method with a hypothetical traditional survival curve to mimic a typical lifespan study. The hypothetical traditional survival curve was generated using the same data set shown in **Figure 1**, with 120 days added to all removed subjects as an estimate of how long they could have potentially lived if they would not have been euthanized (120 days was estimated as a rough average). The hypothetical traditional

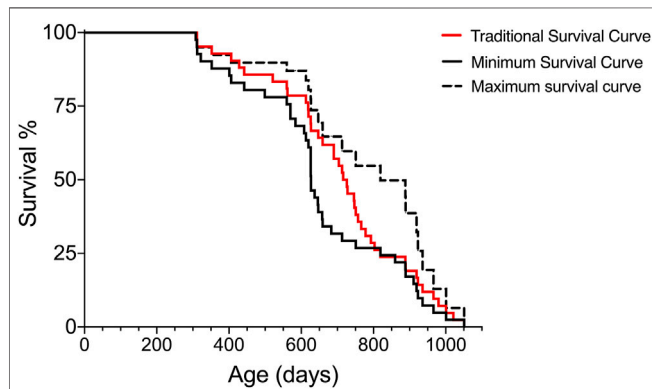
**FIGURE 2** | Extrapolation of 75, 50 and 25% survival for both minimum and maximum survival curves generated with Kaplan-Meier analysis for one group of subjects.

lifespan curve lies, as predicted, within the span of the maximum and minimum lifespan curves generated by the Survival-span method (**Figure 3**).

For comparison of survival intervals between different groups, we recommend performing a log-rank test (if Kaplan-Meier assumptions are met) for all minimum survival curves amongst cohorts and then repeating these analyses for all maximum survival curves. Analyzing the minimum and maximum survival curves separately allows for adhering to the assumption of similarity of censoring. In addition, comparing the minimum and maximum survival curves can result in valuable lifespan observations, such as if there were significant differences in minimum survival but not maximum survival, as illustrated in **Figure 4** and **Table 6**. This is a hypothetical example of a scenario where there is no difference between groups when considering only subjects that reach old age and die of “natural causes”, as shown by the maximal survival curves of group A and B (**Figure 4A**), but subjects in group B are more likely to have earlier onset of ill health, as indicated by the minimal survival curves (**Figure 4B**). If the animals in group B would not have been euthanized, they would most likely have died from “natural causes” earlier than subjects in group A. Thus, only looking at one survival curve when conducting an aging study could yield an analysis indicating that group B has a shorter lifespan than

TABLE 5 | Extrapolated 75, 50 and 25% survival for both minimum and maximum survival curves in **Figure 2**.

	75% survival (Days)	50% (median) survival (Days)	25% survival (Days)
Minimum Survival Curve	628	683	911
Maximum Survival Curve	714	889	936
Actual Lifespan	628–714	683–889	911–936

**FIGURE 3 |** Hypothetical comparison of a traditional survival curve with minimum and maximum survival curves generated by the Survival-span method. Subjects in the hypothetical “traditional” survival analysis have been generated by adding 120 days to the euthanized subjects in the data set of **Figure 1**. The 120 days addition is an estimated average of potential extended survival.

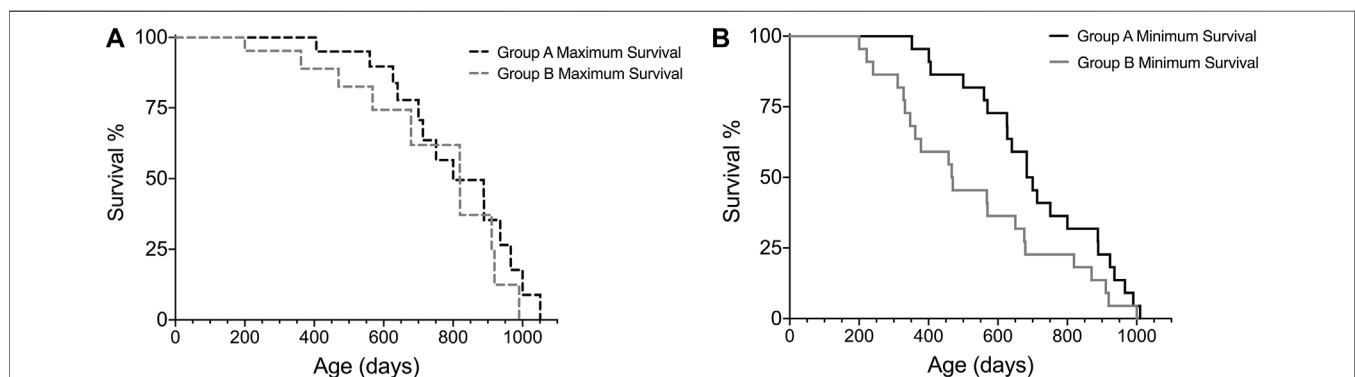
group A, which might be interpreted as a difference in the aging process. The same scenario, however, presented using our Survival-span method, highlights that disease states, and not necessarily aging *per se*, skew lifespan of group B, since in this example the subjects in group B that do not die early from disease are in fact just as long-lived as the subjects in group A.

In general, researchers need to have clear and consistent censorship criteria when conducting animal lifespan studies. These criteria become even more important for survival

analyses when applying the Survival-span method. Causes for euthanization may differ depending on the animal species, disease model, therapeutic treatment, researcher, institution, or country, all which can affect outcomes of the Survival-span method, highlighting a possible limitation of the method. We thus recommend researchers to standardize the criteria for the removal of animals in their lifespan studies. Notably, even in animals that appear healthy, full necropsy can show otherwise, thus the existence of disease can be concealed in animals that are not removed. A limitation related to the removal of animals is reflected in disease presentation that could potentially introduce removal inconsistencies. For example, an animal with a visible tumor may be euthanized earlier than an animal with an internal tumor, with the latter possibly not euthanized until signs of secondary effects from the tumor. In this scenario, these two animals would most likely be removed from the study at different degrees of disease. Taken together, the limitations of the Survival-span method can be considered relatively minor, but important to take into consideration.

DISCUSSION

Lifespan studies are a crucial element to aging research and have been used to identify genes or pathways important in the regulation of lifespan, such as insulin/insulin-like growth factor 1 (IGF-1) signaling (Kenyon et al., 1993), mitochondrial DNA (mtDNA) mutation load (Trifunovic et al., 2004; Ross et al., 2013), as well to test drug intervention, such as rapamycin (Harrison et al., 2009) and

**FIGURE 4 |** Hypothetical example on how the Survival-span method adds valuable information on survival. Subjects in group B tend to have a higher prevalence of early ill health causing early euthanization (~200–300 days of age), which results in no difference in **(A)** maximum survival, but a significant difference in **(B)** minimum survival, when comparing group A and B ($p = 0.0438$, Log-rank test) ($n_{\text{groupA}} = 22$, $n_{\text{groupB}} = 22$, $\text{censored}_{\text{max-curveA}} = 9$, $\text{censored}_{\text{max-curveB}} = 9$).

metformin, and lifestyle factors, such as dietary restriction (reviewed in Fontana et al., 2010). The most commonly used statistical test to analyze lifespan is Kaplan-Meier survival analysis. Although statistical tests, like Kaplan-Meier, are essential for good experimental practice, it is sometimes difficult to fit biology into statistical analysis models. Due to the impossible compliance of the Kaplan-Meier assumption of bias, it is very challenging to generate an exact lifespan curve while adhering to animal health and welfare. In addition, the intertwining of aging with disease onset and progression further complicates the analysis of aging cohorts. Since statistics do not take into account fundamental insights of aging, it is important for researchers to try to modify statistical tests into models that serve the purpose of providing truthful scientific results as well as ethical considerations.

Here, we present a novel approach to the Kaplan-Meier survival analysis, the Survival-span method, which generates a lifespan analysis model to address these central issues of aging studies. Our method utilizes the assumption of independence for censoring of events (Kaplan-Meier assumption 3), and allows removed subjects to be designated as either “natural death” or “censored”, which creates an under- and overestimation of true lifespan. Importantly, and as demonstrated by examples presented herein and recently published (Adelöf et al., 2019), the Survival-span method still allows for qualitative comparisons with other aging studies, irrespective of where the research was conducted, and can also be used to assess differences between experimental groups (e.g., **Figure 4; Table 6**). In addition, allowing for the inclusion of all enrolled animals, even those removed for decreased health, adds valuable information about the cohort, which in turn improves translatability to humans.

Considering that aging and disease are tightly associated, it is not straightforward as how to, or if one should try to, distinguish between these two parameters in survival and aging analyses. Nonetheless, including animals with significant decreased health in an aging study yields variation that may reflect differences of the diseased states and not actually the aging process *per se*, which could affect conclusions of studies applicable to humans. In addition, how the removal of animals is statistically maneuvered impacts lifespan studies aiming to understand molecular mechanisms of aging. The Survival-span method is the first model to integrate an effect of decreased health into a survival analysis and this gives important biological information which may have been previously overlooked. For example, a recent aging study reported that overexpression of SIRT6, but not SIRT1, extended healthy lifespan; however, the mice that were euthanized were considered equal to mice that died from

“natural causes” (Roichman et al., 2021). In this study, it is not stated how many or which mice were removed. Interestingly, autopsies at the time of “natural death” showed that the incidence of gastrointestinal adenoma was approximately 60% in SIRT1 overexpressing (SIRT1-OE) mice as compared to 30% in wild-type (WT) mice. The gastrointestinal adenoma induced in the SIRT1-OE mice is most likely independent of aging since the percentage of disease was not reflected in the WT mice. Given the high incidence, removal of SIRT1-OE mice may therefore be a result of disease at old age and not aging *per se*. Since the lifespan analysis in this study made no distinction between removed mice and mice that died from “natural causes”, any disease induced by SIRT1 overexpression is concealed but nonetheless shortens the survival curve of the SIRT1-OE cohort. Consequently, the outcome of SIRT1 overexpression, which the authors address as effects on lifespan, most likely also includes an effect of disease progression, independent of aging. Thus, it is mechanistically possible that a SIRT1 effect on healthy aging was undetected because it was counteracted by disease induction in this cohort. This example elucidates that lifespan analyses, as they are often conducted, may incorrectly assign results of lifespan interventions to aging, although in fact they can be independent of aging.

Using the Survival-span method may also provide valuable insights into sex differences in aging studies. In a recent study aiming to investigate the effect of restricting dietary branched-chain amino acids (BCAAs) on lifespan, the authors showed an increase on lifespan and reduction of frailty in male, but not female mice (Richardson et al., 2021). In our experience, a sudden drop in a survival curve (as shown in Figures 1A, 4A, 5D in Richardson et al., 2021) can signify incidence of disease, as demonstrated by our example shown in **Figure 4**; thus, employing the Survival-span method could have helped to differentiate between sex-specific BCAA-associated effects of disease incidence (minimum survival curve) and of aging (maximum survival curve) in Richardson et al., 2021. Hence, using the Survival-span method allows for visualization and measurements of findings that may be otherwise interpreted incorrectly and/or not discovered.

In addition to distinguishing decreasing health due to diseased states from actual aging, using the Survival-span method also promotes animal welfare. Beyond the field of aging, this method can be applied to any study across disciplines, such as the effects of various treatments on cancer. We hope that this method will be used as a standard for survival estimation in future lifespan studies as it provides a way to: 1) include all enrolled animals, 2) perform lifespan analysis while considering animal welfare, and 3) increase the quality of behavioral/biochemical analyses of the aging process.

TABLE 6 | Comparison of experimental groups A and B survival curves by log rank test.

Log-rank values	Minimal survival curves	Maximal survival curves
χ^2	4.064	2.870
df	1	1
p	0.0438	0.0903

The total number of subjects in this example is 22 for each group, in the maximal survival curves analysis, nine subjects/group have been censored.

DATA AVAILABILITY STATEMENT

The original contributions presented in the study are included in the article/Supplementary Material, further inquiries can be directed to the corresponding authors.

AUTHOR CONTRIBUTIONS

JA and MH conceptualized and formulated the model; JR and MZ provided valuable discussions and insights to the model; JA and JR wrote the manuscript; all co-authors critically revised and approved the final manuscript.

FUNDING

This work was supported by the National Institute on Aging (R00AG055683 to JR), the George and Anne Ryan Institute for Neuroscience (JR), the College of Pharmacy at the University of

Rhode Island (JR), grants from the Swedish state under the agreement between the Swedish Government and the county councils (MZ), the ALF-agreement (ALFGBG-725041 to MZ) and from De Blindas Vänner (MZ).

ACKNOWLEDGMENTS

We thank Prof. Marija Cvijovic for valuable discussions, and Dr. John Wiseman for scientific input. We would also like to acknowledge previous support by the Swedish Foundation for Strategic Research (SSF ID14-0087) and AstraZeneca (AZ postdoc program), which enabled published research that this work is based on.

REFERENCES

- Adelöf, J., Ross, J. M., Lazic, S. E., Zetterberg, M., Wiseman, J., and Hernebring, M. (2019). Conclusions from a Behavioral Aging Study on Male and Female F2 Hybrid Mice on Age-Related Behavior, Buoyancy in Water-Based Tests, and an Ethical Method to Assess Lifespan. *Aging* 11 (17), 7150–7168. doi:10.18632/aging.102242
- Adelöf, J., Wiseman, J., Zetterberg, M., and Hernebring, M. (2021). PA28α Overexpressing Female Mice Maintain Exploratory Behavior and Capacity to Prevent Protein Aggregation in hippocampus as They Age. *Aging Cell* 20, e13336. doi:10.1111/accel.13336
- Bland, J. M., and Altman, D. G. (2004). The Logrank Test. *BMJ* 328 (7447), 1073. doi:10.1136/bmj.328.7447.1073
- Breslow, N. (1974). Covariance Analysis of Censored Survival Data. *Biometrics* 30 (1), 89–99. doi:10.2307/2529620
- Cox, D. R. (1972). Regression Models and Life-Tables. *J. R. Stat. Soc. Ser. B (Methodological)* 34, 187–202. doi:10.1111/j.2517-6161.1972.tb00899.x
- Fontana, L., Partridge, L., and Longo, V. D. (2010). Extending Healthy Life Span-From Yeast to Humans. *Science* 328 (5976), 321–326. doi:10.1126/science.1172539
- Harman, D. (1991). The Aging Process: Major Risk Factor for Disease and Death. *Proc. Natl. Acad. Sci.* 88 (12), 5360–5363. doi:10.1073/pnas.88.12.5360
- Harrison, D. E., Strong, R., Sharp, Z. D., Nelson, J. F., Astle, C. M., Flurkey, K., et al. (2009). Rapamycin Fed Late in Life Extends Lifespan in Genetically Heterogeneous Mice. *Nature* 460, 392–395. doi:10.1038/nature08221
- Kaplan, E. L., and Meier, P. (1958). Nonparametric Estimation from Incomplete Observations. *J. Am. Stat. Assoc.* 53, 457–481. doi:10.1080/01621459.1958.10501452
- Kenyon, C., Chang, J., Gensch, E., Rudner, A., and Tabtiang, R. (1993). A *C. elegans* Mutant that Lives Twice as Long as Wild Type. *Nature* 366, 461–464. doi:10.1038/366461a0
- Mantel, N. (1966). Evaluation of Survival Data and Two New Rank Order Statistics Arising in its Consideration. *Cancer Chemother. Rep.* 50 (3), 163–170.
- Niccoli, T., and Partridge, L. (2012). Ageing as a Risk Factor for Disease. *Curr. Biol.* 22 (17), R741–R752. doi:10.1016/j.cub.2012.07.024
- Peto, R., and Peto, J. (1972). Asymptotically Efficient Rank Invariant Test Procedures. *J. R. Stat. Soc.* 135 (2), 185–198. doi:10.2307/2344317
- Richardson, N. E., Konon, E. N., Schuster, H. S., Mitchell, A. T., Boyle, C., Rodgers, A. C., et al. (2021). Lifelong Restriction of Dietary Branched-Chain Amino Acids Has Sex-specific Benefits for Frailty and Life Span in Mice. *Nat. Aging* 1, 73–86. doi:10.1038/s43587-020-00006-2
- Roichman, A., Elhanati, S., Aon, M. A., Abramovich, I., Di Francesco, A., Shahar, Y., et al. (2021). Restoration of Energy Homeostasis by SIRT6 Extends Healthy Lifespan. *Nat. Commun.* 12, 3208. doi:10.1038/s41467-021-23545-7
- Ross, J., Stewart, J., Hagström, E., Brené, S., Mourier, A., Coppotelli, G., et al. (2013). Germline Mitochondrial DNA Mutations Aggravate Ageing and Can Impair Brain Development. *Nature* 501, 412–415. doi:10.1038/nature12474
- Strong, R., Miller, R. A., Astle, C. M., Baur, J. A., de Cabo, R., Fernandez, E., et al. (2013). Evaluation of Resveratrol, green tea Extract, Curcumin, Oxaloacetic Acid, and Medium-Chain Triglyceride Oil on Life Span of Genetically Heterogeneous Mice. *J. Gerontol. A. Biol. Sci. Med. Sci.* 68 (1), 6–16. doi:10.1093/gerona/gls070
- Trifunovic, A., Wredenberg, A., Falkenberg, M., Spelbrink, J. N., Rovio, A. T., Bruder, C. E., et al. (2004). Premature Ageing in Mice Expressing Defective Mitochondrial DNA Polymerase. *Nature* 429, 417–423. doi:10.1038/nature02517
- Yuan, R., Tsaih, S. W., Petkova, S. B., Marin de Evsikova, C., Xing, S., Marion, M. A., et al. (2009). Aging in Inbred Strains of Mice: Study Design and Interim Report on Median Lifespans and Circulating IGF1 Levels. *Aging Cell* 8 (3), 277–287. doi:10.1111/j.1474-9726.2009.00478.x

Conflict of Interest: JA is, as of September 2021, employed by AstraZeneca.

The remaining authors declare that the research was conducted in the absence of any commercial or financial relationships that could be construed as a potential conflict of interest.

Publisher's Note: All claims expressed in this article are solely those of the authors and do not necessarily represent those of their affiliated organizations, or those of the publisher, the editors and the reviewers. Any product that may be evaluated in this article, or claim that may be made by its manufacturer, is not guaranteed or endorsed by the publisher.

Copyright © 2021 Adelöf, Ross, Zetterberg and Hernebring. This is an open-access article distributed under the terms of the Creative Commons Attribution License (CC BY). The use, distribution or reproduction in other forums is permitted, provided the original author(s) and the copyright owner(s) are credited and that the original publication in this journal is cited, in accordance with accepted academic practice. No use, distribution or reproduction is permitted which does not comply with these terms.



Progerin-Induced Impairment in Wound Healing and Proliferation in Vascular Endothelial Cells

Yizhi Jiang[†] and Julie Y. Ji^{*†}

Department of Biomedical Engineering, Indiana University Purdue University Indianapolis, Indianapolis, IN, United States

OPEN ACCESS

Edited by:

Matilde Alique,
University of Alcalá, Spain

Reviewed by:

María Arufe,
University of A Coruña, Spain
Silvia Ortega-Gutierrez,
Complutense University of Madrid,
Spain

*Correspondence:

Julie Y. Ji
jji@iupui.edu

[†]These authors have contributed
equally to this work

Specialty section:

This article was submitted to
Molecular Mechanisms of Aging,
a section of the journal
Frontiers in Aging

Received: 28 December 2021

Accepted: 27 January 2022

Published: 14 March 2022

Citation:

Jiang Y and Ji JY (2022) Progerin-Induced Impairment in Wound Healing and Proliferation in Vascular Endothelial Cells.
Front. Aging 3:844885.
doi: 10.3389/fragi.2022.844885

Progerin as a mutated isoform of lamin A protein was first known to induce premature atherosclerosis progression in patients with Hutchinson-Gilford progeria syndrome (HGPS), and its role in provoking an inflammatory response in vascular cells and accelerating cell senescence has been investigated recently. However, how progerin triggers endothelial dysfunction that often occurs at the early stage of atherosclerosis in a mechanical environment has not been studied intensively. Here, we generated a stable endothelial cell line that expressed progerin and examined its effects on endothelial wound repair under laminar flow. We found decreased wound healing rate in progerin-expressing ECs under higher shear stress compared with those under low shear. Furthermore, the decreased wound recovery could be due to reduced number of cells at late mitosis, suggesting potential interference by progerin with endothelial proliferation. These findings provided insights into how progerin affects endothelial mechanotransduction and may contribute to the disruption of endothelial integrity in HGPS vasculature, as we continue to examine the mechanistic effect of progerin in shear-induced endothelial functions.

Keywords: progerin, wound healing, shear stress, proliferation, endothelial cells, vascular

INTRODUCTION

The global prevalence of cardiovascular diseases (CVD) has led to numerous studies investigating the associated lifestyle-related or genetic risk factors. While the mortality rate of CVD has declined in the past few decades, and improvement in cardiovascular health components was observed at all ages, as the aging population steadily increases worldwide, the projected CVD cost would rise sharply by 2035 (Lloyd-Jones et al., 2010; Virani et al., 2020).

The intactness of endothelium is one of the most fundamental indices of vascular healthiness. Endothelial injury or denudation at the local area as well as a delayed or impaired re-endothelialization process could result in the exposure of the internal membrane and vascular smooth muscle cells (VSMCs) to the circulating blood, creating a pro-thrombotic environment that provoked platelet adhesion and the aggregation of inflammatory cells (Shirali et al., 2016; Mastenbroek et al., 2020). Interestingly, the capacity of endothelial cells (ECs) to restore their integrity from injuries can be enhanced by applying normal shear stress (Xia et al., 2012). The correlations between local wall shear stress (WSS) and atherosclerosis revealed by *in vivo* observations and computational modeling studies (Heo et al., 2014; Park et al., 2016) also indicate the beneficial roles of steady laminar flow in providing athero-protective effect *via* regulating EC proliferation and further remodeling process (Gimbrone and Garcia-Cardena, 2013; Roux et al., 2020). On the other hand, disturbed flow found at bifurcations and curvatures

posed stress on ECs and resulted in enhanced EC turnover rate at the denuded area (Xu, 2009; Antoniadis et al., 2015).

Lamin A/C, as one of the structural components of the nuclear lamina, not only serves as a mechanically supportive structure but also mediates many cellular events, including cell proliferation by interactions with nuclear membrane proteins and other binding factors (Moiseeva et al., 2011; Vidak et al., 2015). In the vascular system, lamin A/C was also found to be sensitive to mechanical forces and to participate in force-induced cell proliferation, such as its ability to prevent stretch-induced hyperproliferation of VSMC (Han et al., 2015). Genetic mutation in exon 11 on the lamin A/C gene (LMNA) was found to be related to the premature aging process (Simha et al., 2003; Schreiber and Kennedy, 2013). This creates a cryptic splice site responsible for the deletion of 50 amino acids on prelamin A (lamin A precursor) during the post-translational process, resulting in an absence of the recognition site for Zmpste24 (a zinc metallo-endoprotease) to remove the last 15 amino acids at the C-terminus on the precursor. This lack of post-translational modification leads to the generation of a truncated prelamin A called progerin that possesses a permanently farnesylated tail at the C-terminus. Patients carrying that mutation were referred to as having Hutchinson-Gilford progeria syndrome (HGPS). Studies have indicated progerin-induced proliferation impairment in various types of cells and its role in interfering with tissue repair (Wheaton et al., 2017; Hu et al., 2020).

Surprisingly, the McClintock group observed the ubiquitous presence of progerin mRNA transcripts in skin sections derived from healthy donors from all ages, whereas the protein level was elevated with donor's age (McClintock et al., 2007). Increased misuse of the cryptic splice site on prelamin A was also detected in normal fibroblasts over prolonged *in vitro* culture regardless of donor's age. Moreover, mechanisms such as telomere shortening, the hyperactivation of p53 tumor suppressor pathway, the extensive damage in DNA repairing, changes in histone methylation, and other age-dependent factors were also found to play a part in both progerin-induced premature aging and normal aging process (Varela et al., 2005; Benson et al., 2010; Holly et al., 2013; Arancio et al., 2014; Kubben et al., 2016; Kubben and Misteli, 2017). In the vascular system, progerin-induced premature aging syndrome also shared many characteristics with physiological aging at cellular and molecular levels (Olive et al., 2010; Hamczyk et al., 2018a). For example, the Ragnauth group found that lamin A precursor was accumulated in late-passage VSMCs or VSMCs derived from elderly donors, which was proposed to be related to the downregulation of the Zmpste24 gene due to its sensitivity toward oxidative stress over passages (Ragnauth et al., 2010). The evidence suggests that progerin may play a part in vascular aging during the normal aging process.

Considering the low number of HGPS individuals worldwide, many progeroid mouse models have been developed to facilitate HGPS research (Hamczyk et al., 2018a), among which the mice that specifically expressed progerin in the vascular system provided valuable information on how the affected vascular cells contribute to cardiovascular dysfunctions. In these models, restrictive progerin expression in VSMCs resulted in

arterial structural alternations and contractile impairment (Del Campo et al., 2019; Del Campo et al., 2020), while endothelial progerin expression tended to provoke systematic inflammatory responses, and the endothelium showed defects in response to shear stress (Osmanagic-Myers et al., 2019; Sun et al., 2020). In a progeroid model where only ECs expressed progerin, premature deaths occurred in these mice at the age approaching 25 weeks, probably due to left ventricle diastolic dysfunction. Extensive interstitial fibrosis and adventitial thickening were also reported through histological examination (Osmanagic-Myers et al., 2019).

Besides extracting cells from progeroid mice models, ECs that expressed progerin were also obtained by differentiation from iPSC (induced pluripotent stem cell) derived from fibroblasts of HGPS patients, or by transfection using constructed progerin plasmids. These progerin-expressing ECs presented features of senescence ECs in terms of shortened telomere length and nuclear dysmorphology, as well as cell cycle arrest and reduced proliferation rate (Matrone et al., 2019; Bidault et al., 2020). Attenuated response of gene regulation toward laminar flow (12 dynes/cm²) was reported, such as atheroprotective gene KLF2 and the downstream targets of NRF2. On the other hand, the expression of pro-inflammatory genes, including E-selection and VCAM-1, was upregulated. Also, observations of altered NOS regulation and abnormal expression levels of elastin and collagen indicated progerin's impact on endothelial functions in regulating vascular tone (Atchison et al., 2020).

Although many *in vitro* and *in vivo* studies have been conducted to examine changes in the phenotypes and gene expression profiles of vascular cells expressing progerin, it is not yet known how EC integrity was compromised by progerin to initiate premature atherosclerosis progression in HGPS patients. On the other hand, while flow pattern has been proven to regulate vascular EC functions, few studies were conducted to reveal the relationship between progerin and the local shear stress environments that ECs may be exposed to. In this study, we established stable cell lines of vascular ECs that overexpressed wild-type lamin A or progerin and studied the effects of progerin on the re-endothelialization process under shear stress. Furthermore, the regenerative capabilities of progeria cells at the wound front under different flow patterns were also examined. Our study helps demonstrate how progerin interferes with endothelial wound repair events in a flow environment.

MATERIALS AND METHODS

Cell Culture and Reagents

Bovine aortic endothelial cells (BAEC, pooled donors from Lonza) were grown in Dulbecco's Modification of Eagle's Medium (DMEM, Corning) containing 10% heat-inactivated fetal bovine serum (FBS, JR Scientific), 1% L-glutamine, and 2% penicillin-streptomycin (Cellgro). Human embryonic kidney (HEK) cells 293T were grown in DMEM supplemented with 10% FBS and 1% L-glutamine without antibiotics. Cells were maintained in a humidified incubator with 5% CO₂ at 37°C.

Stable Transfection

HEK293T cells were utilized to produce the retrovirus carrying either GFP-fused wt-lamin A or progerin gene. Viral production was achieved by the assembly of a retroviral packaging system that contains the packaging plasmid pUMVC (Addgene #8449), the envelope plasmid pCMV-VSV-G (Addgene #8454), and the target plasmid—pBABE-puro-GFP-wt lamin A (Addgene #17662) or pBABE-puro-GFP-progerin (Addgene #17663). Viral supernatants were collected after 48, 72, and 96 h of transfection, and were added on ECs in the presence of polybrene at a concentration of 8 µg/ml. The infection medium was replaced with regular DMEM after 4 h of infection. Drug selection began 48 h after the transduction, and the selection process continued for 10 days until 95% of cells were GFP positive.

Western Blot

The monolayer of ECs was harvested and lysed by RIPA buffer containing 20 mM Tris-HCl, 150 mM NaCl, 1 mM EDTA, 0.1% SDS, 1% Triton-X, 1 mM DTT, 0.5 mM PMSF, and 150 mM protease inhibitor. Protein concentration was determined by BCA assay and normalized before being loaded on a polyacrylamide gel for electrophoresis. After that, the gel was transferred to a PVDF membrane by the semi-dry blotting method. The membrane was blocked for an hour by 5% BSA or non-fat milk dissolved in 1F0B4 TBST. Primary antibodies included anti-lamin A/C antibody (Cell Signaling, #4777), anti-actin antibody (Sigma, A2066), and anti-GAPDH antibody (Cell Signaling, #2118) as well as corresponding secondary antibodies conjugated with HRP (Bio-rad). Chemiluminescence HRP substrate was used to image the blot. The expression levels of interested bands were normalized by its loading control on ImageJ.

Nuclear Morphology Quantifications

To characterize nuclei with unusual morphologies, including double nuclei and nuclei with foci and folds, 250–300 cell nuclei were randomly chosen from images acquired from three independent experiments. Results were expressed as the average of the number of these nuclei over the total number of nuclei.

Wound Healing Assay

Transduced ECs expressing exogenous progerin or wild-type lamin A were seeded on a glass slide at least 24 h before wound formation, and scratches were made by 200-F06D1 pipette tips, with one line parallel to the length of the slide and two lines parallel to the width. Prior to wound healing assay, cells were either kept under static conditions or pre-treated with shear stress for 16 h at 15 dynes/cm², and slides were imaged under the microscope for the next 4 h with 5% CO₂. Alternatively, the wound was formed before shear application at either low magnitude (2 dynes/cm²) or normal magnitude (15 dynes/cm²) for 4 h, and slides were imaged as described above. Phase-contrast images were acquired every hour, and the wounded area was quantified at each time point by the wound healing tool on ImageJ. About 10–20 wounded areas were randomly selected for each group for the analysis, and

wound length was 974 µm for both horizontal and vertical wounds. Results were presented as recovered area over time, which was calculated by subtracting wounded area at each time point from the initial wounded area at T = 0, and averaged to get the mean value.

Proliferation Assay

EdU proliferation assay was performed utilizing Click-iT EdU proliferation kit with Alexa Fluor 594 (Invitrogen C10339). Cells were incubated with 10 µM EdU (5-ethynyl-2'-deoxyuridine) in the growth medium for 2 h, after which they were fixed and permeabilized in 3.7% PFA solution and 0.5% Triton X-100, respectively. Fixed samples were then incubated in Click-it reaction cocktail for another 30 min according to the manufacturer's instruction. Only cells within the first 4 rows at wound edges were included for proliferation analysis. These wounded areas were further categorized by their wound orientation in relation to flow, where the "Horizontal" group denotes the wound edges that were parallel to the shear direction, and "Vertical Downstream" and "Vertical Upstream" denote the wound edges that were oblique to the shear direction and were the downstream and upstream to the flow, respectively. For areas away from wound, 8–15 fields of view at a size of 650 µm² × 487 µm² were randomly chosen for analysis for each group. The proliferation ratio was calculated as the fraction of cells stained positive by Alexa Fluor 594 over the total number of GFP-positive cells. Additionally, to characterize cells at the wounded area that were entering anaphase and telophase after flow application, images were taken at a 5-min interval for 2 h and cells undergoing nuclear expansion and separation were counted. Bi-nucleated cells were also included in the analysis.

Statistical Analysis

Data were expressed as mean ± SEM. Unpaired two-tailed Student's *t*-test was performed to compare two groups. To compare more than two groups, ordinary one-way ANOVA was performed and was followed by Tukey multiple comparisons. A *p* value of less than 0.05 was regarded as statistically significant.

RESULTS

Confirmation and Characterization of ECs With Exogenous Wild-Type Lamin A or Progerin Expression

The plasmids pBABE-puro-GFP-progerin and pBABE-puro-GFP-wt-lamin were incorporated into host cells using a retroviral packaging system, respectively, to generate cell lines with stable exogenous expressions of these proteins. After selection for single colonies, transduced cells were expanded for stable cell lines. Western blots and fluorescence images were performed to verify the external gene expressions in these cells (Figures 1A, C).

Quantification results of transduced cells with unusual nuclear morphologies (Figure 1E) revealed that a

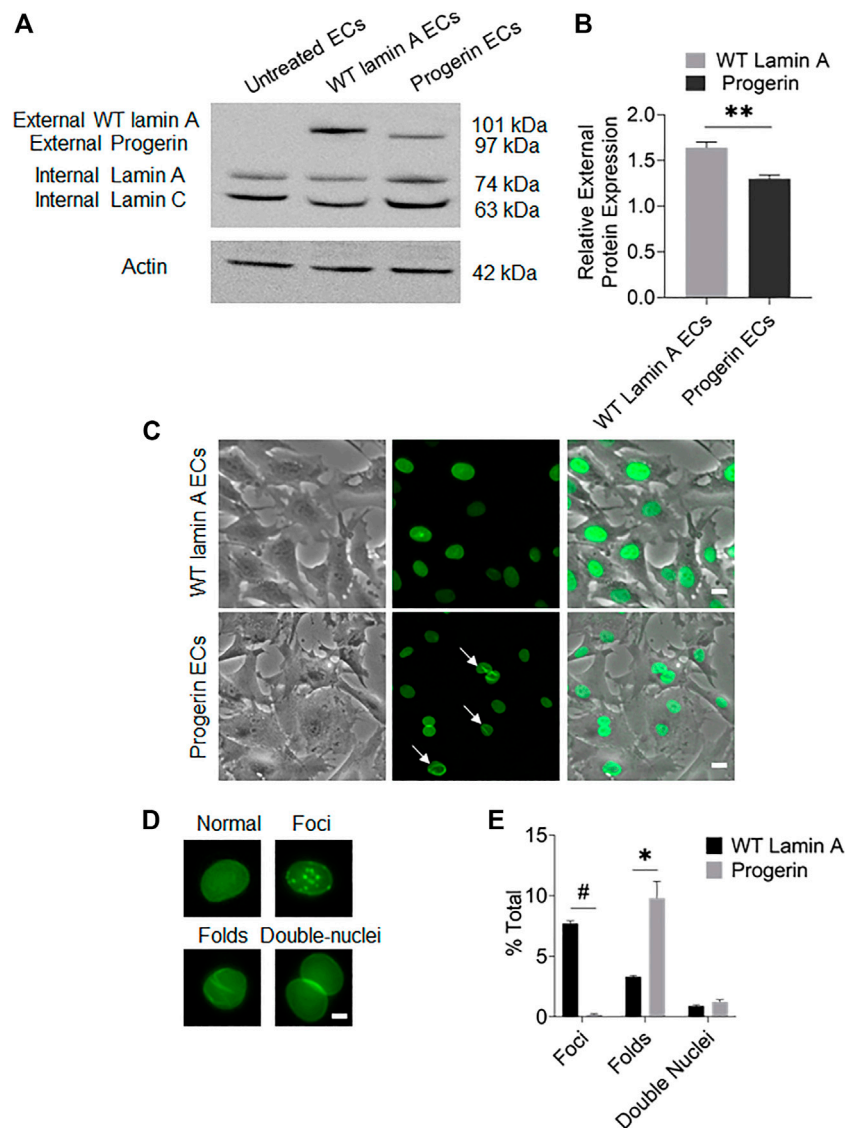


FIGURE 1 | Characterization of targeted protein expression in transduced ECs. **(A)** Western blot showed the presence of endogenous lamin A and exogenous GFP-conjugated proteins in transduced ECs. The sizes of GFP-fused proteins were determined by adding the molecular weights of GFP and the fused protein. **(B)** Quantification of wild-type lamin A and progerin protein expression levels in wild-type lamin A- and progerin-expressing ECs, respectively. **(C)** Representative images of cells showed that the GFP-conjugated proteins were specifically located at nuclei. A substantial population of cells with GFP-progerin expression showed abnormal nuclear shapes (indicated by white arrows). Scale bar: 20 μ m. **(D)** Examples of wild-type lamin A-expressing ECs with or without unusual nuclear shapes, including nuclear foci, folds and double nuclei. Scale bar: 5 μ m. **(E)** The graph showed the frequency of unusually shaped nuclei in WT lamin A- and progerin-expressing cell population. * $p < 0.01$, # $p < 0.001$.

substantial population of progerin-expressing nuclei showed wrinkles and folds, which was also one of the common characteristics of HGPS cells (Denecke et al., 2006; Constantinescu et al., 2010). Wild-type lamin A-expressing cells, on the other hand, showed an increased number of nuclear foci. The Mallampalli group also observed similar trends in their HELA cells that were transiently transfected with GFP-tagged WT lamin A, which was proposed to be related to the overexpression of the external lamin A in cells (Mallampalli et al., 2005). Our quantitative results also indicated a higher expression level of the external protein in

WT-lamin A-expressing ECs (Figure 1B). The number of double nuclei was not significantly different between these 2 cell lines.

Progerin-Expressing ECs Exhibited Differential Wound Healing Responses That Were Dependent on Flow Patterns

Wound repair in WT lamin A- or progerin-expressing endothelial monolayer was investigated by observing wound recovery rate after cells were exposed to acute wounds. First,

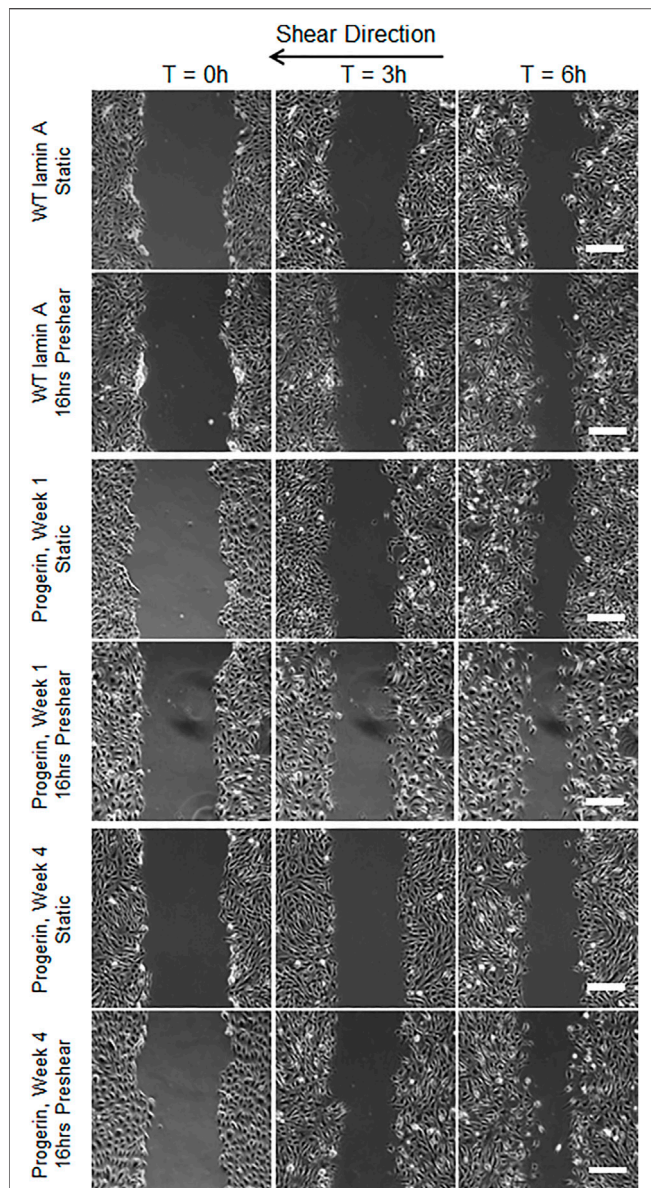


FIGURE 2 | Representative images of wound healing process with or without 16-h-preshearing condition. Wounds were formed following flow application, and images were taken for the next 6 h. Images taken at time points of 0, 3, and 6 h were shown in different columns. Scale bar: 200 μ m.

cells were either pre-treated with normal arterial shear stress of 15 dynes/cm² for 16 h or kept in the incubator before being exposed to acute wound at T = 0 h. Wound recovery for up to 6 h are shown in **Figure 2**. After recovery areas were quantified, results showed that WT lamin A-expressing ECs with pre-shearing condition showed a faster wound recovery rate than those without flow application (**Figure 3A**). The trend gradually disappeared after 5 h past wound formation, probably due to the attenuated shearing effects over time. However, progerin-expressing cells exhibited more complex recovery patterns, which were dependent on the length of

in vitro culture, especially under static state. At the first week upon transfection, progerin-expressing cells exhibited a high recovery rate without flow exposure. However, after 3 weeks of culture, the rate declined substantially (**Figure 3B**), although the external protein expression levels were not found to be altered over 4 weeks of culture (**Figure 3C**). This could be due to the reduction in proliferation rate and the associated LAP2 downregulation by progerin over serial culture (Vidak et al., 2015). Interestingly, progerin-expressing cells pretreated with 16-h flow showed similar wound recovery rates regardless of their culture period. To minimize the effects of culture time on transduced cells, only cells cultured within weeks 2 and 3

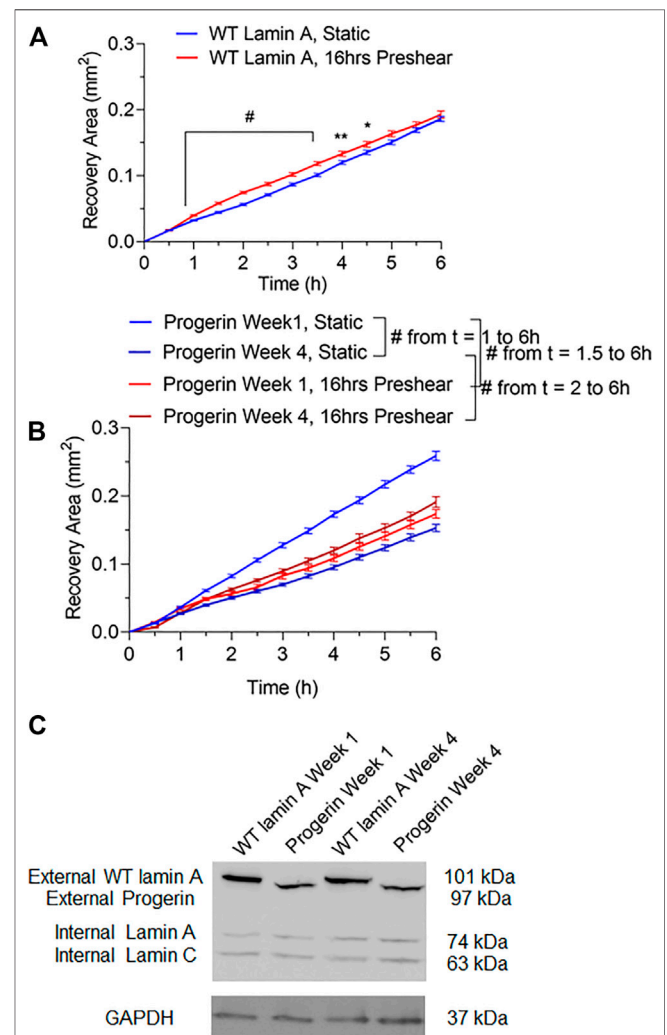


FIGURE 3 | Quantifications of wounded area covered by cells during the 6-h window after wound formation in wild-type lamin A-expressing ECs (**A**) and progerin-expressing ECs (**B**). Blue lines represent the recovery area of cells that were under static state before wound formation over time, and red lines represent that of cells that underwent 16-h pre-shearing before wounds were created. **p* < 0.05, ***p* < 0.01, #*p* < 0.001. (**C**) Representative Western blot showed external protein expression levels in transduced ECs over serial culture.

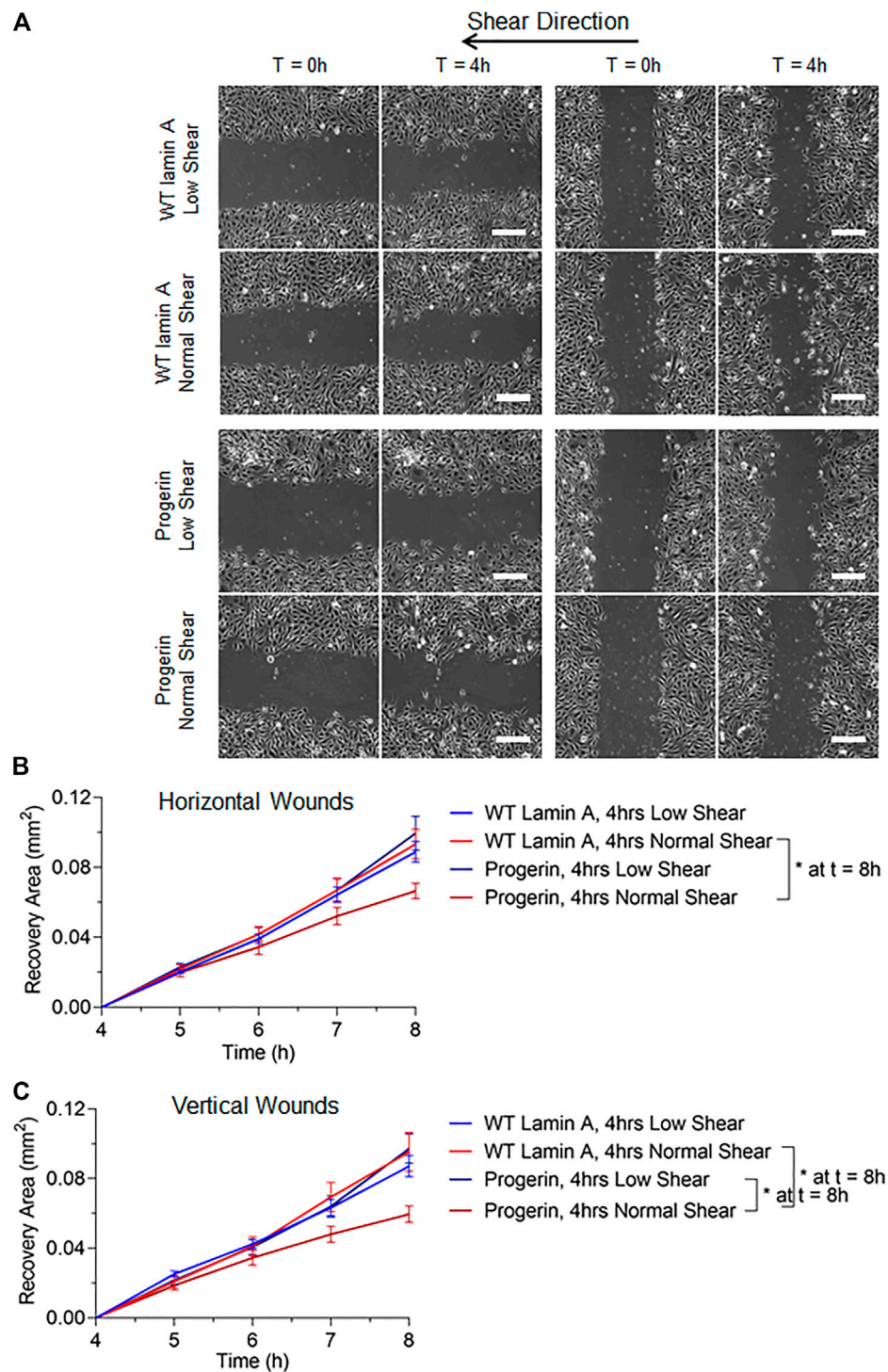


FIGURE 4 | (A) Representative images of transduced ECs during the 4-h wound healing window after exposure to flow at low (2 dynes/cm²) or normal (15 dynes/cm²) magnitude. Scale bar: 200 μ m. **(B,C)** Quantifications of wounded area covered by cells after wound formation for wild-type lamin A-expressing ECs and progerin-expressing ECs at horizontal and vertical wounds with shear stress at low or normal magnitude. Blue lines represent the recovery area of cells that were sheared at low magnitude after wound formation, and red lines represent that of cells that were sheared at normal magnitude after wound formation. * $p < 0.05$.

were used for further examinations, where the proliferation rates of these 2 cell lines were comparable under static state (Figures 5A,B).

To better mimic the continual mechanical forces that ECs are exposed to *in vivo*, we also examined the effect of low magnitude shear stress at 2 dynes/cm². In addition, post-shear experiments,

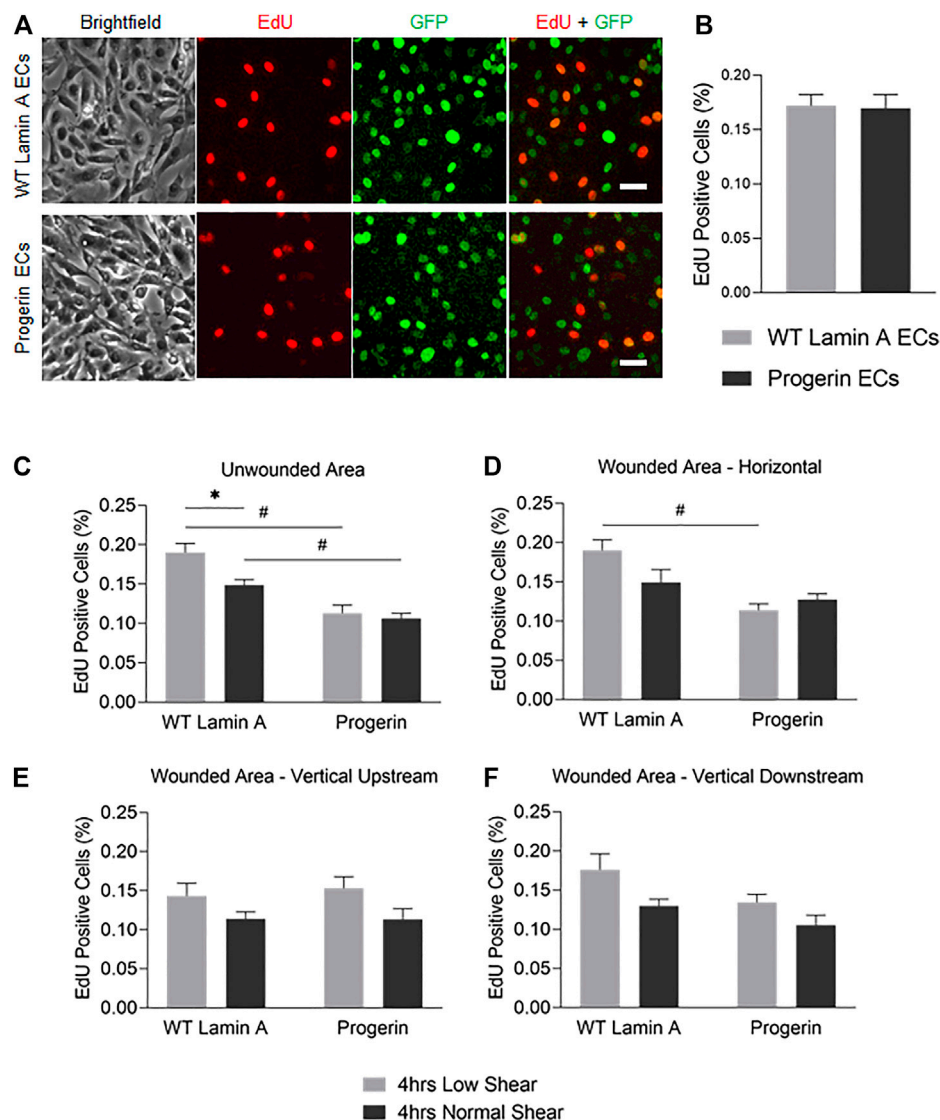


FIGURE 5 | (A) Demonstrative images of comparable proliferation rates in wild-type lamin A- and progerin-expressing ECs that were cultured within weeks 2 and 3. Cells were incubated in 10 μM EdU in growth medium for 2 h before fixation. Dyes and channels used: red channel for EdU, green channel for the presence the external proteins fused with GFP. Scale bar: 40 μm. **(B)** Quantification of comparable proliferation rates in transduced ECs that were cultured within weeks 2 and 3. **(C–F)** The percentages of EdU-positive cells at unwounded area **(C)**, horizontal wound edges **(D)**, and vertical wound edges at upstream **(E)** and downstream regions **(F)** as to flow in transduced ECs following flow application. * $p < 0.05$, # $p < 0.001$.

where wound was formed before flow applications, were carried out at both low and normal magnitudes for 4 h, to account for wound recovery under flow. Wounded areas were imaged after flow application for the next 4 h, as shown in **Figure 4A**. Wounds were further categorized as horizontal and vertical wounds in relation to the direction of flow they were exposed. Quantitative results indicated a slowdown in wound recovery rate in progerin-expressing cells after the exposure to normal shear stress regardless of wound orientation (**Figures 4B,C**). However, these flow patterns did not have a significant effect on the wound recovery rates in WT-lamin A-expressing cells in the 4-h time window. The observed difference in wound recovery event in cells overexpressing progerin may indicate its role in

suppressing endothelial wound repair ability and suggest its ability to interfere with endothelial function.

DNA Replication was Reduced by Normal Shear Stress in Wild-type Lamin A (Compared to Low, Shear Stress), but Not in Progerin-Expressing ECs

We next examined if the proliferation potential in progerin-expressing ECs was compromised at the wound edge. Cells were exposed to 4-h laminar flow at low or normal magnitude as described above, after which EdU was added to the growth medium for 2 h before fixation. At regions where endothelial

monolayer remained intact, we observed a reduction in the portion of EdU-positive cells in WT-lamin A-expressing cells exposed to normal shear stress, compared to low shear stress. This response is consistent with healthy vascular ECs from literature (Akimoto et al., 2000; Kadohama et al., 2007). On the other hand, cells expressing progerin did not show different DNA replication capacity between low or normal shear stress applied, and the percentages in both conditions were reduced compared to control cells (**Figure 5C**).

At wound edges, normal shear stress similarly reduced the portion of EdU-positive WT lamin A-expressing cells, compared to low shear, though the difference was more diminished. In contrast, the portion of EdU-positive cells did not change significantly in progerin-expressing cells, at all wound edges (**Figures 5D–F**). This suggests that wound formation could stimulate DNA synthesis in cells near wound edges, in WT lamin A-expressing ECs under normal shear stress. Progerin-expressing ECs, however, did not show altered portion of cells in S phase, between low and normal shear levels, which would not have contributed to their delayed wound healing response under normal shear (**Figure 4**).

Overall, the percent of EdU-positive cells show a similar trend between the two shear levels in both WT lamin A and progerin-expressing cells at either vertical wound (**Figures 5E,F**), suggesting that direction of flow perpendicular to wound did not impact cell proliferation between the cell lines. Also, fractions of EdU-positive cells in both WT lamin A and progerin-expressing cells at the horizontal wound are similar to those observed unwounded area (**Figures 5C,D**). However, the reduced DNA replication under normal compared to low shear seen in WT lamin A-expressing ECs is absent in progerin-expressing cells, which suggests a sensitivity in cell division toward physiological shear levels that are missing with progerin.

The Number of Cells Undergoing Late Mitosis at Wound Front Upstream to the Flow Was Reduced in Progerin-Expressing Cells

To access other cell proliferation activities besides DNA replication, the number of cells that entered anaphase and prophase at the first 4 rows near wound edges were also counted. These were identified by nuclear expansion and separation during the 2-h window after flow was applied (Takemoto et al., 2016), as shown in **Figure 6A**. Progerin-expressing cells presented an overall reduction in the portion of cells under late mitosis compared to WT lamin A-expressing ECs, especially at horizontal wounds (**Figure 6B**). Moreover, at wound edges where the wound recovery direction was against the physiological flow, i.e., at vertical downstream edges, the number of cells at anaphase and prophase was also significantly decreased in progerin-expressing ECs (**Figure 6D**). Within progerin-expressing ECs, the decrease in cells at anaphase and prophase is more pronounced when cells are exposed to the higher, normal shear stress, compared to low shear, especially at vertical downstream edges. On the other hand, the number of

binucleated cells in the progerin group is higher than that of the WT lamin A group, regardless of flow condition or shear level (**Figures 6E–G**). Binucleation appears to be a hallmark of progerin-expressing ECs, and shear-induced binucleation could be a result of cytokinesis failure in progerin-expressing ECs (Nishimura et al., 2016). No significant changes were observed in WT lamin A-expressing cells under different flow conditions, indicating that normal shear stress did not prevent these cells from entering the G2/M phase.

Taken together, our results suggest that the drop in the number of progerin-expressing cells at late mitosis could contribute to delayed wound healing response, especially at normal shear level. The difference in cell cycle observed between WT lamin A- and progerin-expressing ECs in their response toward different shear levels also suggests reduced sensitivity toward mechanical stress in progerin-expressing ECs.

DISCUSSION

Recent research has highlighted the importance of endothelial and vascular cell dysfunction in HGPS models, as well as progerin-induced mechano-sensitivity in the endothelium (Benedicto et al., 2021). While progerin in endothelial cells has been shown to induce inflammatory responses and impaired mechanotransduction (Osmanagic-Myers et al., 2019), this is a more specific study on how progerin interferes with an endothelial wound recovery. Vascular endothelial injury that may occur *in vivo* following endothelial apoptosis or during post-angioplasty restenosis disrupts endothelial integrity and permeability. Endothelial denudation would expose other vascular cells to the blood flow and trigger a cascade of inflammatory responses (Durand et al., 2004; Curcio et al., 2011). The subsequent healing responses involve endothelial proliferation and migration that occurs under blood flow *in vivo*. Recent studies have revealed the key role of progerin in vascular aging as well as the presence of similar aberrant lamin A isoform in aged people (Minamino and Komuro, 2008; Olive et al., 2010; Ragnauth et al., 2010; Gerhard-Herman et al., 2012). Progerin was also found to impair VSMC proliferation and the metabolism of low-density lipoprotein that involved crosstalk between ECs and VSMCs (Hamczyk et al., 2018b; Goldberg et al., 2018; Hamczyk et al., 2019).

In this paper, we were focusing on the effect that progerin has on endothelial healing response upon denudation under flow, as well as the how cell division and cell cycle during wound recovery are affected in progerin-expressing ECs. We hypothesize that progerin interferes with endothelial integrity under physiological flow and provided evidence of progerin-induced endothelial wound healing delay under normal shear stress (**Figure 4**). Furthermore, we investigated cell proliferation activities at wound front and wound healing direction relative to flow and found that late mitosis cells at wound edges downstream of flow were most affected by shear stress during the repair event (**Figure 6**).

Stable cell lines that expressed either wild-type lamin A or progerin protein were generated using a retrovirus packaging

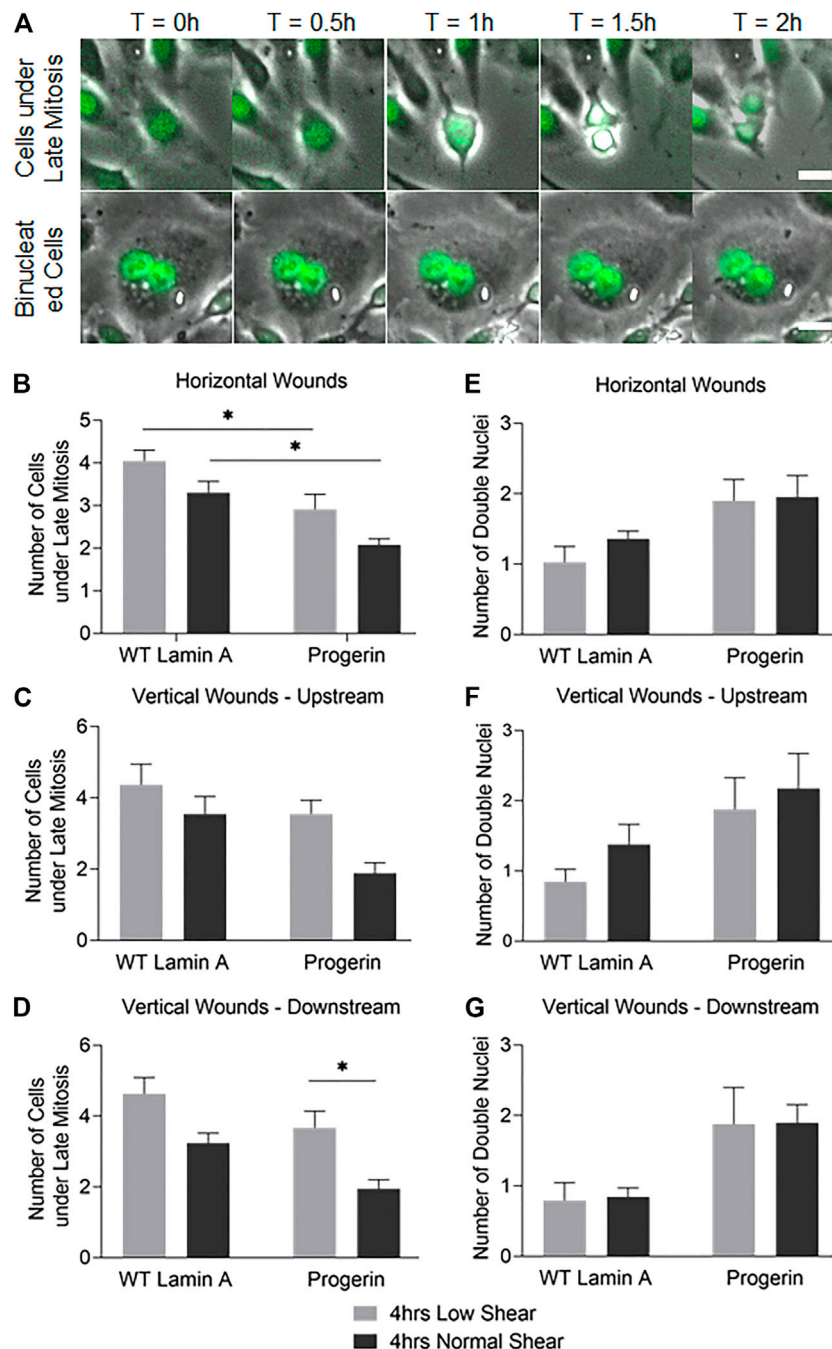


FIGURE 6 | (A) Examples of cells under late mitosis that were recognized by nuclear expansion and separation (first row), as well as cells containing double nuclei and were not followed by cytokinesis (second row) during the first 2 h following flow application. Scale bar: 20 μm. **(B–G)** Quantifications of cells that were undergoing late mitosis **(B–D)** or contained double nuclei **(E–G)** within the first 4 rows at horizontal or vertical wound edges (upstream and downstream as to flow) after flow application. * $p < 0.05$.

system. Wild-type lamin A-expressing cells exhibited nuclei foci that could be due to the overexpression of the external protein, and progerin-expressing cells were characterized as more wrinkles and folds on nuclei. Subsequent wound healing assay revealed delay in endothelial repair in progerin-expressing cells with the application of physiological shear stress, regardless of

wound directions (**Figure 4**). Further data analysis indicated that cell proliferation abilities were compromised at wound front in these ECs, where the number of cells at late mitosis was significantly reduced at vertical wound edges downstream of flow at normal shear stress compared to low shear (**Figure 6**). These data suggest that endothelial recovery in progerin-

expressing ECs was particularly sensitive to physiological shear when it is against the direction of wound recovery.

Additionally, progerin-expressing cells also showed reduced fraction of cells undergoing DNA replication under flow, although the DNA synthesis rate was comparable between wild-type lamin A- and progerin-expressing cells under static state (**Figure 5**). Normal shear stress reduced number of cells in S phase in WT lamin A-expressing cells, which agrees with previous studies that showed laminar physiological suppressed proliferation as a way to maintain EC quiescent phenotype at athero-protective regions (Chistiakov et al., 2017). The attenuation of fraction of cells in S phase by normal shear is not seen in progerin-expressing cells, which suggests their loss of mechano-sensitivity to shear stress, in regulating the cell cycle.

On the other hand, the number of binucleated cells at the wound front is more prominent in progerin ECs under different patterns of flow (**Figure 6**). In normal tissues and tumors, cells with double nuclei were also observed and are thought to be a result of cytokinesis failure or cell fusion (Nishimura et al., 2016). Although binucleated cells were also present in healthy primary culture, the amount was dramatically increased in HGPS fibroblast and adipocytes, which could be related to abnormal chromosome segregation and accelerated cell senescence (Dominici et al., 2001; Cao et al., 2007; Xiong et al., 2013). However, the underlying mechanisms of binucleated cells remain unknown, and the clinical significance is controversial (Chen et al., 2007).

In summary, we found decreased wound healing rate in progerin-expressing ECs under physiological level of laminar shear stress compared with those under low magnitude shear, and the effect was independent on wound orientations relative to flow direction. Further examination showed that the delayed wound recovery coincided with a reduced number of cells at late mitosis, suggesting potential interference by progerin with delayed cell division. Attenuation of DNA synthesis by normal level of shear stress observed in WT lamin A endothelial cells also disappeared in progerin cells. Both findings support the conclusion that endothelial responses toward athero-protective levels of shear stress were not seen in progerin-expressing ECs, which demonstrates a reduced sensitivity toward mechanical stress in endothelial cells in the presence of progerin. This finding is also in agreement with other recent studies on progerin-expressing endothelium (Osmanagic-Myers et al., 2019).

Research on how progerin affects vascular aging is still ongoing. For example, the exact isoform of prelamin A in elderly people remains unclear. The detection of progerin in cells or tissues derived from normal healthy people has been reported (Scaffidi and Misteli, 2006; McClintock et al., 2007), while the accumulation of the farnesylated prelamin A that retains the 50 amino acids near the carboxyl-terminus was observed in late-passage VSMCs or those from aged donors (Ragnauth et al., 2010). Although the difference in those prelamin A isoforms seemed to be minor in structure, its

accumulation mechanisms and downstream effects could be varied.

Moreover, it is still unclear if the toxicity of progerin in HGPS patients was induced by its farnesyl lipid anchor or the 50-amino-acid deletion near the C-terminus. This stems from the purpose of prelamin A processing based on our current understanding. It was found that prelamin A farnesylation in mammalian cells was critical in anchoring lamin A to nuclear lamina during interphase (Lutz et al., 1992; Hennekes and Nigg, 1994). The absence of the farnesylation step on prelamin A also resulted in reduced binding affinity with heterochromatin in HEK293 cells (Lattanzi et al., 2007). However, further studies revealed that the elimination of the farnesylated tail on progerin did not rescue all phenotypes in HGPS cells (Verstraeten et al., 2008). A mouse model that bypassed the modifications and only expressed mature lamin A exhibited normal body weight and survived without developing severe disease phenotypes (Yang et al., 2008; Coffinier et al., 2010).

Current treatment plan for HGPS is still being under development. The first and only drug approved by the US Food and Drug Administration (FDA), Zokinvy (lonafarnib), is a farnesyltransferase inhibitor that detaches progerin from the nuclear membrane. However, farnesyltransferase inhibitors did not rescue all phenotypes in HGPS cells, probably due to the retainment of progerin within nucleoplasm (Verstraeten et al., 2008). Other therapies have been recognized recently, such as isoprenylcysteine carboxyl methyltransferase (ICMT) inhibitor and progerin-lamin A binding inhibitors (Chen et al., 2021; Kang et al., 2021; Macicior et al., 2021; Marcos-Ramiro et al., 2021). More investigations in the functional roles of the deleted 50 amino acids could shed light on alleviating the effect of progerin as well as better HGPS treatment regimens (Lai and Wong, 2020).

We are currently working to continue to examine the mechanistic effect of progerin in shear-induced endothelial functions such as migration, which also plays a key role in the re-endothelialization process. Our findings provided insights into how progerin affects endothelial mechanotransduction in our effort to understand the presence of plaques in HGPS vasculature (Hamczyk et al., 2018a); while further emphasizing the importance of physiological shear in promoting and maintaining endothelial integrity.

DATA AVAILABILITY STATEMENT

The raw data supporting the conclusions of this article will be made available by the authors, without undue reservation.

AUTHOR CONTRIBUTIONS

YJ was responsible for most of the experimental procedures. YJ and JJ contributed to data analysis. YJ and JJ helped write the manuscript.

REFERENCES

- Akimoto, S., Mitsumata, M., Sasaguri, T., and Yoshida, Y. (2000). Laminar Shear Stress Inhibits Vascular Endothelial Cell Proliferation by Inducing Cyclin-dependent Kinase Inhibitor P21 Sdi1/Cip1/Waf1. *Circ. Res.* 86 (2), 185–190. doi:10.1161/01.res.86.2.185
- Antoniadis, A. P., Giannopoulos, A. A., Wentzel, J. J., Joner, M., Giannoglou, G. D., Virmani, R., et al. (2015). Impact of Local Flow Haemodynamics on Atherosclerosis in Coronary Artery Bifurcations. *EuroIntervention* 11 (Suppl. V), V18–V22. doi:10.4244/EIJV11SVA4
- Arancio, W., Pizzolanti, G., Genovese, S. I., Pitrone, M., and Giordano, C. (2014). Epigenetic Involvement in Hutchinson-Gilford Progeria Syndrome: a Mini-Review. *Gerontology* 60 (3), 197–203. doi:10.1159/000357206
- Atchison, L., Abutaleb, N. O., Snyder-Mounts, E., Gete, Y., Ladha, A., Ribar, T., et al. (2020). iPSC-Derived Endothelial Cells Affect Vascular Function in a Tissue-Engineered Blood Vessel Model of Hutchinson-Gilford Progeria Syndrome. *Stem Cell Rep.* 14 (2), 325–337. doi:10.1016/j.stemcr.2020.01.005
- Benedicto, I., Dorado, B., and Andrés, V. (2021). Molecular and Cellular Mechanisms Driving Cardiovascular Disease in Hutchinson-Gilford Progeria Syndrome: Lessons Learned from Animal Models. *Cells* 10 (5), 1157. doi:10.3390/cells10051157
- Benson, E. K., Lee, S. W., and Aaronson, S. A. (2010). Role of Progerin-Induced Telomere Dysfunction in HGPS Premature Cellular Senescence. *J. Cell. Sci.* 123 (Pt 15), 2605–2612. doi:10.1242/jcs.067306
- Bidault, G., Garcia, M., Capeau, J., Morichon, R., Vigouroux, C., and Bérézat, V. (2020). Progerin Expression Induces Inflammation, Oxidative Stress and Senescence in Human Coronary Endothelial Cells. *Cells* 9 (5), 1201. doi:10.3390/cells9051201
- Cao, K., Capell, B. C., Erdos, M. R., Djabali, K., and Collins, F. S. (2007). A Lamin A Protein Isoform Overexpressed in Hutchinson-Gilford Progeria Syndrome Interferes with Mitosis in Progeria and normal Cells. *Proc. Natl. Acad. Sci.* 104 (12), 4949–4954. doi:10.1073/pnas.0611640104
- Chen, E. H., Grote, E., Mohler, W., and Vignery, A. (2007). Cell-Cell Fusion. *FEBS Lett.* 581 (11), 2181–2193. doi:10.1016/j.febslet.2007.03.033
- Chen, X., Yao, H., Kashif, M., Revéchon, G., Eriksson, M., Hu, J., et al. (2021). A Small-Molecule ICMT Inhibitor Delays Senescence of Hutchinson-Gilford Progeria Syndrome Cells. *Elife* 10, e63284. doi:10.7554/eLife.63284
- Chistiakov, D. A., Orekhov, A. N., and Bobryshev, Y. V. (2017). Effects of Shear Stress on Endothelial Cells: Go with the Flow. *Acta Physiol.* 219 (2), 382–408. doi:10.1111/apha.12725
- Coffinier, C., Jung, H.-J., Li, Z., Nobumori, C., Yun, U. J., Farber, E. A., et al. (2010). Direct Synthesis of Lamin A, Bypassing Prelamin A Processing, Causes Misshapen Nuclei in Fibroblasts but No Detectable Pathology in Mice. *J. Biol. Chem.* 285 (27), 20818–20826. doi:10.1074/jbc.M110.128835
- Constantinescu, D., Csoka, A. B., Navara, C. S., and Schatten, G. P. (2010). Defective DSB Repair Correlates with Abnormal Nuclear Morphology and Is Improved with FTI Treatment in Hutchinson-Gilford Progeria Syndrome Fibroblasts. *Exp. Cell Res.* 316 (17), 2747–2759. doi:10.1016/j.yexcr.2010.05.015
- Curcio, A., Torella, D., and Indolfi, C. (2011). Mechanisms of Smooth Muscle Cell Proliferation and Endothelial Regeneration after Vascular Injury and Stenting - Approach to Therapy -. *Circ. J.* 75 (6), 1287–1296. doi:10.1253/circj.cj-11-0366
- Del Campo, L., Sánchez-López, A., Salas, M., von Kleck, R. A., Expósito, E., González-Gómez, C., et al. (2019). Vascular Smooth Muscle Cell-specific Progerin Expression in a Mouse Model of Hutchinson-Gilford Progeria Syndrome Promotes Arterial Stiffness: Therapeutic Effect of Dietary Nitrite. *Aging Cell* 18 (3), e12936. doi:10.1111/acer.12936
- Del Campo, L., Sánchez-López, A., González-Gómez, C., Andrés-Manzano, M. J., Dorado, B., and Andrés, V. (2020). Vascular Smooth Muscle Cell-Specific Progerin Expression Provokes Contractile Impairment in a Mouse Model of Hutchinson-Gilford Progeria Syndrome that Is Ameliorated by Nitrite Treatment. *Cells* 9 (3), 656. doi:10.3390/cells9030656
- Denecke, J., Brune, T., Feldhaus, T., Robenek, H., Kranz, C., Auchus, R. J., et al. (2006). A Homozygous ZMPSTE24null Mutation in Combination with a Heterozygous Mutation in the LMNA gene Causes Hutchinson-Gilford Progeria Syndrome (HGPS): Insights into the Pathophysiology of HGPS. *Hum. Mutat.* 27 (6), 524–531. doi:10.1002/humu.20315
- Dominici, M., Campioni, D., Lanza, F., Luppi, M., Barozzi, P., Pauli, S., et al. (2001). Angiogenesis in Multiple Myeloma: Correlation between *In Vitro* Endothelial Colonies Growth (CFU-En) and Clinical-Biological Features. *Leukemia* 15 (1), 171–176. doi:10.1038/sj.leu.2401984
- Durand, E., Scoazec, A., Lafont, A., Boddaert, J., Al Hajzen, A., Addad, F., et al. (2004). *In Vivo* Induction of Endothelial Apoptosis Leads to Vessel Thrombosis and Endothelial Denudation: a Clue to the Understanding of the Mechanisms of Thrombotic Plaque Erosion. *Circulation* 109 (21), 2503–2506. doi:10.1161/01.CIR.0000130172.62481.90
- Gerhard-Herman, M., Smoot, L. B., Wake, N., Kieran, M. W., Kleinman, M. E., Miller, D. T., et al. (2012). Mechanisms of Premature Vascular Aging in Children with Hutchinson-Gilford Progeria Syndrome. *Hypertension* 59 (1), 92–97. doi:10.1161/HYPERTENSIONAHA.111.180919
- Gimbrone, M. A., Jr., and García-Cardeña, G. (2013). Vascular Endothelium, Hemodynamics, and the Pathobiology of Atherosclerosis. *Cardiovasc. Pathol.* 22 (1), 9–15. doi:10.1016/j.carpath.2012.06.006
- Goldberg, I. J., Reue, K., Abumrad, N. A., Bickel, P. E., Cohen, S., Fisher, E. A., et al. (2018). Deciphering the Role of Lipid Droplets in Cardiovascular Disease. *Circulation* 138 (3), 305–315. doi:10.1161/CIRCULATIONAHA.118.033704
- Hamczyk, M. R., del Campo, L., and Andrés, V. (2018a). Aging in the Cardiovascular System: Lessons from Hutchinson-Gilford Progeria Syndrome. *Annu. Rev. Physiol.* 80, 27–48. doi:10.1146/annurev-physiol-021317-121454
- Hamczyk, M. R., Villa-Belostá, R., Gonzalo, P., Andrés-Manzano, M. J., Nogales, P., Bentzon, J. F., et al. (2018b). Vascular Smooth Muscle-Specific Progerin Expression Accelerates Atherosclerosis and Death in a Mouse Model of Hutchinson-Gilford Progeria Syndrome. *Circulation* 138 (3), 266–282. doi:10.1161/CIRCULATIONAHA.117.030856
- Hamczyk, M. R., Villa-Belostá, R., Quesada, V., Gonzalo, P., Vidak, S., Nevado, R. M., et al. (2019). Progerin Accelerates Atherosclerosis by Inducing Endoplasmic Reticulum Stress in Vascular Smooth Muscle Cells. *EMBO Mol. Med.* 11 (4), e9736. doi:10.15252/emmm.201809736
- Han, Y., Wang, L., Yao, Q.-P., Zhang, P., Liu, B., Wang, G.-L., et al. (2015). Nuclear Envelope Proteins Nesprin2 and LaminA Regulate Proliferation and Apoptosis of Vascular Endothelial Cells in Response to Shear Stress. *Biochim. Biophys. Acta (Bba) - Mol. Cell Res.* 1853 (5), 1165–1173. doi:10.1016/j.bbamcr.2015.02.013
- Hennekes, H., and Nigg, E. A. (1994). The Role of Isoprenylation in Membrane Attachment of Nuclear Lamins. A Single point Mutation Prevents Proteolytic Cleavage of the Lamin A Precursor and Confers Membrane Binding Properties. *J. Cell. Sci.* 107 (Pt 4), 1019–1029. doi:10.1242/jcs.107.4.1019
- Heo, K.-S., Fujiwara, K., and Abe, J.-i. (2014). Shear Stress and Atherosclerosis. *Mol. Cell.* 37 (6), 435–440. doi:10.14348/molcells.2014.0078
- Holly, A. C., Melzer, D., Pilling, L. C., Fellows, A. C., Tanaka, T., Ferrucci, L., et al. (2013). Changes in Splicing Factor Expression Are Associated with Advancing Age in Man. *Mech. Ageing Dev.* 134 (9), 356–366. doi:10.1016/j.mad.2013.05.006
- Hu, X.-T., Song, H.-C., Yu, H., Wu, Z.-C., Liu, X.-G., and Chen, W.-C. (2020). Overexpression of Progerin Results in Impaired Proliferation and Invasion of Non-Small Cell Lung Cancer Cells. *Ott* 13, 2629–2642. doi:10.2147/OTT.S237016
- Kadomata, T., Nishimura, K., Hoshino, Y., Sasajima, T., and Sumpio, B. E. (2007). Effects of Different Types of Fluid Shear Stress on Endothelial Cell Proliferation and Survival. *J. Cell. Physiol.* 212 (1), 244–251. doi:10.1002/jcp.21024
- Kang, S.-m., Yoon, M.-H., Ahn, J., Kim, J.-E., Kim, S. Y., Kang, S. Y., et al. (2021). Progerin, an Optimized Progerin-Lamin A Binding Inhibitor, Ameliorates Premature Senescence Phenotypes of Hutchinson-Gilford Progeria Syndrome. *Commun. Biol.* 4 (1), 5. doi:10.1038/s42003-020-01540-w
- Kubben, N., and Misteli, T. (2017). Shared Molecular and Cellular Mechanisms of Premature Ageing and Ageing-Associated Diseases. *Nat. Rev. Mol. Cell Biol.* 18 (10), 595–609. doi:10.1038/nrm.2017.68
- Kubben, N., Zhang, W., Wang, L., Voss, T. C., Yang, J., Qu, J., et al. (2016). Repression of the Antioxidant NRF2 Pathway in Premature Aging. *Cell* 165 (6), 1361–1374. doi:10.1016/j.cell.2016.05.017
- Lai, W. F., and Wong, W. T. (2020). Progress and Trends in the Development of Therapies for Hutchinson-Gilford Progeria Syndrome. *Aging Cell* 19 (7), e13175. doi:10.1111/acer.13175

- Lattanzi, G., Columbaro, M., Mattioli, E., Cenni, V., Camozzi, D., Wehnert, M., et al. (2007). Pre-Lamin A Processing Is Linked to Heterochromatin Organization. *J. Cel. Biochem.* 102 (5), 1149–1159. doi:10.1002/jcb.21467
- Lloyd-Jones, D., Lloyd-Jones, D., Adams, R. J., Brown, T. M., Carnethon, M., Dai, S., et al. (2010). Executive Summary: Heart Disease and Stroke Statistics-2010 Update: A Report from the American Heart Association. *Circulation* 121 (7), 948–954. doi:10.1161/CIRCULATIONAHA.109.192666
- Lutz, R. J., Trujillo, M. A., Denham, K. S., Wenger, L., and Sinensky, M. (1992). Nucleoplasmic Localization of Prelamin A: Implications for Prenylation-dependent Lamin A Assembly into the Nuclear Lamina. *Proc. Natl. Acad. Sci.* 89 (7), 3000–3004. doi:10.1073/pnas.89.7.3000
- Macicior, J., Marcos-Ramiro, B., and Ortega-Gutiérrez, S. (2021). Small-Molecule Therapeutic Perspectives for the Treatment of Progeria. *Ijms* 22 (13), 7190. doi:10.3390/ijms22137190
- Mallampalli, M. P., Huyer, G., Bendale, P., Gelb, M. H., and Michaelis, S. (2005). Inhibiting Farnesylation Reverses the Nuclear Morphology Defect in a HeLa Cell Model for Hutchinson-Gilford Progeria Syndrome. *Proc. Natl. Acad. Sci.* 102 (40), 14416–14421. doi:10.1073/pnas.0503712102
- Marcos-Ramiro, B., Gil-Ordóñez, A., Marín-Ramos, N. I., Ortega-Nogales, F. J., Balabasquer, M., Gonzalo, P., et al. (2021). Isoprenylcysteine Carboxylmethyltransferase-Based Therapy for Hutchinson-Gilford Progeria Syndrome. *ACS Cent. Sci.* 7 (8), 1300–1310. doi:10.1021/acscentsci.0c01698
- Masterbroek, T. G., Karel, M. F. A., Nagy, M., Chayoua, W., Korsten, E. I. J., Coenen, D. M., et al. (2020). Vascular Protective Effect of Aspirin and Rivaroxaban upon Endothelial Denudation of the Mouse Carotid Artery. *Sci. Rep.* 10 (1), 19360. doi:10.1038/s41598-020-76377-8
- Matrone, G., Thandavarayan, R. A., Walther, B. K., Meng, S., Mojiri, A., and Cooke, J. P. (2019). Dysfunction of iPSC-Derived Endothelial Cells in Human Hutchinson-Gilford Progeria Syndrome. *Cell Cycle* 18 (19), 2495–2508. doi:10.1080/15384101.2019.1651587
- McClintock, D., Ratner, D., Lokuge, M., Owens, D. M., Gordon, L. B., Collins, F. S., et al. (2007). The Mutant Form of Lamin A that Causes Hutchinson-Gilford Progeria Is a Biomarker of Cellular Aging in Human Skin. *PLoS One* 2 (12), e1269. doi:10.1371/journal.pone.0001269
- Minamino, T., and Komuro, I. (2008). Vascular Aging: Insights from Studies on Cellular Senescence, Stem Cell Aging, and Progeroid Syndromes. *Nat. Rev. Cardiol.* 5 (10), 637–648. doi:10.1038/nrcardio.1324
- Moiseeva, O., Bourdeau, V., Vernier, M., Dabauvalle, M.-C., and Ferbeyre, G. (2011). Retinoblastoma-independent Regulation of Cell Proliferation and Senescence by the P53-P21 axis in Lamin A/C-Depleted Cells. *Aging Cell* 10 (5), 789–797. doi:10.1111/j.1474-9726.2011.00719.x
- Nishimura, K., Watanabe, S., Hayashida, R., Sugishima, S., Iwasaka, T., and Kaku, T. (2016). Binucleated HeLa Cells Are Formed by Cytokinesis Failure in Starvation and Keep the Potential of Proliferation. *Cytotechnology* 68 (4), 1123–1130. doi:10.1007/s10616-015-9869-6
- Olive, M., Harten, I., Mitchell, R., Beers, J. K., Djabali, K., Cao, K., et al. (2010). Cardiovascular Pathology in Hutchinson-Gilford Progeria: Correlation with the Vascular Pathology of Aging. *Atvb* 30 (11), 2301–2309. doi:10.1161/ATVBAHA.110.209460
- Osmanagic-Myers, S., Kiss, A., Manakanatas, C., Hamza, O., Sedlmayer, F., Szabo, P. L., et al. (2019). Endothelial Progerin Expression Causes Cardiovascular Pathology through an Impaired Mechanoreponse. *J. Clin. Invest.* 129 (2), 531–545. doi:10.1172/JCI121297
- Park, J.-B., Choi, G., Chun, E. J., Kim, H. J., Park, J., Jung, J.-H., et al. (2016). Computational Fluid Dynamic Measures of wall Shear Stress Are Related to Coronary Lesion Characteristics. *Heart* 102 (20), 1655–1661. doi:10.1136/heartjnl-2016-309299
- Ragnauth, C. D., Warren, D. T., Liu, Y., McNair, R., Tajsic, T., Figg, N., et al. (2010). Prelamin A Acts to Accelerate Smooth Muscle Cell Senescence and Is a Novel Biomarker of Human Vascular Aging. *Circulation* 121 (20), 2200–2210. doi:10.1161/CIRCULATIONAHA.109.902056
- Roux, E., Bougaran, P., Dufourcq, P., and Couffignal, T. (2020). Fluid Shear Stress Sensing by the Endothelial Layer. *Front. Physiol.* 11, 861. doi:10.3389/fphys.2020.00861
- Scaffidi, P., and Misteli, T. (2006). Lamin A-Dependent Nuclear Defects in Human Aging. *Science* 312 (5776), 1059–1063. doi:10.1126/science.1127168
- Schreiber, K. H., and Kennedy, B. K. (2013). When Lamins Go Bad: Nuclear Structure and Disease. *Cell* 152 (6), 1365–1375. doi:10.1016/j.cell.2013.02.015
- Shirali, A. S., McDonald, A. I., Mack, J. J., and Iruela-Arispe, M. L. (2016). Reproducible Arterial Denudation Injury by Infraarenal Abdominal Aortic Clamping in a Murine Model. *JoVE* 117, 54755. doi:10.3791/54755
- Simha, V., Agarwal, A. K., Oral, E. A., Fryns, J.-P., and Garg, A. (2003). Genetic and Phenotypic Heterogeneity in Patients with Mandibuloacral Dysplasia-Associated Lipodystrophy. *J. Clin. Endocrinol. Metab.* 88 (6), 2821–2824. doi:10.1210/jc.2002-021575
- Sun, S., Qin, W., Tang, X., Meng, Y., Hu, W., Zhang, S., et al. (2020). Vascular Endothelium-Targeted Sirt7 Gene Therapy Rejuvenates Blood Vessels and Extends Life Span in a Hutchinson-Gilford Progeria Model. *Sci. Adv.* 6 (8), eay5556. doi:10.1126/sciadv.aay5556
- Takemoto, A., Kawashima, S. A., Li, J.-J., Jeffery, L., Yamatsugu, K., Elemento, O., et al. (2016). Nuclear Envelope Expansion Is Critical for Proper Chromosomal Segregation during a Closed Mitosis. *J. Cel Sci* 129 (6), 1250–1259. doi:10.1242/jcs.181560
- Varela, I., Cadiñanos, J., Pendás, A. M., Gutiérrez-Fernández, A., Folgueras, A. R., Sánchez, L. M., et al. (2005). Accelerated Ageing in Mice Deficient in Zmpste24 Protease Is Linked to P53 Signalling Activation. *Nature* 437 (7058), 564–568. doi:10.1038/nature04019
- Verstraeten, V. L. R. M., Ji, J. Y., Cummings, K. S., Lee, R. T., and Lammerding, J. (2008). Increased Mechanosensitivity and Nuclear Stiffness in Hutchinson-Gilford Progeria Cells: Effects of Farnesyltransferase Inhibitors. *Aging Cell* 7 (3), 383–393. doi:10.1111/j.1474-9726.2008.00382.x
- Vidak, S., Kubben, N., Dechat, T., and Foisner, R. (2015). Proliferation of Progeria Cells Is Enhanced by Lamina-Associated Polypeptide 2a (LAP2a) through Expression of Extracellular Matrix Proteins. *Genes Dev.* 29 (19), 2022–2036. doi:10.1101/gad.263939.115
- Virani, S. S., Alonso, A., Benjamin, E. J., Bittencourt, M. S., Callaway, C. W., Carson, A. P., et al. (2020). Heart Disease and Stroke Statistics-2020 Update: A Report from the American Heart Association. *Circulation* 141 (9), e139–e596. doi:10.1161/CIR.0000000000000757
- Wheaton, K., Campuzano, D., Ma, W., Sheinis, M., Ho, B., Brown, G. W., et al. (2017). Progerin-Induced Replication Stress Facilitates Premature Senescence in Hutchinson-Gilford Progeria Syndrome. *Mol. Cel. Biol.* 37 (14), e00659–16. doi:10.1128/MCB.00659-16
- Xia, W. H., Yang, Z., Xu, S. Y., Chen, L., Zhang, X. Y., Li, J., et al. (2012). Age-related Decline in Reendothelialization Capacity of Human Endothelial Progenitor Cells Is Restored by Shear Stress. *Hypertension* 59 (6), 1225–1231. doi:10.1161/HYPERTENSIONAHA.111.179820
- Xiong, Z.-M., LaDana, C., Wu, D., and Cao, K. (2013). An Inhibitory Role of Progerin in the Gene Induction Network of Adipocyte Differentiation from iPS Cells. *Aging* 5 (4), 288–303. doi:10.18632/aging.100550
- Xu, Q. (2009). Disturbed Flow-Enhanced Endothelial Turnover in Atherosclerosis. *Trends Cardiovasc. Med.* 19 (6), 191–195. doi:10.1016/j.tcm.2009.12.002
- Yang, S. H., Andres, D. A., Spielmann, H. P., Young, S. G., and Fong, L. G. (2008). Progerin Elicits Disease Phenotypes of Progeria in Mice whether or Not it Is Farnesylated. *J. Clin. Invest.* 118 (10), 3291–3300. doi:10.1172/JCI35876

Conflict of Interest: The authors declare that the research was conducted in the absence of any commercial or financial relationships that could be construed as a potential conflict of interest.

Publisher's Note: All claims expressed in this article are solely those of the authors and do not necessarily represent those of their affiliated organizations, or those of the publisher, the editors, and the reviewers. Any product that may be evaluated in this article, or claim that may be made by its manufacturer, is not guaranteed or endorsed by the publisher

Copyright © 2022 Jiang and Ji. This is an open-access article distributed under the terms of the Creative Commons Attribution License (CC BY). The use, distribution or reproduction in other forums is permitted, provided the original author(s) and the copyright owner(s) are credited and that the original publication in this journal is cited, in accordance with accepted academic practice. No use, distribution or reproduction is permitted which does not comply with these terms.



OPEN ACCESS

EDITED BY
Anders Olsen,
Aalborg University, Denmark

REVIEWED BY
Ilke Sen,
Karolinska Institutet (KI), Sweden
Alexander Mendenhall,
University of Washington, United States

*CORRESPONDENCE
Rex A. Kerr,
rex@calicolabs.com

†PRESENT ADDRESS
Jerome Goudeau,
Pfizer, San Diego, CA, United States.

SPECIALTY SECTION
This article was submitted to Molecular
Mechanisms of Aging,
a section of the journal
Frontiers in Aging

RECEIVED 30 April 2022
ACCEPTED 12 July 2022
PUBLISHED 29 August 2022

CITATION
Kerr RA, Roux AE, Goudeau J and
Kenyon C (2022), The *C. elegans*
Observatory: High-throughput
exploration of behavioral aging.
Front. Aging 3:932656.
doi: 10.3389/fragi.2022.932656

COPYRIGHT
© 2022 Kerr, Roux, Goudeau and
Kenyon. This is an open-access article
distributed under the terms of the
[Creative Commons Attribution License](#)
(CC BY). The use, distribution or
reproduction in other forums is
permitted, provided the original
author(s) and the copyright owner(s) are
credited and that the original
publication in this journal is cited, in
accordance with accepted academic
practice. No use, distribution or
reproduction is permitted which does
not comply with these terms.

The *C. elegans* Observatory: High-throughput exploration of behavioral aging

Rex A. Kerr*, Antoine E. Roux, Jérôme Goudeau† and
Cynthia Kenyon

Calico Life Sciences LLC, South San Francisco, CA, United States

Organisms undergo a variety of characteristic changes as they age, suggesting a substantial commonality in the mechanistic basis of aging. Experiments in model organisms have revealed a variety of cellular systems that impact lifespan, but technical challenges have prevented a comprehensive evaluation of how these components impact the trajectory of aging, and many components likely remain undiscovered. To facilitate the deeper exploration of aging trajectories at a sufficient scale to enable primary screening, we have created the *Caenorhabditis elegans* Observatory, an automated system for monitoring the behavior of group-housed *C. elegans* throughout their lifespans. One Observatory consists of a set of computers running custom software to control an incubator containing custom imaging and motion-control hardware. In its standard configuration, the Observatory cycles through trays of standard 6 cm plates, running four assays per day on up to 576 plates per incubator. High-speed image processing captures a range of behavioral metrics, including movement speed and stimulus-induced turning, and a data processing pipeline continuously computes summary statistics. The Observatory software includes a web interface that allows the user to input metadata and view graphs of the trajectory of behavioral aging as the experiment unfolds. Compared to the manual use of a plate-based *C. elegans* tracker, the Observatory reduces the effort required by close to two orders of magnitude. Within the Observatory, reducing the function of known lifespan genes with RNA interference (RNAi) gives the expected phenotypic changes, including extended motility in *daf-2(RNAi)* and progeria in *hsf-1(RNAi)*. Lifespans scored manually from worms raised in conventional conditions match those scored from images captured by the Observatory. We have used the Observatory for a small candidate-gene screen and identified an extended youthful vigor phenotype for *tank-1(RNAi)* and a progeric phenotype for *cdc-42(RNAi)*. By utilizing the Observatory, it is now feasible to conduct whole-genome screens for an aging-trajectory phenotype, thus greatly increasing our ability to discover and analyze new components of the aging program.

KEYWORDS

aging, automation, behavior, *C. elegans*, lifespan

1 Introduction

A characteristic decrease over time in the capability and health of adults can be observed in the vast majority of species. However, despite its ubiquity, this process of aging has thus far resisted a mechanistic description that accounts for both the nature of the process and its similarity across organisms. Although there are conceptual frameworks that provide an account of how aging could occur—antagonistic pleiotropy, for instance—these give us little insight into the physical basis of the phenomenon. Moreover, although a variety of cellular systems have been implicated in regulating aging (López-Otín et al., 2013) and many of those are broadly conserved across species (Taormina et al., 2019), it is nonetheless unclear how these and, perhaps, other undiscovered systems, cause the aging process to unfold. Thus, the mechanistic basis of aging remains one of the great unsolved mysteries of biology. Additionally, aging has profound practical consequences for human well-being and human society. For instance, in the United States, the cost of medical care for someone in their 70s is more than triple the cost for someone in their 30s (Dieleman et al., 2016). Thus, the lack of a mechanistic basis of aging also leaves unrealized one of the areas of greatest cost savings and therapeutic potential in medicine.

Much of what we know about the mechanistic basis of aging comes from experiments in model organisms. Aging experiments are fundamentally challenging because they necessarily take a long period of time, even in comparatively short-lived model organisms. Furthermore, it has historically not been tractable to monitor the full range of phenotypes that might change over an organism's life. Indeed, the greatest portion of research has used lifespan as a proxy for aging, and for good reasons: death is the ultimate endpoint of aging, the death phenotype is usually unambiguous, and once dead, animals stay dead, thus loosening the requirements for precise temporal control over one's readout.

However, despite the advantages, there are also sizable drawbacks to using lifespan as a proxy for aging. Firstly, lifespan is low-dimensional: upon discovering a lifespan mutant, although the identity of the gene may tell us about the biological process involved, the lifespan phenotype itself provides no additional clues as to whether the effect is from a known cellular process or an as-yet-unrecognized one. Secondly, critical parts of the mechanism may occur long before death; therefore, the lifespan phenotype may be much less useful in revealing the mechanism than an aging trajectory phenotype would be. Thirdly, by using lifespan as a primary readout, we leave undetected any processes that affect the quality but not the quantity of life. For instance, antagonistic pleiotropy anticipates tradeoffs between youthful and aged performance, but monitoring lifespan alone renders us unaware of early-life advantages or detriments.

Therefore, we sought to examine higher-dimensional phenotypes over time to define an aging trajectory, and to do

so at sufficient scale to make practical the discovery of genes involved in biological processes and pathways that are not yet appreciated to have a role in aging. We do not assume such processes necessarily exist, though we suspect they do. It would be equally informative if, through a reasonably exhaustive search, we could rule out major processes beyond those discovered *via* lifespan experiments.

C. elegans has been a highly useful model organism for aging studies due to a fortuitous combination of factors, including a short lifespan, easy genetic manipulation, and a wide variety of genetic and molecular tools. We found behavior to be a particularly appealing readout for quantifying an aging trajectory: different behaviors decline at different ages (Stein and Murphy, 2012), monitoring behavior can be noninvasive and minimally perturbative, and a substantial amount of effort has already been devoted to automating measurement of worm behavior (Husson et al., 2013), both individually (Baek et al., 2002; Nagy et al., 2015; Hebert et al., 2021) or when group-housed (Ramot et al., 2008; Swierczek et al., 2011; Javer et al., 2018; Pitt et al., 2019). Furthermore, detailed analysis of behavior has already revealed that genes with common molecular mechanisms tend to cluster together in phenotypic space (Yemini et al., 2013). Behavioral analysis has revealed that the EGF pathway acts as a regulator of healthy aging (Iwasa et al., 2010) and has illuminated a distinction between lifespan and time until cessation of large-scale movement (Podshivalova et al., 2017; Oswal et al., 2021) in *C. elegans*. Although reports of interventions that cause both increased longevity and an improved “healthspan” are common, suggesting a common underlying mechanism, it is unclear to what extent this is due to selection by researchers for more promising phenotypes. A comparison of lifespan and climbing assay performance across the *Drosophila* Genetic Reference Panel showed little if any correlation between the two (Wilson et al., 2020), though only one of a variety of age-affected behaviors (Overman et al., 2022) was studied. We must surmise that there may be a considerable number of undiscovered regulators of healthy aging that are distinct from known regulators of lifespan.

The search for such regulators would be considerably aided by unbiased whole-genome-scale screening. However, no existing methods appeared to scale sufficiently to allow this at a reasonable level of sensitivity. Therefore, we sought to create such a method for *C. elegans* behavior. Systems that record many individually housed animals have the advantage of being able to gather longitudinal data for aging (Churgin et al., 2017; Pittman et al., 2017). However, we elected to focus on a system tailored for plate-based group-housed assays, reasoning that the decreased effort to prepare samples and increased throughput was important. Further, we worried that in some formats, individually housed animals might have some of their behaviors governed primarily by interactions with the edge of their necessarily small enclosures, and we wished to have a

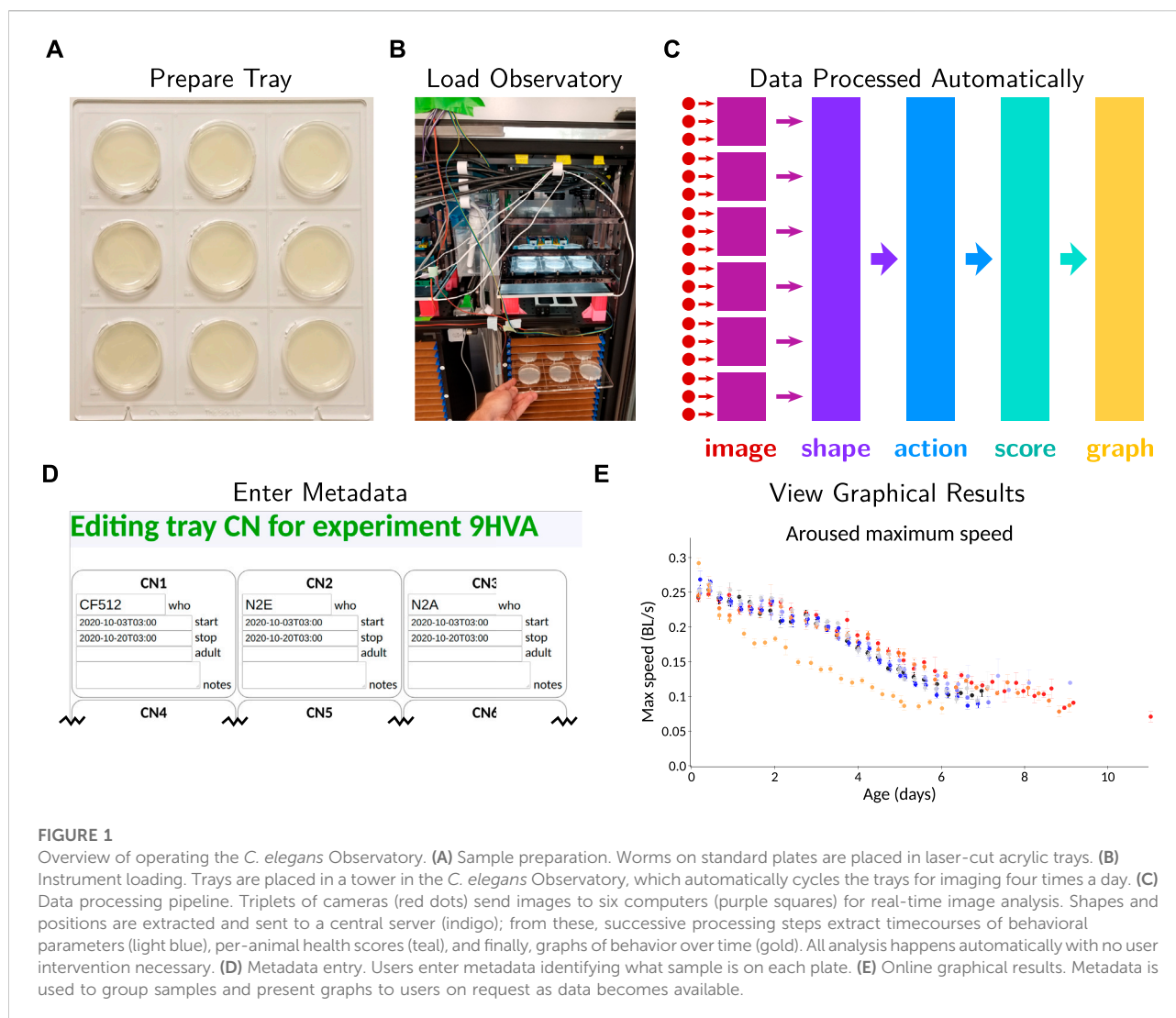


FIGURE 1

Overview of operating the *C. elegans* Observatory. **(A)** Sample preparation. Worms on standard plates are placed in laser-cut acrylic trays. **(B)** Instrument loading. Trays are placed in a tower in the *C. elegans* Observatory, which automatically cycles the trays for imaging four times a day. **(C)** Data processing pipeline. Triplets of cameras (red dots) send images to six computers (purple squares) for real-time image analysis. Shapes and positions are extracted and sent to a central server (indigo); from these, successive processing steps extract timecourses of behavioral parameters (light blue), per-animal health scores (teal), and finally, graphs of behavior over time (gold). All analysis happens automatically with no user intervention necessary. **(D)** Metadata entry. Users enter metadata identifying what sample is on each plate. **(E)** Online graphical results. Metadata is used to group samples and present graphs to users on request as data becomes available.

greater ability to examine behaviors without this being as great a concern.

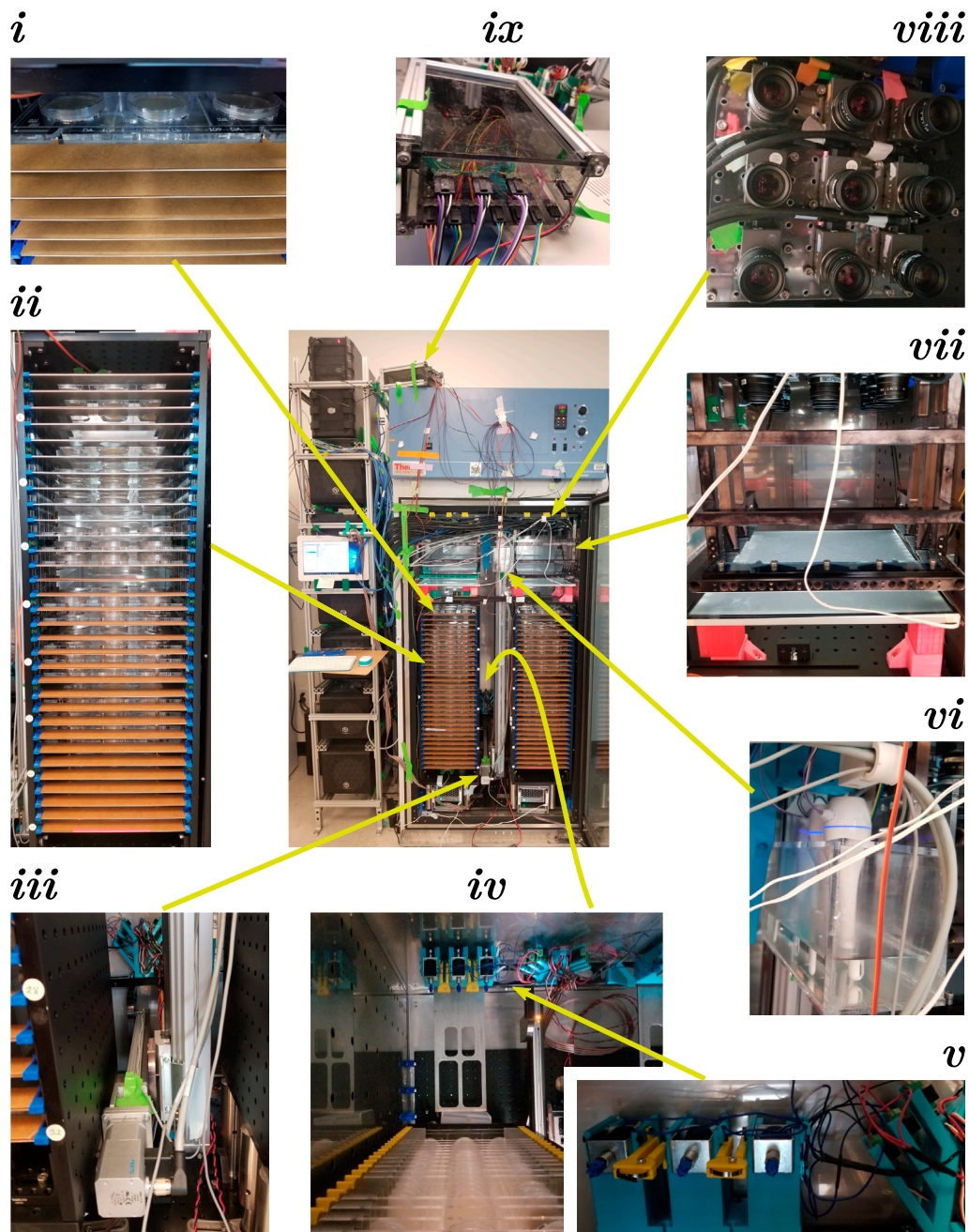
Therefore, we decided to extend the Multi-Worm Tracker (MWT) (Swierczek et al., 2011), which we had already used to study a variety of behaviors during aging (Podshivalova et al., 2017), to operate in a high-throughput automated setting. A particular advantage of the MWT is that it was designed to be highly computationally efficient both in terms of processing time and storage requirements, thereby reducing the danger of computational requirements becoming limiting.

The result of our automation effort is a system we call the *C. elegans* Observatory. As described below, the *C. elegans* Observatory captures the behavior of worms in a high-throughput automated system. Because its hardware costs and demands on experimenter time are moderate, large-scale screening, such as a whole-genome RNAi screen, is within reach of a single researcher or a small team.

2 Materials and equipment

The development of the *C. elegans* Observatory has taken place over several years, culminating in a system that provides a straightforward workflow for experimentalists (Figure 1). Through successive rounds of development and refinement, we have continually improved the device, worked around unexpected challenges, and discovered that some strategies were not as ideal as we had hoped.

Here, we describe the critical pieces of hardware and the design principles that have proved important, pointing out where appropriate what we actually did during development and what a superior solution would be if building another system. The descriptions are not intended to be adequate to create a part-for-part identical copy, nor would this be advisable. Indeed, it would be a substantial engineering effort for us to create a duplicate system ourselves. However, as we continue to work

**FIGURE 2**

C. elegans Observatory Hardware. Center: Assembled Observatory including computer tower (left) and incubator with custom hardware (right). Worms on 6 cm plates are mounted in acrylic trays that are placed into a tower (i); the full tower contains 32 slots for trays (ii), and there are two towers per incubator. Trays are moved via a two-axis linear motion system (iii), with a forklift-style assembly to lift the trays from behind (iv). The forklift also braces the tray in position when on the imaging platform and contains solenoids to deliver mechanical stimuli (v). A custom humidifier box (tank + mini-desktop humidifiers) maintains humidity (vi). The imaging platform (vii) consists of a light box mounted on top of the tower, and a frame mounted to the ceiling that holds the tray in a fixed position relative to the ceiling-mounted camera array (viii). Temperature and humidity are monitored and maintained with the aid of a custom electronics box (ix) containing a small Arduino-style processor (Teensy 3.2) that reads sensors and controls humidifiers and the incubator chiller.

on the system, we will make any parts lists and assembly diagrams that we generate available at <https://github.com/calico/elegans-observatory>, in addition to the latest versions of the source code, with the ultimate goal of fully documenting the necessary steps to create additional instances of the Observatory. If other groups are interested in reproducing the Observatory, we are happy to provide guidance and accelerate the completion of the public repository.

2.1 Observatory Hardware

Physically, the Observatory consists of an incubator with motion-control, sample holding, and imaging systems, plus an associated computer tower (Figure 2, central panel). Subcomponents are described below.

2.1.1 Incubator and environmental control

Because *C. elegans* lifespan is strongly temperature-dependent and we have a variety of heat sources within the incubator, we use a Thermo Scientific Forma 5920 incubator with lateral airflow (Stroustrup et al., 2013), as the path and volume of airflow reduce temperature gradients compared to other designs. To provide sufficient attachment points for hardware, we mounted 75 × 45 cm ThorLabs breadboards (MB4575/M) to the floor and ceiling using custom 3D-printed brackets that hook into holes in the incubator walls. The 3D printing orientation was chosen for maximum strength to shear forces applied vertically; ABS and PLA were used as materials.

To reduce mold and bacterial contamination, we placed two small air purifiers on the floor of the unit. During the time of construction, HEPA purifiers of appropriate size were unavailable at our location, so, instead, we used electrostatic plate air purifiers (Alford Industries HexaOne—now apparently discontinued, but as of this writing, the same unit is available under the brand name Nectar HexaOne or DWM-HexaOne).

The heating caused by the electronics in the incubator would have caused the internal temperature to exceed 25°C if we had only relied on passive cooling. Unfortunately, the aggressive chiller/heater logic used in the Forma 5920 incubator, though good for tight and rapid temperature control, resulted in low (~40%) relative humidity, which caused excessive drying of worm plates. Therefore, we spliced into the chiller power control line (equivalent to flipping the incubator's front panel "refrigeration" switch), selected a target set point lower than the desired temperature, and wrote logic to run the chiller as needed. A cycle time of 90 s was chosen as a compromise between temperature stability and possible wear and tear on the chiller. Under normal conditions, the chiller is on for approximately 30 s out of every 90, which is adequate to maintain a stable temperature of $24.6 \pm 0.2^\circ\text{C}$. Note that the

desired temperature can be adjusted in software; we have also run experiments at 20°C and 15°C. However, for this study, the temperature-sensitive sterile strain we used required 25°C.

Although our modifications reduced the dehumidification rate, the resting humidity level was still too low when only a few plates were in the incubator. To raise the relative humidity to ~80%, we built a box with the capacity to hold roughly 1 L of water; the box was constructed from laser-cut panels of 6 mm thickness acrylic glued together with acrylic cement (IPS corporation #10315, #16 fast set, clear, medium-bodied solvent cement). We then placed three desktop humidifiers (Jaywayne Portable Mini USB Humidifier) into this box (Figure 2 detail vi) under programmatic control *via* splicing into their on/off switches.

Although this scheme was effective at maintaining humidity and temperature in the desired range, we recommend an incubator with humidity control instead.

2.1.2 *C. elegans* housing

The *C. elegans* Observatory is designed to use standard 6 cm worm plates for the convenience of experimenters. Because precise dimensions differ between manufacturers, we had to settle on a particular model. We chose Fisher Brand FB0875713A. We laser cut 25 × 26 cm trays out of 6 mm thick acrylic to hold nine plates at a time (Figure 1A), using a precisely sized circular socket (hole) to allow plates to be inserted and held firmly without a clamp mechanism. The design we used, viewable in the files used for laser cutting in <https://doi.org/10.5281/zenodo.6645842>, is effective but could be improved further; the thin elements tend to break, albeit without compromising adequate function. Additionally, we engraved human-readable and machine-readable identifiers by every plate socket so that the identity of each position is unambiguous merely from viewing an image. This prevents any misattribution, providing that the user correctly provides metadata about the strain and condition at a particular position.

To enable precise alignment of the tray, we cut a pair of triangular notches, with tips cut out in circles (visible at the bottom of Figure 1A), that slide into matching triangular teeth in a brace on the imaging platform. This allows repeatability of a few tens of microns between successive deliveries of the tray. Trays are named *via* a two-letter code with a decimal equivalent for redundancy; these were engraved at the bottom of each tray (visible in Figure 1A). Because mistaking the tray identity would be a critical error, the user interface requires experimenters to enter both the letter-code and the numeric code in metadata; it alerts the user if there is a mismatch.

To store the trays in the incubator, we built two tray towers that each hold 32 trays on C-shaped sheet metal shelves with 25 mm vertical spacing (Figure 2, detail ii). We also tried 20 mm spacing, but it was challenging to meet positional targets with sufficient accuracy, so we settled on the wider spacing. The open part of the C faces backward to allow the

forklift to lift the tray from the center (Figure 2, detail iv). The outside walls of the tower are made from 90 × 30 cm breadboards (ThorLabs MB3090/M) for the sides and 30 × 30 cm breadboards for the floor and ceiling (ThorLabs MB3030/M). The breadboards are attached in a box shape *via* metal or 3D-printed plastic angled brackets, with the side walls inset to be flush with the edges of the top and bottom breadboards. Within this open box, oriented with the long axis vertical, we attached sheet metal shelves (dimensions 26 × 30 cm, 4 cm wide rim along the long edges and one short edge) *via* a combination of 3D-printed retaining brackets (blue in front, visible in Figure 2, detail ii; yellow in back, visible in Figure 2, detail iv) and laser-cut 6 mm acrylic guide rails (oriented vertically, attached to the inner sides of the box *via* 3D-printed brackets, with notches to allow the shelves to be inserted). A superior design would have included small notches on the metal shelves to allow the shelves to be retained by an internal element instead of the yellow back retainers.

Additional features of the towers include optical posts for legs (Thorlabs P150/M), allowing easier removal than if the box were affixed to the incubator's floor breadboard, and guide strips of 1 mm thick acrylic with triangular alignment teeth to allow precise hand loading of trays by drawing the corresponding triangular notches in the trays against the guide teeth. We left the paper coating on one side of the acrylic to aid visual alignment (Figure 2, detail i).

2.1.3 Imaging platform

Successful imaging requires high-quality illumination. We judged that the spatial constraints in the incubator favored brightfield imaging, where optical elements can be stacked vertically, rather than darkfield, where illumination sources must be placed at an oblique angle. Because *C. elegans* in brightfield generates much of its contrast by scattering rather than absorption, the incident light must be reasonably collimated. To achieve a broad and uniform collimated light field, we used a custom 12" × 12" LED light panel (GLS, Green LED Lighting Solutions; 5700K color temperature) covered by a diffusing sheet (Lee Filters #216) to increase uniformity, followed by a pair of computer privacy screens (we tested several vendors' and all worked fine) cut to size and placed at 90° angles. We then designed a metal housing that affixes to the ceiling and holds trays roughly 5 cm above the light panel (Figure 2, detail vii). The housing consists of mostly open side walls connected with braces in the front but open in the back; attachment points were machined into the side walls to allow 3D-printed guide-and-retaining wedges for precise tray alignment. The final position was achieved by pushing the tray into place against a 6 mm thick laser-cut acrylic guide bar with two triangular alignment teeth (visible on top of the lowest brace in Figure 2, detail vii; alignment notch visible at the bottom of the tray in Figure 1A).

This design allowed highly reproducible positioning (<40 μm) and acceptable contrast (>1.6:1 between background and worm body).

2.1.4 Motion and stimulus delivery

The core of the motion system consists of a pair of Festo linear stages (Figure 2, detail iii): a larger vertical stage (EGC-80-1200-TB-KF-0H-GKZUB-6M2C with motor EMMS-ST-57-M-SEB-G2 and gear unit EMGA-60-P-G5-SST-57) clamped to both floor and ceiling breadboards in the incubator, and a smaller horizontal stage (EGSK-33-300-6P with motor EMMS-ST-42-S-SE-G2) mounted on the vertical one and on which the forklift tines are mounted. These run a fixed pattern of motions generated *via* a program written in CODESYS 2.3 (Festo variant) running on a dedicated NUC-style mini-PC using the Microsoft Windows 10 operating system. We had judged that the increased reliability of a stand-alone motion system was important. However, given the high in-practice reliability of our server—higher than the motion-control system—this concern proved unwarranted, and allowing the server to coordinate motion would have been the superior option.

To physically move the trays, a horizontal bar was placed at right angles to the horizontal stage (Figure 2, detail iv). On either side of this bar, aligned with the left and right towers, we attached a broad single-tine forklift blade (Figure 2, detail iv) with a beveled front edge to reduce the chance of colliding with a tray (not shown). Above the blade, we also mounted a 3D-printed bracing assembly with circular coils of spring wire (Figure 2, detail iv; silver band in front of yellow mounting arm; two layers of 301 spring tempered stainless steel, 0.005" × 1/8", Lyon Industries) to contact the tray with appropriate force.

In order to help determine animals' capability rather than their intrinsic drive, we wished to provide an aversive stimulus to induce activity. We selected a mechanical tap as an easy and precisely deliverable stimulus. Therefore, we mounted solenoids (RobotGeek ASM-SOL-MD) aligned with the spring-wire brace (Figure 2, detail iv; silver boxes with blue plastic-tipped probes).

Mechanical stimuli are triggered as part of the consensus detection algorithm that also signals the initiation of a recording session. The striking of the solenoids is controlled by custom real-time stimulus delivery and voltage monitoring software running on an Arduino-compatible Teensy 3.2 computer-on-a-chip (PJRC). High-speed imaging confirmed that the impacts provide sufficient acceleration at all positions on the tray to expect a tap withdrawal response (data not shown), and observation of animals confirmed this.

Unfortunately, the mechanical design of the system admitted longer-lasting vibration than had previous non-automated rigs, reducing the reliability of our existing algorithms to detect tap-induced behavior such as reversals. Therefore, we focused on highly reliable general activity measures (speed). We intend to develop high-reliability response-detection algorithms and improve vibration control in the future.

2.1.5 Camera array

To image the plates of worms, we installed two 3×3 arrays of 5-megapixel USB3 cameras (Pixelink PL-D725MU-T, 2592×2048 8-bit grayscale, USB-3 interface, maximum frame rate 75 Hz) with 25 mm focal length lenses (Navitar NMV-25M1) situated with the camera sensors roughly 25 cm above the positions of the plates in trays mounted in the left and right imaging platforms (Figure 2, detail viii). This provided an appropriate field of view with one pixel corresponding to a $40 \mu\text{m}$ square. We ran the cameras at 50 frames per second with 19 ms exposure.

The magnification achieved with the cameras, which yields images with $40 \mu\text{m}/\text{pixel}$, is moderately less than in previous studies using the MWT. If a more precise estimate of worm posture were desired, higher resolution cameras could be chosen to yield equal ($29 \mu\text{m}/\text{pixel}$ from a 12-megapixel sensor) or better ($20 \mu\text{m}/\text{pixel}$ from a 20-megapixel sensor) resolving power compared to previous studies. However, this would necessitate some decrease in frame rate unless a 10 GigE interface was used instead of USB-3.

To affix the cameras to the ceiling breadboard, we used a laser-cut acrylic mounting sheet with camera positions pre-defined. Because of the low rigidity of the acrylic, it was necessary to cut fixed holes to allow screws to be placed into the breadboard near the cameras. This solution was chosen for expediency as we were still adjusting the tray format at the time. With the tray format now defined, the superior solution would be a machined aluminum mounting plate to allow all cameras to be adjusted together and affixed with clamps at the edge of the mounting plate.

Residual discrepancies between the precise centering of each camera over each plate were corrected in software. Focus and aperture were adjusted by hand to give a sharp image and bright but non-saturated background when looking at a plate (8-bit pixel values of 200 or higher).

2.1.6 Environmental monitoring and control

In order to monitor the temperature and humidity inside the incubator and verify that there were no variations in temperature and humidity large enough to confound our results, we installed six temperature/humidity sensors (DHT22; Adafruit #Ada385) and modified the Ticklish software to read the temperature/humidity values using a Teensy 3.2 device. We calibrated the sensors' temperature readings by placing them with an alcohol lab thermometer; we assumed the sensors' mean humidity reading was correct. Each sensor's readout was then corrected in software to match the ground truth result. The sensors were then deployed in a variety of locations throughout the incubator. Unfortunately, the DHT22 sensors have not proven very reliable under the environmental conditions in the incubator, and we have had to replace them multiple times. A more robust solution would be preferable.

We used the Teensy 3.2 device to run the desktop humidifiers and the incubator's chiller and read the DHT22 sensors. The Teensy 3.2 chip, together with wiring and the minimal circuitry needed, was placed in a custom box (Figure 2, detail ix) made from aluminum rails and laser-cut acrylic.

2.2 Observatory computational resources

In order to acquire images from the 18 cameras, we custom-built six PCs ("imaging computers") with Intel i7-6700 CPUs, 16 GB of RAM, a 512 GB local SSD, and a PCIe four-port full-speed USB3 expansion card (Renesas, though we have used other vendors also). For the operating system, we installed Ubuntu 16.04 LTS. Because the MWT software is highly efficient, this provided more than adequate computation to track and segment the animals from three cameras simultaneously. The fourth USB port is unused. To avoid possible breakage or intrusion, we keep these computers disconnected from the internet and do not apply any updates.

To gather the results and coordinate the separate computers, we also built a custom server PC that included the following components: Intel i7-6700K CPU, 32 GB RAM, 128 GB SSD boot drive, 512 GB NVMe M.2 SSD data transfer drive, 14 TB raw data storage hard drive ("Tier 1" pipeline output), 6 TB analyzed data storage hard drive (other tiers), and 6 TB auxiliary hard drive. Again, we used Ubuntu 16.04 LTS as the operating system. The server has both a connection to our internal network and, through a second NIC and a switch (NetGear ProSafe 8 port GB ethernet switch), a local network shared only with the imaging computers. The server PC shares *via* NFS one subdirectory on the data transfer drive with each of the imaging computers. The imaging computers use this to transfer data to the server and coordinate activity. The server PC also mounts our cluster filesystem, allowing backup of all data and the ability to serve the user interface from a cluster node.

Although we elected to use our local cluster filesystem, using cloud-based storage should also be possible. We chose the local approach mostly for ease of use and speed of access for operations such as traversing the entire directory structure. There is no reason in principle that cloud storage could not be used; one would just have to be thoughtful about caching certain types of information to avoid excessive access. Additionally, one might need a more vigorous security policy if the server had greater exposure to the outside world.

The motion-control software required the Windows operating system, for which we used a NUC-style mini-PC (smaller than an actual Intel NUC, though in the future, we would just use an Intel NUC). For stability, this also is disconnected from all networks and operated without updates.

Of the computers, only the last requires a keyboard, mouse, and monitor. The others are accessed *via* the network: the server

is accessed directly, whereas the imaging PCs can only be accessed through the server.

3 Methods

3.1 Hardware manufacturing and assembly

Because the instrument was designed and built over a period of years, the assembly process was highly *ad hoc*. We followed several principles during the design and construction process. First, if in-house 3D printing or laser-cut acrylic could suffice for a mechanical component, we used that rather than commercial parts or custom machining. Second, when laser-cut acrylic would suffice, we would use that due to the greater speed and accuracy and mostly superior mechanical properties, as opposed to additive 3D printing. Third, when making 3D-printed parts, we paid special attention to the layer adhesion of the material, as this is typically critical in parts that are load-bearing along multiple axes; we found PLA-based materials worked fairly well from among the materials we tried. However, as manufacturers introduced new products, we found that we were best informed if we tried each material. Fourth, tapping holes (i.e., cutting in screw threads with the appropriate cutting tool) in either acrylic or 3D-printed materials is fast and easy, so we took extensive advantage of this.

Most 3D-printed parts were printed on a LulzBot Mini 1.0. A variety of 40–60 W laser cutters were used to cut acrylic. Sheet metal cutting and machining were outsourced. 3D parts were designed with SolidWorks 16 (Dassault Systèmes), OpenSCAD 2015.03 or later, and/or Onshape. 2D parts were designed with SolidWorks 16, manually in Inkscape 0.92, or programmatically (written to SVG files).

Assembly of the instrument proceeded broadly in this order: first, breadboards were installed on the floor and ceiling of the incubator. Second, the vertical stage was installed using 3D-printed mounting blocks to hold the stage and fill the excess space between the floor and ceiling. Third, the horizontal stage and forklift assembly were installed. Fourth, we added the housing to hold trays above the illumination platform, as the housing is designed to screw directly into the breadboard and thus is not very movable. Fifth, the towers were situated under the tray-holding housing. Sixth, the light source was added on top of the tower. Seventh, the cameras were installed on the ceiling (unscrewing the front braces from the imaging frame to allow easier access). Finally, all remaining components were added (sensors, humidifier, etc.).

A custom aluminum-frame rack was constructed next to the incubator for the imaging and server computers, which were situated in the rack with 3D-printed mounting brackets. Ethernet switches and motor controllers, among other devices, were also attached to this rack *via* 3D-printed brackets.

3.2 Software

3.2.1 Programming languages

Our philosophy has been to select languages that are particularly appropriate for the most challenging computational tasks we face rather than pick a single language and then solve challenges to the extent possible within the constraints of that language. Image processing and hardware control were, therefore, written in C++ (compiled with GCC 7.5) for its performance and low-level hardware access, with one module in Rust (version 1.52 or later) due to Rust's equally good performance and superior facilities for handling complex data structures. Post-capture analysis was mostly written in Scala, as it has excellent (Java-class) performance and JVM compatibility, and its type of system prevents broad classes of bugs, thereby increasing stability despite a development team consisting primarily of a single person. Some older post-capture code (Choreography) was written in Java, and one part was written in Rust for additional speed and confidence in correctness. Motion control was written in CoDeSys 2.3, and some coordination tasks were written in Bourne Again SHell (bash, version 4.3).

Although the benefits of this approach have been considerable, it is worth noting one major drawback: few people have the requisite skills to rapidly begin development on any arbitrary part of the system. Indeed, we were not familiar with all the tools when we began using them. Thus, although the benefits we gained will also apply to anyone else—for instance, the Scala and Rust type systems prevent broad classes of errors common to new developers and to the original developer who has not looked at the code in too long and forgotten some essential details—the barrier to entry is higher than that for the typical project written in Python, R, or MATLAB. In our defense, we can only add that mastering the tools used will also considerably advance one's skill as a programmer *via* exposure to the concepts and strategies common to the different languages.

3.2.2 Motion control

The motor controllers (Festo CMMO-ST-C5-1-DION) for the stages were attached, as recommended, to a programmable logic controller (PLC), Fest CPX-GE-EV-S. We used the provided CoDeSys 2.3 environment to develop a control program for the PLC based around preprogrammed locations and step sizes downloaded into the motor controllers. We mostly used the continuous function chart (CFC) programming language, which represents data flow as occurring through wires between control blocks; we first developed primitives for tasks such as picking up a tray from the tower, chained these primitives together to cycle through all the trays, and chained these cycles together to make a multi-day protocol that would run independently of external control. In retrospect, using a serial-over-USB or similar controller, commanded from our

server *via* a program written in a standard procedural or functional programming language, would have simplified all aspects of the process while yielding equal or greater reliability.

3.2.3 Ticklish

In order to deliver precisely timed stimuli, it is helpful to have dedicated hardware that is not subject to the same type of operating-system-induced delays as is a general-purpose computer. Although one can purchase hardware specifically for signal generation, we elected instead to write custom software for the Arduino-compatible Teensy 3.2 processor on a chip. We defined a set of commands to be delivered *via* serial-over-USB to the Arduino device, specifying a protocol of precisely timed (typical temporal precision < 100 μ s) voltage switches on desired output pins. We also allowed live commands to query status, including reading voltage on pins. Once a protocol is downloaded, the device then runs it independently of the host computer, preventing any asynchronous interrupts or heavy workloads from interfering with precise timing. Our temperature/humidity sensors offered a slightly more complex trigger-and-readout scheme, which we also implemented in the software. This readout is somewhat slow and, therefore, could delay a protocol that is running at the same time. However, as we use two separate Teensy 3.2 devices to deliver taps and to sense and control the environment, with the latter not requiring precise timing, the readout delay is not an issue in practice.

Note that precise timing is important for the operation of the solenoid-based tappers. Typically, only a few tens of milliseconds of current are sufficient to drive the solenoid to collide with the tray; therefore, relatively small (millisecond-scale) variations can change the nature of the tap from a ballistic-like impact to a strike-and-briefly-hold motion.

We named the software Ticklish as our primary use is to deliver mechanical stimuli. Because it works as a general-purpose stimulus delivery and voltage querying device, we gave it its own repository <https://github.com/Ichoran/ticklish>. It is written in Arduino-themed C++.

3.2.4 The Multi-Worm Tracker

The detection and segmentation of worms from the background are accomplished *via* the MWT (Swierczek et al., 2011). We separated the core image processing routines from the LabView-based UI and established a new repository for maintenance and development of the image processing portion <https://github.com/Ichoran/mwt-core>. The core routines remain essentially unchanged. In brief, the MWT calculates a decaying average of the image to estimate a background, then segments worms as differences from the background that exceed a threshold. In order to better detect moving worms, we amended the decay algorithm to be asymmetric: to quickly accept darkening pixels but only slowly lighten them. This better detects slower-moving animals that gradually move into a new area. Regions that

pass a threshold are flood-filled using a less stringent threshold, and the outer contour is extracted and saved. The region around detected animals no longer updates its background, so a once-moving animal stays at a high contrast from the local background even if it stops moving.

We also added SIMD-based commands to project an image onto the horizontal or vertical axis; these are used to help detect the octicon symbol block as part of tray identification and to detect the position of high-contrast edges (part of our vibration compensation routine). The operation is trivial (summing pixels along rows or columns); only the use of SIMD instructions (with a roughly 4 \times speedup, though we did not measure carefully) is noteworthy.

3.2.5 Tray identification

Because the motion automation is decoupled from both the imaging and server computers, robust and rapid tray detection is essential for allowing the computers to respond promptly and synchronously to the arrival of a tray. We created a custom numbering scheme for trays and a custom set of eight easily line-engraved characters, “octicons,” to read *via* template matching. Engraving both the human-readable and this machine-readable format allowed both humans and software to rapidly and uniquely identify every slot in every tray. More information about the implementation is available in [Supplementary Figure S1](#).

3.2.6 Spanner

The central task of the imaging computers is to detect when a tray has arrived and to run the MWT to segment worms when it has. This task is made more complex because of the need to establish two types of consensus. First, one imaging computer sees only one column of three plates, not the whole tray, so the start of any protocol has to be made in coordination with the other imaging computers that may have different timelines for positive identification of the tray. Secondly, within the imaging computer itself, the identification from the three different image streams has to be coordinated.

To perform these operations, we wrote custom software, Spanner. Spanner is written mostly in C++ (C++14 dialect); it captures frames from the camera using vendor-supplied Pixelink camera drivers, detects when an octicon block appears in a per-camera specified region, and determines a consensus detection time across the three cameras it controls. In order to include adequate handling of error conditions, we developed a state machine of nontrivial size to seek the octicon block and positively identify the tray for a predefined amount of time (to ensure stability had been achieved—the system observes the tray in motion before it reaches its final braced position), and coordinate across cameras. We wrote the state machine logic module in Rust (2018 dialect) instead of C++, as its pattern-matching capacity simplifies the logic of state switching while also considerably reducing the chance of error. For details, one should refer to the source code.

Additionally, Spanner saves a snapshot image at the beginning and end of each time window where we have decided to measure speeds. Thus, the complete data consists of six full-frame images plus a timecourse of outer contour and centroid position for each detected moving object. Note that due to collisions, one animal may be found as distinct temporally separated objects.

3.2.7 Controller

A key function of the server computer is to coordinate the different imaging computers so that a behavioral protocol is run in a way that is synchronized across those computers. Another key function of the server is to monitor and control environmental parameters (temperature and humidity). Because both functions require attention to timing and communication with Teensy devices running Ticklish, we decided to combine the functions into a single program, written in Scala, which we called Controller.

The behavioral protocol aspect of the Controller functions as a simple synchrony-detection device: it watches a set of directories for the appearance of a file to indicate a tap request; if enough (in practice, two) requests come in within one second, the commands to run the standard behavioral protocol are sent to the Teensy device connected to the solenoids that impact the trays. It also writes a file in each directory that specifies the time at which the protocol will start. Each imaging computer (*via* Spanner) reads this file when it appears and waits until the specified time to begin processing the image stream. The server computer functions as an NTP server for the imaging computers, which, in practice, generally results in time synchrony of under one frame (20 ms).

The environmental control runs on simple threshold-based logic; if heat is too high or humidity too low (based on the average value of the sensors, with any nonworking sensors ignored), the chiller or humidifiers, respectively, are turned on; how long they are turned on depends on how many thresholds are exceeded. This is very simple to tune, though it provides less precision and speed of return to baseline than would a software-based PID controller with appropriate parameters. The environmental control portion also outputs the environmental parameters to a log file, which is then conveyed to the web interface.

3.2.8 Pipeline

The Spanner software extracts the outlines and centroids of worms in each frame and stores them locally. However, this leaves a sizable amount of processing necessary to obtain any biological insights: the data are distributed, organized by camera instead of sample identity, and very low-level. To assist with the rapid development of insight, we built a processing pipeline that runs in batch mode after each recording from a tray (Figure 3A) and computes summary data as the data becomes available.

The data that feed into this pipeline are transferred from the image computer's local drive to the server's networked drive. This is accomplished by a program called Saver, written in Scala, that moves the data and compresses the image snapshots as PNG files instead of uncompressed TIFF (which is used by Spanner for speed). Saver and Spanner alternate runs: Saver can complete its tasks in less time than it takes to load a new tray, and this way, the imaging computer can devote all of its resources to Spanner when a tray is present.

Data are then processed through four subsequent stages in a sequential batch mode. For robustness, we designed these stages to depend only on the saved state on the various drives, not on any other record of previous work. Although this has been a good choice initially, in the future, this may need to change as it involves inspecting the entire directory structure each time a stage is run, which does not scale well as data size continues to increase. One solution is simply to archive old data. However, this would make it difficult to browse and reanalyze old data. It would be preferable to mark older data as handled and avoid examining them unless we had reason to believe they changed.

Each stage is time-limited, as the first stage must run frequently to keep the comparatively small data transfer drive free. When everything is running normally (no interruptions or manual intervention requiring extensive recomputation), all stages are complete in less time than a recording from a single tray (roughly 10 min). Out of an abundance of caution, we wait for one cycle for newly produced data to be run through the next stage of processing (in case of long-running external processes that do not complete before the next stage starts). Therefore, the final stages of analysis are available approximately 40 min after the data are taken. This could, with appropriately careful engineering, be sped up to a just-in-time scheme that should complete in minutes; however, given that animals are only examined once every 6 hours and the experiments unfold over many days, we have not found in practice that the 40 min delay impedes us in any significant way.

Each processing stage is a stand-alone program (albeit using shared libraries) written in Scala. Coordination of the different stages is achieved with a bash shell script running in a loop.

The first stage, Tier1, gathers the data from the six separate subdirectories shared with the imaging computers, moves the data to a large local drive for further processing, compresses the contour data, and saves the contours and images to the cluster filesystem for backup. This completes the transformation, started on the imaging computer, of raw images (Figure 3B) to outlines and positions ready for further processing (Figure 3C).

The second stage, Tier2, extracts low-level parameters from the contour and centroid data using the Choreography program that is part of the original MWT distribution; Choreography now has its own repository <https://github.com/Ichoran/choreography>. In brief, we use the standard command-line parameters `-N all --shadowless -S -t 30 -M 1.5 -p 0.04 -s 0.2`, the

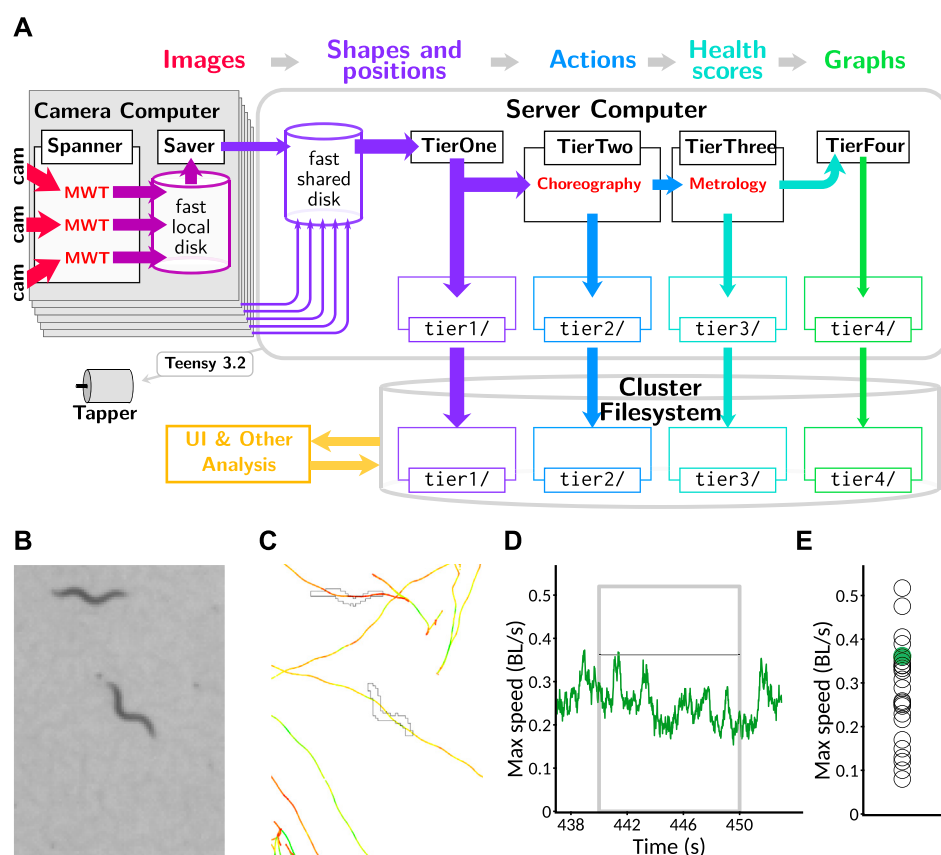


FIGURE 3

Data processing pipeline and data reduction. (A) Information flow within pipeline. Image data from cameras (red: 2.3 TB per session across 18 plates imaged simultaneously) are processed in real time with the MWT software into animal shapes and positions (purple: 1 GB per session). This is transmitted to a central server where the Choreography software is used to compute timecourses of behavioral parameters and actions, including speed (blue: 400 MB per session), from which per-animal health scores such as maximum speed in a time window are computed using the Metrology software (teal: 1 MB per session). Finally, this is collated into timecourses for visualization by averaging across animals at each timepoint (green: 10 kB per session). All categories of data, except for the full video feeds which are processed live, are backed up to a cluster filesystem, which is accessible to the web server that runs the user interface (gold). (B) Portion of a raw image as captured by the Observatory. Image covers 3.4 × 4.68 mm. (C) Example of a worm outline and path, extracted from (B) with the MWT and visualized with Choreography. Outline corresponding to the image is shown; paths of animals' centroids are plotted for all times. Paths are colored according to movement speed: yellow is faster and red is slower. Scale as in (B). (D) The speed of the centered animal in (C) over the "aroused speed" window (post-stimulation). Measurement window indicated by a gray box. Thin black line indicates the maximum speed measured from this animal (after a 5-point median filter). (E) Maximum speed for the animal of interest (green dot) and others on the plate (open black circles) as measured by Metrology.

plugin commands --plugin mwt.plugins.
Reoutline::exp --plugin mwt.plugins.Respine
--plugin mwt.plugins.SpinesForward, and the
output directive -o area,speed,midline,loc_
x,loc_y. Together, these gather the per-animal output
of length, area, x and y position, and speed measured
over an 0.2 s time window while rejecting likely low-quality
data from putative animals that have moved less than 1.5 body
lengths or were followed for less than 30 s. When
computations are completed, the results are also
compressed and saved to the cluster filesystem. This
transforms the data into per-animal parameters, such as
speed, measured over time (Figure 3D).

The third stage, Tier3, selects animals that were followed
successfully during three windows of interest: "initial," 10–20 s
after protocol start; "calm," 275–295 s after protocol start, where
animals have had time to return to a calm state after the initial
taps; and "aroused," 440–450 s, 30 s after the last of the twelve
taps given with a 10 s inter-stimulus interval. In addition to
inducing per-tap habituation, this protocol results in a prolonged
increase in activity in response to the repeated agitating stimuli.
Key parameters (length, size, and speed) are calculated over this
window (mean length, mean size, and both mean and maximum
speed, though the speed is first passed through a median filter of
window size 5 to reduce outliers). Finally, the results are again
compressed and saved to the cluster filesystem as a backup. This

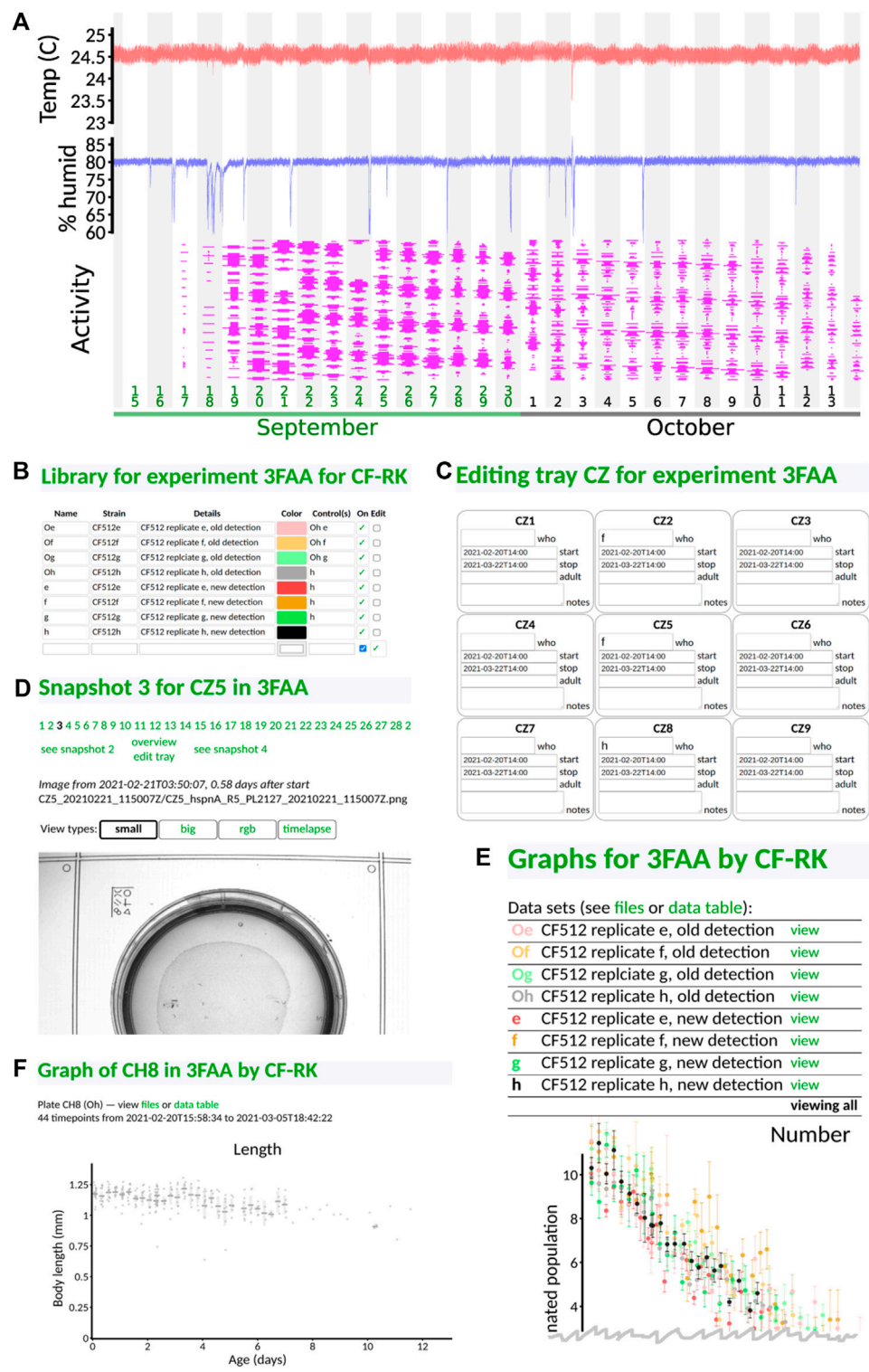


FIGURE 4 Web-based user interface. All panels taken directly from the interface with no editing save cropping. **(A)** Front page status monitoring. Users can see at a glance temperature (red), humidity (blue), and instrument utilization (magenta; width indicates the fraction of each tray filled with plates, and time throughout the day runs from low to high). Downward spikes in humidity are caused by opening the incubator to, for instance, load samples. **(B)** Library definitions. Users can give nicknames and colors to their samples, in addition to specifying strains and condition information. **(C)** Assignment of samples to tray positions. Only the sample nickname is required, and only in plates that exist; dates are auto-populated from experiment-level metadata. **(D)** Visual checking of snapshots. Users may see snapshots of any recorded plate in order to, for instance, check for mold (Continued)

FIGURE 4

or drying. (E) Viewing of results. By default, all samples are shown. Data points are averaged across six-hour time bins (one complete cycle through all trays). A variety of graphs are presented (only the top of the first graph, sample number, is shown). (F) Viewing of per-plate detail. Data underlying each sample can be viewed if desired. Gray dots indicate the measured length of individual animals for one particular plate of one sample type. Additional graphs are situated below the first (not shown).

results in a transformation of the data to per-animal scores that can be used as a quantification of animal health (Figure 3E).

The final stage, Tier4, was intended to group this per-animal data by biological condition and compute and draw key plots for examination by the user. However, we found that this posed an architectural problem, as users would want to update information on the user interface—to, for example, remove from consideration a plate that was observed to be contaminated with mold—and see it immediately reflected in the output. Because this was incompatible with the batch-mode processing, and we observed the Tier4 computations to be very fast, we moved the logic from Tier4 into the user interface code. In the future, we plan to partially restore Tier4 by keeping track of which metadata was used to create each graph and modularize the code such that either Tier4 or the UI code can call the same module to create graphs. However, for now, Tier4 exists mostly in conception; technically, the last stage of computation is done upon request by the user, and thus the Tier4 code only coordinates metadata between the cluster and server. In any case, this conceptual tier results in a transformation of the data to graphs of parameters, with animals averaged across plates with the same biological condition during the same 6 h recording cycle forming each data point.

3.2.9 Webservatory

Previous studies utilizing the MWT have required considerable post-capture processing before any biological insight could be gleaned (Ohshima et al., 2013; Podshivalova et al., 2017). However, because the output of the *C. elegans* Observatory has a natural biologically interpretable form—graphing of parameters against age, with different strains or conditions compared to each other—we were able to create a web interface, the “webservatory,” that allows the experimenter to view these key graphs without performing any data processing tasks themselves.

The front page of the interface gives a graphical display of key environmental parameters and device utilization (Figure 4A). It also allows each experimentalist to log in to view their experiments. Each experiment is given a unique four-character identifier (one digit, three capital letters). Within an experiment, users can define their library of distinct conditions or strains (Figure 4B) and specify a nickname by which to refer to them and what other conditions or strains should be plotted as a control. Then, they can specify which slots in which tray have which sample (Figure 4C), along with a start and stop time and notes, if applicable. When the experiment begins, the *C. elegans*

Observatory gathers snapshots of each plate for each session (6 h between sessions), which can be viewed to check for mold or other problems (Figure 4D). If a plate has a problem, its entry in the tray can be removed, or the duration of validity can be shortened so that the final results do not contain bad data.

This allows results to be grouped by strain or condition and presented to the user graphically (Figure 4E). We show only a small portion of the interface here: each strain/condition is listed under its user-specified color, and by default, all data are plotted together (the top portion of the number-of-animals graph is shown, as that appears first on the interface). By clicking on a strain/condition name, one can get a direct comparison of the condition and its control(s) (not shown), and from there, one can click on individual plates to see the underlying animal-by-animal data (Figure 4F).

This way, an experimentalist can rapidly understand phenotypes as they become visible and can navigate the data to check for quality issues.

The web interface is written in Scala, using the open-source HTTP framework Cask (which is fashioned after the better-known Python framework Flask).

3.2.10 Statistics

Whenever possible, we have attempted to visually display contrasting conditions in a way that lends itself to an intuitive understanding of variability within conditions and differences across them. For this, we either plot the underlying data points or a Monte Carlo sampling of underlying data that serves as a null-hypothesis distribution. We typically utilize a one-sequence implementation of the RXS M XS 64 variant of the PCG64 pseudorandom number generator (O'Neill, 2014) for our random number source; an initial 64-bit seed is arbitrarily chosen by mashing fingers on the number keys.

Internally, the software uses basic statistical functionality and distributions to, for instance, calculate standard error estimates. These are mostly programmed from first principles and are available in KSE <https://github.com/Ichoran/kse>, a Scala library adding the general-purpose functionality not found in Scala but commonly used by one of the authors. The PCG64 random number generator is also in this library. This basic functionality was adequate for the error analysis in Figure 9.

The Kaplan–Meier survival estimates in Figure 8B were computed in R version 3.5 using the survival and rms packages.

We expect that reasoning based on the visual impression will typically be at least as valid as that based upon a quoted *p*-value but provide *p*-values for key contrasts, nonetheless. *p*-values for

day 3/day 0 ratios (Figure 7) were computed using the Mann–Whitney test (`wilcox.test` in R 3.5 or `MannWhitneyTest` in Mathematica 12.1). *p*-values for different day 3 and day 0 scores from control (Figure 10; Supplementary Table S1) were computed by first projecting onto the first principle component of the points in this space, then using the Mann–Whitney test on those values. Proportions of animals detected between day 9 and day 0 were tested using the chi-square test (R 3.5) on the number of animals in each case. All *p*-values are reported without correction for the number of comparisons of different samples. Because not all sources of variability are adequately understood—true in many studies—these *p*-values should be interpreted primarily as a statement about the numerical structure of the data. Although we have done our best to ensure that systematic variation is due solely to the condition we intended to vary, it would be wise, as always, to maintain appropriate skepticism regarding batch effects and other potential confounds.

3.3 Experiment design

3.3.1 Strains and sample preparation

One of the key challenges to overcome in lifespan experiments and whole-life experiments in *C. elegans* is the appearance of progeny. Because *C. elegans* is a self-fertile hermaphrodite, unless active measures are taken to prevent this, one will get a new generation of animals every 3 or 4 days (precise timing dependent on temperature, strain, and/or perturbation). One common way to prevent progeny from accumulating is to induce sterility chemically. For example, 5'-fluorodeoxyuridine (FUdR) is a nucleoside analog that interferes with development sufficiently to prevent eggs from hatching (Gandhi et al., 1980). However, although we have successfully used FUdR in Observatory experiments, we note that the drug must be added at the correct developmental stage to be effective at preventing progeny while avoiding defects in the adults; this is challenging when interventions or genetic backgrounds could also affect the rate of development. Another approach is to use microfluidic devices that retain adult animals but allow young animals to be washed away (Rahman et al., 2020). This, however, at a minimum, would require automated attachment and detachment of a fluid handling system, which we judged to be impractical. A third approach, which we took, is to perform experiments in a temperature-sensitive sterile genetic background. In our case, we used *rrf-3; fem-1* (strain CF512) animals, which have largely normal egg-laying at 15°C but no progeny (< 1/10000 from our observations) at 25°C. The primary downside of this approach is that mutations have to be crossed or re-engineered into this background; but, as we were mostly interested in performing RNA interference experiments, this was an acceptable tradeoff. Fortunately, the *rrf-3*

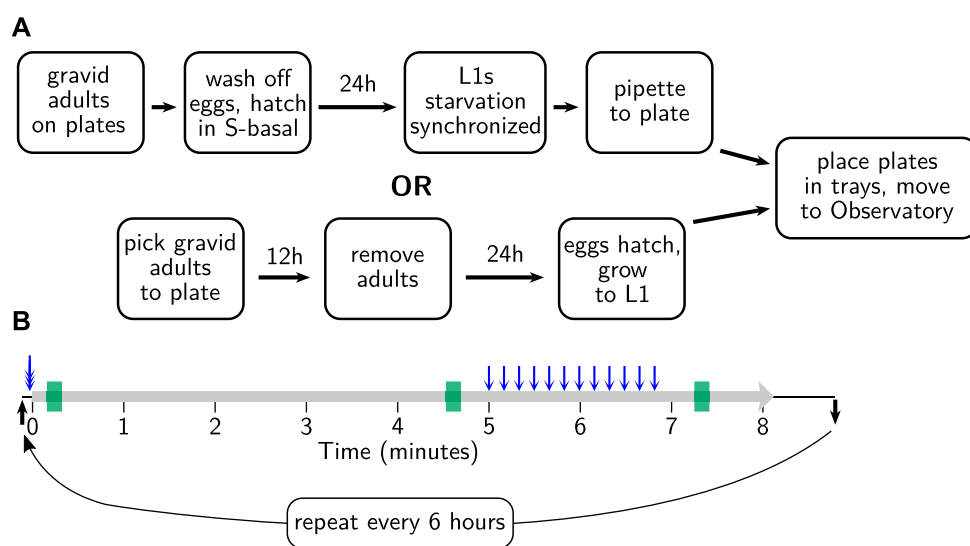
mutation enhances the effectiveness of RNAi (Simmer et al., 2002) in addition to preventing reproduction at higher temperatures (for which the *rrf-3* gene was independently isolated as *fer-15*). All data in this paper are from CF512 animals (i.e., *rrf-3; fem-1*). Animals were housed at 15°C unless otherwise indicated.

To prepare worms for recording, we used one of two methods to achieve an age-synchronized population. For experiments with a small number of plates per strain and relaxed requirements for synchronization, we picked two day-one adults to a seeded plate, left them for 10–12 h to lay eggs, and then removed the adults. For experiments with larger numbers of animals or where we wished to have tighter synchronization, we used an L1 larval arrest protocol (streamlined from Stiernagle (2006)). In brief, we left hundreds of adult animals to lay eggs on seeded 6 cm plates and then washed off the adults and any already-hatched progeny with 2 ml filter-sterilized S-basal plus 0.01% PEG. The eggs, which mostly remain behind with washing, were scooped off, cleaned with 30 s immersion in 1/2x worm bleach solution (1:2:7 ratio of 1 M KOH, bleach, and water), rinsed 4x with S-basal + PEG, and left to hatch overnight at 25°C in S-basal + PEG. Without food, the hatched L1s arrest their development, increasing the synchrony between the recently hatched and less recently hatched animals. The hatched L1s were then pipetted onto plates (volume determined by the density of animals in the liquid, aiming for 40–60 animals per plate) and maintained at 25°C. These two methods are diagrammed in Figure 5A.

Assays run on OP50 had plates (NGM) and bacteria prepared using standard methods. Generally, 50 or 100 ml of OP50 culture was used. We spread the culture near but not all the way to the edges of the plate to provide a large area for animals to roam without visual occlusion or loss of focus caused by the edges of the plate. Plates were left to grow for 2–3 days, though neither the precise timing nor the amount of bacteria appear to have a substantial impact on the aging trajectory (preliminary results; see Supplementary Figure S1).

RNAi assays had bacteria prepared using a protocol we have previously found successful (based largely on Kamath et al. (2001)). Frozen stocks of RNAi were grown overnight at 35°C on LB plates with 100 µg/ml of carbenicillin. Single colonies or a streak were picked from plates to LB liquid media with 12.5 µg/ml tetracycline and 100 µg/ml carbenicillin and grown overnight at 37°C. The media then was diluted 1:1 into LB with carbenicillin only and grown for two more hours at 37°C. Next, 1 mM IPTG was added, and the culture was placed at 30°C for 4 h. Finally, 100 µl culture was pipetted to each assay plate. Plates were NGM with 1 mM IPTG and 100 µg/ml carbenicillin; the culture was spread with a glass rod to cover most of the plate, and plates were left to grow for 24 h at 30°C.

After plates were loaded with animals, the lids were coated with an anti-fogging agent (FogTech DX wipes). They were then parafilm, and 2–4 small holes were punched in the parafilm

**FIGURE 5**

Sample preparation and behavioral assay protocols. (A) Age synchronization. One of two standard methods is used to synchronize progeny at 15°C, as shown, before moving to the Observatory at 25°C. (B) Behavioral assay. Tray arrives at the imaging platform (black arrow); tray is triple-tapped (blue triple-headed arrow) prior to the onset of recording (thick gray line). After 300 s, 12 taps are delivered (blue arrows) with a 10 s inter-stimulus interval; after 80 more seconds, recording ceases. Tray is removed shortly thereafter (black arrow) until the next session, 6 h later. Summary parameters are gathered in 10 s windows at 10, 275, and 440 s (green rectangles), corresponding to initially active, calmed, and tap-aroused behavioral states.

between the lid and plate to allow a small degree of venting. This prevents any fogging while also reducing drying sufficiently to allow month-long experiments.

3.3.2 Standard behavioral assay

We used a behavioral assay slightly modified from Podshivalova et al. (2017). Previously, recordings made using the MWT would happen after the normal lid of the plate was swapped for a custom glass-covered lid, providing a strong multi-sensory experience (changes in temperature, humidity, oxygen, etc.) that agitated the animals. However, with the *C. elegans* Observatory, no such agitation is an inherent part of the process: the delivery to the imaging platform is quite gentle. Because the MWT requires animals to move in order to detect and quantify their behavior, we needed an initial pre-recording stimulus to assist detection. Blue light stimulation has been reported to be robust (Churgin et al., 2017), but the logistics of deploying it were complicated. Because we already wished to give mechanical stimuli, we tested whether a closely spaced trio of taps could serve as an effective agitating stimulus before recording. We found that it could do so, at least for young and middle-aged animals. In contrast to the lid-change stimulus, after the mechanical stimulus, animals rapidly returned to baseline activity. Therefore, we devised the protocol as shown in Figure 5B: the agitating triple-tap, 5 min of cooldown, a tap habituation assay consisting of 12 taps with a ten-second inter-stimulus interval, and finally, an 80 s cooldown. Note that we do

not presently score the habituation to tap, but as we plan to in the future, and it also induces long-lasting elevated movement that we do quantify; we have included it in the protocol.

Given that switching trays take about 1 minute, the protocol allows for slightly over 9 min between sessions, which with 32 trays works out to just under 6 h per cycle, or four sessions for each tray per day. Although it is possible to detect reproducible changes on a 6 h timescale, such changes are very small, and a slower cycle time would almost surely be adequate (every 8 h or every 12).

3.4 Lifespan scoring

The MWT behavioral analysis algorithms rely critically on motion for the segmentation of animals from the background. However, animals exhibit an extended period of limited mobility before death. This leaves the system unaware of both dead and very slow-moving animals, thereby preventing the number of detected animals from being used to calculate the number of living animals. However, because existing automated systems score lifespan based on static images (Stroustrup et al., 2013), we expected that we would be able to score lifespan from the handful of images stored each session. Although we intend to automate the process, we initially sought only to score the images manually to verify that lifespans in the *C. elegans* Observatory were as expected. To highlight changes over time, we took images from

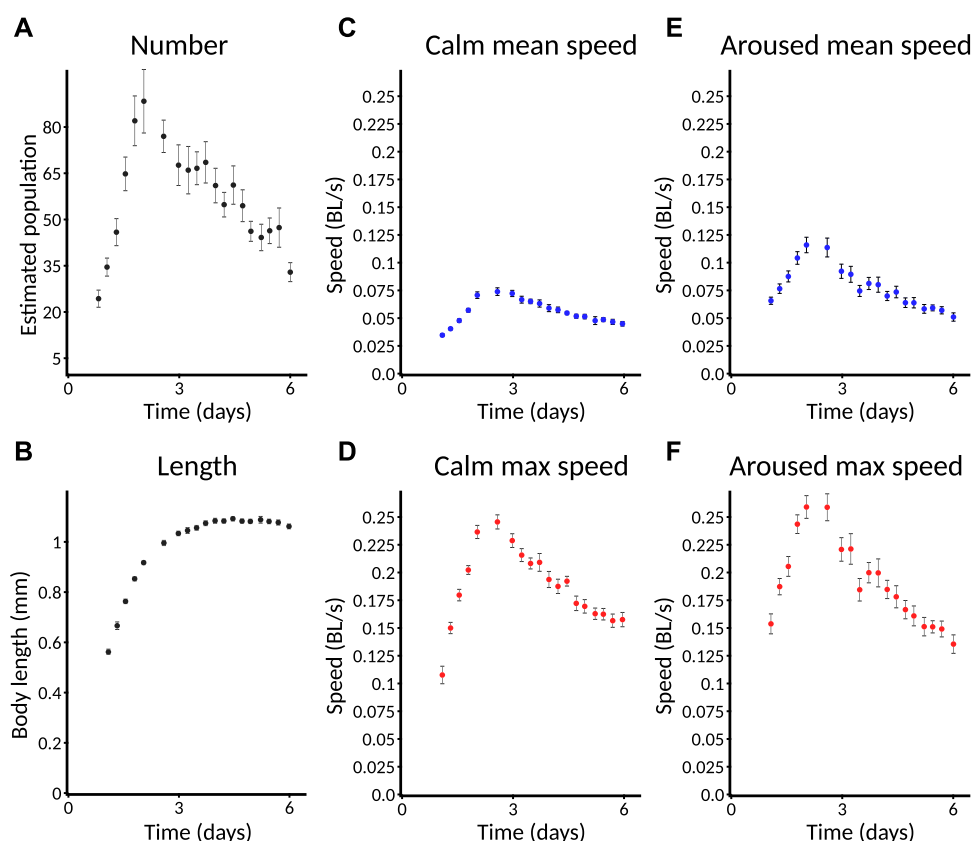


FIGURE 6

Selected standard behavioral measures. Plates imaged from L1 are used as an example and are followed for only 6 days. Error bars indicate SEM. Data from a plate are only included for plotting if at least three animals are detected on that plate. **(A)** Estimated number of animals. Animals are counted only if they move enough for their behavior to be quantified. Specific speed scores may have a smaller sample size as not all animals are followed at all times. Error bars represent SEM. across plates, not within-plate error. **(B)** Length of animals. Note that data do not appear at the earliest timepoints because the animals are too small to detect. **(C)** Calm mean speed. Mean speed of animals in measurement window shortly before taps are delivered (275–285 s), when animals have had time to return to baseline activity after the taps at the start of recording. **(D)** Calm maximum speed. Maximum speed of animals in **(C)**. Each animal's maximum speed is computed within the window; from these per-animal maximum scores, a population mean and standard error are computed. **(E)** Aroused mean speed. Mean speed of animals in measurement window shortly after taps are delivered (440–450 s), when animals still exhibit overall arousal in behavior following repeated stimuli. **(F)** Aroused maximum speed. Maximum speed of animals in **(E)** using the method described in **(D)**.

three successive sessions (spanning 12 h) and encoded them, intensity-inverted, in red, green, and blue channels. Thus, truly motionless worms appear gray, whereas slightly moving worms have patches of color about them. This considerably accelerates the task of manually scoring the time of death.

4 Results

4.1 Validation

4.1.1 Quantification of behavior

Our first task upon completing the construction of the *C. elegans* Observatory was to decide which behavioral metrics to compute and display for users. Initially, we favored those that

were highly robust and easy to interpret biologically. As the size and movement speed met these criteria, we focused on validating these. We intend to add additional metrics in the future, including the propensity for dwelling *versus* forward or backward motion, rate and magnitude of response to individual taps, and frequency of turning.

Because the MWT only detects moving animals and does not try to maintain animal identity when animals collide, it cannot be used to provide an accurate count of animals. Firstly, some animals may never move enough to be detected and, secondly, those detected may appear as several independent records punctuated by collisions, with no indication that these records, in fact, belong to the same animal. However, it is highly desirable for an experimentalist to have at least an estimate of the number of animals on the plate to tell if the

plate has been loaded properly and to tell when the behavioral data from an experiment are effectively over. We use a simple greedy heuristic to try to join up records by judging whether an animal could have traveled from the position of loss to the newly found position. This provides a more accurate estimate of the number of moving animals. We observed that young adults are most easily detected. As animals age, an increasing fraction of them fail to move enough to meet the detection threshold. Thus, fewer are detectable (Figure 6A).

In order to increase the ability to judge quantitative differences between conditions, all Observatory graphs, except for animal number, include only data from plates with three or more detected animals. Thus, the absence of plotted data at a particular timepoint does not indicate that zero animals have been detected but that too few have to trust a quantitative comparison.

For size metrics, we compute length (length of an 11-point segmented line that runs down the center of the outline contour) and area (corresponding to the number of segmented pixels). These, obviously, are highly correlated. As the area adds little, we typically focus on length (Figure 6B), which shows an increase through mid-adulthood, followed by a decline during aging, as expected (Hulme et al., 2010).

For speed metrics, we plot speeds calculated over short windows at three different times. The first window, “initial,” is 10–20 s after the beginning of the recording and captures the behavior of worms freshly agitated by the triple-tap protocol. However, only worms near their peak activity can be detected quickly, so this metric is of limited use in reporting aging phenotypes. The second window, “calm,” is 275–295 s after the beginning of the recording, by which time speeds have returned to baseline (Figures 6C,D). The third window, “aroused,” is 440–450 s after the beginning of the recording and 30 s after the end of the tap protocol. This protocol induces a sizable increase in the animals’ movement speed (Figures 6E,F; compare to “calm” speeds). For each time window, we computed speed in two ways: the mean speed across the window (Figures 6C,E) and the maximum speed (after noise reduction with median filter; Figures 6D,F). Though the calm and aroused speeds are similarly robust, we favor the latter as a better measure of the animals’ capacity rather than their motivation. Similarly, between mean and maximum speed, we favor maximum as we judge that more likely to represent the animals’ capacity—this is an important consideration for *daf-2* mutants (Hahm et al., 2015), for instance.

Hereafter, we focus on “aroused maximum speed” as a single behavioral metric that captures how an animal’s capacity for motility changes throughout life. In cases where we wish to compare the number of animals across conditions, we compare the number of animals successfully measured for aroused maximum speed. Graphs are plotted with time measured

relative to initiation of recording (typically, animals are L1, though this can vary).

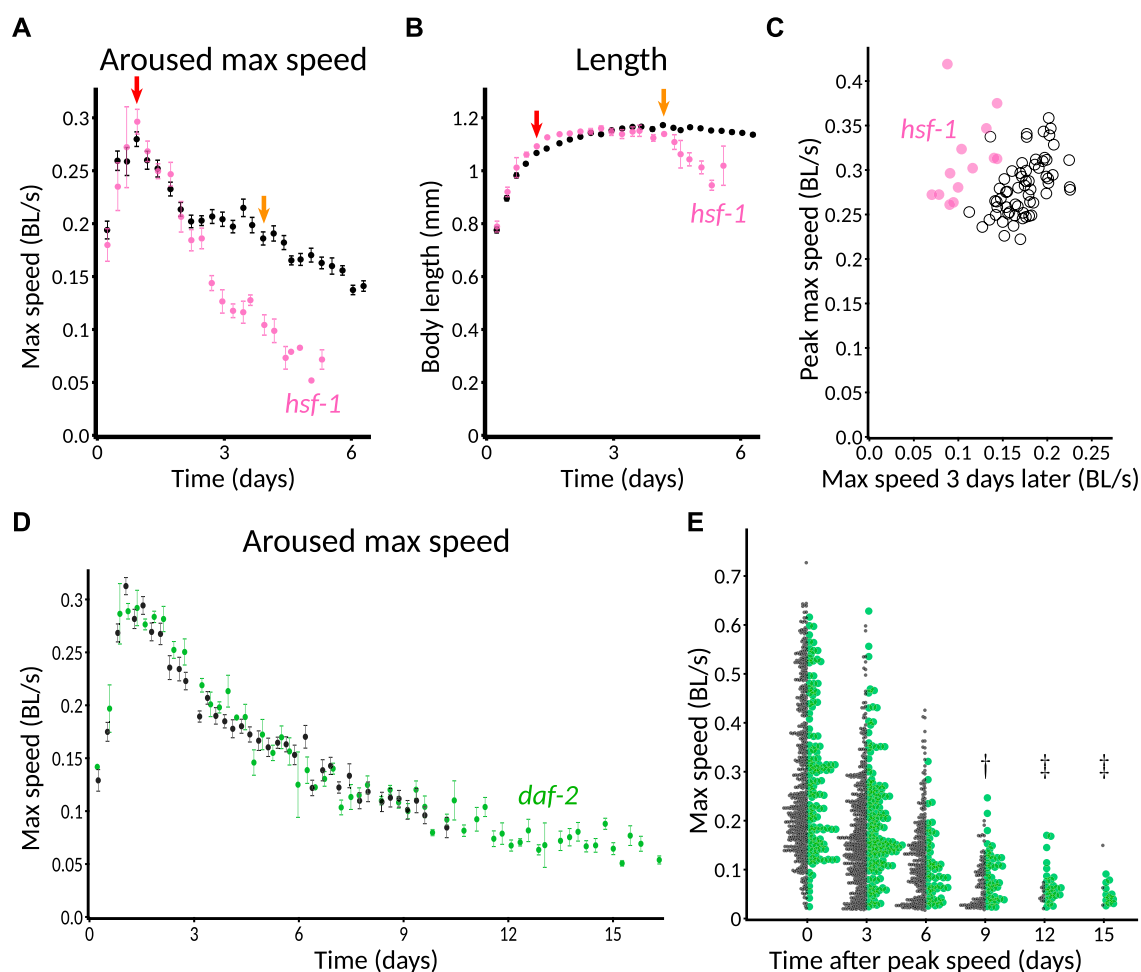
Because quantification of behavior relies on a minimum amount of movement for worms to be distinguished from the background, the behavioral parameters cannot be computed late in life when animals’ movement drops below this minimum. However, the degree to which animals have become undetectable is itself determined by movement. Thus, in addition to comparing aroused maximum speed earlier in life, we also compare changes in the number of animals detected and measured for a later-life estimate of behavioral vigor.

4.1.2 Validation of known mutants

We expected that the *C. elegans* Observatory would reveal behavioral phenotypes for genes known to be involved in longevity. In particular, we wished to find both an example of progeria, where young adult behavior was normal but the decline in behavior was faster than normal, and an example of extended health, where young adult behavior was normal but the decline in behavior during aging was slower than normal.

As part of running controls for other experiments, we found that *hsf-1(RNAi)* produced a particularly clear progeria phenotype (Figure 7A), consistent with its shortened lifespan and accelerated tissue damage (Garigan et al., 2002). We also found normal growth but a markedly early and severe age-related decrease in length (Figure 7B). To provide a more quantitative metric for progeria, we plotted animals’ peak speed (averaged over the plate) against the speed 3 days later (Figure 7C) and found that even plate-by-plate, *hsf-1(RNAi)* showed a sufficiently large early decrease in speed to lie almost completely outside of the control distribution. Thus, we anticipate that significant progeria could be detected in a screen that uses only a single plate per condition.

Although our controls for other experiments included gene knockdowns expected to extend lifespan, we did not find any that markedly increased motility 3 days after peak speed. This included *daf-2(RNAi)* animals, though not entirely unexpectedly. Previously, in manual experiments with the MWT, we also found that *daf-2(RNAi)* was insufficient to show an early motility phenotype. Specifically, although long-lived *daf-2(e1368)* hypothesized ligand-binding-domain mutants exhibited increased motility relative to wild type from mid-adulthood onward, *daf-2(RNAi)* animals differed from control only in that they continued to move (detectably) after the control animals had stopped (Podshivalova et al. (2017), Figure 1B; Supplementary Figure S2C). The reason for the difference was unclear; one possible explanation could involve the fact that neurons tend to be insensitive to RNAi because they do not express the dsRNA transporter SID-1 (Calixto et al., 2010). In the *C. elegans* Observatory, *daf-2(RNAi)* animals appeared indistinguishable from control throughout the time when speeds could be compared using automatically generated graphs (Figure 7D).

**FIGURE 7**

Validation of genetic perturbations resulting in reduced and extended maintenance of youthful behavior. **(A)** Aroused maximum speed of control (black, $n = 14$ plates) or *hsf-1(RNAi)* (pink, $n = 5$ plates). Red arrow indicates the time of peak activity. Orange arrow indicates 72 h later. Note the marked decrease in speed of *hsf-1(RNAi)* animals at the timepoint indicated in orange, but not at red. 40–60 animals per plate. **(B)** Length of CF512 animals on control (black) or *hsf-1* RNAi bacteria (pink). Arrows and sample size as in **(A)**. **(C)** Consistency of progeric phenotype in *hsf-1(RNAi)*. Each plate is characterized by peak speed (y-axis) and speed after 3 days (x-axis), corresponding to the values of graphs at the red and orange arrows in **(B)**. Replicates across four experiments and two experimenters are shown. Pink dots, *hsf-1(RNAi)* ($n = 13$ plates). Black circles, control ($n = 62$ plates). $p < 10^{-6}$ that the two sets of points have the same ratio of day 3 over day 0, by Mann–Whitney U test. **(D)** Aroused maximum speed of control (black, $n = 12$ plates) or *daf-2(RNAi)* (green, $n = 4$ plates). Data points are plotted only when at least one plate has at least three animals detected and measured, so the extended detection of *daf-2(RNAi)* reflects greater motion overall, if not higher speed among detected animals. 60 animals per plate. **(E)** Extended maintenance of moving fraction of *daf-2(RNAi)* with age. The aroused maximum speed of every detected animal is shown in a one-sided beeswarm-style plot for control (black) and *daf-2(RNAi)* (green) at 3-day intervals. Each dot corresponds to the score for one animal on that day. Because the *daf-2* data set ($n = 123$ measurements on day 0) is smaller than the control ($n = 536$ on day 0), the dot size is normalized such that the total area of dots is equal at day 0, providing a visually faithful representation of the decreasing fraction of detectable animals. The underlying data are the same as in **(D)**. $^{\dagger}, p < 0.01$ and $^{\ddagger}, p < 0.0001$, probability by chi-squared test that the reduction from day 0 in the number of animals measured is the same for wild-type and *daf-2(RNAi)*.

To gain a clearer picture of how detectability varied, especially given that automatic graphing rejects as potentially unreliable data from plates with two or fewer worms, we also plotted the data animal-by-animal at various timepoints. Consistent with Podshivalova et al. (2017), we observed that a significantly higher fraction of *daf-2(RNAi)* animals moved enough to be detected after control animals did not (Figure 7E, day 9 after peak speed and later). We also used

animal-by-animal plotting to verify that *hsf-1(RNAi)* animals could not be detected for as long as controls (Supplementary Figure S2; significant difference on day 3 after peak speed and thereafter).

4.1.3 Lifespan in the Observatory

To verify that lifespan was not affected by conditions in the *C. elegans* Observatory—for instance, by the repeated behavioral

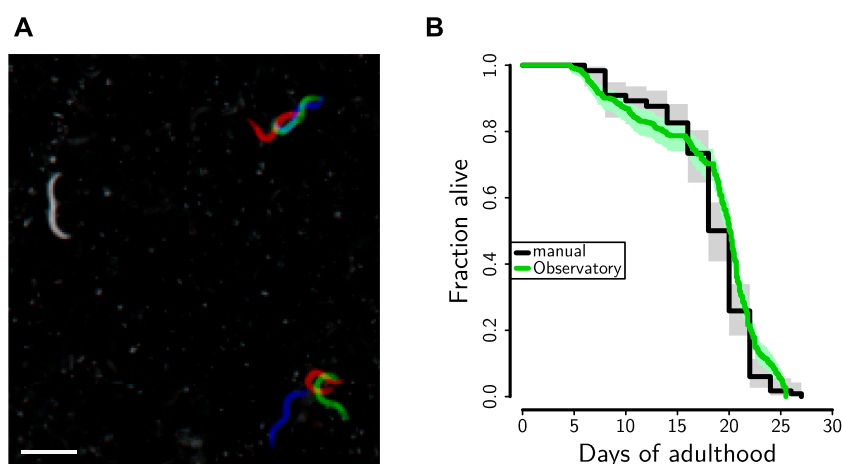


FIGURE 8

Lifespan determination. **(A)** Snapshots saved during successive recording sessions (6 h apart) were overlaid in red, green, and blue. This allows rapid visual identification of animals who are dead (gray; left), are moving their whole bodies (red, green, and blue; lower right), or are moving part of their bodies (part gray, part color; upper right). Scale bar is 1 mm. **(B)** Lifespan of CF512 on RNAi control bacteria either in the Observatory (green, median lifespan 20.1 days, $n = 343$ deaths) or in a 25°C incubator (black, median lifespan 20.0 days, $n = 119$ deaths).

assays—we compared a manual lifespan conducted in a separate 25°C incubator with one scored off of images from the *C. elegans* Observatory using our red-green-blue method that helps call attention to the time of death (Figure 8A). We observed good agreement between the two (Figure 8B; additional data not shown), indicating that, as expected, worms were living normal-length lives within the *C. elegans* Observatory.

4.1.4 Variability in behavioral parameters

To understand the reproducibility we could expect from the *C. elegans* Observatory, we collected the control data from three experimenters across ten separate experiments. The different experiments had different goals, but in all cases, the control conditions were nominally the same. This revealed broad agreement between maximum-speed aging profiles computed for each plate. Nonetheless, there was substantial variability around the mean (Figure 9A). In order to understand the source of this variability, we decomposed it into variability across experiments (Figure 9B) and variability within experiments (i.e., between a plate and the population mean for all plates in that experiment, Figure 9C). Surprisingly, we found that the variability from each, by eye, was roughly comparable. Therefore, we quantified the variance explained both by the experiment and the plate within the experiment at each timepoint and plotted it as the coefficient of variation (standard deviation over mean; Figure 9D). This revealed that, indeed, the two do contribute comparable variability.

Variation from plate to plate within an experiment could result from either systematic plate-level factors or simply from the stochastic nature of sampling (both in the random selection

of animals that appear on a plate, if animals have characteristic variations, and in the sampling of random fluctuation of behavior during the assay). By sampling from the distribution of observed speeds normalized to the plate mean, we created fictitious plates where, by construction, there was no systematic plate-level variation, and only stochastic sampling remained. The predicted variability of these stochastic-only plates closely matched the observed variability of real plates (Figure 9D, closed blue circles vs. open blue circles), indicating that, under these conditions, a majority of the variability comes from stochastic sampling; differing conditions between the plates do not seem to be a significant concern. Note, however, that we prepare all plates at the same time and remove from consideration any plates contaminated with mold or undesired strains of bacteria precisely to avoid systematic differences between plates.

4.1.5 Power analysis

Our goal, setting out, was in part to create a system that could, in principle, scale up to the level of performing whole-genome screens. In our existing experiments, we have typically run four plates per condition, giving us a coefficient of variation of slightly over 5% for aroused maximum speed (predicted value: Figure 9D, green line). With this level of noise, what size of effect can we reasonably expect to recover? First, consider the approximation where all measured values and ratios thereof have a normal distribution. If we choose a significance cutoff of 0.05 (not corrected for multiple comparisons) as our threshold for detection and desire an 80% chance of detecting a variation that increases only the mean and not the noise (another simplifying approximation), this is equivalent to requiring that

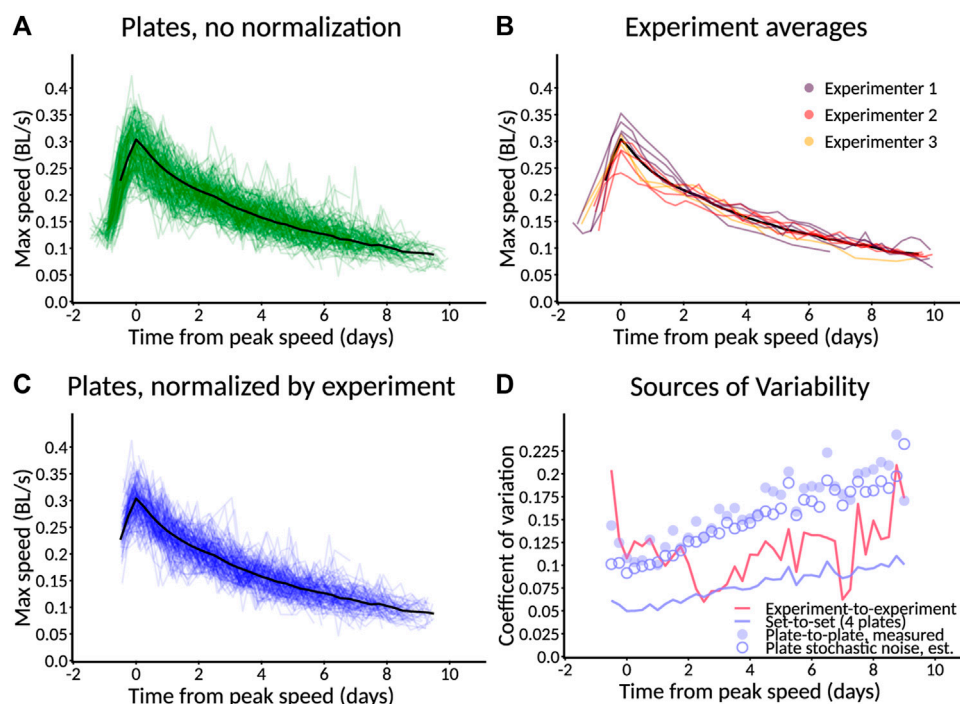


FIGURE 9

Estimation of sources of variability. (A) Measured variation in aroused maximum speed. Scores for 201 individual plates of control animals (green) across 10 experiments, plus population average (black). Typically, 40–60 animals per plate. (B) Variation between experiments. Experiment averages (colors) and population average (black) for data in (A). (C) Variation normalized by experiment. Scores for 154 plates normalized relative to their experiment (blue) by scaling the mean of the experiment to match the population average (black). Data from (A), with low-*n* plates filtered out. (D) Relative scale of sources of variability. Variation between experiments (red line) is larger than the variation between a 4-plate set of samples (blue line). Measured plate-to-plate variability (filled blue circles) closely matches expectations from stochastic sampling (open blue circles), indicating minimal systematic plate-to-plate effects. Variability is expressed as the coefficient of variation compared to the population average (black lines in (A–C)).

only 0.2 of the distribution of the shifted mean falls below the 0.95 + point on the tail of the null hypothesis distribution. Thus, for a one-sided test, we require a difference of

$$\Delta\mu \geq \sigma_0 \cdot (\text{icdf}_{N(0,1)}(0.95) + \text{icdf}_{N(0,1)}(0.8)),$$

where icdf represents the inverse cumulative distribution of a probability distribution, $N(0, 1)$ is the normal distribution with mean 0 and standard deviation 1, and σ_0 is the standard deviation of the measurement of the peak-to-day-three ratio of activities. This works out to roughly 2.5× the coefficient of variation for a single-sided test or 2.8× a two-sided test to reach $p < 0.05$ 80% of the time. For a ratio of peak speed to day 3 speed (with measured coefficients of variation of 0.055 and 0.077, respectively) and naive propagation of error to the ratio, this works out to an 80% detection chance for a roughly 24% change in mean for a one-sided test, or 27% for a two-sided test.

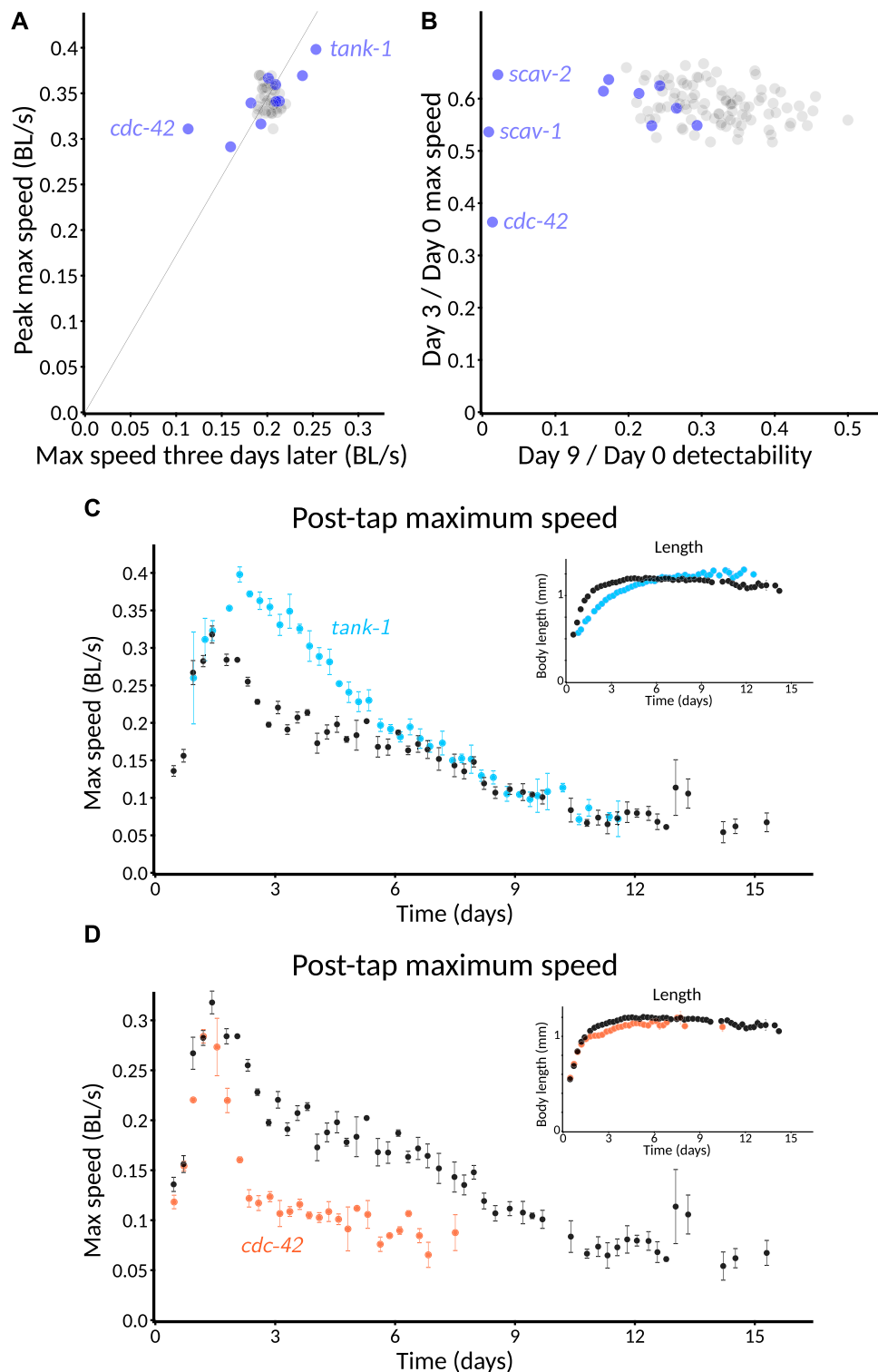
Monte Carlo sampling of the wild-type data in Figure 9, assuming a control set of 30 plates and a sample size of 4 plates per experimental condition, with true mean peak speed assumed not to vary across conditions and day three varying multiplicatively, gives an empirical 80% chance of passing a

two-sided test threshold of $p < 0.05$ when the value is changed by 1.31x, in line with the approximate result.

These results inform our expectations about what reasonably could be found in a whole-genome screen. Smaller changes could be robustly detected using more of the data, thereby lowering the measurement noise. For instance, instead of comparing a single timepoint, values could be averaged over a wider temporal window—perhaps three sessions (18 hours) centered on peak speed and five sessions centered on day three.

4.2 Novel aging-trajectory phenotypes

Although the *C. elegans* Observatory has the potential throughput to enable an unbiased screen, we were curious whether a candidate-gene approach could reveal novel behavioral trajectory phenotypes. Via computational analysis of human health data (Libert et al., 2022) and literature search, a variety of candidate mammalian genes were selected. We picked *C. elegans* genes corresponding to some of these based

**FIGURE 10**

Pilot screen of gene candidates implicated in healthy mammalian aging. (A) Effect on early vigor. Aroused maximum speed at peak vs. three days later for RNAi of ten candidate genes with 3–4 plates per condition and 30–60 worms per plate (blue) compared to random 3–4 plate samples out of the 16 control plates representing the expected distribution (gray). The thin line indicates a constant peak to 3-day speed ratio. The slowest and fastest 3-day conditions are named (slow: *cdc-42*, fast: *tank-1*; $p < 0.01$ that each is from the control distribution), corresponding to the best candidates for reduced and extended vigor, respectively. RNAi began at L1. (B) Effect on detectable motility. Ratio of animals detected on day nine vs. day zero (horizontal axis) against the ratio of early vigor (day three/day zero speed), with samples from (A). The three genes showing dramatic loss of (Continued)

FIGURE 10

detectable motility are named (*cdc-42*, *scav-1*, and *scav-2*). Experiment averages (blue) and random control sets (gray) for data in (A). (C) Speed timecourse for *tank-1(RNAi)* (average of four plates). Inset shows the length of the animal, illustrating slower development of *tank-1(RNAi)* animals. (D) Speed timecourse for *cdc-42(RNAi)* (average of three plates). Inset shows length, illustrating a normal developmental timecourse.

on the existence of orthologs, paralogs, or at least reasonably closely related gene families and the presence of corresponding RNAi constructs in the Ahringer RNAi library (Kamath et al., 2003).

Despite having only ten candidate genes (Supplementary Table S1), we found several interesting RNAi phenotypes. For early aging, we found both considerably elevated and reduced maintenance of youthful movement (Figure 10A) in *tank-1(RNAi)* and *cdc-42(RNAi)*, respectively. For later-life aging, we found no candidates that clearly increased detectability after 9 days, but we found three that markedly reduced it: *cdc-42(RNAi)*, *scav-1(RNAi)*, and *scav-2(RNAi)*.

The full behavioral trajectory of *tank-1(RNAi)* revealed an intriguing phenotype: animals grew slowly (Figure 10C, inset), yet they did not simply “live slow,” and display slowed movement as well as development. Instead, young *tank-1(RNAi)* animals were equally vigorous or even more vigorous than were control animals. Furthermore, they exhibited this youthful vigor for an extended period of time before eventually returning to match controls at older ages.

In contrast, *cdc-42(RNAi)* showed a consistent progeric phenotype reminiscent of *hsf-1(RNAi)*: despite growth and peak speed that closely matched controls, movement speed dropped more rapidly in treated animals than in controls (Figure 10D).

More generally, these results demonstrate the effectiveness of the *C. elegans* Observatory at discovering when a gene can influence aging trajectories.

5 Discussion

The *C. elegans* Observatory was conceived of as a high-throughput yet approachable tool for studying factors that influence how animals age. Thus far, we have focused on usability and throughput rather than a diverse set of behavioral metrics, reasoning that the ability to easily measure one primary behavior—stimulus-aroused motility—throughout life was the most important advance in our capabilities. However, we also plan to re-analyze existing data, taking advantage of both positional and postural data (exemplified in Figure 3C) to quantify additional behaviors. The MWT has been used to quantify a variety of behaviors in young and aging animals (Swierczek et al., 2011; Podshivalova et al., 2017), but the algorithms make assumptions about magnification and stability that are not fully met in the *C. elegans* Observatory

configuration. Therefore, each behavior requires validation, and some will require algorithmic adjustments. We anticipate that the additional richness will provide deeper insight into the biology of aging. For instance, we would like to ask whether genes that affect youthful motility coordinately affect the youthful presentation of other behaviors. Being able to acquire the data, as we are now, is the first and most critical step.

Thanks to its use of standard plates and its relatively straightforward user interface, it is easy to use for small-scale experiments, and this is mostly how we have used it thus far. Nonetheless, its ability to scale to larger screens is promising. A single individual can load the entire *C. elegans* Observatory in roughly 2 days of intensive work, with four plates per RNAi condition. Although this would be a grueling activity to keep up for months on end, if one had five Observatories, a single individual could, in principle, run over 2,500 conditions (10,000 experimental plates) per month for two-week assays. This would allow the entire updated Ahringer RNAi library, containing roughly 20,000 samples, to be screened in approximately 8 months, with 80% power to detect changes of 30% at a 5% false positive rate. Alternatively, a less sensitive single-plate assay, which would require no more than twice the effect size for the same detection chance, could be performed on a single Observatory in well under a year. These capabilities position the *C. elegans* Observatory favorably for a thorough understanding of the genetics of behavioral aging.

Among worm trackers, the *C. elegans* Observatory occupies a useful position along the outer envelope of throughput and precision, reminiscent of a quote from journalist A. J. Liebling: “I write faster than anyone who can write better, and I write better than anyone who can write faster.” In comparison to our system, the behavioral detail provided by a multi-camera 96-well format processed with the Tierpsy tracker (Barlow et al., 2022) is considerably greater (due to the focus on detailed analysis of morphology and behavior and also the 8 μ m pixel size as opposed to 40 μ m here) and has the advantage of easily switching to longitudinal mode (one worm per well; they typically use three). However, compared to their full 30-camera system, the *C. elegans* Observatory will run five times the number of conditions with 3–4x the number of animals per condition. Interestingly, a hybrid system is conceptually straightforward: their arrangement of five 96-well plates fits comfortably within the area of a single Observatory tray. In contrast, the WormCamp (Fouad et al., 2021) system makes tradeoffs to go faster: they use a stage-mounted camera assembly to traverse over a large field of 24-well plates, giving them access to roughly 4x more wells than

the Observatory holds plates but with reduced assay time (5 min compared to 9 in the Observatory) and activity only scored at the population level, not animal-by-animal. For our purposes, the *C. elegans* Observatory strikes the right balance between throughput and power to detect behavioral phenotypes, but other systems that push the outer edge of the throughput-precision space also have considerable potential to expand our understanding of the aging process.

We do not yet know what fraction of genes will produce an appreciable phenotype when knocked down with RNAi. Our very limited candidate-gene approach was surprisingly successful, though it is difficult to tell to what extent this is a function of the prevalence of good targets and to what extent it is due to astute selection. Although a longevity phenotype had not, to our knowledge, previously been demonstrated in *C. elegans*, *cdc-42* was predicted to be a candidate aging/longevity pathway gene (Witten and Bonchev, 2007) in addition to its known role in the establishment of cell polarity (Cowan and Hyman, 2007). Likewise, no *C. elegans* longevity phenotype has been reported for the PARP-family gene *tank-1*; in mammals, tankyrase was originally identified as a telomere-associated protein (Azarm and Smith, 2020) and has a diversity of other roles (Damale et al., 2020). In *Drosophila*, mutations in tankyrase have been reported to reduce both lifespan and climbing behavior (Li et al., 2018), but we are not aware of any reports that reduced tankyrase might also increase the duration of youthful vigor. Understanding the molecular basis of the *cdc-42(RNAi)* and *tank-1(RNAi)* phenotypes would obviously require additional study, starting with a longer recording or a manual assay to determine the lifespans. Nonetheless, finding that at least two out of ten candidate genes had interesting RNAi-knockdown phenotypes was encouraging.

Seemingly intractable biological problems often require the development of new techniques and technologies before they at last yield and we begin to gain insight. It is our hope that the *C. elegans* Observatory and tools like it will play a part in developing a mechanistic understanding of the basis of aging.

Data availability statement

The datasets presented in this study can be found in online repositories. The names of the repository/repositories and accession number(s) can be found below: <https://doi.org/10.5281/zenodo.6645842>.

Author contributions

RK and CK conceived and designed the study. RK designed, built, and programmed the automated system. AR, JG, and RK conducted experiments. RK wrote the manuscript and

constructed the figures. All authors reviewed, improved, and approved the manuscript.

Funding

All funding was provided internally by Calico Life Sciences LLC.

Acknowledgments

We are grateful to many members of Calico Life Sciences LLC. Alfred Millet-Sicking and Andrew York assisted with the mechanical and optical design of the system, and Alfred additionally helped with electronics. Eddie Xue, Jacob Kimmel, and Adam Baker provided feedback on software engineering and user interface design. Peter Noone and Alex Chekholko supported our needs for computational infrastructure, including networking and cluster storage. Katie Podshivalova and Peichuan Zhang ran trial experiments as the system was being developed, providing feedback on improving the system. Sergiy Libert provided a list of candidate mammalian genes. Ashok Shah ensured ample supplies of media and worm plates of various sorts. We are also grateful to Zachary Pincus, who is not from Calico, for his advice on the prioritization and scope of the project. Strains from the *C. elegans* Genetics Center (CGC), which is funded by the NIH Office of Research Infrastructure Programs (P40 OD010440), were used during testing and development.

Conflict of interest

The authors RK, AR, JG, and CK were employees of and fully funded by Calico Life Sciences LLC, a for-profit company.

Publisher's note

All claims expressed in this article are solely those of the authors and do not necessarily represent those of their affiliated organizations or those of the publisher, the editors, and the reviewers. Any product that may be evaluated in this article, or claim that may be made by its manufacturer, is not guaranteed or endorsed by the publisher.

Supplementary material

The Supplementary Material for this article can be found online at: <https://www.frontiersin.org/articles/10.3389/fragi.2022.932656/full#supplementary-material>

References

- Azarm, K., and Smith, S. (2020). Nuclear parps and genome integrity. *Genes Dev.* 34, 285–301. doi:10.1101/gad.334730.119
- Back, J.-H., Cosman, P., Feng, Z., Silver, J., and Schafer, W. R. (2002). Using machine vision to analyze and classify *Caenorhabditis elegans* behavioral phenotypes quantitatively. *J. Neurosci. Methods* 118, 9–21. doi:10.1016/s0165-0270(02)00117-6
- Barlow, I. L., Feriani, L., Minga, E., McDermott-Rouse, A., O'Brien, T. J., Liu, Z., et al. (2022). Megapixel camera arrays enable high-resolution animal tracking in multiwell plates. *Commun. Biol.* 5, 253. doi:10.1038/s42003-022-03206-1
- Calixto, A., Chelur, D., Topalidou, I., Chen, X., and Chalfie, M. (2010). Enhanced neuronal RNAi in *C. elegans* using sid-1. *Nat. Methods* 7, 554–559. doi:10.1038/nmeth.1463
- Churgin, M. A., Jung, S.-K., Yu, C.-C., Chen, X., Raizen, D. M., Fang-Yen, C., et al. (2017). Longitudinal imaging of *Caenorhabditis elegans* in a microfabricated device reveals variation in behavioral decline during aging. *Elife* 6, e26652. doi:10.7554/eLife.26652
- Cowan, C. R., and Hyman, A. A. (2007). Acto-myosin reorganization and par polarity in *C. elegans*. *Development* 134, 1035–1043. doi:10.1242/dev.000513
- Damale, M. G., Pathan, S. K., Shinde, D. B., Patil, R. H., Arote, R. B., Sangshetti, J. N., et al. (2020). Insights of tankyrases: A novel target for drug discovery. *Eur. J. Med. Chem.* 207, 112712. doi:10.1016/j.ejmech.2020.112712
- Dieleman, J. L., Baral, R., Birger, M., Bui, A. L., Bulchis, A., Chapin, A., et al. (2016). US spending on personal health care and public health, 1996–2013. *JAMA* 316, 2627–2646. doi:10.1001/jama.2016.16885
- Fouad, A. D., Churgin, M. A., Hayden, J., Xu, J., Park, J.-I., Liu, A., et al. (2021). High-throughput imaging of *Caenorhabditis elegans* aging using collective activity monitoring. Cold Spring Harbor Laboratory. Available at: <https://www.biorxiv.org/content/early/2021/10/19/2021.10.18.464905>.
- Gandhi, S., Santelli, J., Mitchell, D. H., Stiles, J. W., and Sanadi, D. R. (1980). A simple method for maintaining large, aging populations of *Caenorhabditis elegans*. *Mech. Ageing Dev.* 12, 137–150. doi:10.1016/0047-6374(80)90090-1
- Garigan, D., Hsu, A.-L., Fraser, A. G., Kamath, R. S., Ahringer, J., Kenyon, C., et al. (2002). Genetic analysis of tissue aging in *Caenorhabditis elegans*: a role for heat-shock factor and bacterial proliferation. *Genetics* 161, 1101–1112. doi:10.1093/genetics/161.3.1101
- Hahm, J.-H., Kim, S., DiLoreto, R., Shi, C., Lee, S.-J. V., Murphy, C. T., et al. (2015). *C. elegans* maximum velocity correlates with healthspan and is maintained in worms with an insulin receptor mutation. *Nat. Commun.* 6, 8919. doi:10.1038/ncomms9919
- Hebert, L., Ahamed, T., Costa, A. C., O'Shaughnessy, L., and Stephens, G. J. (2021). Wormpose: Image synthesis and convolutional networks for pose estimation in *C. elegans*. *PLoS Comput. Biol.* 17, e1008914. doi:10.1371/journal.pcbi.1008914
- Hulme, S. E., Shevkoplyas, S. S., McGuigan, A. P., Apfeld, J., Fontana, W., Whitesides, G. M., et al. (2010). Lifespan-on-a-chip: microfluidic chambers for performing lifelong observation of *C. elegans*. *Lab. Chip* 10, 589–597. doi:10.1039/b919265d
- Husson, S. J., Costa, W. S., Schmitt, C., and Gottschalk, A. (2012). "Keeping track of worm trackers," in *WormBook* Editors The *C. elegans* Research Community. WormBook. Available at: <http://www.wormbook.org>
- Iwasa, H., Yu, S., Xue, J., and Driscoll, M. (2010). Novel egf pathway regulators modulate *C. elegans* healthspan and lifespan via egf receptor, plc-gamma, and ip3r activation. *Aging Cell* 9, 490–505. doi:10.1111/j.1474-9726.2010.00575.x
- Javer, A., Ripoll-Sánchez, L., and Brown, A. E. X. (2018). Powerful and interpretable behavioural features for quantitative phenotyping of *Caenorhabditis elegans*. *Philos. Trans. R. Soc. Lond. B Biol. Sci.* 373, 20170375. doi:10.1098/rstb.2017.0375
- Kamath, R. S., Martinez-Campos, M., Zipperlen, P., Fraser, A. G., and Ahringer, J. (2001). Effectiveness of specific RNA-mediated interference through ingested double-stranded RNA in *Caenorhabditis elegans*. *Genome Biol.* 2, RESEARCH0002. doi:10.1186/gb-2000-2-1-research0002
- Kamath, R. S., Fraser, A. G., Dong, Y., Poulin, G., Durbin, R., Gotta, M., et al. (2003). Systematic functional analysis of the *Caenorhabditis elegans* genome using RNAi. *Nature* 421, 231–237. doi:10.1038/nature01278
- Li, P., Huang, P., Li, X., Yin, D., Ma, Z., Wang, H., et al. (2018). Tankyrase mediates K63-linked ubiquitination of JNK to confer stress tolerance and influence lifespan in *Drosophila*. *Cell Rep.* 25, 437–448. doi:10.1016/j.celrep.2018.09.036
- Libert, S., Chekholko, A., and Kenyon, C. (2022). *A physiology clock for human aging*. Cold Spring Harbor Laboratory. Available at: <https://www.biorxiv.org/content/early/2022/04/14/2022.04.14.488358>.
- López-Otín, C., Blasco, M. A., Partridge, L., Serrano, M., and Kroemer, G. (2013). The hallmarks of aging. *Cell* 153, 1194–1217. doi:10.1016/j.cell.2013.05.039
- Nagy, S., Goessling, M., Amit, Y., and Biron, D. (2015). A generative statistical algorithm for automatic detection of complex postures. *PLoS Comput. Biol.* 11, e1004517. doi:10.1371/journal.pcbi.1004517
- O'Neill, M. E. (2014). *PCG: A family of simple fast space-efficient statistically good algorithms for random number generation*. Tech. Rep. Claremont, CA: Harvey Mudd College. HMC-CS-2014-0905.
- Ohya, T., Jovanic, T., Denisov, G., Dang, T. C., Hoffmann, D., Kerr, R. A., et al. (2013). High-throughput analysis of stimulus-evoked behaviors in *Drosophila* larva reveals multiple modality-specific escape strategies. *PLoS One* 8, e71706. doi:10.1371/journal.pone.0071706
- Oswal, N., Martin, O. M. F., Stroustrup, S., Bruckner, M. A. M., and Stroustrup, N. (2021). *A hierarchical process model links behavioral aging and lifespan in C. elegans*. Cold Spring Harbor Laboratory. Available at: <https://www.biorxiv.org/content/early/2021/09/27/2021.03.31.437415>.
- Overman, K. E., Choi, D. M., Leung, K., Shaevitz, J. W., and Berman, G. J. (2022). Measuring the repertoire of age-related behavioral changes in *Drosophila melanogaster*. *PLoS Comput. Biol.* 18, e1009867. doi:10.1371/journal.pcbi.1009867
- Pitt, J. N., Strait, N. L., Vayndorf, E. M., Blue, B. W., Tran, C. H., Davis, B. E. M., et al. (2019). Wormbot, an open-source robotics platform for survival and behavior analysis in *C. elegans*. *Geroscience* 41, 961–973. doi:10.1007/s11357-019-00124-9
- Pittman, W. E., Sinha, D. B., Zhang, W. B., Kinser, H. E., and Pincus, Z. (2017). A simple culture system for long-term imaging of individual *C. elegans*. *Lab. Chip* 17, 3909–3920. doi:10.1039/c7lc00916j
- Podshivalova, K., Kerr, R. A., and Kenyon, C. (2017). How a mutation that slows aging can also disproportionately extend end-of-life decrepitude. *Cell Rep.* 19, 441–450. doi:10.1016/j.celrep.2017.03.062
- Rahman, M., Edwards, H., Birze, N., Gabrilka, R., Rumbaugh, K. P., Bławdziewicz, J., et al. (2020). NemaLife chip: a micropillar-based microfluidic culture device optimized for aging studies in crawling *C. elegans*. *Sci. Rep.* 10, 16190. doi:10.1038/s41598-020-73002-6
- Ramot, D., Johnson, B. E., Berry, T. L., Carnell, L., and Goodman, M. B. (2008). The parallel worm tracker: a platform for measuring average speed and drug-induced paralysis in nematodes. *PLoS One* 3, e2208. doi:10.1371/journal.pone.0002208
- Simmer, F., Tijsterman, M., Parrish, S., Koushika, S. P., Nonet, M. L., Fire, A., et al. (2002). Loss of the putative RNA-directed RNA polymerase rrf-3 makes *C. elegans* hypersensitive to RNAi. *Curr. Biol.* 12, 1317–1319. doi:10.1016/s0960-9822(02)01041-2
- Stein, G. M., and Murphy, C. T. (2012). The intersection of aging, longevity pathways, and learning and memory in *C. elegans*. *Front. Genet.* 3, 259. doi:10.3389/fgene.2012.00259
- Stiernagle, T. (2006). "Maintenance of *C. elegans*," in *WormBook* Editors The *C. elegans* Research Community. WormBook. Available at: <http://www.wormbook.org>
- Stroustrup, N., Ulmschneider, B. E., Nash, Z. M., López-Moyado, I. F., Apfeld, J., Fontana, W., et al. (2013). The *Caenorhabditis elegans* lifespan machine. *Nat. Methods* 10, 665–670. doi:10.1038/nmeth.2475
- Swierczek, N. A., Giles, A. C., Rankin, C. H., and Kerr, R. A. (2011). High-throughput behavioral analysis in *C. elegans*. *Nat. Methods* 8, 592–598. doi:10.1038/nmeth.1625
- Taormina, G., Ferrante, F., Vieni, S., Grassi, N., Russo, A., Mirisola, M. G., et al. (2019). Longevity: Lesson from model organisms. *Genes (Basel)* 10, E518. doi:10.3390/genes10070518
- Wilson, K. A., Beck, J. N., Nelson, C. S., Hilsabeck, T. A., Promislow, D., Brem, R. B., et al. (2020). Gwas for lifespan and decline in climbing ability in flies upon dietary restriction reveal decima as a mediator of insulin-like peptide production. *Curr. Biol.* 30, 2749–2760.e3. doi:10.1016/j.cub.2020.05.020
- Witten, T. M., and Bonchev, D. (2007). Predicting aging/longevity-related genes in the nematode *Caenorhabditis elegans*. *Chem. Biodivers.* 4, 2639–2655. doi:10.1002/cbdv.200790216
- Yemini, E., Jucikas, T., Grundy, L. J., Brown, A. E. X., and Schafer, W. R. (2013). A database of *Caenorhabditis elegans* behavioral phenotypes. *Nat. Methods* 10, 877–879. doi:10.1038/nmeth.2560



OPEN ACCESS

EDITED BY

Lene Juel Rasmussen,
University of Copenhagen, Denmark

REVIEWED BY

Peter Fedichev,
Gero LLC, Russia
Markus Schosserer,
Medical University of Vienna, Austria

*CORRESPONDENCE

Andreas Hermann,
✉ andreas.hermann@med.uni-
rostock.de

SPECIALTY SECTION

This article was submitted to Molecular
Mechanisms of Aging,
a section of the journal
Frontiers in Aging

RECEIVED 21 December 2022

ACCEPTED 02 February 2023

PUBLISHED 15 February 2023

CITATION

Hartmann C, Herling L, Hartmann A,
Köckritz V, Fuellen G, Walter M and
Hermann A (2023), Systematic estimation
of biological age of *in vitro* cell culture
systems by an age-associated
marker panel.
Front. Aging 4:1129107.
doi: 10.3389/fragi.2023.1129107

COPYRIGHT

© 2023 Hartmann, Herling, Hartmann,
Köckritz, Fuellen, Walter and Hermann.
This is an open-access article distributed
under the terms of the [Creative
Commons Attribution License \(CC BY\)](#).
The use, distribution or reproduction in
other forums is permitted, provided the
original author(s) and the copyright
owner(s) are credited and that the original
publication in this journal is cited, in
accordance with accepted academic
practice. No use, distribution or
reproduction is permitted which does not
comply with these terms.

Systematic estimation of biological age of *in vitro* cell culture systems by an age-associated marker panel

Christiane Hartmann¹, Luise Herling¹, Alexander Hartmann²,
Verena Köckritz¹, Georg Fuellen^{3,4}, Michael Walter^{2,4} and
Andreas Hermann^{1,4,5*}

¹Translational Neurodegeneration Section “Albrecht-Kossel”, Department of Neurology, University Medical Center Rostock, Rostock, Germany, ²Institute of Clinical Chemistry and Laboratory Medicine, University Medical Center Rostock, Rostock, Germany, ³Institute for Biostatistics and Informatics in Medicine and Ageing Research, Rostock University Medical Center, Rostock, Germany, ⁴Center for Transdisciplinary Neurosciences Rostock (CTNR), University Medical Center Rostock, Rostock, Germany, ⁵Deutsches Zentrum für Neurodegenerative Erkrankungen (DZNE) Rostock/Greifswald, Rostock, Germany

Aging is a process that affects almost all multicellular organisms and since our population ages with increasing prevalence of age-related diseases, it is important to study basic processes involved in aging. Many studies have been published so far using different and often single age markers to estimate the biological age of organisms or different cell culture systems. However, comparability of studies is often hampered by the lack of a uniform panel of age markers. Consequently, we here suggest an easy-to-use biomarker-based panel of classical age markers to estimate the biological age of cell culture systems that can be used in standard cell culture laboratories. This panel is shown to be sensitive in a variety of aging conditions. We used primary human skin fibroblasts of different donor ages and additionally induced either replicative senescence or artificial aging by progerin overexpression. Using this panel, highest biological age was found for artificial aging by progerin overexpression. Our data display that aging varies depending on cell line and aging model and even from individual to individual showing the need for comprehensive analyses.

KEYWORDS

age marker, biological age - chronological age, age panel, skin fibroblast, progeria syndrome

1 Introduction

Aging, usually described as a time-dependent functional decline (López-otín et al., 2013), is a physiological process that affects nearly all multicellular organisms. It is, however, the most important risk factor for the development of age-associated diseases (Rodgers et al., 2019). In general, aging includes processes that reduce health and survival of an individual (Fuellen et al., 2019). However, an individual's chronological (the amount of years since birth) and biological age (reflecting actual physiological health state) can differ remarkably (Jylhävä, Pedersen, and Hägg, 2017; Kudryashova et al., 2020). In *in vitro* cell culture conditions, there are mainly two main contributors of the latter, which are the age of the donor at biopsy as well as the replicative aging/senescence that the respective cells have

undergone so far. If we wish to consider physiological health state, the age of the donor at biopsy should be his or her estimated biological age. In practice, however, this biological age is rarely available and it must be substituted by the donor's chronological age, which we call "donor age" in the following. In principle, the two main contributors cannot easily be distinguished with respect to their effects on the physiological "health" state of the cells. Thus, for the purpose of this paper, we define the age of cells in a cell culture (that is, their biological age) as the donor age plus the effects of continued culturing expressed as a time period in terms of donor age. This biological age can be *estimated* by biomarkers (which we call age markers) and it corresponds to a physiological "health" state which is predictive of the future behaviour of the cells. This affords a more precise description of the respective cell models used in scientific studies concerning their biological age, before they are used for experiments, which is recommended for a better characterization of the cells.

Aging processes have been studied in a variety of model systems. In addition to the various mouse models, *in vitro* cell cultures are the most commonly used systems. There are a variety of cell models for aging and all types of (age-related) diseases including simple cell models with heterogeneous expression systems (HeLa, HEK, etc.), patient-derived primary cells (e.g., fibroblasts) as well as induced-pluripotent stem cell (iPSC) models. Since the discovery of the latter, cell models of disease and/or aging have become of even greater interest. While these technologies enable to investigate patient-derived cell models of so far not available origins (e.g., neurons), these seem to significantly alter general aspects of cell physiology including their biological age. Especially in research on age-related diseases, it is therefore important to also consider the effects of such rejuvenation, e.g., by the process of iPSC generation, on various age markers.

An age marker is a measurable characteristic for estimating biological age or a related condition (Atkinson et al., 2001) in a biological system/organism. In the past, numerous suggestions for age markers have been made for the estimation of the biological age and its deviation from chronological age.

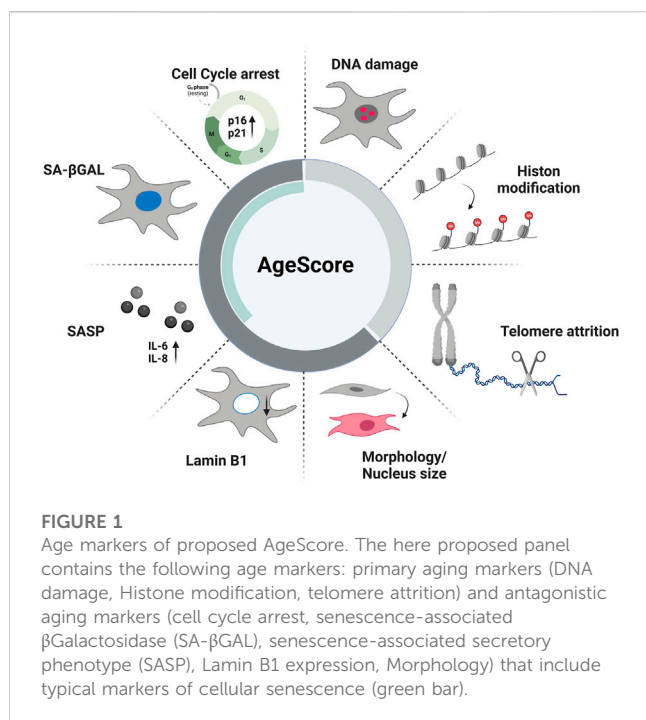
There are different aging hallmarks, and for some of them there are established markers to characterize biological age. For example, López-Otín described nine hallmarks of aging in three different main categories (López-otín et al., 2013). The primary hallmarks of aging (genomic instability, telomere attrition, epigenetic alterations, impaired proteostasis) are considered to be the main causes of cellular damage associated with rising age. These primary hallmarks lead to the antagonistic hallmarks of aging (deregulated nutrient sensing, mitochondrial dysfunction and cellular senescence), reactions that initially mitigate the damage but—if chronically present—can become harmful themselves. Finally, there are the integrative hallmarks of aging (stem cell exhaustion, altered intercellular communication), which are results of the previous two groups that are ultimately responsible for the loss of function associated with aging. These aging hallmarks can be investigated by various markers and methods (for summary see [Supplementary Table S1](#)).

Many putative age markers have thus been described and the age markers investigated in different studies often differ significantly (Hartmann et al., 2021). For this reason, a comparison of these studies among each other is often difficult and a specific comparison

e.g., between different cell lines and conditions (rejuvenated cells and aged cells) is even more difficult. Since the latter can also affect age markers differentially, it seems meaningful to rely on a broader spectrum of age markers to better examine the variety of components of the aging process especially in *in vitro* cell culture systems.

The epigenome, especially DNA methylation, thereby is the most often reported singular factor to quantify an individual's age. DNA methylation marks are the basis of so called "aging clocks" and often correlate well with the chronological age of the donor from which the tissue was derived. Furthermore, there is evidence that they can be used to estimate biological age. In 2013, Horvath developed one of the first "aging clocks" that allows to estimate the chronological age by DNA methylation markers, for many tissues and some cell types. In this study, a collection of available DNA methylation data sets was used to define and evaluate a specific age predictor, based on CpG islands whose DNA methylation levels correlate with the chronological age of individuals, referred to as DNAm age. The difference between the predicted chronological age and the actual chronological age is then considered to be an estimate of biological age. Accordingly, DNAm age showed high accuracy in estimating chronological age (Horvath, 2013). Of note are, however, the reported exceptions: amongst others, high accuracy was not found for dermal fibroblasts in general as well as B cells from patients suffering from progeria syndromes. The issue was resolved in a follow up study, by the so called "Skin and blood clock" (Horvath et al., 2018). Another methylation clock that predicts human age by using the Illumina Infinium HumanMethylation450 assay in human whole blood samples additionally showed an influence of sex and genetic variants on the DNAm age, but also that aging rates are different in different tissues (Hannum et al., 2013).

Using the so called "CultureAge" score, it was shown that *in vitro* cellular aging resembled tissue aging *in vivo*. This study established an algorithm using replicative aged mouse embryonic fibroblasts and subsequently validated it in multiple murine tissues. Interestingly, it was sensitive to detect rejuvenation during cellular reprogramming, but it was reported that this progressive kind of cellular aging is different from non-replicative senescence (e.g., induced by etoposide treatment or gamma irradiation) and reported a lack of correlation of SA- β -Galactosidase with the CultureAge score (Minteer et al., 2022). Kabacik and colleagues also reported that epigenetic aging—using the skin and blood clock—is different from cellular senescence, telomere attrition and genomic instability, but is influenced by nutrient sensing and mitochondrial activity (Kabacik et al., 2022). Based on single cell methylation data, Trapp and colleagues established the epigenetic clock "scAge" using different murine tissues and cells, capable of representing chronological age at single cell level, and their algorithm is independent of which CpGs are covered in each cell. Nevertheless, the study showed remarkable heterogeneity among cells. Whether the use of this epigenetic clock is applicable to cultured cells, needs to be clarified in further studies (Trapp, Kerepesi, and Gladyshev, 2021). Fleischer et al. claimed to be able to predict biological age by analyzing the transcriptome of human fibroblasts. They generated a big dataset of genome-wide RNA-seq profiles of human fibroblasts to estimate the biological age of these cells. The predicted age correlated with the chronological donor age (Fleischer et al., 2018).



While these “-omic” approaches are very useful in generating hypotheses, they lack information about how cells behave in cell culture and thus lack the biological meaning of the respective changes. Furthermore, these investigations are often expensive and need specific equipment not necessarily available. Additionally, these have reported quite a significant diversity of aging and senescence processes, partly lacking correlation to classical age markers such as SA-βgalactosidase.

Thus, our overall aim was to allow comparison of different aspects of aging in *in vitro* cell culture models with different donor background, different donor ages and accelerating age diseases, including different modes of aging e.g., replicative and artificial aging. Therefore, we first made an extensive literature search to identify established markers that are most likely relevant in cellular aging processes. We chose often-used markers from the primary and antagonistic hallmarks of aging as they are quantifiable by *in vitro* assays to investigate whether they can clearly depict the different aspects of aging. Subsequently, we developed a novel biomarker-based panel, consisting of well established classical age markers, to estimate the biological age of different cell culture aging systems that additionally can be used in standard cell culture laboratories (Figure 1). We hypothesized that this panel of age markers would better account for differences between individual cell lines and aging models and individuals than single markers. After confirming the aging-relevance of the single age markers we selected, we propose a scoring system, referred to as AgeScore, to calculate an individual absolute value as an estimate of the biological age of different human fibroblasts. Further validation of this proposed scoring system took place in human fibroblasts with replicative senescence and artificial aging by overexpression of progerin. Finally, we tested whether our aging panel is applicable in typical aging diseases (premature aging syndromes Hutchinson-Gilford-Progeria syndrome, HGPS, and Werner Syndrome, WS).

Conclusively, we propose an age score consisting of different well established markers representing aging and the consequences of aging as follows: 1) markers of the primary hallmarks of aging (DNA damage, telomere attrition, Histone modification) displaying the cellular damage, cell division and methylation status of the cells and 2) markers of the antagonistic hallmarks of aging (cellular senescence [cell cycle arrest, SA-β-Gal expression, activation of SASP], change of morphology, decrease in Lamin B1 expression) displaying how much the primary damage has already influenced cell homeostasis which display together a fundamental AgeScore estimating the biological age of cells in cell culture systems.

2 Materials and methods

2.1 Cell culture

Human skin fibroblasts from apparently healthy young, mid-age and old as well as diseased (Progeria) donors were purchased from Coriell Institute or prepared in our lab as described before (Naumann et al., 2018; Pal et al., 2018, 2021). Cells were cultured in Dulbecco-modified Eagle's medium (DMEM-Glutamax, ThermoFisher Scientific, #10569010) supplemented with 15% fetal bovine serum (FBS superior, ThermoFisher Scientific, #10270106) and penicillin/streptomycin (100 µg/mL, Fisher Scientific, #15140-122) on ventilated culture flasks (75 cm², Fisher Scientific, #658175) at 37°C and 5% CO₂. Fibroblasts were subcultured after trypsinisation (0.25% trypsin-EDTA, ThermoFisher Scientific, #25200-056). Culture medium was changed every 3–4 days.

2.2 Determination of population doubling level (PDL)

For determination of PDL, human fibroblasts were seeded into 6-well-plates (Sarstedt, #833.920) at a density of 2x10⁵ per well. When fibroblasts reached confluency, cells were counted and again seeded at a density of 2x10⁵. This was continued over 75–150 days. PDL was calculated as $PDL = 3.2^{(\log_{10} \text{harvested cells} - \log_{10} \text{seeded cells})} + \text{actual passage number}$.

2.3 Immunofluorescence staining

Fibroblasts were seeded at a density of 2.5x10⁴ per well in an 8-well µ-Slide (ibidi, #80806) and incubated for 48 h. Cells were fixed with 4% PFA at 37°C for 20 min followed by permeabilization with 0.2% of TritonX and blocked with Blocking Buffer (Pierce Protein-Free T20 (TBS) Blocking Buffer, ThermoFisher Scientific, #37571) at RT for 1 h. Primary antibodies (Anti-phospho-Histone H2A.X (Ser139), #05-636-25ug, 1:500, Millipore; Anti-Histone H3 (di methyl K9), #ab1220, 1:500, abcam; Anti-Lamin B1, #ab16048, 1:500, abcam; Anti-Vimentin, #PA1-16759, 1:300, Thermo Fisher Scientific) were incubated overnight at 4°C. After washing, secondary antibodies (Goat anti-Mouse IgG (H + L) Highly Cross-Adsorbed Secondary Antibody, Invitrogen; Goat anti-Rabbit IgG (H + L) Highly Cross-Adsorbed Secondary Antibody,

Invitrogen) were incubated for 90 min. Finally, after repeated washing, cells were mounted with 4,6-diamidino-2-phenylindole (DAPI) Fluoromount-G (Southern Biotech, #0100-20) and images were taken with a LSM900 confocal microscope (Zeiss). Analysis was done with Fiji software. γ H2A.X foci were counted per nucleus (threshold: 20–200; size: 5). Corrected total cell fluorescence (CTCF) was calculated as following: (CTCF) = Integrated Density—(Area of selected Cell/Region * Mean Grey Value of background readings). Nucleus size was determined with area (pixel units) of nucleus with Fiji software.

2.4 Telomere length measurement via monochromal multiplex qPCR (MM-qPCR)

A standard extraction kit (DNeasy Blood and Tissue Kit, Qiagen, Cat. # 69504) was used for DNA extraction. Mean telomere length was determined using the modified MM-qPCR as described previously (Cawthon, 2009). DNA samples (20 ng/ μ L) and a reference DNA standard (0.137–100 ng/ μ L) were assayed in triplicates on different plates and the average of three measurements was used to report the mean telomere length for each sample. A non-template control (water) and a positive control (human leukemia cell line 1301 DNA) were prepared in duplicates and run on every plate. The standard includes DNA samples of 352 healthy donors, with an average age of 40.14 years (18–70 years old; 38.35% males and 61.65% females). The assay was performed using a BioRad CFX384 real-time C1000 thermal cycler with the following profile: 1 cycle of 15 min at 95°C; 2 cycles of 15 s at 94°C, 1 cycle of 15 s at 49°C; 40 cycles of 15 s at 94°C, 1 cycle 10 s at 62°C, 1 cycle 15 s at 72°C with T signal acquisition, 10 s at 85°C, and 15 s at 89°C with signal acquisition. PCR reagents were used at the following final concentrations: 1 U titanium Taq DNA polymerase per reaction with provided titanium Taq PCR buffer (Cat. # 639208), SYBR Green I (Invitrogen, #S7563), 0.2 mM of each dNTP, 1 mM DTT, 1 M betaine, 900 nM of each telomere primer (*Telg*, *Telc*) and 300 nM of each single copy gene primer (*ALBu*, *ALBd*). Following primer sequences were used: *Telg* 5'ACA CTAAGGTTTGGGTTTGGGTTTGGGTTTGGGTTAGTGT'3; *Telc* 5'TGTTAGGTATCCCT ATCCCTATCCCTATCCCTATCCCT AACAA'3; *Albu* 5'CGGCGGCGGGCGGCGGGGCTGGGCGG AAATGCTGCACAGA ATCCTTG'3; *Albd* 5'GCCCCGCCCCGCGCGCCGTCGCCGCGGAAAAGCATGGTCGCCTGTT'3. Ratio of telomere to single-copy gene content (TLR) is taken as relative measurement of telomere length and expressed in arbitrary units. The intra-assay coefficients of variation were <0.3 for all samples.

2.5 Quantification of p21 and p16 expression levels

Total RNA was isolated using the “Quick RNA Miniprep” Kit (Zymo Research, #R1054) according to the manufacturer's protocol and cDNA was generated from 200 ng isolated RNA with High-Capacity cDNA Reverse Transcription Kit (Thermo Fisher Scientific, #4368814). mRNA expression levels were determined using Rotor Gene (QIAGEN) with Rotor-Gene

SYBR® Green PCR Kit (QIAGEN, #204074) using the following primers: *CDKN1A*(*p21*)-Fwd 5'-GACACCACTGGA GGGTGACT-3', *CDKN1A*(*p21*)-Rev 5'-CAGGTCCACATGGTCT TCCT-3', *CDKN2A*(*p16*)-Fwd 5'-CTCGTGCTGATGCTACTG AGGA-3', *CDKN2A*(*p16*)-Rev 5'-GGTCGGCGCAGTT GGGCTCC-3'. qPCRs were performed in duplicates for each sample ($n = 1$ correspond to 2 replicates). Data sets were normalized relative to *GAPDH* (*GAPDH*-Fwd 5'-GTCTCCTCT GACTTCAACAGCG-3', *GAPDH*-Rev 5'-ACCACCCTGTTGCTG TAGCCAA-3') using delta-delta-CT method.

2.6 Senescence-associated β -galactosidase (SA- β GAL)-Assay

Activity of SA- β -Gal was determined using the “Senescence β -Galactosidase staining” Kit (Cell signaling, #9860) according to the manufacturer's protocol and referred to as X-Gal staining in the figures. Cells with cytoplasmic staining were scored as positive. Relative amount to total cell numbers was quantified.

2.7 IL-6 and IL-8 medium concentration

ELISA from cell culture supernatants was performed using “Human IL-6/Interleukin-6 ELISA Kit PicoKine™” (BosterBio, #EK0410) or “Human IL-8/Interleukin-8 ELISA Kit PicoKine™” (BosterBio, #EK0413) according to the manufacturer's recommended procedures. ELISA were performed in duplicates for each sample ($n = 1$ correspond to 2 replicates).

2.8 Statistics

Statistical analyses were performed using GraphPad Prism 8 (LaJolla). Experimental groups were compared using one-way-ANOVA (followed by Dunnett's multiple comparison test). Statistical significance was set up at p -values <0.05 (*), <0.01 (**), <0.001 (***). Data were plotted using GraphPad Prism 8 (LaJolla) showing mean and standard error of the mean.

3 Results

3.1 Single age markers yield heterogeneous results in human fibroblasts of healthy donors with different ages

We first wanted to analyze how selected age markers relate to chronological donor age. Therefore, we performed a systematic comparison of the selected age markers, considering these one by one as single markers, in human fibroblasts from 14 donors from apparently healthy young (2–9 years), mid-age (34–48 years), and old individuals (78–96 years) (Figure 2A; Table 1). Both male and female donors were included. Furthermore, we examined the youngest available cell culture passages of each fibroblast line. To observe growth rates of cells, we investigated the population doubling level (PDL) under stable conditions (37°C, 5% CO₂) (Figure 2B). Primary

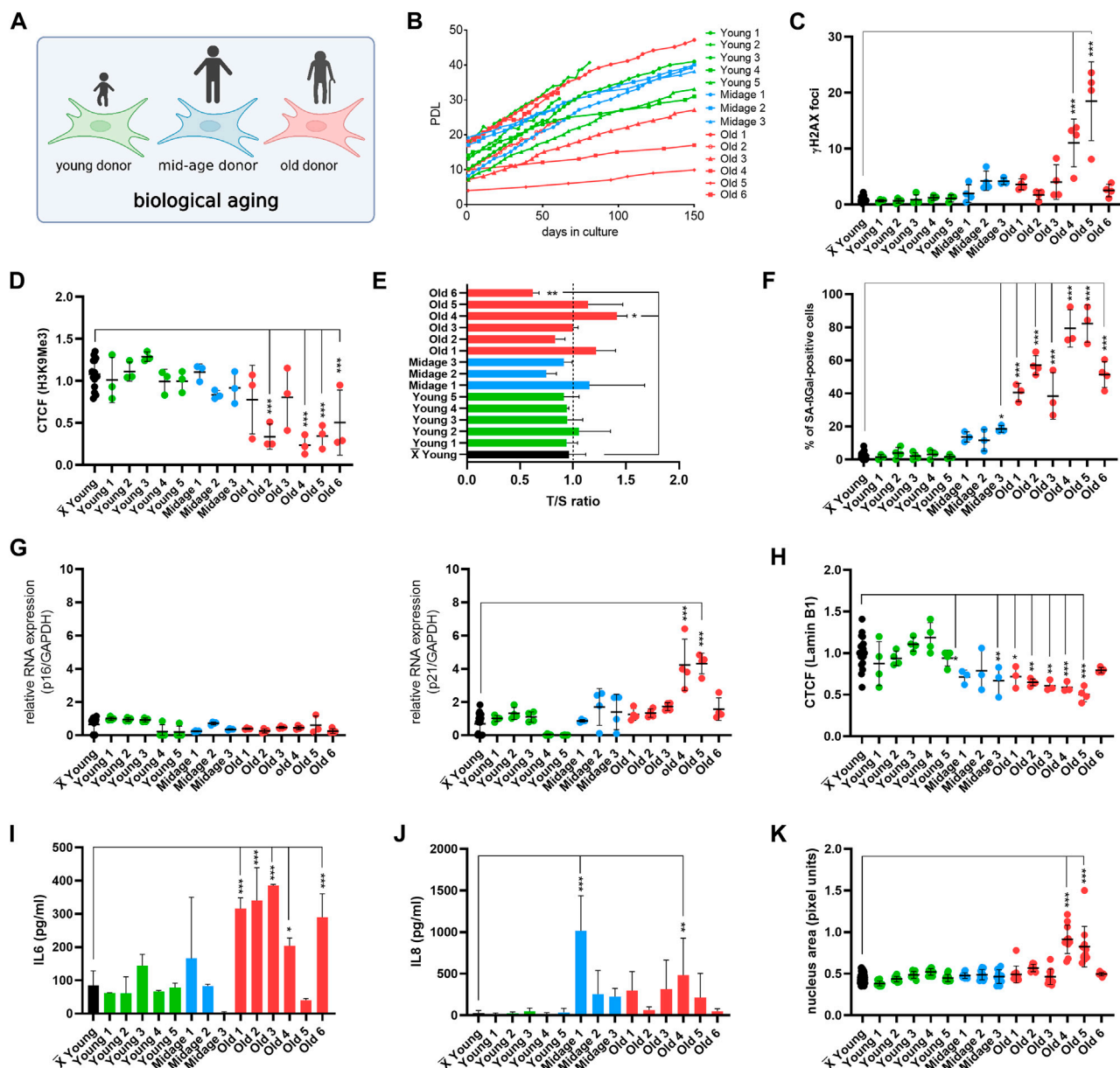


FIGURE 2

Establishment of the age marker-based panel in human fibroblasts of young, mid-age and old donors. **(A)** Cell Model. For initial experiments, fibroblasts with different donor age was used. **(B)** Replicative potential of human fibroblasts. Cells were cultured under stable conditions (37°C, 5% CO₂) in DMEM medium (with 15% FBS, 1% Pen-Strep). PDL was observed for max. 150 days. Fibroblasts from young (Young 1–5) and mid-age (Midage 1–3) donors display healthy growth. In contrast, fibroblasts from old donors (Old 3, Old 4, Old 5 and 6) showed slower growth except for Old 1 and Old 2. **(C–K)** X = Mean value of all young donor fibroblasts. **(C)** Amount of γH2AX foci per cell examined by IF staining to investigate DSBs in human fibroblasts. Cells of very old individuals (Old 4 and 5) displayed an increase in γH2AX foci in comparison to the mean of all young donors. Mid-age and old (Old 1, Old 2, Old 3 and Old 6) donor fibroblast showed no DSBs. [*n* = 3–4 (each *n* tested >15 cells), mean ± SEM, **p* < 0.05, ***p* < 0.001, ****p* < 0.0001, one-way ANOVA] **(D)** CTCF of H3K9Me3 in human fibroblasts. Donor fibroblasts from tested individuals (Old 2, Old 4, Old 5 and Old 6) displayed a decrease in CTCF of H3K9Me3 compared to the mean of young donors. There were no changes in CTCF of H3K9Me3 in mid-age cells (Midage 1–3). [*n* = 3–4 (each *n* tested >15 cells), mean ± SEM, **p* < 0.05, ***p* < 0.001, ****p* < 0.0001, one-way ANOVA] **(E)** Telomere length was measured by MM-qPCR in comparison to a standard of healthy mixed aged individuals. In comparison to grouped young donor cells, Old 6 displayed a shortening of telomere length. [*n* = 3, mean ± SEM, **p* < 0.05, ***p* < 0.001, ****p* < 0.0001, one-way ANOVA] **(G)** RNA expression levels measured by qRT-PCR of p21 and p16 was examined to investigate activation of cell cycle arrest. Old 4 and Old 5 displayed an increase in RNA expression level of p21. All other cells did not show altered RNA expression levels. [*n* = 3–4, mean ± SEM **p* < 0.05, ***p* < 0.001, ****p* < 0.0001, one-way ANOVA] **(F)** Quantification of SA-βGAL positive cells by X-Gal staining. In comparison to grouped young donor cells, Midage 3 and all old human fibroblasts (Old 1–6) displayed a significant increase of SA-βGAL positive cells. [*n* = 3–4 (each *n* tested >15 cells), mean ± SEM, **p* < 0.05, ***p* < 0.001, ****p* < 0.0001, one-way ANOVA] **(H)** CTCF of Lamin B1 expression. A significant decrease in Lamin B1 expression could be observed in mid-age (Midage 1 and Midage 3) and old (Old 1–5) cells compared to the mean of young donor fibroblasts. [*n* = 4 (each *n* tested >15 cells), mean ± SEM, **p* < 0.05, ***p* < 0.001, ****p* < 0.0001, one-way ANOVA] **(I, J)** Determination of cytokine secretion (IL-6, IL-8) in conditioned medium by ELISA. In comparison to grouped young donor cells, old donor fibroblasts (Old 1, Old 2, Old 3, Old 4, and Old 6) showed an increase in levels of IL-6. An increase in concentration with respect to IL-8 could be observed in Midage 1 and Old 4 in comparison to grouped controls. [*n* = 3–4, mean ± SEM, **p* < 0.05, ***p* < 0.001, ****p* < 0.0001, one-way ANOVA] **(K)** Change in nucleus morphology shown as nucleus area (pixel units) in human fibroblast. Nucleus area is significantly increased in very old donor fibroblasts (Old 4 and 5) compared with grouped young controls. [*n* = 6–8 (each *n* tested >15 cells), mean ± SEM **p* < 0.05, ***p* < 0.001, ****p* < 0.0001, one-way ANOVA].

TABLE 1 Characteristics of human fibroblasts used in this study.

Primary cells	Alias (Coriell/PRF ID)	Age at biopsy	Sex	Youngest passage available	Source
Apparently healthy	Young 1 (AG07095)	2	Male	6	Coriell
	Young 2 (GM00969)	2	Female	13	Coriell
	Young 3 (GM05565)	3	Male	3	Coriell
	Young 4 (GM00498)	3	Male	10	Coriell
	Young 5 (GM00038)	9	Female	11	Coriell
	Mid-age 1	34	Male	5	Own lab
	Mid-age 2 (GM01653)	37	Male	14	Coriell
	Mid-age 3	48	Female	15	Own lab
	Old 1 (GM09918)	78	Male	15	Coriell
	Old 2 (GM03525)	80	Female	9	Coriell
	Old 3 (GM01706)	82	Female	5	Coriell
	Old 4 (AG09602)	92	Female	9	Coriell
	Old 5 (AG04059)	96	Male	7	Coriell
	Old 6 (GM00731)	96	Male	13	Coriell
HGPS	HGPS 1 (HGADFN003)	2	Male	13	Progeria research foundation
	HGPS 2 (HGADFN188)	2	Female	16	Progeria research foundation
WS	WS 1 (AG03141)	30	Female	14	Coriell
	WS 2 (AG06300)	37	Male	5	Coriell

cells from young (Young 1–5) and mid-age (Midage 1–3) donors showed healthy exponential growth. In contrast, fibroblasts from old (Old 3) and very old donors (Old 4, 5 and 6) displayed slower growth except for the fibroblasts Old 1 and 2, which resembled young donor cells in terms of growth (Figure 2B).

Next, the primary hallmarks of aging (DNA damage, telomere attrition and histone modification) were examined. DNA damage is a driving force of aging because it has a number of molecular consequences that are also hallmarks of aging, such as genomic instability, telomere attrition, epigenetic changes, and/or impaired mitochondrial function (Schumacher et al., 2021). To analyze the number of DNA double-strand breaks (DSBs), we examined the number of γ H2A.X foci by immunofluorescence staining (Figure 2C). Human fibroblasts from very old individuals (Old 4 and 5) showed significant higher amounts of DSBs compared with the average number of DSBs in young individuals. We next examined histone modification by immunofluorescence staining and quantifying the corrected total cell fluorescence (CTCF) of H3K9Me3 (Figure 2D). The heterochromatin loss model of aging assumes that heterochromatin domains which are formed early in embryogenesis decrease during aging and contribute to a global loss of heterochromatin-induced gene silencing, resulting in aberrant gene expression patterns (Villeponteau, 1997). In our study, we observed no changes in mid-age (Midage 1–3) but a decrease in H3K9Me3 expression in old donor fibroblasts (Old 2, Old 4, Old 5, and Old 6). In addition, we measured telomere length by monochromatic multiplex qPCR (MM-qPCR) (Figure 2E). Telomeres are specialized chromatin structures at the end of eukaryotic chromosomes that serve to

protect chromosome ends. Telomere shortening with aging is observed in most human tissues in which it has been tested (Lange, 2005) and is one of the best understood mechanisms limiting the growth of normal cells in culture, a phenomenon referred to as “replicative senescence” (Collado, Blasco, and Serrano, 2007). Compared to the mean of young donor fibroblasts (Young 1–5), Old 6 was the only cell line exhibiting significant telomere shortening.

Following, single antagonistic age markers were systematically investigated, including induction of cell cycle arrest, expression of SA- β Gal, activation of senescence-associated secretory phenotype (SASP), Lamin B1 expression and morphological changes (i.e., size of nucleus). Cell cycle arrest in senescence is largely mediated by activation of one or both of the tumor suppressor pathways p53/p21 and p16/pRB (Kumari and Jat, 2021). These two pathways are very complex, involving many upstream regulators and downstream effectors, as well as several side branches (Chen et al., 2002; Rovillain et al., 2011). Our readout for cell cycle arrest were RNA expression levels of p21 and p16 (Figure 2G). Old 4 and Old 5 showed a raise in RNA expression level of p21. Otherwise, none of the human fibroblasts showed altered RNA expression levels of p21 or p16. Subsequently, we determined the number of cells positive for SA- β GAL, one of the most used markers of cellular senescence. The lysosomal hydrolase β -galactosidase cleaves terminal β -galactose from compounds such as lactose, keratin sulfates, sphingolipids, etc. It is present in almost all tissues. The activity of this enzyme increases with development of cellular senescence (Dimri et al., 1995). We determined the amount of SA- β GAL positive cells (Figure 2F). In

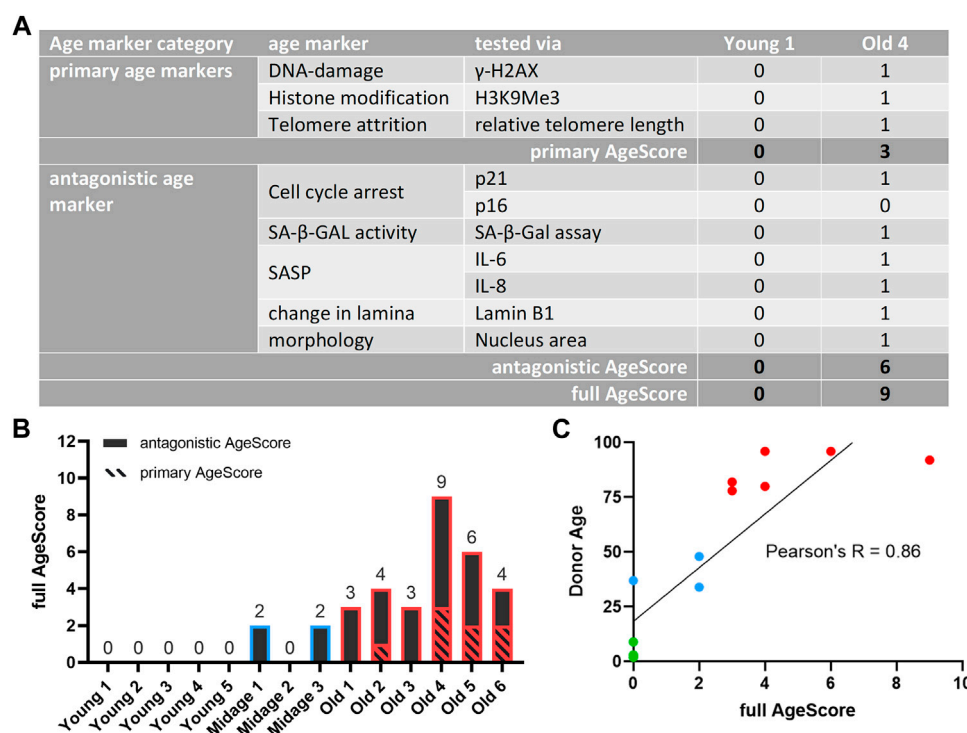


FIGURE 3

Calculated full AgeScore correlates with fibroblasts donor age. The here proposed full AgeScore (primary AgeScore + antagonistic AgeScore) correlates with donor age of examined human fibroblasts. (A) Calculation of proposed AgeScore for given examples (Young 1, Old 4). Each fibroblast tested receives a 0 for a non-significant age marker and a 1 for a significant age marker tested. These values are summed up to the primary AgeScore and the antagonistic AgeScore. The sum of both is the full AgeScore. (B) Calculated AgeScore for examined human fibroblasts displays an increase of the AgeScore with upcoming donor age. (C) Pearson correlation of full AgeScore and donor age of tested fibroblasts. The donor age correlates with our calculated AgeScore with a Pearson's R of 0.86.

comparison to the mean of young donor cells (Young 1–5), old human fibroblasts (Old 1–6) displayed a significant increase of SA-βGAL positive cells, while in mid-age donors, only Midage 3 showed a significant increase in SA-βGAL positive cells. Following, we investigated expression levels of nuclear protein Lamin B1 by determining the CTCF (Figure 2H). Lamin B1 expression decreases with age and is considered as an age marker (Wang et al., 2017; Kristiani, Miri, and Youngjo, 2020). Recent studies have shown that the nuclear lamina regulates both the organization of three-dimensional chromatin structure at the nuclear periphery (Yue, Zheng, and Zheng, 2019) and gene expression, e.g., of inflammatory response genes (Shah et al., 2013). A significant decrease in Lamin B1 expression was observed in mid-age and old donor fibroblasts (Midage 1, Midage 3, Old 1–5) compared with the mean of young donor cells. For studying SASP activation, reflecting senescent cells (Coppé et al., 2008), we examined secreted concentrations of two principle SASP factors, the inflammatory cytokines interleukin 6 (IL-6) and interleukin 8 (IL-8) in conditioned medium of donor cells by ELISA (Figures 2I, J). An increase in concentration of IL-6 was detected in old donor fibroblasts (Old 1–Old 4 and Old 6) in comparison to grouped controls. Additionally, Midage 1 and Old 4 displayed a significant increase in levels of IL-8. Furthermore, it is known that nucleus size changes with age and in pathological conditions (Capell et al., 2005; Glynn and Glover, 2005; Haithcock et al., 2005; Webster, Wikin, and Cohen-Fix, 2009). To study morphological changes occurring with aging or during pathogenesis of

age-associated diseases, we examined the size of the nucleus using pixel area of DAPI staining (Figure 2K). Nucleus size was significantly enlarged only in very old human donor fibroblasts (Old 4 and Old 5) compared to grouped young controls (Heckenbach et al., 2022).

In summary, when systematically investigating above mentioned well known single age markers, there was a remarkable heterogeneity between single human donors of different ages and it might thus be hard to judge upon the biological age if only investigating one single aging marker alone. While SA-βGAL was the best single age marker to depict old donor age, it did not perfectly distinguish midage from young donor age. Therefore, we went on to develop a strategy to use above mentioned markers together in one panel to finally yield an integrated AgeScore result.

3.2 Calculation of proposed AgeScore correlates with donor age of examined human fibroblasts

To take the individual cell line variabilities better into account we used above mentioned single markers to generate one panel with a single absolute value from the tested age markers and asked ourselves whether this value then depicts the chronological age of fibroblasts of different donor ages as good as or even better than single markers (Figure 3A). To create this score (hereinafter referred to as AgeScore) each primary cell

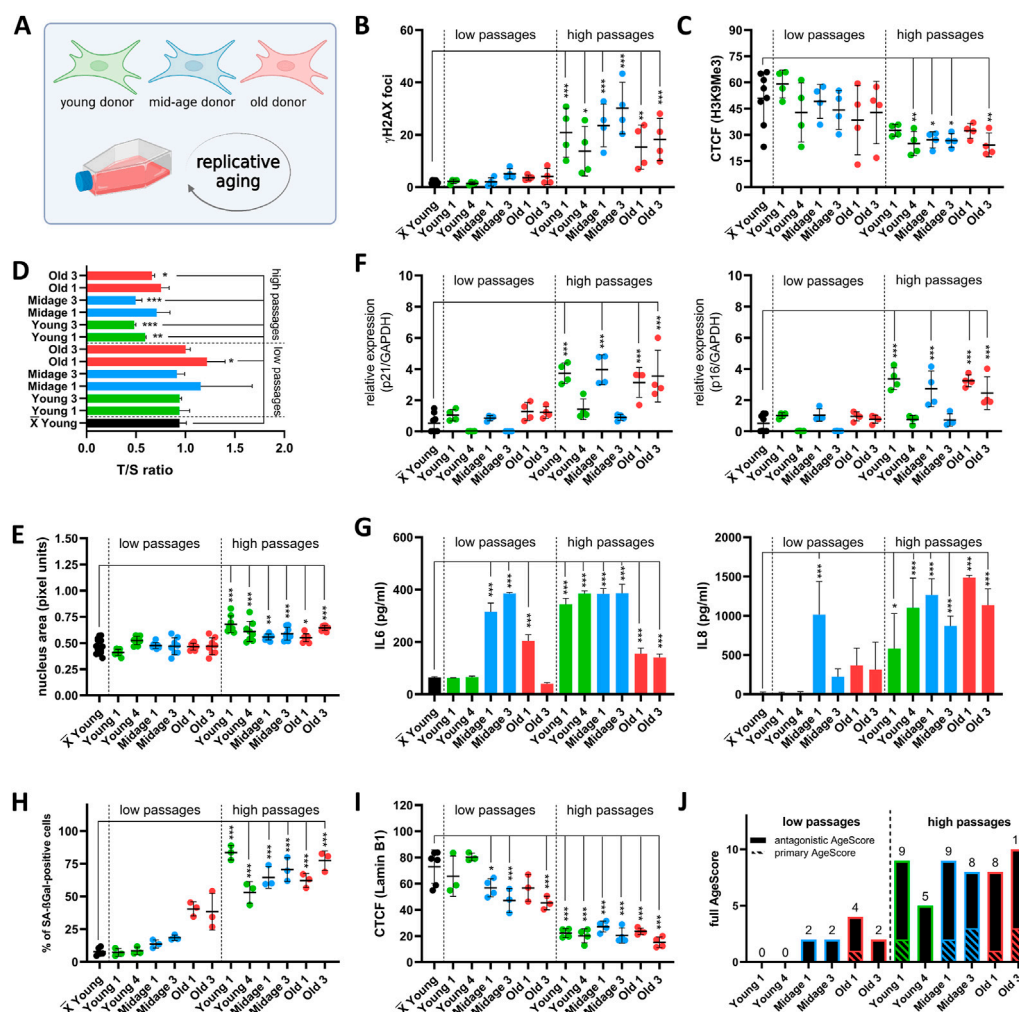


FIGURE 4

Examination of the AgeScore in human fibroblasts under replicative senescence. (A) Cell Model for validation of proposed AgeScore, fibroblasts from young, mid-age and old donors were replicative aged. (B–I) X = Mean value of all young donors. (B) Quantification of γ H2AX in fibroblasts in high passages ($p > 35$) in comparison to the mean of all Young^{low}. Amount of γ H2AX foci per cell increased in all cells in high passages. [$n = 4$ (each n tested >15 cells), mean \pm SEM, $*p < 0.05$, $**p < 0.001$, $***p < 0.0001$, one-way ANOVA] (C) Quantification of H3K9Me3 by IF staining. CTCF displayed a significant decrease of H3K9Me3 expression in high passages of Young 4, Midage 1, Midage 3 and Old 3 compared to grouped Young^{low}. [$n = 4$ (each n tested >15 cells), mean \pm SEM, $*p < 0.05$, $**p < 0.001$, $***p < 0.0001$, one-way ANOVA] (D) Telomere length was measured by MM-qPCR in comparison to a standard of healthy mixed aged individuals. In comparison to grouped Young^{low}, high passages of Young 1, Young 2, Midage 3 and Old 3 displayed a shortening of telomere length. [$n = 3$, mean \pm SEM, $*p < 0.05$, $**p < 0.001$, $***p < 0.0001$, one-way ANOVA] (E) RNA expression levels by qRT-PCR of p21 and p16. Cell cycle arrest was detected by upregulation of p21 and p16 in Young 1^{high}, Midage 1^{high}, Old 1^{high} and Old 3^{high} [$n = 4$, mean \pm SEM $*p < 0.05$, $**p < 0.001$, $***p < 0.0001$, one-way ANOVA] (F) Investigation of cytokine secretion (IL-6, IL-8) in conditioned medium by ELISA. SASP activation was elevated in all fibroblasts under replicative senescence in comparison to the mean of all Young^{low} [$n = 3-4$, mean \pm SEM, $*p < 0.05$, $**p < 0.001$, $***p < 0.0001$, one-way ANOVA] (G) Quantification of nucleus area by pixel units. Nucleus area was significantly increased in all high passages of human fibroblasts in comparison to grouped low passages of Young^{low}. [$n = 8$ (each n tested >15 cells), mean \pm SEM $*p < 0.05$, $**p < 0.001$, $***p < 0.0001$, one-way ANOVA] (H) Quantification of SA- β Gal positive cells by X-Gal staining. Amount of positive SA- β Gal stained cells was significantly increased in all cells in high passage in comparison to the mean of all Young^{low}. [$n = 4$ (each n tested >15 cells), mean \pm SEM, $*p < 0.05$, $**p < 0.001$, $***p < 0.0001$, one-way ANOVA] (I) Quantification of Lamin B1 expression by IF staining. A significant decrease in Lamin B1 expression was observed in low passages of Midage 1, Midage 2 and in all high passages [$n = 4$ (each n tested >15 cells), mean \pm SEM, $*p < 0.05$, $**p < 0.001$, $***p < 0.0001$, one-way ANOVA] (J) Calculated AgeScore. The AgeScore increases in cells with replicative senescence.

culture system examined received an equal weight of “1” for a significant (positive) age marker result and a weight of “0” for each non-significant (negative) result. Subsequently, results of tested age markers were summed up to calculate the (A) primary AgeScore and (B) the antagonistic AgeScore. Finally, both scores together resulted in the (C) full AgeScore that was able to distinguish between young and old donor derived fibroblasts showing an increase with age (Figure 3B). For every

used age marker we calculated Pearson’s correlation and most age markers correlate with the AgeScore (Supplementary Figure S1). We observed a very high correlation for the markers H3K9Me3, p21, nucleus size and SA- β -Gal and a high correlation for Lamin B1 and H2AX. However, there is a moderate correlation for telomere length and a low correlation for p16, IL6, and IL8. Whereby all young donor fibroblasts showed a full AgeScore of 0, only the antagonistic AgeScore increased in

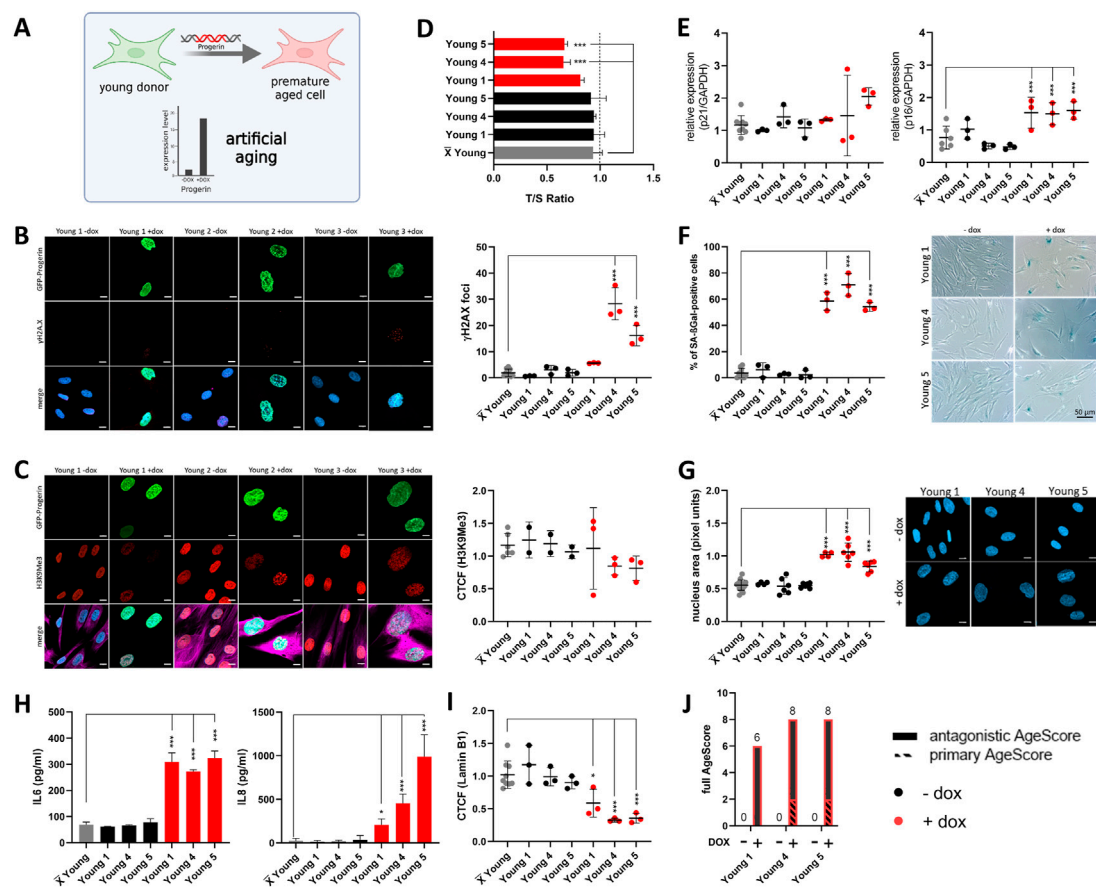


FIGURE 5

Examination of the AgeScore in prematurely aged human fibroblasts of young donors. Data for prematurely aged fibroblasts (induced with Doxycyclin) are marked in red. **(A)** For validation of the proposed AgeScore, young donor fibroblasts were prematurely aged by dox-inducible Progerin overexpression. **(B)** Representative IF images of γH2A.X and GFP-Progerin signal in absence and presence of doxycycline (1 μg/mL) after 4 days. Amount of γH2A.X foci per cell increased in cell lines with GFP-Progerin expression (Young 4, Young 5) in comparison to non-induced fibroblasts. [$n = 3$ (each n tested >15 cells), mean \pm SEM, $*p < 0.05$, $**p < 0.001$, $***p < 0.0001$, one-way ANOVA, scale bar = 10 μm] **(C)** Representative IF images of H3K9Me3 and GFP-Progerin signal in absence and presence of doxycycline (1 μg/mL) after 4 days (merge includes magenta = Vimentin). CTGF displayed no change in prematurely aged young donor of H3K9Me3 [$n = 3$ (each n tested >15 cells), mean \pm SEM, $*p < 0.05$, $**p < 0.001$, $***p < 0.0001$, one-way ANOVA, scale bar = 10 μm] **(D–I)** X = Mean value of all young donors. **(D)** Telomere length was measured by MM-qPCR in comparison to a standard of healthy mixed aged individuals. In comparison to non-induced cells, Young 4 and Young 5 with progerin expression displayed a shorting of telomere length. [$n = 3$, mean \pm SEM, $*p < 0.05$, $**p < 0.001$, $***p < 0.0001$, one-way ANOVA] **(E)** RNA expression levels by qRT-PCR of p21 and p16 was measured to investigate activation of cell cycle arrest in human fibroblasts. Young 1, Young 4 and Young 5 with progerin expression displayed a raise of relative RNA expression level of p16 in comparison to non-induced controls. [$n = 3$, mean \pm SEM, $*p < 0.05$, $**p < 0.001$, $***p < 0.0001$, one-way ANOVA] **(F)** Representative IF images and quantification of SA-βGAL positive cells by X-Gal staining. All three young donor cell lines with induced GFP-Progerin expression showed an increase in amount of positive stained SA-βGAL cells. [$n = 3$ (each n tested >15 cells), mean \pm SEM, $*p < 0.05$, $**p < 0.001$, $***p < 0.0001$, one-way ANOVA] **(G)** Representative IF images and quantification of nucleus area (pixel units) in prematurely aged human fibroblast. Nucleus area was significantly increased in all three young donor fibroblasts with induced GFP-Progerin. [$n = 6$ (each n tested >15 cells), mean \pm SEM, $*p < 0.05$, $**p < 0.001$, $***p < 0.0001$, one-way ANOVA, scale bar: 10 μm] **(H)** Determination of cytokine secretion (IL-6, IL-8) in conditioned medium of human fibroblasts with GFP-Progerin expression in comparison to non-induced cells by ELISA. All prematurely aged fibroblasts showed a significant increase in IL-6 and IL-8 concentrations in comparison to grouped controls. [$n = 3-4$, mean \pm SEM, $*p < 0.05$, $**p < 0.001$, $***p < 0.0001$, one-way ANOVA] **(I)** Representative IF images and quantification of Lamin B1 IF staining. A significant decrease in Lamin B1 expression was observed in all three prematurely aged human fibroblasts [$n = 3$ (each n tested >15 cells), mean \pm SEM, $*p < 0.05$, $**p < 0.001$, $***p < 0.0001$, one-way ANOVA] **(J)** Calculated AgeScore for prematurely aged fibroblasts of young donors in comparison to non-induced controls.

mid-age fibroblasts (antagonistic AgeScore = 2). In old donor fibroblasts, primary as well as antagonistic AgeScores increased and resulted in the highest full AgeScore calculated. The Pearson's correlation of $R = 0.86$ (Figure 3C) demonstrated that our AgeScore tended to increase with donor age of examined human fibroblasts.

We next aimed to examine the external validity of our proposed age-associated marker panel in two specific scenarios of aging, namely, during

replicative aging/senescence (Figure 4) and artificial aging (Figure 5) by overexpression of Progerin (Miller et al., 2013).

For replicative aging (Figure 4A) we systematically compared low ($p = 5-15$) and high passages ($p = > 30$ except Old 2-4) of young, mid-age and old age donor-derived human fibroblasts. From every age group we choose two different fibroblast lines that display sufficient growth to enable passaging until high passage.

First, we investigated primary age markers. All fibroblasts in high passages (^{high}) displayed significant increase in DSBs measured by γ H2A.X foci in comparison to the mean of all low passages (^{low}) of young donor cells (Figure 4B). We always compared to the mean of the controls and did not use a paired *t*-test to the respective low passage cell line to depict not-isogenic conditions. Expression of H3K9Me3 was reduced in Young 4^{high}, Midage 1^{high}, Midage 2^{high} and Old 3^{high} in comparison to grouped Young^{low} (Figure 4C). Shortening of telomeres was seen in Young 1^{high}, Young 2^{high}, Midage 3^{high} and Old 3^{high} compared to the mean of all Young^{low} (Figure 4D). Nucleus area (Figure 4E) and amount of positive SA- β Gal stained cells (Figure 4H) was significantly increased in all cells in high passages. Next, we checked antagonistic age markers. We detected an upregulation of cell cycle arrest markers p21 and p16 in Young 1^{high}, Midage 1^{high}, Old 1^{high} and Old 3^{high} (Figure 4F). Furthermore, SASP activation tested by release of IL-6 and IL-8 in the cell culture medium was found in all fibroblasts with high passages in comparison to the mean of all Young^{low} (Figure 4G). Moreover, high passages of all fibroblasts displayed a decreased expression of Lamin B1 (Figure 4I). In summary, all high passaged cells homogeneously display the various age markers and showed a high full AgeScore (Figure 4J).

For artificial aging, we used a doxycycline-inducible GFP-Progerin expression system (Kubben et al., 2016) in young donor cells as a model system for artificial aging. This allowed us to prematurely age the cells in a timely well-defined manner. Progerin expression indeed induced a homogenous and very rapid expression of a multitude of age markers. Four days after GFP-Progerin induction with doxycycline (1 μ g/mL), prematurely aged human fibroblasts showed formation of age-related nuclear envelope phenotypes paralleled by the expression of various primary age markers. We always compared to the mean of the controls and not paired *t*-test to the respective low passage cell line to not cause a bias due to isogenic genetic background. All fibroblasts from young donors with GFP-Progerin expression displayed a significant increase of γ H2A.X foci in comparison to non-induced fibroblasts (Figure 5B) whereas there were no changes in histone modification (Figure 5C). In comparison to non-induced cells, Young 4 and Young 5 with GFP-Progerin expression showed a shortening of telomere length (Figure 5D). Subsequently, we investigated the antagonistic age markers in prematurely aged fibroblasts from young donors. We observed significant increase in RNA expression of p16 in all fibroblasts with GFP-Progerin expression (Figure 5E). All prematurely aged fibroblasts showed significant increases in SA- β Gal positive cell numbers (Figure 5F), nucleus area (Figure 5G) and cytokine release (Figure 5H) in comparison to non-induced cells. Furthermore, Lamin B1 expression was significantly decreased in all prematurely aged fibroblasts (Figure 5I). Generally, the AgeScore showed an increase under GFP-Progerin expression in young donor fibroblasts (Figure 5J). Progerin overexpression rapidly induced a premature aging that was in fact very similar to replicative senescence (Figure 4).

3.3 Fibroblasts from patients with progeria syndromes express age markers to a higher degree

Finally, we wanted to address the question how the different aging markers behave in cell culture models of premature aging diseases. For this we studied low passage fibroblasts from patients suffering from the

Progeria syndromes HGPS and WS in comparison to age matched controls, respectively (Figure 6A). Controls for HGPS were thus significantly younger than controls for WS.

The growth rates of progeria fibroblasts were investigated by PDL under stable conditions (37°C, 5% CO₂) (Supplementary Figure S2). Fibroblasts from donors of HGPS patients showed no changes in PDL, whereas WS patient's fibroblasts displayed slower growth compared with the mean of age-matched controls. Next, we investigated primary age markers. In progeria syndrome's fibroblasts, we determined an increase in γ H2A.X foci in all tested cells (HGPS1, HGPS 2, WS 1, and WS 2) in comparison to the mean of all age-matched controls (Figure 6B). Furthermore, we observed a decrease in H3K9Me3 expression in donor fibroblasts of HGPS patients (HGPS 1 and HGPS 2). There were no changes in fibroblasts from WS patients (Figure 6C). In comparison to grouped age-matched controls, fibroblasts of progeria patients displayed no changes in telomere length (Figure 6D).

Secondly, we checked antagonistic age markers. Activation of cell cycle arrest was detected in WS by upregulated RNA expression levels of p16 (Figure 6E). Furthermore, in all fibroblasts from progeria patients we observed a rise of SA- β GAL positive cells (Figure 6F) and a significant decrease in Lamin B1 expression in HGPS 1, HGPS 2 and WS 1 (Figure 6G). In fibroblasts of HGPS patients we observed a significant increase in concentration of IL-8 in conditioned media. There were no changes in the levels of SASP marker IL-6 or IL-8 in WS fibroblasts (Figures 6H, I). All progeria fibroblasts displayed an increase in nucleus area (Figure 6J). The AgeScores of human fibroblasts of progeria patients (HGPS 1 and 2, WS 1 and 2) were thus higher in comparison to age-matched controls and similar to those of old donor fibroblasts (Figure 6K).

Interestingly, the pattern of individual markers within the AgeScore was different between HGPS cells and the cells of artificial aging, which were aged by overexpression of Progerin (Figure 7). Furthermore, the pattern of individual markers within the AgeScore were very similar between the different donors of the respective progeria syndrome, however did also differ between HGPS and WS (Figure 7). A summary of age marker expression by individual cell lines and aging conditions is presented in Table 2.

4 Discussion

Despite the existence of a variety of putative age markers, comparison of different studies on aging cells is hampered by the fact that often only single markers are used (López-otín et al., 2013; Hartmann et al., 2021). Here, we systematically investigated a set of established age markers in diverse cellular aging conditions. Doing so, we propose a panel of various commonly used age markers that together seem to measure the effect of aging processes on cells at least as good as single markers but additionally giving insights in the complexity of the aging process (Figure 7; Table 2). Additionally, the panel might be helpful to compensate for bias due to genetic background differences.

Cell models of disease and/or aging are of even greater importance since the discovery of iPSC and other "induced" cell technologies. While these technologies enable to investigate patient-derived cell models of previously unavailable origin (e.g., neurons), they significantly alter also general aspects of the cell including their biological age. Different age scores/clocks have thus been proposed

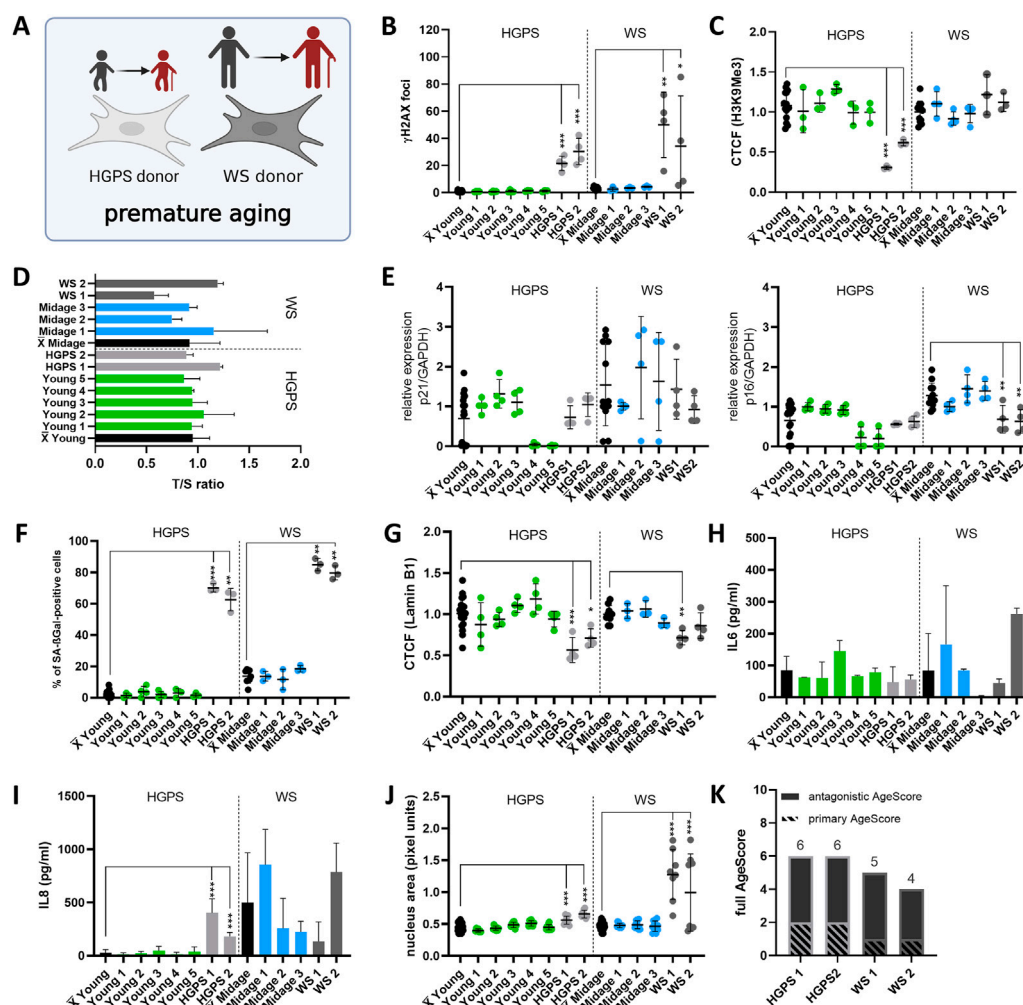


FIGURE 6

Application of the AgeScore on Progeria syndromes. (A) Cell Model for validation of proposed AgeScore in fibroblasts of donors with Progeria Syndrome in comparison to young/mid-age donors. (B) Amount of γ H2AX foci per cell examined by IF stainings to investigate DSBs. There were an increase in γ H2AX foci in all cells of the premature aging syndromes. [$n = 3-4$ (each n tested >15 cells), mean \pm SEM, $*p < 0.05$, $**p < 0.001$, $***p < 0.0001$, one-way ANOVA] (C) CTCF of H3K9Me3 in human fibroblasts of Progeria patients. There was a decrease in H3K9Me3 expression in donor fibroblasts of HGPS patients (HGPS 1 and HGPS 2). [$n = 3-4$ (each n tested >15 cells), mean \pm SEM, $*p < 0.05$, $**p < 0.001$, $***p < 0.0001$, one-way ANOVA] (D) Telomere length were measured by MM-qPCR in comparison to a standard of healthy mixed aged individuals. There were no change in telomere length of human fibroblasts of progeria syndrome patients in comparison to age-matched controls. [$n = 3$, mean \pm SEM, $*p < 0.05$, $**p < 0.001$, $***p < 0.0001$, one-way ANOVA] (E) RNA expression levels measured by qRT-PCR of p21 and p16. Activation of cell cycle arrest were detected in WS by upregulated RNA expression levels of p16. [$n = 3-4$, mean \pm SEM $*p < 0.05$, $**p < 0.001$, $***p < 0.0001$, one-way ANOVA] (F) Quantification of SA- β GAL positive cells by X-Gal staining. Donor fibroblasts from premature aging syndromes showed a significant rise of SA- β GAL positive cells. [$n = 3-4$ (each n tested >15 cells), mean \pm SEM, $*p < 0.05$, $**p < 0.001$, $***p < 0.0001$, one-way ANOVA] (G) CTCF of Lamin B1 expression. A significant decrease in Lamin B1 expression was observed in HGPS1, HGPS 2 and WS1. [$n = 4$ (each n tested >15 cells), mean \pm SEM, $*p < 0.05$, $**p < 0.001$, $***p < 0.0001$, one-way ANOVA] (H,I) Determination of cytokine secretion (IL-6, IL-8) in conditioned medium of human fibroblasts by ELISA. From studied progeria donor fibroblasts, HGPS1 and HGPS 2 displayed an increase in IL-8 concentration in comparison to the mean of age-matched controls. [$n = 3-4$, mean \pm SEM, $*p < 0.05$, $**p < 0.001$, $***p < 0.0001$, one-way ANOVA] (J) Change in nucleus morphology shown as nucleus area (pixel units). Nucleus area was significantly increased in all cells of progeria syndrome patients in comparison to age-matched controls. [$n = 6-8$ (each n tested >15 cells), mean \pm SEM $*p < 0.05$, $**p < 0.001$, $***p < 0.0001$, one-way ANOVA] (K) Calculated AgeScore of tested human fibroblasts. The AgeScores of progeria syndrome patients (HGPS 1 and 2, WS 1 and 2) are higher in comparison to the age-matched controls.

in the last years which are estimating biological age with various degrees of accuracy (Lu et al., 2019; Tarkhov, Denisov, and Fedichev, 2022). It is well known, that aging leads to epigenetic changes in DNA methylation, through several distinct and overlapping age-associated mechanisms (Hannum et al., 2013; López-otín et al., 2013). Also, many DNA methylation clocks, which allow the indirect inference of biological age from age-specific DNA

methylation patterns, have been recently established and enable the estimation of biological age of organisms in large tissue samples followed by multivariate machine learning models (Hannum et al., 2013; Horvath, 2013; Robinson et al., 2020; Van Den Akker et al., 2020; Hwangbo et al., 2021). Nevertheless, for the use in standard cell culture these investigations are often expensive and need specific equipment not necessarily available.

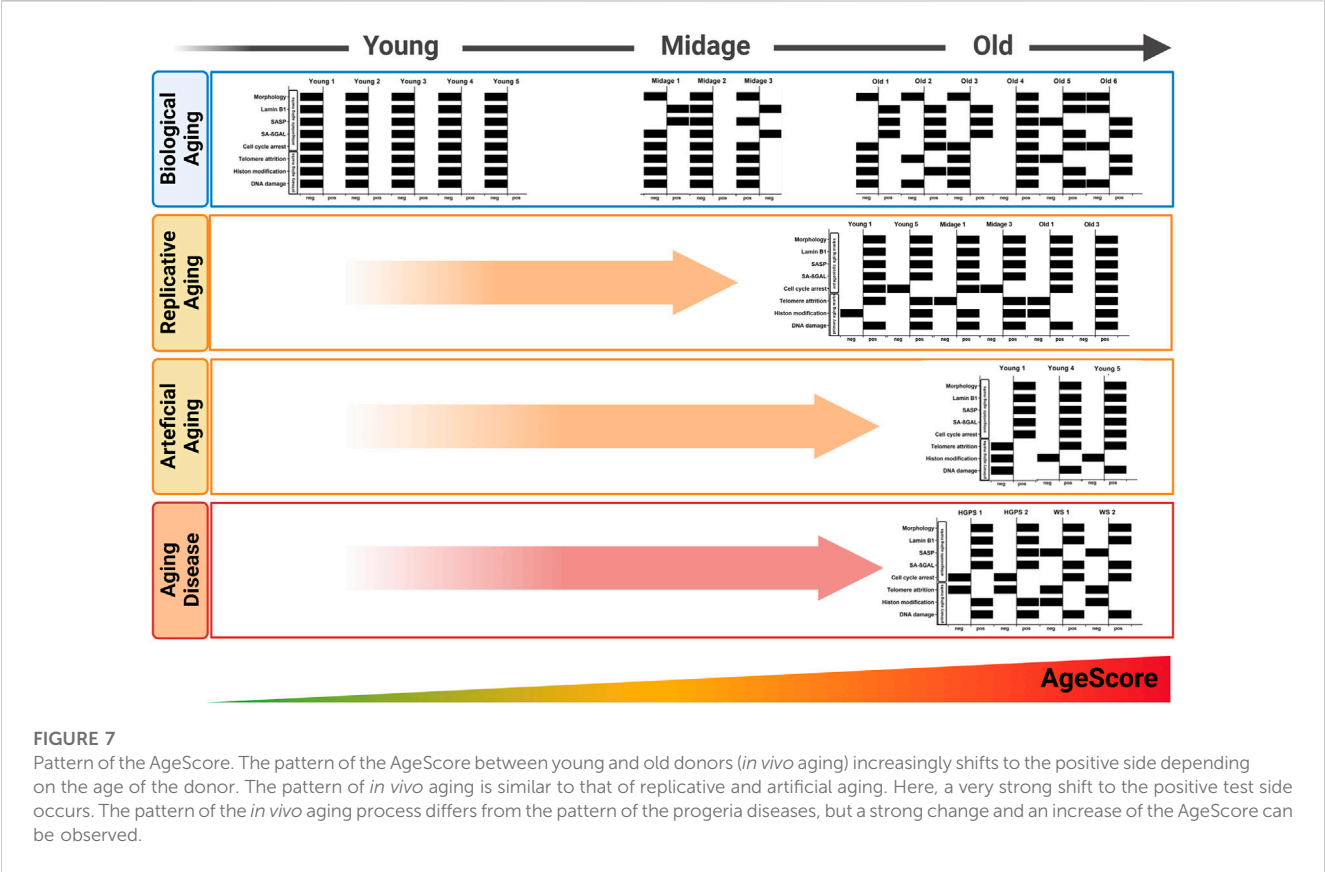


FIGURE 7 Pattern of the AgeScore. The pattern of the AgeScore between young and old donors (*in vivo* aging) increasingly shifts to the positive side depending on the age of the donor. The pattern of *in vivo* aging is similar to that of replicative and artificial aging. Here, a very strong shift to the positive test side occurs. The pattern of the *in vivo* aging process differs from the pattern of the progeria diseases, but a strong change and an increase of the AgeScore can be observed.

TABLE 2 Frequency of age marker expression per cell line investigated. Depicted is the frequency of the investigated primary and antagonistic age marker expression in the respective condition. Depicted are amount of positively tested cell lines and in brackets the total number of investigated cell lines per marker conditions, respectively.

	Donor age			Replicative aging	Artificial aging	Progeria syndromes	Frequency (total)
	Young	Midage	Old				
Primary AgeScore							
DNA damage	0 (5)	0 (3)	2 (6)	6 (6)	2 (3)	4 (4)	14 (27)
Telomere attrition	0 (5)	0 (3)	2 (6)	4 (6)	2 (3)	0 (4)	8 (27)
Histon modification	0 (5)	0 (3)	4 (6)	5 (6)	0 (3)	2 (4)	11 (27)
Antagonistic AgeScore							
SA-β-Gal	0 (5)	1 (3)	6 (6)	6 (6)	3 (3)	4 (4)	20 (27)
SASP	0 (5)	1 (3)	5 (6)	6 (6)	3 (3)	2 (4)	17 (27)
Cell cycle arrest	0 (5)	0 (3)	2 (6)	4 (6)	3 (3)	2 (4)	11 (27)
Morphology	0 (5)	0 (3)	2 (6)	6 (6)	3 (3)	4 (4)	15 (27)
LMNB1	0 (5)	2 (3)	5 (6)	6 (6)	3 (3)	3 (4)	19 (27)

All cells characterized in this study showed quite diverse age marker expression, visible in the here proposed age-associated marker panel (Figure 7; Table 2). This demonstrates two concepts: On the one hand it potentially depicts the individuality of the aging process *per se*, which is based, amongst others, on the genetic heterogeneity of donors (Schneider and Mitsui, 1976). On the other hand, it also displays the heterogeneity of individual marker expression and the flaws when only looking at individual markers. The age-associated marker panel from donors with different ages showed an increase with chronological age, whereby old donor cells displayed a higher heterogeneity. For example, fibroblasts from Old 4 had the highest score of 9, but

the donor of Old 4 was younger than Old 6 with a score of 4. Nevertheless, in comparison with young donors (all scoring 0) and mid-age donors (scoring 0–2), it becomes clear that scores increased markedly with age. Furthermore, replicative aging induced highest scores, higher than donor age itself. Thus, the score might be most sensitive for the detection of replicative senescence, or the markers chosen might be overrepresented in replicative senescence. Of note, the score still increased with replicative aging even in case of being already increased due to donor age. In addition, initial studies on premature aging diseases (Figure 6) pointed towards increased scores in both. One might discuss to introduce an additional weighting system for the AgeScore, e.g., by taking into account the frequency of the respective marker expression in the different age/aging conditions (Table 2). Such a weighting might, however, not generalize to other cell lines or “induced” cell models, thus requiring further refinement and validation.

Interestingly, “antagonistic age markers” appeared earlier than “primary age markers”. Antagonistic age markers were always expressed in replicative/artificial aging and were already present in mid-age donors. While these were also positive without primary age markers being increased, this was never the case *vice versa*. We cannot, however, rule out that this might be due to detection limits of the respective markers.

Heterogeneity of the different marker expression was highest when investigating donor age dependency. This heterogeneity might be due to differences in the genetic background of the different donors but also due to differences in the biological age (meaning their health state at biopsy) of the respective donors themselves. Ideally this would mean that the biological age of the respective donor has also been estimated using an age score. In practice, however, this biological age of the donors is often not available. This heterogeneity was less pronounced in case of replicative senescence and induced accelerated aging. In order to minimize this heterogeneity in the latter, we compared the replicative senescence and the progerin overexpression induced aging not to the respective donor cell (=isogenic background) but to the mean of all control conditions. Nevertheless, replicative and progerin induced senescence experimental settings might be more defined than aging in an individual prior to cell isolation with or without premature aging disease.

In addition, we examined the pattern of the individual markers within the age-associated marker panel of the cells and in the conditions studied (Figure 7). This additionally underpins the observation that aging processes are diverse, and might also account for deviations between the plurality of AgeClocks described so far. When looking at the panel, we saw a clear change in the pattern of these different markers according to donor age, but also marked differences between different donors of similar age. Even though all markers chosen were reported to be age associated or increase with aging, we only rarely found all of them increased together. Specific markers such as SA- β -Galactosidase were associated clearly with aging and positive cells increase in nearly all aging conditions (Figure 7; Table 2), but they still had minor problems e.g., to label clearly all mid-age donors (Figure 2). Interestingly, another age scoring system—so called CultureAge—did even report a lack of correlation of SA- β -Galactosidase with CultureAge (Minteer et al., 2022). Other age markers like p21 displayed an increase only in few of the tested cells. Replicative senescence and artificial aging induced a stronger and especially more homogenous change of the overall marker

pattern. While total score of the age marker panel was even higher in Werner syndrome fibroblasts, the patterns of HGPS and WS were remarkable different.

A limitation of our study is the exclusive use of human dermal fibroblasts. It is well accepted that cellular aging differs across tissues *in vivo* and *in vitro*. In addition, the expression of specific markers, e.g., p16 and p21, is tissue dependent. Consequently, the AgeScore might be affected as well by the cell origin. Furthermore, some markers investigated only seldomly became positive in aged conditions despite having been described as established age markers (Table 2). Thus future studies are warranted to both investigate the value of the AgeScore and its marker panel in cells from diverse tissue/germ layer origin including (re-) programming conditions, and to eventually reduce the AgeScore to a panel of markers, which all become positive in aged conditions, irrespective of tissue origin.

In summary, we here propose the use of an age-associated marker panel, which considers key age markers for application in *in vitro* cell culture and demonstrated its validity in estimating donor age, replicative and artificial aging as well as premature aging. This AgeScore can be easily investigated in standard cell culture laboratories yielding both an individual value but also marker patterns that allow good comparability of the diversity of the aging processes. Further studies are needed to further validate the use of the AgeScore proposed here, also for other *in vitro* and *in vivo* applications.

Data availability statement

The raw data supporting the conclusion of this article will be made available by the authors, without undue reservation.

Ethics statement

The studies involving human participants were reviewed and approved by Ethikkommission der Technischen Universität Dresden, Germany. Written informed consent to participate in this study was provided by the participants' legal guardian/next of kin.

Author contributions

CH and AHe drafted the manuscript with input of MW, GF, and AHa. CH, LH, VK, and AHa did the experiments and analyses underlying the preparation of the tables. AHe provided main resources and funding and supervised the study. All authors approved the final version of the manuscript and made substantial, direct and intellectual contribution to the work, and approved it for publication.

Funding

This work was supported, in part, by the FORUN2000 of the University Medical Center Rostock to CH and the NOMIS foundation to AHe. AHe is supported by the Hermann und Lilly

Schilling-Stiftung für medizinische Forschung im Stifterverband. GF is supported by the BMBF (FKZ 01ZX1903A).

Acknowledgments

We deeply thank the great cell culture help of Jette Abel. **Figures 1, 2A, 4A, 5A, 7** were created with the online software **BioRender.com**.

Conflict of interest

The authors declare that the research was conducted in the absence of any commercial or financial relationships that could be construed as a potential conflict of interest.

References

- Atkinson, A. J., Colburn, W. A., DeGruttola, V. G., DeMets, D. L., Downing, G. J., Hoth, D. F., et al. (2001). Biomarkers and surrogate endpoints: Preferred definitions and conceptual framework. *Clin. Pharmacol. Ther.* 69 (3), 89–95. doi:10.1067/mcp.2001.113989
- Capell, B. C., Erdos, M. R., Madigan, J. P., Fiordalisi, J. J., Varga, R., Karen, N., et al. (2005). Inhibiting farnesylation of progerin prevents the characteristic nuclear blebbing of hutchinson-gilford progeria syndrome. *Proc. Natl. Acad. Sci. U. S. A.* 102 (36), 12879–12884. doi:10.1073/pnas.0506001102
- Cawthon, R. M. (2009). Telomere length measurement by a novel monochrome multiplex quantitative PCR method. *Nucleic Acids Res.* 37 (3), e21–e27. doi:10.1093/nar/gkn1027
- Chen, X., Zhang, W., Gao, Y. F., Su, X. Q., and Zhong, H. Z. (2002). Senescence-like changes induced by expression of P21Waf1/cip1 in NIH3T3 cell line. *Cell Res.* 12 (3–4), 229–233. doi:10.1038/sj.cr.7290129
- Collado, M., Blasco, M. A., and Serrano, M. (2007). Cellular senescence in cancer and aging. *Cell* 130 (2), 223–233. doi:10.1016/j.cell.2007.07.003
- Coppé, J. P., Patil, C. K., Rodier, F., Sun, Y., Goldstein, J., and Nelson, P. S. (2008). Senescence-associated secretory phenotypes reveal cell-nonautonomous functions of oncogenic RAS and the P53 tumor suppressor. *PLoS Biol.* 6 (12), 2853–2868. doi:10.1371/journal.pbio.0060301
- Dimiri, G. P., Lee, X., George, B., Acosta, M., Scott, G., Roskelley, C., et al. (1995). A biomarker that identifies senescent human cells in culture and in aging skin *in vivo*. *Proc. Natl. Acad. Sci. U. S. A.* 92 (20), 9363–9367. doi:10.1073/pnas.92.20.9363
- Fleischer, J. G., Schulte, R., Tsai, H. H., Tyagi, S., Ibarra, A., and Shokhirev, M. N. (2018). Predicting age from the transcriptome of human dermal fibroblasts. *Genome Biol.* 19 (1), 221–228. doi:10.1186/s13059-018-1599-6
- Fueller, G., Jansen, L., Cohen, A. A., Walter, L., Gogol, M., et al. (2019). Andreas Simm, Nadine Saul, et al. Health and Aging: Unifying Concepts, Scores, Biomarkers and Pathways. *Aging Dis.* 10 (4), 883–900. doi:10.14336/AD.2018.1030
- Glynn, M. W., and Glover, T. W. (2005). Incomplete processing of mutant Lamin A in hutchinson-gilford progeria leads to nuclear abnormalities, which are reversed by farnesyltransferase inhibition. *Hum. Mol. Genet.* 14 (20), 2959–2969. doi:10.1093/hmg/ddi326
- Haithcock, E., Dayani, Y., Neufeld, E., Zahand, A. J., Feinstein, N., and Anna, M. (2005). Age-related changes of nuclear architecture in *Caenorhabditis elegans*. *Proc. Natl. Acad. Sci. U. S. A.* 102 (46), 16690–16695. doi:10.1073/pnas.0506955102
- Hannum, G., Zhao, L., Zhang, L., Hughes, G., Klotzle, B., Bibikova, M., et al. (2013). Genome-wide methylation profiles reveal quantitative views of human aging rates. *Mol. Cell* 49 (2), 359–367. doi:10.1016/j.molcel.2012.10.016
- Hartmann, A., Hartmann, C., Secci, R., Hermann, A., Fueller, G., and Walter, M. (2021). Ranking biomarkers of aging by citation profiling and effort scoring. *Front. Genet.* 12, 686320–686415. doi:10.3389/fgene.2021.686320
- Heckenbach, I., Garik, V., Ezra, M. B., Bakula, D., Madsen, J. S., Nielsen, M. H., et al. (2022). Mkrtychyan, Michael Ben Ezra, Daniela Bakula, Jakob Sture Madsen, Malte Hasle Nielsen, Denise Oró, et al. Nuclear Morphology Is a Deep Learning Biomarker of Cellular Senescence. *Nat. Aging* 2 (8), 742–755. doi:10.1038/s43587-022-00263-3
- Horvath, S. (2013). DNA methylation age of human tissues and cell types. *Genome Biol.* 14 (10), R115. doi:10.1186/gb-2013-14-10-r115
- Horvath, S., Oshima, J., Martin, G. M., Ake, T. L., Austin, Q., Felton, S., et al. (2018). “Epigenetic clock for skin and blood cells applied to Hutchinson gilford progeria syndrome and *ex vivo* studies” 10 (7): 1758–1775.
- Hwangbo, N., Zhang, X., Raftery, D., Gu, H., Hu, S.-C., Montine, T. J., et al. (2021). An aging clock using metabolomic CSF. *BioRxiv*. Available at: <https://www.biorxiv.org/content/10.1101/2021.04.04.438397v1> Abstract. doi:10.1101/2021.04.04.438397v1.abstract
- Jylhävä, J., Pedersen, N. L., and Sara, H. (2017). Biological age predictors. *EBioMedicine* 21, 29–36. doi:10.1016/j.ebiom.2017.03.046
- Kabacik, S., Lowe, D., Fransen, L., Leonard, M., Lan, S. A., Whiteman, C., et al. (2022). The relationship between epigenetic age and the hallmarks of aging in human cells. *Nat. Aging* 2 (6), 484–493. doi:10.1038/s43587-022-00220-0
- Kristiani, L., Kim, M., and Kim, Y. (2020). Role of the nuclear lamina in age-associated nuclear reorganization and inflammation. *Cells* 6. Available at: <https://www.mdpi.com/2073-4409/9/3/718>.
- Kubben, N., Brimacombe, K. R., Donegan, M., Li, Z., and Misteli, T. (2016). A high-content imaging-based screening pipeline for the systematic identification of anti-progeroid compounds. *Methods* 96, 46–58. doi:10.1016/j.ymeth.2015.08.024
- Kudryashova, K. S., Ksenia, B., Kulaga, A. Y., Vorobyeva, N. S., and Kennedy, B. K. (2020). Aging biomarkers: From functional tests to multi-omics approaches. *Proteomics* 20 (5–6), e1900408–e1900415. doi:10.1002/pmic.201900408
- Kumari, R., and Jat, P. (2021). Mechanisms of cellular senescence: Cell cycle arrest and senescence associated secretory phenotype. *Front. Cell Dev. Biol.* 9, 645593–645624. doi:10.3389/fcell.2021.645593
- Lange, T. De. (2005). Shelterin: The protein complex that shapes and safeguards human telomeres. *Genes Dev.* 19 (18), 2100–2110. doi:10.1101/gad.1346005
- López-Carlos, M. A. B., Partridge, L., Serrano, M., and Guido, K. (2013). The Hallmarks of Aging Carlos. *Cell* 153 (6), 1194–1217. doi:10.1016/j.cell.2013.05.039
- Lu, A. T., Austin, Q., Wilson, J. G., Reiner, A. P., Abraham, A., Raj, K., et al. (2019). DNA methylation GrimAge strongly predicts lifespan and healthspan. *Aging* 11 (2), 303–327. doi:10.18632/aging.101684
- Miller, J. D., Ganat, Y. M., Kishinevsky, S., Bowman, R. L., Becky, L., Tu, E. Y., et al. (2013). Human iPSC-based modeling of late-onset disease via progerin-induced aging. *Cell Stem Cell* 13 (6), 691–705. doi:10.1016/j.stem.2013.11.006
- Minteer, C., Morselli, M., Meer, M., Cao, J., Higgins-Chen, A., and Lang, S. M. (2022). Tick tock, tick tock: Mouse culture and tissue aging captured by an epigenetic clock. *Aging Cell* 21 (2), 13553–e13614. doi:10.1111/ace.13553
- Naumann, M., Pal, A., Goswami, A., Lojewski, X., Japtok, J., Vehlow, A., et al. (2018). Impaired DNA damage response signaling by FUS-nls mutations leads to neurodegeneration and FUS aggregate formation. *Nat. Commun.* 9 (1), 335. doi:10.1038/s41467-017-02299-1
- Pal, A., Glaß, H., Naumann, M., Kreiter, N., Japtok, J., Szech, R., et al. (2018). High content organelle trafficking enables disease state profiling as powerful tool for disease modelling. *Sci. Data* 5, 180241–180315. doi:10.1038/sdata.2018.241
- Pal, A., Kretner, B., Abo-Rady, M., Glab, H., Dash, B. P., Naumann, M., et al. (2021). Concomitant gain and loss of function pathomechanisms in C9ORF72 amyotrophic lateral sclerosis. *Life Sci. Alliance* 4 (4), 2020007644–e202000826. doi:10.26508/LSA.202000764

Publisher's note

All claims expressed in this article are solely those of the authors and do not necessarily represent those of their affiliated organizations, or those of the publisher, the editors and the reviewers. Any product that may be evaluated in this article, or claim that may be made by its manufacturer, is not guaranteed or endorsed by the publisher.

Supplementary material

The Supplementary Material for this article can be found online at: <https://www.frontiersin.org/articles/10.3389/fragi.2023.1129107/full#supplementary-material>

- Robinson, O., Chadeau Hyam, M., Karaman, I., Pinto, R. C., Ala-Korpela, M., Handakas, E., et al. (2020). Determinants of accelerated metabolomic and epigenetic aging in a UK cohort. *Aging Cell* 19 (6), 131499–e13213. doi:10.1111/accel.13149
- Rodgers, J. L., Jones, J., Bolleddu, S. I., Vanthenapalli, S., Rodgers, L. E., and Shah, K. (2019). Cardiovascular risks associated with gender and aging. *J. Cardiovasc. Dev. Dis.* 6 (2), 19. doi:10.3390/jcdd6020019
- Rovillain, E., Mansfield, L., Lord, C. J., Ashworth, A., and Jat, P. S. (2011). An RNA interference screen for identifying downstream effectors of the P53 and PRB tumour suppressor pathways involved in senescence. *BMC Genomics* 12, 355. doi:10.1186/1471-2164-12-355
- Schneider, E. L., and Mitsui, Y. (1976). The relationship between *in vitro* cellular aging and *in vivo* human age. *Proc. Natl. Acad. Sci. U. S. A.* 73 (10), 3584–3588. doi:10.1073/pnas.73.10.3584
- Schumacher, B., Pothof, J., Jan, V., Jan, H., and Hoeijmakers, J. (2021). The central Role of DNA damage in the ageing process. *Nature* 592 (7856), 695–703. doi:10.1038/s41586-021-03307-7
- Shah, P. P., Greg, D., Gabriel, L. O., Brian, C. C., David, M. N., Kajia, C., et al. (2013). Lamin B1 depletion in senescent cells triggers large-scale changes in gene expression and the chromatin landscape. *Genes Dev.* 27 (16), 1787–1799. doi:10.1101/gad.223834.113
- Tarkhov, A. E., Denisov, K. A., and Peter, O. F. (2022). Aging clocks, entropy, and the limits of age-reversal. *BioRxiv*, 1–12. Available at: <https://www.biorxiv.org/content/10.1101/2022.02.06.479300v1>.
- Trapp, A., Kerepesi, C., and Gladyshev, V. N. (2021). Profiling epigenetic age in single cells. *Nat. Aging* 1 (12), 1189–1201. doi:10.1038/s43587-021-00134-3
- Van Den Akker, E. B., Trompet, S., Jurriaan, J., Barkey Wolf, H., Beekman, M., Suchiman, H. E. D., et al. (2020). Metabolic age based on the BBMRI-NL 1H-nmr metabolomics repository as biomarker of age-related disease. *Circulation Genomic Precis. Med.* 13, 541–547. October: 541–47. doi:10.1161/CIRCGEN.119.002610
- Villeponteau, B. (1997). The heterochromatin loss model of aging. *Exp. Gerontol.* 32 (4–5), 383–394. doi:10.1016/S0531-5565(96)00155-6
- Wang, A. S., Ong, P. F., Chojnowski, A., Clavel, C., and Oliver, D. (2017). Loss of Lamin B1 is a biomarker to quantify cellular senescence in photoaged skin. *Sci. Rep.* 7 (1), 15678–8. doi:10.1038/s41598-017-15901-9
- Webster, M., Wikin, K. L., and Cohen-Fix, O. (2009). Sizing up the nucleus: Nuclear shape, size and nuclear-envelope assembly. *J. Cell Sci.* 122 (10), 1477–1486. doi:10.1242/jcs.037333
- Yue, S., Zheng, X., and Zheng, Y. (2019). Cell-type-specific Role of Lamin-B1 in thymus development and its inflammation-driven reduction in thymus aging. *Aging Cell* 18 (4), 129522–e13018. doi:10.1111/accel.12952



OPEN ACCESS

EDITED BY

Augusto Schneider,
Federal University of Pelotas, Brazil

REVIEWED BY

Michael John Sherratt,
The University of Manchester,
United Kingdom
Venu Varanasi,
University of Texas at Arlington,
United States

*CORRESPONDENCE

Laurent Bozec,
✉ l.bozec@utoronto.ca

[†]These authors share senior authorship

RECEIVED 03 March 2023

ACCEPTED 16 May 2023

PUBLISHED 31 May 2023




CITATION

Huang S, Strange A, Maeva A, Siddiqui S,
Bastien P, Aguayo S, Vaez M,
Montagu-Pollock H, Ghibaudo M,
Potter A, Pigeon H and Bozec L (2023),
Quantitative nanohistology of aging
dermal collagen.
Front. Aging 4:1178566.
doi: 10.3389/fragi.2023.1178566

COPYRIGHT

© 2023 Huang, Strange, Maeva, Siddiqui,
Bastien, Aguayo, Vaez, Montagu-Pollock,
Ghibaudo, Potter, Pigeon and Bozec.
This is an open-access article distributed
under the terms of the [Creative
Commons Attribution License \(CC BY\)](#).
The use, distribution or reproduction in
other forums is permitted, provided the
original author(s) and the copyright
owner(s) are credited and that the original
publication in this journal is cited, in
accordance with accepted academic
practice. No use, distribution or
reproduction is permitted which does not
comply with these terms.

Quantitative nanohistology of aging dermal collagen

Sophia Huang¹, Adam Strange², Anna Maeva², Samera Siddiqui²,
Phillipe Bastien³, Sebastian Aguayo ^{4,5}, Mina Vaez ¹,
Hubert Montagu-Pollock⁶, Marion Ghibaudo³, Anne Potter³,
Herve Pigeon^{3†} and Laurent Bozec ^{1,2*†}

¹Faculty of Dentistry, University of Toronto, Toronto, ON, Canada, ²Eastman Dental Institute, University College London, London, United Kingdom, ³L'Oréal Research and Innovation, Aulnay-sous-Bois, France, ⁴Faculty of Medicine, School of Dentistry, Pontificia Universidad Católica de Chile, Santiago, Chile, ⁵Schools of Engineering, Medicine, and Biological Sciences, Institute for Biological and Medical Engineering, Pontificia Universidad Católica de Chile, Santiago, Chile, ⁶Physics Department, Lancaster University, Lancaster, United Kingdom

The skin is the largest organ in the body and is essential for protecting us from environmental stressors such as UV radiation, pollution, and pathogens. As we age, our skin undergoes complex changes that can affect its function, appearance, and health. These changes result from intrinsic (chronological) and extrinsic (environmental) factors that can cause damage to the skin's cells and extracellular matrix. As higher-resolution microscopical techniques, such as Atomic Force Microscopy (AFM), are being deployed to support histology, it is possible to explore the biophysical properties of the dermal scaffold's constituents, such as the collagen network. In this study, we demonstrate the use of our AFM-based quantitative nanohistology, performed directly on unfixed cryosections of 30 donors (female, Caucasian), to differentiate between dermal collagen from different age groups and anatomical sites. The initial 420 (10 × 10 μm²) Atomic Force Microscopy images were segmented into 42,000 (1 × 1 μm²) images before being classified according to four pre-defined empirical collagen structural biomarkers to quantify the structural heterogeneity of the dermal collagen. These markers include interfibrillar gap formation, undefined collagen structure, and registered or unregistered dense collagen fibrillar network with evident D-banding. The structural analysis was also complemented by extensive nanoindentation (~1,000 curves) performed on individual fibrils from each section, yielding 30,000 indentation curves for this study. Principal Component Analysis was used to reduce the complexity of high-dimensional datasets. The % prevalence of the empirical collagen structural biomarkers between the papillary and reticular dermis for each section proves determinant in differentiating between the donors as a function of their age or the anatomical site (cheek or breast). A case of abnormal biological aging validated our markers and nanohistology approach. This case also highlighted the difference between chronological and biological aging regarding dermal collagen phenotyping. However, quantifying the impact of chronic and pathological conditions on the structure and function of collagen at the sub-micron level remains challenging and lengthy. By employing tools such as the Atomic Force Microscope as presented here, it is possible to start evaluating the complexity of the dermal matrix at the nanoscale and start identifying relevant collagen morphology which could be used toward histopathology standards.

KEYWORDS

collagen, aging, atomic force microscopy, nanomechanics, histology, dermis, skin, statistical methods

Introduction

The skin is a complex and multi-layered connective tissue that defines the external appearance of all individuals. Specific pathologies or the unavoidable aging process directly impact this appearance (Khavkin and Ellis, 2011). Genetic influences (Venkatesh et al., 2019) and internal factors such as hormones (Tobin, 2017) or metabolic substances (Khavkin and Ellis, 2011) govern the intrinsic aging of the skin. It illustrates the naturally occurring skin modifications with age, leading to wrinkles and skin dryness (Swift et al., 2021). The wrinkle formation in human skin has been associated with marked decreases in skin elasticity (Fenske and Lober, 1986). Extrinsic skin aging arrives earlier and is due, for example, to exposure to sunlight (Fisher et al., 2002), pollution (Salsberg et al., 2019), or lifestyle choices such as a lack of balanced nutrition (Bonté et al., 2019). More generally, in aging skin, cell replacement is continuously declining (Franco et al., 2022), the barrier function and mechanical protection are compromised (Wong et al., 2016), wound healing and immune responses are delayed (Chambers and Vukmanovic-Stejic, 2020), thermoregulation is impaired, and sweat and sebum productions are decreased (Terao and Katayama, 2016).

The aging of the dermis is a complex process with several changes occurring to both collagen and non-collagenous components of the dermal Extracellular Matrix (ECM). Both collagen and elastin undergo enzymatic and non-enzymatic crosslinks in the ECM as a function of aging (Monnier et al., 2005; Saito and Marumo, 2010). Lysyl oxidase (LOX) is the primary enzyme that crosslinks collagen during the final step of its biosynthesis to stabilize the supramolecular assembly of collagen molecules into fibrils (Bailey, 2001). However, the proportion of LOX-derived crosslinks reduces with age (Szauder et al., 2005), while the proportion of non-enzymatic (glycation) crosslinks increases with age. Glycation is the reaction of carbonyl groups of reducing sugars with free amino groups of lipids and proteins to form a Schiff base, which then undergoes a time-dependent rearrangement to form a reasonably stable Amadori product. These structures are still reactive and convert to stable substances called Advanced Glycation End-products (AGEs). The low turnover of collagen (as found in the skin) causes AGEs to accumulate within the collagen fibrils in our tissues and organs during normal aging or some pathological conditions such as diabetes (Snedeker and Gautieri, 2014). In diabetic conditions, glycation is expected to proceed faster due to an increase in available free sugars that are available to react with collagen residues. While these crosslinks' biochemical and mechanical impact on collagen has been extensively studied in tissue development, repair, and diseases (Tanzer, 1973; Singh et al., 2001; Szauder et al., 2005; Cox et al., 2013; Stammers et al., 2020), few studies have explored their association with dermal collagen fibril organization (Fang et al., 2012; Strange et al., 2017; Penuela et al., 2018). An early study by Achterberg et al. (2014) investigated how the nanoscale mechanical properties of the extracellular matrix regulate dermal fibroblast function by systematically exploring the mechanical and structural dermis

properties (human) as a function of age (26–55). Alongside presenting the first ultra-topography images of native skin by Atomic Force Microscopy (AFM) (Binnig et al., 1986), they found that the dermis elasticity ranged from 0.1 to 10 kPa in hydrated sections. These results were further explored by Ahmed et al. who proposed the first phenotypic markers for collagen aging in the reticular dermis, also measured by AFM. In addition, Ahmed explored the relationship between advanced glycation products and the elasticity of individual collagen fibrils within the reticular dermis of young and older individuals. Thus, despite being one of the most imaged proteins by AFM, collagen remains largely uncharacterized at the fibrils scale within the dermis, especially as a function of aging. Here, we present the first large cohort study (30 donors) in which we explore the use of AFM-based quantitative nanohistology to quantify the biophysical properties of dermal collagen at the nanoscale and to demonstrate how the variations in these properties can be used to reveal the skin's biological age.

Materials and methods

Human skin histological sections

In this study, cryo-preserved historical skin samples (30 Caucasian female donors, 18–75 years, cosmetic surgery procedures) collected under informed consent were analyzed as part of this explorative study. All the samples were anonymized, and the donors' age, biological sex, and ethnicity were made available for this study. The sample cohort was split into three groups according to both the donors' age and anatomical site: Breast Young Skin (BYS, N = 11, age range: 18–29 year-old, median: 22.0 ± 4.2 years), Breast Old Skin (BOS, N = 9, age range: 49–78 year-old, median: 69.0 ± 13.2 years), and Cheek Old Skin (COS, N = 10, age range: 56–80 year-old, median: 65.0 ± 7.7 years). Samples of skin obtained from these donors were split in two for processing. For histology, the skin samples were fixed in neutral formalin and then embedded in paraffin before being sectioned (5 μ m). The sections were stained using Hematoxylin and Eosin Stain (HES), Orcein, and Sirius Red (SR). For quantitative nanohistology (AFM), the skin samples were not fixed but cryo-embedded in optimum cutting temperature media before being cryo-sectioned (8–10 μ m thickness). All sections were physisorbed directly on individual glass slides.

Histological imaging

A Leica (Wetzlar, Germany) light microscope (LM) was used for histology imaging of the fixed and stained sections. This microscope was equipped with two crossed-light polarizers (90°) to allow for polarization (darkfield) LM and with an 8-megapixel digital camera (EOS Rebel 100, Canon). Complete histological sections were digitized using the auto-stitch function in Image-Pro Plus software (Meyer Instr. Inc., Houston, United States).

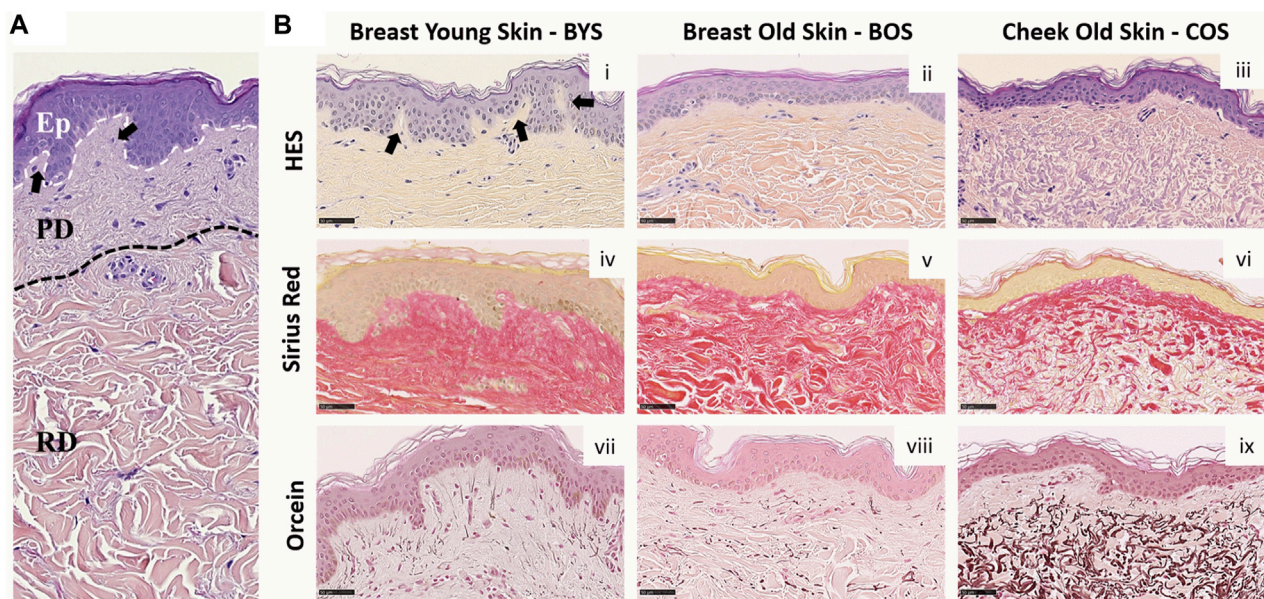


FIGURE 1

Histology of Normal Human Skin: **(A)** Normal human skin from a young donor (22 yo). The dotted lines separate the epidermis (Ep), papillary (PD), and reticular (RD) dermis. **(B)** Histological colorations of human skin from breast young (i, iv, and vii) and old (ii, v, and viii) skin (respectively 22 and 74 yo) and cheek old (iii, vi, and ix) skin (75 yo). Different types of colorations were performed: Hematoxylin Eosin Saffron–HES (i–iii), Sirius red (iv–vi), and Orcein (vii–ix). Scale Bar = 50 μm . Arrows highlight the rete ridges.

Quantitative nanohistological imaging

Topological images ($10 \times 10 \mu\text{m}^2$) of the tissue were acquired on the unfixed sections by Atomic Force Microscopes (AFM Nanowizard I and III, Bruker-JPK, Berlin–Germany) operated in contact mode (MSNL cantilevers (Nom. tip radius: 2 nm, triangular geometry, Bruker, Santa Barbara) operated in ambient conditions at a scanning rate of 1.0 Hz or above. To avoid bias in selecting the area to be imaged, we used a random walk approach to land the probe in each dermal layer by using the AFM sample holders' x-y translation screws to move the sample (within each dermal layer). Images were then acquired and optimized where the probe came into contact with the sample regardless of the topology seen in the image acquired. A total of 14 images were acquired for each donor (papillary dermis 7; reticular dermis: 7 on a minimum of 2 sections per donor), leading to a dataset of 420 ($10 \times 10 \mu\text{m}^2$) images. Following their acquisition, each AFM image was plane-fitted before being segmented into $100 \times (1 \times 1 \mu\text{m}^2)$ images using ImageJ, creating a final topology dataset of 42,000 ($1 \times 1 \mu\text{m}^2$) images to be analyzed.

Quantitative nanomechanical analysis

The mechanical properties of collagen fibrils of the histological sections were acquired by a Nanowizard I AFM (Bruker-JPK, Berlin–Germany) operated in the force-distance mode in ambient conditions. For these measurements, RFESPA cantilevers (Nom Tip Radius: 8nm, rectangular geometry, Bruker, Santa Barbara) with a spring constant $k = 3 \text{ N/m}$ were employed. The selection of the

sample area to be indented was also performed using the same random-walk approach as previously mentioned. First, a low-resolution image ($128 \times 128 \text{ px}$ over $10 \times 10 \mu\text{m}^2$) was performed to ensure that collagen fibrils with defined D-banding periodicity could be observed. Then, indentation sites were manually selected directly on distinct collagen fibrils' D-banding (overlap region). All indentations were carried out at 1Hz, with a maximum indentation load not exceeding 350 nN (yielding an average indentation depth of $d = 25 \pm 5 \text{ nm}$). For each histological section, a minimum of 500 individual collagen fibril measurements were carried out in the papillary and reticular dermis, resulting in a mechanical dataset of 30,000 indentations for the 30 samples. The diameter of each indented fibrils was not measured. All force-distance curves were processed by the JPK Data Processing Software v.5.1.8 using the Sneddon/Hertz model (Harding and Sneddon, 1945). The resultant distribution of Elastic (Young's) Moduli was plotted as histograms with a fixed bin size ($B = 500 \text{ MPa}$) to calculate the median Elastic (Young's) Moduli for the respective dermal layers.

Data management and statistical analyses

All data were processed using Origin Pro (Origin Lab Corporation, Northampton, United States). In this study, each histological block was treated as an individual variable, and data obtained from serial histological sections from the same block were pooled together. Four calibrated analysts were used to quantify the prevalence of the four structural biomarkers in each $42,000 1 \times 1 \mu\text{m}^2$ image. Analysts' calibration was performed by agreeing on the

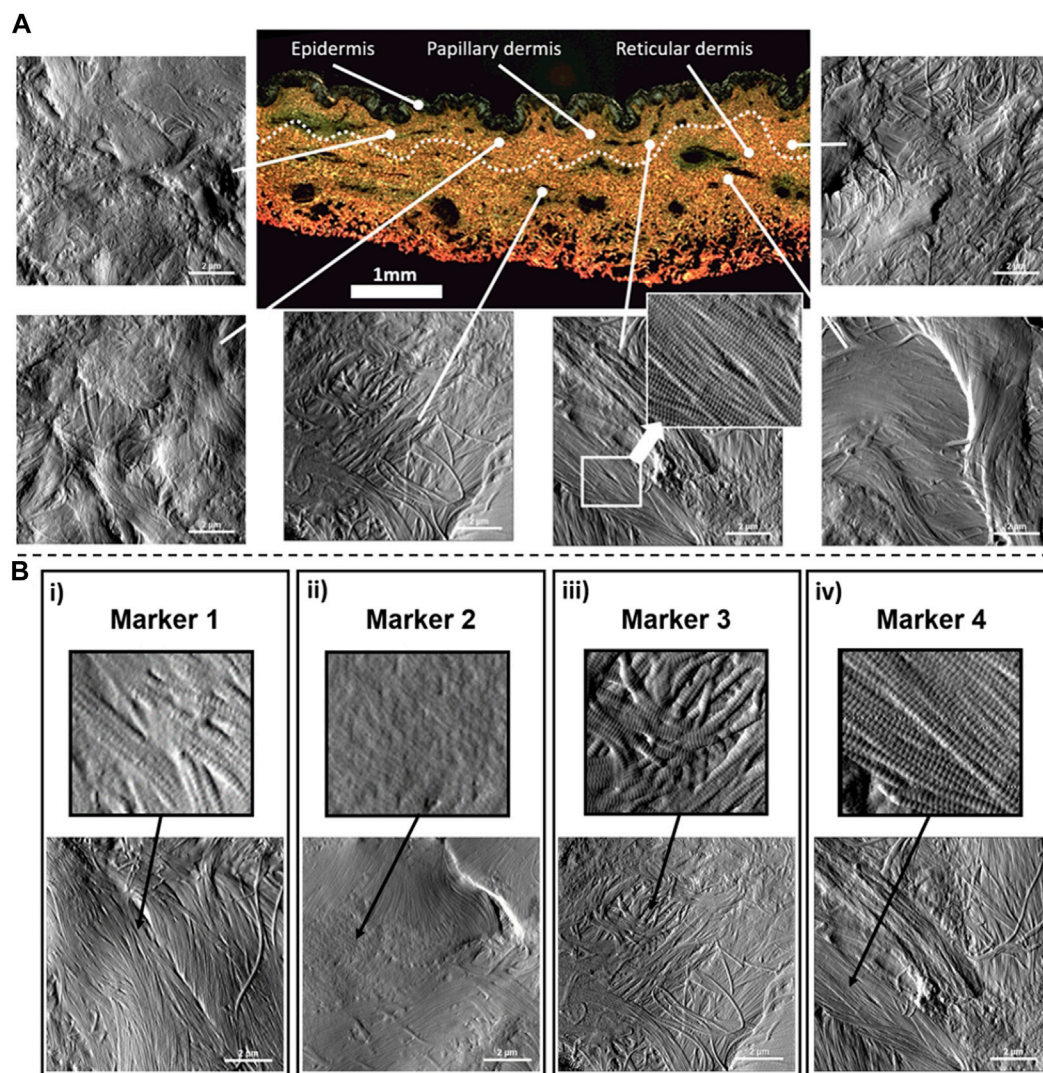


FIGURE 2

Quantitative Nanohistology of dermal collagen performed on histological sections: **(A)** Representative localized AFM topological images ($10 \times 10 \mu\text{m}^2$) obtained from both the papillary and reticular dermal layers obtained directly on a polarised Sirius Red Stain histological section. The boundary between papillary and reticular dermal layers, denoted as a dashed line, was empirically set $500 \mu\text{m}$ below the epidermal junction. **(B)** Structural nanoscale biomarkers for (type I) collagen and their presentation on AFM topological images: i) Marker 1 is defined as the presence of interfibrillar gaps (or holes); ii) Marker 2 characterizes areas where the fibrillar collagen structure is not readily observable and could be associated with cell processes or other extracellular matrix components; iii) Marker 3 characterizes a well-defined collagen matrix, with the fibrillar D-banding apparent on the collagen fibrils, but presenting a disorganized and lack registration between the collagen fibrils; iv) Marker 4 characterizes a well-defined collagen matrix, with the fibrillar D-banding apparent on the fibrils and forming a dense sheet of aligned collagen fibrils.

assignment of marker 1-2-3-4 on 100 AFM $1 \times 1 \mu\text{m}^2$ images. For the remainder of the analysis, all analysts were blinded and did not know the sample groups donors' assignment until the study was analyzed statistically. The Young's modulus of fibrils was compared using a two-sided hypothesis Mann-Whitney U test with a significance level $\alpha = 0.001$. In addition, 2D Principal component analyses (Jolliffe and Cadima, 2016) (PCA) were performed on the dataset using Origin Pro (Origin Lab Corporation, Northampton, United States). The relative position of the variables on the PCA score plot, with their coordinates equal to correlations with the first two principal components, was used to assess the level of discrimination between the variables. Finally, a Partial least Squares Discriminant Analysis (PLS-DA) was performed using

SIMCA® 16.0 multivariate Data Analysis Software (Sartorius Stedim Data Analytics AB, Sweden) with the binary age class as the response variable.

Results and discussion

Histology of an aging dermal section

Histological analysis is routinely used to assess structural changes in tissues, including skin, to prognose or diagnose pathologies such as aging. Figure 1 presents the histology of representative sections from our three groups. The young group

(Breast Young Skin–BYS) represented by the photo-protected breast skin specimen presents distinct epidermis (Ep), papillary (PD), and reticular (RD) dermal layers (Figure 1A). The dermo-epidermal junction is non-uniform and presents well-defined rete ridges (arrow). Structurally, the collagen in both dermal layers is very dense, and there is little evidence of elastin (Figures 1B–i, iv, vii). In the intrinsically aged skin (Breast Old Skin: BOS) specimen, one observes a thinning of the epidermis and papillary dermis (Figures 1B–ii). The dermo-epidermal junction presents a flattening aspect resulting from the disappearance of the rete ridges. The dermis has an atrophic aspect with a loss of cells and extracellular matrix. As a result, the dermal collagen becomes sparser (Figure 1B–v). Finally, the BOS histology shows evidence of loss of oxytalan fibers but not of solar elastosis/elastin deposition (Figure 1B–viii).

In contrast, the primary histological fingerprint for extrinsically aged skin (Cheek Old Skin: COS) is the abundance of abnormally structured elastin accumulated as elastotic material. This accumulation can be found in the reticular dermis, as shown in Figure 1B–ix. In addition, the extrinsically aged skin specimen presents a flattening of the dermis and a loss of rete ridges found for the intrinsically aged skin (Figure 1B–iii). The ratio of elastin to collagen has also increased (Figures 1B–vi, ix), suggesting that the collagen is being replaced by elastin, which explains the altered functional and biomechanical properties of this skin (Uitto, 2008). The histological presentation of these groups: young photo-protected skin and intrinsically and extrinsically aged skin, are well known and are routinely used to define the pathological age of skin (Khavkin and Ellis, 2011).

Defining nanoscale structural biomarkers for (type I) collagen

Type I collagen fibril topology is one of the most recognized protein structures due to its highly conserved annular-banding periodicity along the long axis of the fibrils, namely, the D-banding periodicity (Petruska and Hodge, 1964; Chernoff and Chernoff, 1992; Stylianou, 2022). In our quantitative nanohistology approach, we have used AFM to image collagen structure on the skin groups' histological sections. Figure 2 presents our approach to correlating AFM images site with a polarized image of SR-stained skin sections. We observe the presence of long fibrils with a defined D-banding periodicity in all the images recorded. Fibrils can appear as thick bundles, homogeneous sheets, or interwoven scaffolds. Our original skin study defined several potential structural biomarkers for aging in collagen (Ahmed et al., 2017). Four were present across the three skin groups from a list of 7 candidates' structural (or topological) collagen biomarkers, as presented in Figure 2B. Marker 1 is defined as the presence of interfibrillar gaps, suggesting a loosening of the dense collagen sheet structure, leading to the loss in fibril registration with one another (Figure 2B–i). Marker 2 characterizes areas where the fibrillar collagen structure is not readily observable and could be associated with cell processes or other extracellular matrix components (Figure 2B–ii). Marker 3 characterizes a well-defined collagen matrix, with the fibrillar D-banding apparent (Figure 2B–iii). However, the collagen fibrils in those areas are disorganized and lack registration between them. In

other studies, we found collagen fibrils morphology prevalent in the fibrotic area (Strange et al., 2017). Finally, Marker 4 characterizes a well-defined collagen matrix, with the fibrillar D-banding apparent and the fibrils aligned, forming dense collagen sheets (Figure 2B–iv). The prevalence of each of these structural (or topological) collagen biomarkers in the papillary and reticular dermis by segmenting each $10 \times 10 \mu\text{m}^2$ AFM image into a 100 sub-image $1 \times 1 \mu\text{m}^2$ as presented in Figure 3A. Each sub-image was evaluated independently (1 chosen marker per $1 \times 1 \mu\text{m}^2$ image). In addition to these structural biomarkers, we added the median value of the collagen fibrils Young's modulus for both the papillary and reticular dermis, as presented in Figure 3B. We have already demonstrated the variation of Young's modulus of collagen fibrils (dry) as a function of the aging process (Wenger et al., 2007; Ahmed et al., 2017).

Deciphering the structure of collagen in dermal layers

Dermal collagen phenotype varies among individuals based on biological sex, ethnic origins, and lifestyles (Fenske and Lober, 1986), (Farage et al., 2008). Therefore, to analyze collagen fibril phenotype, one cannot assume that the properties of the dermal collagen for all the individual donors within a given group are similar; thus, markers cannot be represented through a common median value per dermal layer and donor group.

We explored whether the relative structural variations in the collagen matrices between the papillary and reticular dermis could be used to differentiate between the three groups. To do so, we referenced the variations in individual markers in the reticular dermis to those found for the papillary dermis and normalized these variations using Eq. 1 in Figure 4A. The results are plotted in Figure 4A, presenting the %variation of each marker becoming more prevalent towards either the papillary or reticular dermis. Both markers 1 and 2 show an increased prevalence in the papillary dermis of the BYS group. While marker 2 does not readily inform us of the collagen phenotype, marker 1 suggests that the collagen matrix in the papillary dermis of young photo-protected skin exhibits structural loosening due to the increased presence of interfibrillar gaps (or holes) when compared to the reticular dermis. This finding would also suggest that the collagen matrix aging would occur in the papillary dermis before progressing to the reticular dermis. This outcome supports the recent finding by Lynch et al., who established that the mechanical property of the papillary dermis decreases before that of the reticular dermis with age (Lynch et al., 2022). Their study suggested that with aging, the earliest microstructural and mechanical changes occur in the topmost layers of the dermis/skin and then propagate deeper, providing an opportunity for topical preventive treatments acting at the level of the papillary dermis. An earlier study focusing solely on phenotyping the reticular dermis collagen suggested marker 3 is the hallmark of collagen aging. In our present study, marker 3 does not appear more prevalent in either dermal layer, regardless of age. This result does not contradict our previous study but implies that at the nanoscale, one cannot differentiate the two dermal layers solely based on marker 3. Marker 4 shows an increased prevalence in the reticular dermis of the BOS group, suggesting that intrinsic aging

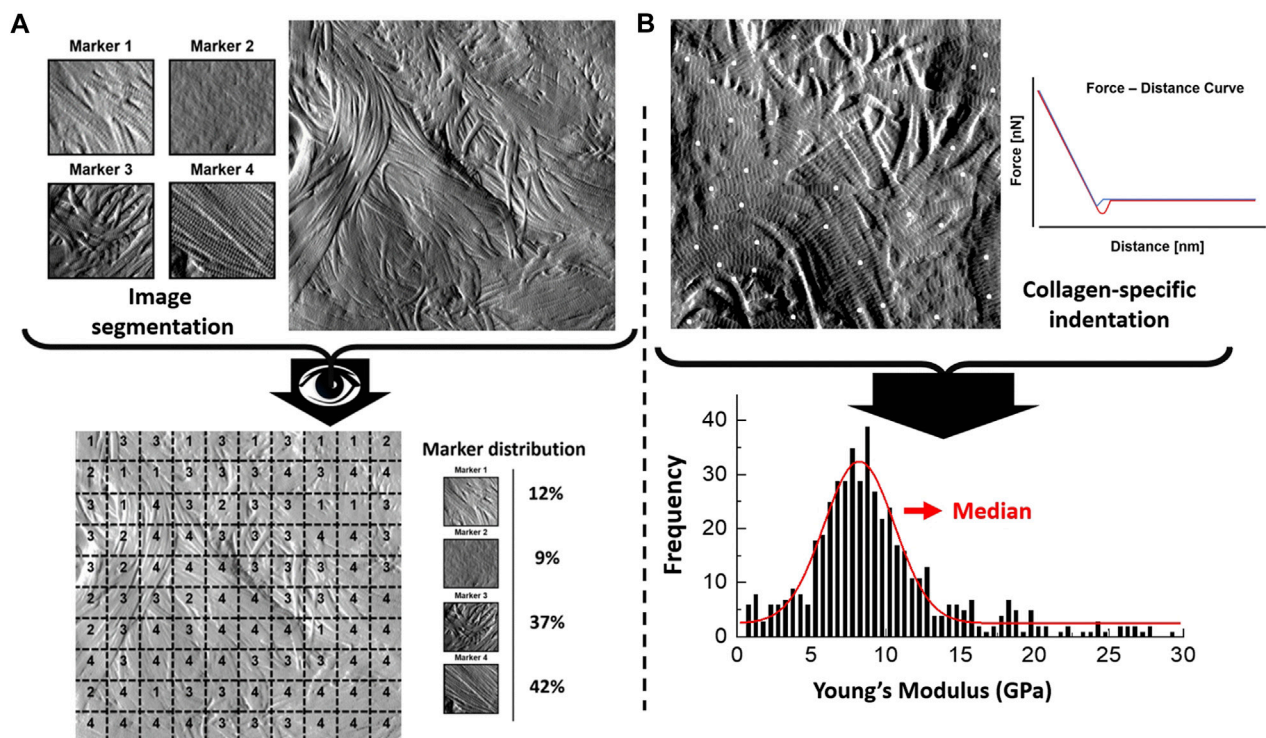


FIGURE 3

Quantitative Nanohistology image analysis and mechanical data analysis: (A) AFM-based image visual segmentation approach presenting the four collagen morphological markers and a representative AFM topological image pre and post-visual segmentation, and the resultant marker distribution. The segmented AFM topological image is analyzed by overlaying a 10 × 10 macro pixel grid and assigning a unique marker in each of the grid areas; (B) specific collagen fibrils AFM-based nanoindentation presenting localized indentation points performed on fibrils (white dots) to generate the frequency distribution of the Young's Moduli which is in turn fitted to extract the median Young's Moduli (compressive) of the fibrils indented in the AFM image.

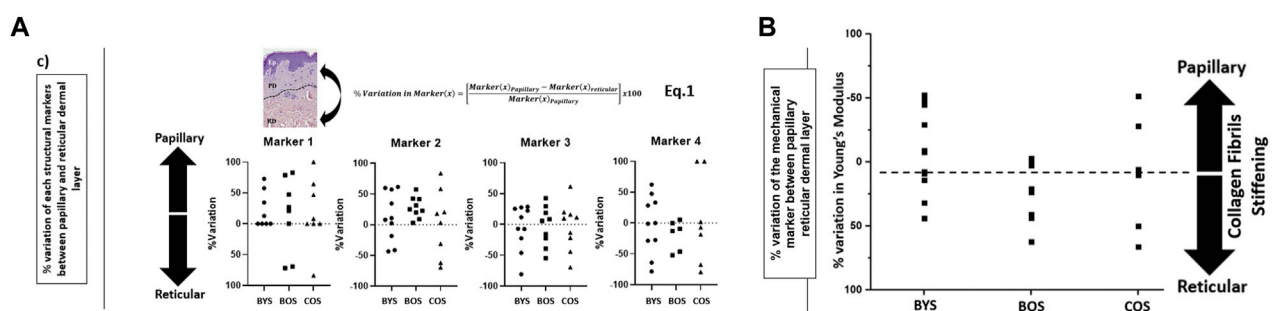


FIGURE 4

Evaluation of the prevalence of structural biomarkers for (type I) collagen as a function of dermal layers and skin groups: (A) %variation in the prevalence of each nanoscale structural biomarkers for (type I) collagen between papillary and reticular dermis (defined in Eq. 1) as a function of the skin groups; (B) variation in the prevalence of the mechanical biomarkers for (type I) collagen between papillary and reticular dermis (as defined in Eq. 1) for each skin group. The direction of the %variation indicates a greater marker prevalence in the papillary or reticular dermis.

promotes the formation of localized, well-aligned collagen fibril bundles. Using our nanohistology approach, we can assert that the reticular collagen is more aligned than the papillary collagen in the sparser region of dermal collagen. This increase in fibril alignment can be directly associated with interfibrillar crosslinks, such as those mediated by the formation of advanced glycation end-products

(Perrone et al., 2020). Finally, no clear trends exist in the % variation of any of the markers associated with the COS group. The lack of a specific structural collagen marker to describe the matrix associated with extrinsically aged skin is unsurprising due to the reduced collagen content favoring elastin fiber formation.

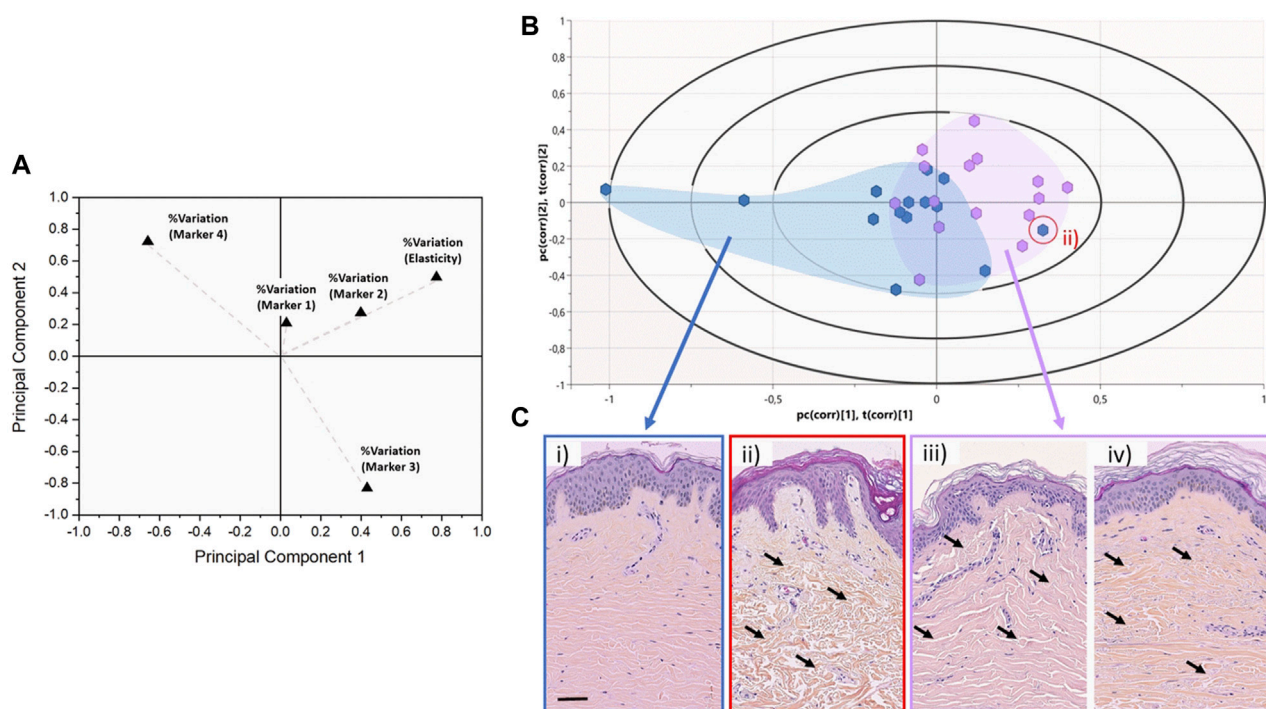


FIGURE 5

Discrimination between chronological and biological aging using multivariate analyses. (A) 2-D PCA score plot associated with the %variation of the markers across the entire dataset for all donors. Variables are presented as vectors extending away from the origin to assess their contribution towards the two principal components. (B) Graphical biplot of the PLS-DA performed on the entire dataset using the donors' age binary class as the response variable. The blue cluster regroups donors belonging to the young group (<30 years old—median 22.0 ± 4.2 years old), whereas the purple cluster regroups donors belonging to the older group (>50 years old - median 66.0 ± 10.4 years old). The red circled data point highlights an outlier belonging to the young group. (C) representative HES Histology of Normal Human Skin from either the young or the older group, as presented in Figure 1. The red circle histological image refers to the outlier (young) case in (B), which presents an old skin phenotype. The black arrows highlight the variations in the dermal layer morphology which can be described as atrophic and sparse in the case of ii), when compared to iii) and iv).

Collagen elasticity as a viable marker for age and anatomical differentiation

In a similar approach for the morphological assessment, we calculated the %variation of Young's moduli between the papillary and reticular dermis, as presented in Figure 4B. This result shows intrinsic aging promotes reticular collagen stiffening over papillary collagen within the intrinsically aged group (BYS compared to BOS). On the other hand, the extrinsically aged group (COS) did not show any trend toward stiffening of the papillary or reticular dermis. This heterogeneity in the mechanical response corroborates our finding in the nanohistology analysis, for which we could not use our pre-defined histomorphological markers. Numerous studies have explored the variations in the collagen mechanical properties at various scales as a function of aging and focused on calculating the nominal values for the elastic modulus of dermal collagen fibrils or scaffolds. (Crichton et al., 2011; Achterberg et al., 2014; Ahmed et al., 2017; Strange et al., 2017; Penuela et al., 2018). Unfortunately, the range of published elastic modulus values for dermal collagen fibrils varies across several orders ranging from a few 100 kPa to a few GPa (Ahmed et al., 2017). This wide range in the elastic modulus values is directly linked to the histological section conditioning, indentation size,

inconsistent indentation load, limited sample size, and collagen hydration level. Unfortunately, comparing study outcomes regarding collagen elasticity measurement is challenging due to the wide variations in the techniques used.

Discrimination between chronological and biological aging

To explore from a multivariate perspective the correlation between the structural (marker 1-2-3-4) and mechanical (elasticity) markers regarding the chronological age of the donors, both unsupervised (regardless of the initially assigned group) PCA and supervised (with the age group as response variable) PLS-DA analyses have been carried out. Figure 5A presents the PCA score plot associated with the %variation of the markers across all donors. The size of the vectors associated with the % variation in markers 3, 4, and elasticity confirm that these three markers are the more potent contributors to the principal components, thus, more prominent differentiators of the entire dataset. On the other hand, the size of the vector associated with marker 1 confirms marker 1 has a limited impact on the dataset. Therefore, we supplemented our PCA analysis with a PLS-DA using the donors' age binary class as the response

variable rather than the markers (Figure 5B). The Biplot chart allows individuals and descriptors (% variation of all markers) to be simultaneously represented and allows us to interpret the individuals in terms of descriptors.

In this biplot, we can observe that the distribution of donors tends to form 2 clusters: all the young donors (<30y.o) are clustered on the left-hand side of the biplot (with two exceptions), whereas the older donors (>50 y.o) tend to cluster on the right-hand side of the biplot. Significant overlap exists between the two sub-populations around the central axis of the PLS-DA. This overlap can be associated with the well-known disparity between the chronological age of the donors and their biological age (Rittie and Fisher, 2015). Although a 20-year gap exists between our younger and old groups, one cannot assume that the chronological age of the donor is the same as their biological age. This is proven by a young donor case on the aged group's outer edge (red circle). Figure 5C-ii presents the histological images of this young donor (22y.o). Despite the dermo-epidermal junction being non-uniform and presenting well-defined rete ridges, the underlying dermal collagen presents significant signs of aging-induced damage, as found in older donors (Figure 5C-iii, iv). The dermal collagen is heavily atrophic and sparse for this young donor, likely associated with significant Sun damage. The quantitative nanohistological assessment performed in this study could classify this donor's collagen phenotype amongst the old group. This 22-year-old donor has the dermal fingerprint of a chronologically old donor, demonstrating the disparity between chronological and biological age again.

Significance

Exploring variations in the phenotypic properties of human largest and most accessible organs has been the subject of much research. However, quantifying the impact of chronic and pathological conditions on the structure and function of collagen at the sub-micron level remains challenging. This is due to a) a lack of current techniques to assess these properties systematically at the nanoscale and b) a lack of histopathology standards (at that scale) in the literature. By employing tools such as the Atomic Force Microscope (Kiio and Park, 2020), we can start cataloging the complexity of the dermal matrix at the nanoscale. All the studies to date present a snapshot of the dermal matrix morphology at the nanoscale, but there is a significant lack of extensive studies. This lack of cohort study poses a challenge for the dermo-cosmetic and dermo-pharmaceutical fields as our study demonstrates an extensive and diverse collagen phenotype across the donors' ages with unique properties for everyone. Such diversity is especially true for the photo-exposed skin with the most heterogeneous biophysical properties.

On the contrary, the photo-protected skin remains more biomechanically homogeneous and presents some evident structural characteristics. Our study suggests that the relative difference in the collagen biophysical properties between the papillary and reticular dermis can be the most effective discriminator to differentiate between chronological and biological aging and the anatomical site. Furthermore, this differential phenotypic assessment of collagen at the nanoscale

can be used to assess subtle variations in the collagen properties in dermal localized pathological or genetic conditions (Arseni et al., 2018), such as Scleroderma or Ehlers-Danlos Syndrome (Angwin et al., 2020), for example. With the advent of artificial intelligence to support image processing and data analysis, we anticipate that such studies' time-consuming (and therefore resource-costly) nature would be significantly reduced. By implementing Convolutional Neural Network (CNN) approaches³⁷ to identify pathology-related morphological collagen fingerprints, it will be possible to create CNN models to predict either early signs or the severity of collagen-based conditions (Arseni et al., 2018).

Conclusion

Our study presents a significant milestone in understanding the complex nature of connective tissue, such as skin, as a function of aging. Here, we demonstrate that we can differentiate between individuals based on their biological age by considering individual skin samples as unique statistical entities with defined structural and mechanical variations in the reticular and papillary dermal collagen. Here, we used an AFM to image and quantify the collagen in the dermis before manually analyzing all the images. Using this approach supported by PCA, we demonstrated how the relative variations in structure and mechanics of the dermal collagen could be used to determine individuals' biological age. Our approach requires advanced knowledge of collagen morphological variations at the nanoscale, for which no established standards exist. Yet, accessing the collagen structure at that scale is fundamental to help define candidate histological markers. As such, we are on course to create a new field of histology: quantitative nanohistology, to probe, quantify and explore connective tissues' structural and functional properties at the sub-micron level.

Data availability statement

The data will be made available upon reasonable request to the corresponding author.

Ethics statement

The studies involving human participants were reviewed and approved by L'Oreal Research & Innovation. The patients/participants provided their written informed consent to participate in this study.

Author contributions

SH contributed to the conception, study design, data interpretation, and curation drafted and critically revised the manuscript; AS, AM, and SS contributed to the data acquisition, and pilot data analysis (not shown here) and critically revised the manuscript; PB contributed to the statistical design and interpretation, drafted and critically revised the manuscript; SA,

MV, and HM-P contributed to the study design, data interpretation, incl. statistical analyses and critically revised the manuscript, MG and AP contributed to the conception and critically revised the manuscript; HP and LB contributed to the conception, study design (both experimental and statistical), data acquisition and analysis, drafted and critically revised the manuscript. All authors contributed to the article and approved the submitted version.

Acknowledgments

We would like to thank the London Centre for Nanotechnology (London United Kingdom) for granting access to the AFM Facility and UCL Consultants for their support.

References

- Achterberg, V. F., Buscemi, L., Diekmann, H., Smith-Clerc, J., Schwengler, H., Meister, J. J., et al. (2014). The nano-scale mechanical properties of the extracellular matrix regulate dermal fibroblast function. *J. Invest. Dermatol* 134, 1862–1872. doi:10.1038/jid.2014.90
- Ahmed, T., Nash, A., Clark, K. E., Ghibaud, M., de Leeuw, N. H., Potter, A., et al. (2017). Combining nano-physical and computational investigations to understand the nature of "aging" in dermal collagen. *Int. J. Nanomedicine* 12, 3303–3314. doi:10.2147/IJN.S121400
- Angwin, C., Ghali, N., Baker, D., Brady, A. F., Pope, F. M., Vandersteen, A., et al. (2020). Electron microscopy in the diagnosis of ehlers-danlos syndromes: Correlation with clinical and genetic investigations. *Br. J. Dermatol* 182, 698–707. doi:10.1111/bjd.18165
- Arseni, L., Lombardi, A., and Orioli, D. (2018). From structure to phenotype: Impact of collagen alterations on human health. *Int. J. Mol. Sci.* 19, 1407. doi:10.3390/ijms19051407
- Bailey, A. J. (2001). Molecular mechanisms of ageing in connective tissues. *Mech. Ageing Dev.* 122, 735–755. doi:10.1016/s0047-6374(01)00225-1
- Binnig, G., Quate, C. F., and Gerber, C. (1986). Atomic force microscope. *Phys. Rev. Lett.* 56, 930–933. doi:10.1103/PhysRevLett.56.930
- Bonté, F., Girard, D., Archambault, J. C., and Desmoulière, A. (2019). "Skin changes during ageing," in *Biochemistry and cell biology of ageing: Part II clinical science*. Editors J. Robin Harris, and V. I. Korolchuk (Singapore: Springer), 249–280.
- Chambers, E. S., and Vukmanovic-Stejic, M. (2020). Skin barrier immunity and ageing. *Immunology* 160, 116–125. doi:10.1111/imm.13152
- Chernoff, E. A. G., and Chernoff, D. A. (1992). Atomic force microscope images of collagen fibers. *J. Vac. Sci. Technol. A* 10, 596–599. doi:10.1116/1.577736
- Cox, T. R., Bird, D., Baker, A. M., Barker, H. E., Ho, M. W. Y., Lang, G., et al. (2013). LOX-mediated collagen crosslinking is responsible for fibrosis-enhanced metastasis. *Cancer Res.* 73, 1721–1732. doi:10.1158/0008-5472.CAN-12-2233
- Crichton, M. L., Donose, B. C., Chen, X., Raphael, A. P., Huang, H., and Kendall, M. A. F. (2011). The viscoelastic, hyperelastic and scale dependent behaviour of freshly excised individual skin layers. *Biomaterials* 32, 4670–4681. doi:10.1016/j.biomaterials.2011.03.012
- Fang, M., Goldstein, E. L., Turner, A. S., Les, C. M., Orr, B. G., Fisher, G. J., et al. (2012). Type I collagen D-spacing in fibril bundles of dermis, tendon, and bone: Bridging between nano- and micro-level tissue hierarchy. *ACS Nano* 6, 9503–9514. doi:10.1021/nn302483x
- Farage, M. A., Miller, K. W., Elsner, P., and Maibach, H. I. (2008). Intrinsic and extrinsic factors in skin ageing: A review. *Int. J. Cosmet. Sci.* 30, 87–95. doi:10.1111/j.1468-2494.2007.00415.x
- Fenske, N. A., and Lober, C. W. (1986). Structural and functional changes of normal ageing skin. *J. Am. Acad. Dermatol* 15, 571–585. doi:10.1016/s0190-9622(86)70208-9
- Fisher, G. J., Kang, S., Varani, J., Bata-Csorgo, Z., Wan, Y., Datta, S., et al. (2002). Mechanisms of photoaging and chronological skin aging. *Arch. Dermatol* 138, 1462–1470. doi:10.1001/archderm.138.11.1462
- Franco, A. C., Avelaira, C., and Cavadas, C. (2022). Skin senescence: Mechanisms and impact on whole-body aging. *Trends Mol. Med.* 28, 97–109. doi:10.1016/j.molmed.2021.12.003
- Harding, J., and Sneddon, I. (1945). The elastic stresses produced by the indentation of the plane surface of a semi-infinite elastic solid by a rigid punch. *Math. Proc. Camb. Philosophical Soc.* 41, 16–26. doi:10.1017/S0305004100022325
- Jolliffe, I. T., and Cadima, J. (2016). Principal component analysis: A review and recent developments. *Philos. Trans. A Math. Phys. Eng. Sci.* 374, 20150202. doi:10.1098/rsta.2015.0202
- Khavkin, J., and Ellis, D. A. (2011). Aging skin: Histology, physiology, and pathology. *Facial Plast. Surg. Clin. North Am.* 19, 229–234. doi:10.1016/j.fsc.2011.04.003
- Kiio, T. M., and Park, S. (2020). Nano-scientific application of atomic force microscopy in pathology: From molecules to tissues. *Int. J. Med. Sci.* 17, 844–858. doi:10.7150/ijms.41805
- Lynch, B., Pagoon, H., Le Blay, H., Brizion, S., Bastien, P., Bornschlög, T., et al. (2022). A mechanistic view on the aging human skin through *ex vivo* layer-by-layer analysis of mechanics and microstructure of facial and mammary dermis. *Sci. Rep.* 12, 849. doi:10.1038/s41598-022-04767-1
- Monnier, V. M., Mustata, G. T., Biemel, K. L., Reihl, O., Lederer, M. O., Zhenyu, D., et al. (2005). Cross-Linking of the extracellular matrix by the maillard reaction in aging and diabetes: An update on "a puzzle nearing resolution". *Ann. N. Y. Acad. Sci.* 1043, 533–544. doi:10.1196/annals.1333.061
- Penuela, L., Negro, C., Massa, M., Repaci, E., Cozzani, E., Parodi, A., et al. (2018). Atomic force microscopy for biomechanical and structural analysis of human dermis: A complementary tool for medical diagnosis and therapy monitoring. *Exp. Dermatol* 27, 150–155. doi:10.1111/exd.13468
- Perrone, A., Giovino, A., Benny, J., and Martinelli, F. (2020). Advanced glycation end products (AGEs): Biochemistry, signaling, analytical methods, and epigenetic effects. *Oxid. Med. Cell. Longev.* 2020, 3818196. doi:10.1155/2020/3818196
- Petruska, J. A., and Hodge, A. J. (1964). A subunit model for the tropocollagen macromolecule. *Proc. Natl. Acad. Sci. U. S. A.* 51, 871–876. doi:10.1073/pnas.51.5.871
- Rittie, L., and Fisher, G. J. (2015). Natural and sun-induced aging of human skin. *Cold Spring Harb. Perspect. Med.* 5, a015370. doi:10.1101/cshperspect.a015370
- Saito, M., and Marumo, K. (2010). Collagen cross-links as a determinant of bone quality: A possible explanation for bone fragility in aging, osteoporosis, and diabetes mellitus. *Osteoporos. Int.* 21, 195–214. doi:10.1007/s00198-009-1066-z
- Salsberg, J., Andriessen, A., Abdulla, S., Ahluwalia, R., Beecker, J., Sander, M., et al. (2019). A review of protection against exposome factors impacting facial skin barrier function with 89% mineralizing thermal water. *J. Cosmet. Dermatol* 18, 815–820. doi:10.1111/jocd.12927
- Singh, R., Barden, A., Mori, T., and Beilin, L. (2001). Advanced glycation end-products: A review. *Diabetologia* 44, 129–146. doi:10.1007/s001250051591
- Snedeker, J. G., and Gautieri, A. (2014). The role of collagen crosslinks in ageing and diabetes - the good, the bad, and the ugly. *Muscles Ligaments Tendons J.* 4, 303–308. doi:10.32098/mltj.03.2014.07
- Stammers, M., Ivanova, I. M., Niewczas, I. S., Segonds-Pichon, A., Streeter, M., Spiegel, D. A., et al. (2020). Age-related changes in the physical properties, cross-linking, and glycation of collagen from mouse tail tendon. *J. Biol. Chem.* 295, 10562–10571. doi:10.1074/jbc.RA119.011031

Conflict of interest

The authors declare that the research was conducted in the absence of any commercial or financial relationships that could be construed as a potential conflict of interest.

Publisher's note

All claims expressed in this article are solely those of the authors and do not necessarily represent those of their affiliated organizations, or those of the publisher, the editors and the reviewers. Any product that may be evaluated in this article, or claim that may be made by its manufacturer, is not guaranteed or endorsed by the publisher.

- Strange, A. P., Aguayo, S., Ahmed, T., Mordan, N., Stratton, R., Porter, S. R., et al. (2017). Quantitative nanohistological investigation of scleroderma: An atomic force microscopy-based approach to disease characterization. *Int. J. Nanomedicine* 12, 411–420. doi:10.2147/IJN.S118690
- Stylianou, A. (2022). Assessing collagen D-band periodicity with atomic force microscopy. *Mater. (Basel)* 15, 1608. doi:10.3390/ma15041608
- Swift, A., Liew, S., Weinkle, S., Garcia, J. K., and Silberberg, M. B. (2021). The facial aging process from the "inside out. *Aesthet. Surg. J.* 41, 1107–1119. doi:10.1093/asj/sjaa339
- Szauter, K. M., Cao, T., Boyd, C. D., and Csiszar, K. (2005). Lysyl oxidase in development, aging and pathologies of the skin. *Pathol. Biol. Paris.* 53, 448–456. doi:10.1016/j.patbio.2004.12.033
- Tanzer, M. L. (1973). Cross-linking of collagen. *Science* 180, 561–566. doi:10.1126/science.180.4086.561
- Terao, M., and Katayama, I. (2016). Local cortisol/corticosterone activation in skin physiology and pathology. *J. Dermatol Sci.* 84, 11–16. doi:10.1016/j.jdermsci.2016.06.014
- Tobin, D. J. (2017). Introduction to skin aging. *J. Tissue Viability* 26, 37–46. doi:10.1016/j.jtv.2016.03.002
- Uitto, J. (2008). The role of elastin and collagen in cutaneous aging: Intrinsic aging versus photoexposure. *J. Drugs Dermatol* 7, s12–s16.
- Venkatesh, S., Maymone, M. B. C., and Vashi, N. A. (2019). Aging in skin of color. *Clin. Dermatol* 37, 351–357. doi:10.1016/j.clindermatol.2019.04.010
- Wenger, M. P., Bozec, L., Horton, M. A., and Mesquida, P. (2007). Mechanical properties of collagen fibrils. *Biophys. J.* 93, 1255–1263. doi:10.1529/biophysj.106.103192
- Wong, R., Geyer, S., Weninger, W., Guimberteau, J. C., and Wong, J. K. (2016). The dynamic anatomy and patterning of skin. *Exp. Dermatol* 25, 92–98. doi:10.1111/exd.12832



OPEN ACCESS

EDITED BY

Anika M. S. Hartz,
University of Kentucky, United States

REVIEWED BY

Stacy A. Hussong,
University of Oklahoma Health Sciences
Center, United States
Beimeng Yang,
Roche Innovation Center China, China

*CORRESPONDENCE

Hoau-Yan Wang,
✉ hywang@med.cuny.edu

[†]Deceased

RECEIVED 27 February 2023

ACCEPTED 21 June 2023

PUBLISHED 29 June 2023

CITATION

Wang H-Y, Pei Z, Lee K-C, Nikolov B,
Doehner T, Puente J, Friedmann N and
Burns LH (2023), Simufilam suppresses
overactive mTOR and restores its
sensitivity to insulin in Alzheimer's disease
patient lymphocytes.
Front. Aging 4:1175601.
doi: 10.3389/fragi.2023.1175601

COPYRIGHT

© 2023 Wang, Pei, Lee, Nikolov, Doehner,
Puente, Friedmann and Burns. This is an
open-access article distributed under the
terms of the [Creative Commons
Attribution License \(CC BY\)](#). The use,
distribution or reproduction in other
forums is permitted, provided the original
author(s) and the copyright owner(s) are
credited and that the original publication
in this journal is cited, in accordance with
accepted academic practice. No use,
distribution or reproduction is permitted
which does not comply with these terms.

Simufilam suppresses overactive mTOR and restores its sensitivity to insulin in Alzheimer's disease patient lymphocytes

Hoau-Yan Wang^{1,2*}, Zhe Pei¹, Kuo-Chieh Lee¹, Boris Nikolov³,
Tamara Doehner⁴, John Puente⁴, Nadav Friedmann^{5†} and
Lindsay H. Burns⁵

¹Department of Molecular, Cellular and Biomedical Sciences, City University of New York School of Medicine, New York, NY, United States, ²Department of Biology and Neuroscience, Graduate School of the City University of New York, New York, NY, United States, ³IMC, Inc., Palmetto Bay, FL, United States, ⁴Cognitive Clinical Trials, Omaha, NE, United States, ⁵Cassava Sciences, Inc., Austin, TX, United States

Introduction: Implicated in both aging and Alzheimer's disease (AD), mammalian target of rapamycin (mTOR) is overactive in AD brain and lymphocytes. Stimulated by growth factors such as insulin, mTOR monitors cell health and nutrient needs. A small molecule oral drug candidate for AD, simufilam targets an altered conformation of the scaffolding protein filamin A (FLNA) found in AD brain and lymphocytes that induces aberrant FLNA interactions leading to AD neuropathology. Simufilam restores FLNA's normal shape to disrupt its AD-associated protein interactions.

Methods: We measured mTOR and its response to insulin in lymphocytes of AD patients before and after oral simufilam compared to healthy control lymphocytes.

Results: mTOR was overactive and its response to insulin reduced in lymphocytes from AD versus healthy control subjects, illustrating another aspect of insulin resistance in AD. After oral simufilam, lymphocytes showed normalized basal mTOR activity and improved insulin-evoked mTOR activation in mTOR complex 1, complex 2, and upstream and downstream signaling components (Akt, p70S6K and phosphorylated Rictor). Suggesting mechanism, we showed that FLNA interacts with the insulin receptor until dissociation by insulin, but this linkage was elevated and its dissociation impaired in AD lymphocytes. Simufilam improved the insulin-mediated dissociation. Additionally, FLNA's interaction with Phosphatase and Tensin Homolog deleted on Chromosome 10 (PTEN), a negative regulator of mTOR, was reduced in AD lymphocytes and improved by simufilam.

Discussion: Reducing mTOR's basal overactivity and its resistance to insulin represents another mechanism of simufilam to counteract aging and AD pathology. Simufilam is currently in Phase 3 clinical trials for AD dementia.

KEYWORDS

filamin A, insulin resistance, mTOR, PTEN, aging, Alzheimer's disease

Introduction

The neurodegenerative process in Alzheimer's disease (AD) is characterized by synaptic damage leading to progressively impaired synaptic plasticity and eventual neuronal loss driven by multiple signaling abnormalities, including the overactivation of mammalian target of rapamycin (mTOR) (Guo et al., 2017). Best known as a driver of cancer, mTOR is a critical protein kinase that regulates cell growth and metabolism via two multiprotein complexes (Liu and Sabatini, 2020; Szwed et al., 2021). mTOR complex 1 (mTORC1) is sensitive to rapamycin and contains regulatory-associated protein of mTOR (Raptor); whereas, mTORC2 instead contains rapamycin-insensitive companion of mTOR (Rictor) (Rosner et al., 2008; Saxton and Sabatini, 2017; Switon et al., 2017; Liu and Sabatini, 2020; Szwed et al., 2021). Controlling energy homeostasis, mTORC1 responds to intracellular and extracellular factors including insulin to regulate protein synthesis, while limiting autophagic breakdown of cellular components (Fingar et al., 2004; Laplante and Sabatini, 2012; Switon et al., 2017; Liu and Sabatini, 2020). mTORC2 can also be activated by growth factors including insulin to regulate cell survival, proliferation, cell mobility and metastasis of cancer cells (Saxton and Sabatini, 2017; Knudsen et al., 2020; Szwed et al., 2021).

With this central role in cellular homeostasis and survival, mTOR, when dysregulated, has been implicated not just in cancer, but also in metabolic syndromes (Yoon, 2017), neurodegeneration, and aging (Rosner et al., 2008; Bloom et al., 2018; Liu and Sabatini, 2020). mTORC1 activation contributes to aging because it accelerates protein synthesis, mitochondrial energy production and resulting oxidative stress, as well as entry into cellular senescence (Liu and Sabatini, 2020; Szwed et al., 2021). By actively suppressing autophagy, mTORC1 contributes to aging by protein accumulation and aggregation (Cai et al., 2012; Kim and Guan, 2015; Perluigi et al., 2015; Liu and Sabatini, 2020). Illustrating mTORC1's role in aging, its inhibition by rapamycin has been shown to increase life span in mice (Harrison et al., 2009; Miller et al., 2014).

In addition to promoting aging, overactivation of mTORC1 appears to contribute specifically to the neuropathology of AD (Rosner et al., 2008; Cai et al., 2012; Cai et al., 2015). Overactive mTORC1 signaling has been demonstrated in AD postmortem hippocampus by elevated phosphorylated serine²⁴⁴⁸ (pS²⁴⁴⁸) mTOR, indicating mTORC1 activation (Talbot et al., 2012; Tang et al., 2015; Majd and Power, 2018), in mouse models of AD (Caccamo et al., 2010) and in AD patient lymphocytes (Paccalin et al., 2006). Sustained activation of mTOR in AD also disables its activation by insulin, contributing to insulin resistance (Perluigi et al., 2015; Bloom et al., 2018). The overactivation of mTOR signaling in AD is evidenced by dysregulation of PTEN, Akt, S6K and mTOR itself (Griffin et al., 2005; Rosner et al., 2008; Talbot et al., 2012; Cai et al., 2015). Activated mTOR in lymphocytes of AD patients correlates with cognitive decline (Paccalin et al., 2006), suggesting a parallel mTOR activation in brain. This overactive mTORC1 signaling in AD appears related to soluble amyloid β_{1-42} (A β_{42}), because A β_{42} activates the PI3K/Akt pathway, leading to mTORC1 activation (Oddo, 2012). Additionally, overactive mTOR and activated p70S6K (a downstream kinase used to confirm mTORC1 activation) are found in brains of AD transgenic mice

(Caccamo et al., 2010) and can be induced by injection of A β_{42} into hippocampi of wildtype mice (Caccamo et al., 2011). Finally, rapamycin administered prior to amyloid plaque formation in these mouse models can ameliorate cognitive deficits and slow the accumulation of amyloid plaques and neurofibrillary tangles (Caccamo et al., 2010; Majumder et al., 2011; Caccamo et al., 2013).

The mTORC1 and mTORC2 signaling pathways involve multiple points of activation, crosstalk and regulation (Xie and Proud, 2013). The mTORC1 pathway is often described as the PI3K/Akt/mTOR pathway: PI3K activates Akt, a serine/threonine kinase via phosphorylation at T³⁰⁸ by phosphoinositide-dependent kinase1 (PDK1) that activates mTORC1 (Laplante and Sabatini, 2012; Yoon, 2017). However, PI3K can also activate mTORC2 via a positive feedback loop between Akt and mTORC2 (Laplante and Sabatini, 2012; Talbot et al., 2012; Xie and Proud, 2013; Yoon, 2017), and mTORC2 directly activates Akt by phosphorylation at S⁴⁷³ (Sarbasov et al., 2005; Xie and Proud, 2013). Hence, mTORC1 activation by Akt is amplified by mTORC2 feedback to further activate Akt and thus mTORC1. mTORC1 activation is indicated by phosphorylation of mTOR at S²⁴⁴⁸ and by phosphorylation of its downstream activation target p70S6K at T³⁸⁹, while mTOR phosphorylation at S²⁴⁸¹ indicates mTORC2 activation (Rosner et al., 2008). Activated p70S6K can phosphorylate Rictor, a key component of mTORC2, at T¹¹³⁵. Although it does not affect mTORC2 assembly or kinase activity, a T1135A genetic modification of Rictor increased mTORC2 activation of Akt, suggesting a negative regulation of Akt and consequently of mTORC1 by Rictor phosphorylation (Julien et al., 2010).

Insulin activates mTOR via the insulin receptor's signaling molecule insulin receptor substrate-1 (IRS-1)'s activation of the PI3K/Akt/mTORC1 pathway. mTORC1's downstream target p70S6K phosphorylates IRS-1 at multiple inhibitory sites, promoting degradation of this signaling adaptor, thereby contributing to insulin resistance, especially with increasing activation of mTORC1 (Rosner et al., 2008). mTOR overactivation has been observed in obese rats in concert with increased inhibitory phosphorylation of IRS-1, indicating impaired insulin signaling to Akt (Khamzina et al., 2005). Insulin resistance has been demonstrated in AD brain (Talbot et al., 2012), and chronic mTOR activation has been proposed to contribute to insulin resistance (Yoon, 2017).

Currently in Phase 3 clinical trials for AD dementia, small molecule drug candidate simufilam was hypothesized to suppress elevated mTOR activation in AD because it disrupts a predominant AD pathogenic pathway, and because it improves insulin receptor signaling (Wang et al., 2012; Wang et al., 2017). Simufilam binds and restores to normal an altered conformation of the scaffolding protein filamin A (FLNA) (Wang et al., 2017). FLNA is a large intracellular protein of 24 immunoglobulin-like repeats that dimerizes at its C-terminal near the cell membrane and crosslinks actin at its N-terminal (Nakamura et al., 2011). Because FLNA interacts with over 90 different proteins (Nakamura et al., 2011), an altered conformation of FLNA in AD could disrupt its normal protein interactions in addition to inducing aberrant ones. Altered FLNA in AD aberrantly links to the $\alpha 7$ nicotinic acetylcholine receptor ($\alpha 7$ nAChR) to enable the toxic signaling of soluble amyloid through this receptor to activate kinases

(Dineley et al., 2002; Nagele et al., 2002; Wang et al., 2003) that hyperphosphorylate tau, leading to neurodegeneration, tau-containing tangles, and even intracellular A β ₄₂ aggregates and amyloid plaques (Wang et al., 2012; Wang et al., 2017; Burns et al., 2023). Simufilam disrupts this toxic pathway by dissociating FLNA from α 7nAChR and similarly disables soluble amyloid's activation of a toll-like receptor 4 (TLR4)-mediated neuroinflammation pathway (Wang et al., 2012; Wang et al., 2017; Burns et al., 2023). The improvement in insulin receptor signaling by simufilam (Wang et al., 2012) was hypothesized to affect mTOR and its responsiveness to insulin.

In the current work, we examined the effects of simufilam on mTOR activity in the lymphocytes of AD subjects who had participated in a Phase 2a clinical trial of simufilam. Lymphocytes were utilized because they are accessible and contain FLNA, mTOR and insulin receptors. We previously reported significant improvements in multiple exploratory CSF and plasma biomarkers in this clinical study, as well as simufilam treatment effects on FLNA's aberrant receptor linkages in lymphocytes (Wang et al., 2020). The reduced linkages of FLNA with α 7nAChR and TLR4 in lymphocytes of simufilam-treated patients had been earlier demonstrated in both brains and lymphocytes of AD transgenic mice as well as in postmortem human AD brain (Wang et al., 2017) (lymphocytes of mice unpublished). To assess mTOR activation and response to insulin in patient lymphocytes in the current work, we compared basal and insulin-stimulated levels of five parameters indicating activation of mTORC1 or mTORC2 signaling before and after simufilam treatment. In addition to assessing simufilam treatment effects on mTOR activation and its insulin response, we compared AD lymphocytes prior to treatment to healthy control lymphocytes.

To explore potential mechanisms, we measured FLNA's linkage to the insulin receptor and its dissociation in response to insulin. We also measured FLNA phosphorylation at S²¹⁵² and FLNA's interaction with PTEN. We considered that by restoring FLNA's normal shape, simufilam might reduce FLNA's hyperphosphorylation and normalize FLNA's interaction with PTEN. PTEN is a dual lipid and protein phosphatase and a well-known tumor suppressor that inhibits mTOR. PTEN negatively regulates the phosphoinositide 3 kinase (PI3K)/Akt/mTOR pathway by dephosphorylating PIP3 (Georgescu, 2010). To explore the potential translation of simufilam's effects on lymphocytes to brain, we used 6 well-matched sets of postmortem AD, amnesic mild cognitive impairment (MCI), non-amnesic MCI and control brain tissue to assess the effect of *ex vivo* simufilam on FLNA's hyperphosphorylation.

Materials and methods

Materials and chemicals

Protease inhibitor cocktail (Complete mini EDTA-free protease inhibitors, Roche, 04693159001), protein phosphatase inhibitor cocktail (Phosphostop phosphatase inhibitors, Roche, 04906837001), anti-mTOR (T-2949) for immunoprecipitation and Histopaque-1077 were purchased from Sigma/Millipore. Anti-mTOR (SC-517464) for Western blotting, -pS²⁴⁴⁸mTOR (SC-293133), -pS²⁴⁸¹mTOR (SC-293089), -Rictor (SC-271081),

-Raptor (SC-81537), -p70S6K α (SC-8418, SC-393967), -Akt1 (SC-5298, SC-55523), -pS⁴⁷³Akt (SC-514032), -FLNA (SC-58764, SC-17749, SC-271440), -IR β (SC-09), and -PTEN (SC-7941, Cell Signaling #9559) were purchased from Santa Cruz Biotechnology. Anti-pS²¹⁵²FLNA antibody (TA313881) was purchased from Origene Technologies. Anti-pT¹¹³⁵Rictor (#3806) and -pT³⁸⁹p70S6K (#9205) were purchased from Cell Signaling Technology. Insulin (human recombinant; #12585014), zinc solution (#12585014), covalently conjugated protein A/G-agarose beads (#20423), PageRuler™ Plus Prestained Protein Ladder, 10–250 kDa (#26619) and SuperSignal™ West Pico PLUS Chemiluminescent Substrate (#34577) were purchased from ThermoFisher Scientific.

Lymphocyte collection and processing

Lymphocytes from AD subjects and age-matched controls, from AD subjects in a clinical trial of simufilam, and from healthy controls of three different age ranges (20–30, 40–50 and 65+) were collected under IRB-approved protocols described below.

To prepare lymphocytes, 8 mL venous blood collected in EDTA-containing tubes was layered onto 8 mL Histopaque-1077 at 25°C and centrifuged (400 g, 30 min, 25°C) to yield plasma (top layer) and lymphocytes (opaque interface). The obtained lymphocytes were washed twice by mixing with 10 mL phosphate-buffered saline (PBS) followed by centrifugation at 250 g for 10 min. The final lymphocyte pellet was resuspended in 600 μ L cell freezing medium (DMEM, 5% DMSO, 10% fetal bovine serum), aliquoted and held at –80°C until assay.

Clinical protocols

All blood samples were collected under IRB-approved protocols and were de-identified to the lab receiving samples. The initial study collecting blood samples from AD and age-matched healthy control subjects (Figures 5A, B, 2 males and 2 females in each group) was approved by Quorum IRB. Both the Phase 2a clinical trial of simufilam and the protocol for collection of healthy control lymphocytes were approved by Advarra. Informed Consent Forms signed by all subjects are retained by the sites. All assays were performed by experimenters blind to AD versus healthy control (Figures 5A, B and 6 data), Day of treatment (Phase 2a trial), and age group (healthy control protocol).

In the first-in-patient clinical trial of simufilam (NCT03748706), 19 subjects screened and 13 enrolled. These were 9 females, 4 males; 3 black, 10 white; 6 Hispanic and 7 non-Hispanic. All 13 were mild-to-moderate AD patients, age 50–85, MMSE \geq 16 and \leq 24, with a CSF total tau/A β ₄₂ ratio \geq 0.30. Subjects received 100 mg oral simufilam b.i.d. for 28 days. CSF was collected at screening and Day 28. Blood samples for plasma biomarkers and lymphocytes were collected Day 1 before dosing, Day 14 and Day 28.

The collection of whole blood from healthy subjects was conducted later and specifically for comparison to the AD subjects. Lymphocytes were isolated from 18 healthy subjects, 6 each in three different age groups (20–30, 40–50 and 65+). These included 12 females and 6 males; 13 white, 2 Asian,

2 American Indian and 1 black participant. Age-matched controls (65+) and two younger cohorts were included so that age differences among healthy controls could be assessed. There were no significant or notable differences between age groups of healthy control subjects on any of the five mTOR parameters due to within group variability and the small group size ($n = 6$). Because there were no age differences, these age ranges were combined into one healthy control group ($n = 18$).

Lymphocyte incubation and prep for immunoprecipitation and immunoblotting

Lymphocytes (200 μ g) from AD patients or healthy controls were incubated at 37°C with oxygenated protease inhibitors containing Kreb's-Ringer (K-R) or either 0.1 μ M A β ₄₂ for 30 min (for experiment to assess FLNA phosphorylation at S²¹⁵² or PTEN—FLNA linkage) or 1 nM insulin for 15 min (for experiments to assess FLNA linkage to IR β or mTOR activation). Total incubation volumes were 250 μ l. Assay mixtures were aerated with 95%O₂/5%CO₂ for 1 min every 10 min. Reactions were terminated by adding ice-cold Ca²⁺-free K-R containing protease and protein phosphatase inhibitors and centrifuged. Lymphocytes were then homogenized in 250 μ l ice-cold immunoprecipitation buffer containing 25 mM HEPES, pH 7.5, 200 mM NaCl, 1 mM EDTA, 0.2% 2-mercaptoethanol, and protease and protein phosphatase inhibitors by sonication for 10 s on ice and solubilized by nonionic detergents: 0.5% NP-40/0.2% Na cholate/0.5% digitonin for 60 min (4°C) with end-to-end rotation. The obtained lysates were cleared by centrifugation at 20,000 g for 30 min (4°C) and the resultant supernatants (0.25 ml) were diluted 4x with 0.75 ml immunoprecipitation buffer for immunoprecipitation and immunoblotting as described below.

To detect phosphorylation of a protein, the protein of interest was immunoprecipitated by a phospho-independent antibody, and the specific phospho-epitope was detected by immunoblotting with a phospho-specific antibody. In the case of co-immunoprecipitation, the first protein was immunoprecipitated, and the interacting protein was detected in the immunoprecipitate by immunoblotting. For all immunoblotting experiments, bands were quantified by densitometric quantitation, and these values for all bands in each group were analyzed statistically. Not all groups were run on the same blots; however, each lane was normalized to its own loading control, i.e., the protein that was immunoprecipitated (mTOR, p70S6K, Akt1 or FLNA). With these internal controls, separate blots and experiments conducted separately can be compared.

Assessment of simufilam treatment on FLNA phosphorylation at pS²¹⁵² and levels of associated PTEN

Ex vivo A β ₄₂ treatment and determination of levels of pS²¹⁵²FLNA and FLNA-associated PTEN were assessed in lymphocytes from healthy controls and age-matched AD patients. After incubating lymphocytes with K-R or 0.1 μ M A β ₄₂ for 30 min and homogenizing and solubilizing as described above,

FLNA-associated protein complexes were immunoprecipitated with immobilized anti-FLNA (SC-58764 + SC-271440) antibodies onto covalently protein A/G-conjugated agarose beads. The resultant immunocomplexes were pelleted by centrifugation (4°C), washed three times with ice-cold PBS, pH 7.2, containing 0.1% NP-40, and centrifuged again. Immunocomplexes were then solubilized by boiling for 5 min in 100 μ l SDS-PAGE sample preparation buffer (62.5 mM Tris-HCl, pH 6.8; 10% glycerol, 2% SDS; 5% 2mercaptoethanol, 0.1% bromophenol blue) and centrifuged to remove antibody-protein A/G agarose beads. Levels of pS²¹⁵²FLNA and PTEN were determined by immunoblotting first with anti-pS²¹⁵²FLNA. Blots were then stripped and re-probed with specific antibodies against PTEN (SC-7974) and FLNA (SC-17749) to access associated PTEN levels and ascertain immunoprecipitation efficiency and gel loading, respectively (Wang et al., 2017).

In a separate experiment, anti-FLNA immunoprecipitates of lymphocyte lysates of the phase 2a subjects were used to assess the effects of simufilam on pS²¹⁵²FLNA and PTEN levels by specific antibodies against pS²¹⁵²FLNA and PTEN (Cell Signaling #9559). Parallel sets of blots with identical amounts of anti-FLNA immunoprecipitates were used to confirm equal loading.

Assessment of FLNA linkages to IR β

Lymphocytes from AD patients and healthy controls were assessed for basal and insulin-stimulated FLNA linkage to IR β . After incubating lymphocytes with K-R or 1 nM insulin for 15 min and homogenizing and solubilizing as described above, FLNA-associated protein complexes were immunoprecipitated with immobilized anti-FLNA (SC-58764 + SC-271440) antibodies onto covalently protein A/G-conjugated agarose beads. The resultant immunocomplexes were pelleted by centrifugation (4°C), washed three times with ice-cold PBS, pH 7.2, containing 0.1% NP-40, and centrifuged again. Immunocomplexes were then solubilized by boiling for 5 min in 100 μ l SDS-PAGE sample preparation buffer (described above) and centrifuged to remove antibody-protein A/G agarose beads. Levels of IR β were determined by immunoblotting with anti-IR β . Blots were stripped and re-probed with specific antibodies against FLNA (SC-17749) to indicate immunoprecipitation efficiency and gel loading (Wang et al., 2017). For healthy control lymphocytes, levels of IR β and FLNA were determined by immunoblotting with anti-IR β and anti-FLNA (SC-17749) simultaneously.

Assessments of basal and insulin-stimulated mTOR activation

Lymphocytes from AD patients and healthy controls were assessed for basal and insulin-stimulated mTOR activation. After incubating lymphocytes with K-R or 1 nM insulin for 15 min and homogenizing and solubilizing as described above, protein complexes were immunoprecipitated with immobilized anti-mTOR (T-2949), -Akt1 (SC-5298, SC-55523), or -p70S6K (SC-8418, SC-393967) antibodies onto covalently protein A/G-conjugated agarose beads. Immunocomplexes were pelleted by centrifugation (4°C), washed three times with ice-cold PBS,

pH 7.2, containing 0.1% NP-40, and centrifuged again. Immunocomplexes were then solubilized by boiling for 5 min in 100 μ L SDS-PAGE sample preparation buffer (described above) and centrifuged to remove antibody-protein A/G agarose beads. Activated mTORC1 was defined by the levels of pS²⁴⁴⁸mTOR in the anti-mTOR immunoprecipitates by immunoblotting and supported by pT³⁸⁹p70S6K in anti-p70S6K immunoprecipitates and pT¹¹³⁵Rictor in mTOR immunoprecipitates. mTORC1—Raptor linkage was assessed by immunoblotting with anti-Raptor. The activity of mTORC2 was defined by the levels of pS²⁴⁸¹mTOR and supported by pS⁴⁷³Akt1 in the anti-Akt1 immunoprecipitates. mTORC2—Rictor association was determined by the levels of Rictor in the anti-mTOR immunoprecipitate by immunoblotting with anti-Rictor. Blots were stripped and re-probed with respective specific antibodies against mTOR (SC-517464), p70S6K (SC-393967) or Akt1 (SC-5298) to indicate immunoprecipitation efficiency and gel loading.

Assessment of pS²¹⁵²FLNA in postmortem human AD brain tissue

Using an established method (Wang et al., 2012), pS²¹⁵²FLNA and IR β proteins in synaptosomes from A β ₄₂-incubated hippocampal slices from 6 sets of age (81–94 years) and postmortem interval (2–8.8 h) matched control, amnesic MCI, non-amnesic MCI and AD subjects (4 females/2 males) with and without 1 nM simufilam were immunoprecipitated with immobilized anti-FLNA (SC-7565). Briefly, hippocampal slices were incubated with K-R, 1 nM simufilam or 1 μ M A β ₄₂ at 37°C for 30 min. Synaptosomes (200 μ g) from K-R, simufilam or A β ₄₂ incubated postmortem hippocampal slices were pelleted by centrifugation, solubilized by brief sonication in 250 μ L of immunoprecipitation buffer (25 mM HEPES, pH 7.5; 200 mM NaCl, 1 mM EDTA, cocktail of protease, and protein phosphatase inhibitors) and incubated at 4°C with end-to-end shaking for 1 h. Following dilution with 750 μ L of ice-cold immunoprecipitation buffer and centrifugation (4°C) to remove insoluble debris, the FLNA-IR β complexes in the lysate were isolated by immunoprecipitation with 16-h incubation at 4°C with respective rabbit anti-FLNA (1 μ g) immobilized on protein A/G-conjugated agarose beads. The resultant immunocomplexes were pelleted by centrifugation at 4°C. After 3 washes with 1 mL of ice-cold PBS (pH 7.2) and centrifugation, the isolated FLNA-IR complexes were solubilized by boiling for 5 min in 100 mL of SDS-polyacrylamide gel electrophoresis (PAGE) sample preparation buffer (62.5 mM Tris-HCl, pH 6.8; 10% glycerol, 2% SDS; 5% 2-mercaptoethanol, 0.1% bromophenol blue). Levels of pS²¹⁵²FLNA and the content of IR β in 50% of the anti-FLNA immunoprecipitates were determined by immunoblotting with purified rabbit anti-pS²¹⁵²FLNA (TA313881, Origene) and mouse monoclonal anti-IR β (SC-81465) antibodies. Blots were stripped and re-probed with monoclonal anti-FLNA (SC-271440) to validate equal immunoprecipitation efficiency and loading.

Statistics

All data were analyzed by an independent statistician using SAS, except for Figures 5, 6, which were analyzed in Excel. Comparisons between healthy controls and AD at Day 0 used the two-sided two-

sample *t*-test (and were not notably different from analyses using the non-parametric Wilcoxon-Mann-Whitney test). Within-subject comparisons between Day 0 and Day 14 or Day 0 and Day 28 were analyzed by two-sided paired *t*-test (and were not notably different from results using non-parametric tests Wilcoxon signed rank or sign test). Because parametric and non-parametric analyses did not produce notably different results, distributions were assumed to be normal, justifying the use of the parametric *t*-test.

Results

Multiple measures of mTORC1 and mTOR2 activation showed elevated basal activity in AD lymphocytes compared to healthy control lymphocytes. The elevated basal activity was paired with very little stimulation by *in vitro* insulin across these measures. Simufilam administered orally to the AD patients reduced the heightened basal activity and enhanced sensitivity to insulin. The first three subsections below show indicators of mTORC1 activation, mTORC2 activation, and Akt1 activation, the latter in the mTORC1 pathway but also stimulated by mTORC2. The fourth subsection reports FLNA's interaction with the insulin receptor, which is dissociated in response to insulin, perhaps to allow recruitment of IRS-1. The FLNA—insulin receptor interaction is higher in AD lymphocytes, and its dissociation by insulin is impaired, but improved by simufilam. The fifth subsection shows another possible mechanistic explanation for the elevated mTOR activation: FLNA linkage to the mTOR suppressor PTEN was reduced in AD lymphocytes compared to healthy controls, coincident with elevated phosphorylation of FLNA at S²¹⁵². Simufilam oral treatment restored the FLNA—PTEN linkage and reduced FLNA's hyperphosphorylation. In the final subsection, elevated pS²¹⁵²FLNA is also shown in postmortem AD and amnesic MCI brain, and this hyperphosphorylation was reduced by *ex vivo* incubation with simufilam.

Simufilam reduced basal mTORC1 signaling and restored its insulin sensitivity

Basal mTORC1 signaling was elevated and its response to insulin was blunted in lymphocytes from AD compared to healthy control subjects. These differences were attenuated after simufilam treatment (Figure 1). Basal activity of mTORC1, indicated by levels of pS²⁴⁴⁸mTOR, was significantly elevated in AD subjects' lymphocytes relative to healthy controls (Figures 1A, B; *p* < 0.001). This heightened basal activity in AD lymphocytes was nearly as high as the insulin-stimulated level in healthy controls and was not further stimulated by insulin. Simufilam treatment of AD subjects significantly reduced this heightened basal mTORC1 activity by Day 14 and Day 28 (*p* < 0.001). The level of mTORC1 activation following insulin stimulation was not different from healthy controls at any treatment day for AD subjects, although the Day 28 insulin-stimulated mTORC1 activation level was significantly higher than at Day 0 for AD subjects (*p* < 0.001). Notably, percent stimulation by insulin of mTORC1 was markedly reduced in AD subjects before simufilam treatment relative to healthy controls

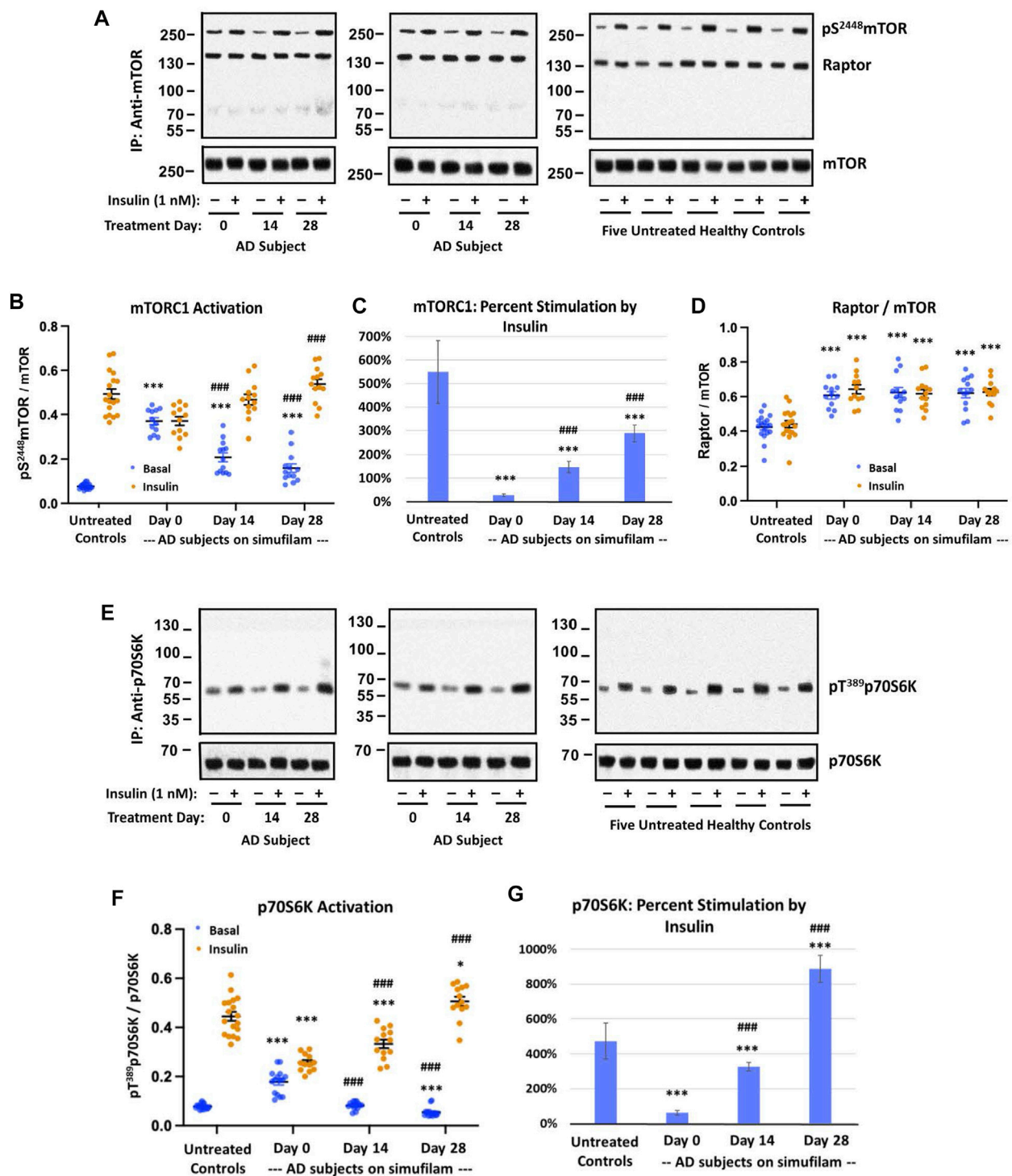


FIGURE 1

Simufilam treatment attenuated basal mTORC1 overactivation and restored its response to insulin in lymphocytes from AD subjects. Representative blot images from two AD and five healthy control subjects (A,E) show increased basal activation of mTORC1 by elevated levels of mTOR phosphorylation at S²⁴⁴⁸ (A) and by increased basal activation of mTORC1's downstream kinase p70S6K, indicated by phosphorylation at T³⁸⁹ (E), in AD subjects versus healthy controls. Blots were analyzed by densitometric quantitation (B,D,F). With heightened basal activity of the mTORC1 signaling pathway in AD subject lymphocytes, its response to *in vitro* insulin was blunted. The elevated basal p70S6K, still lower than insulin-stimulated control levels, also showed a weak response to insulin. Oral simufilam treatment decreased the elevated basal mTORC1 activation and restored its response to insulin across both measures, with insulin-stimulated p70S6K levels slightly higher than untreated healthy controls on Day 28. The simufilam treatment effect is also seen in the dramatic improvement in percent stimulation by insulin (C,G). mTOR association with Raptor was lower in healthy controls but unaffected by insulin or simufilam (D). Data are means \pm SEM. $N = 13$ for AD, 18 for control. * $p < 0.05$, *** $p < 0.001$, vs. respective value in healthy control by two-sided two-sample t -test; ### $p < 0.001$ vs. respective AD value at Day 0 by two-sided paired t -test.

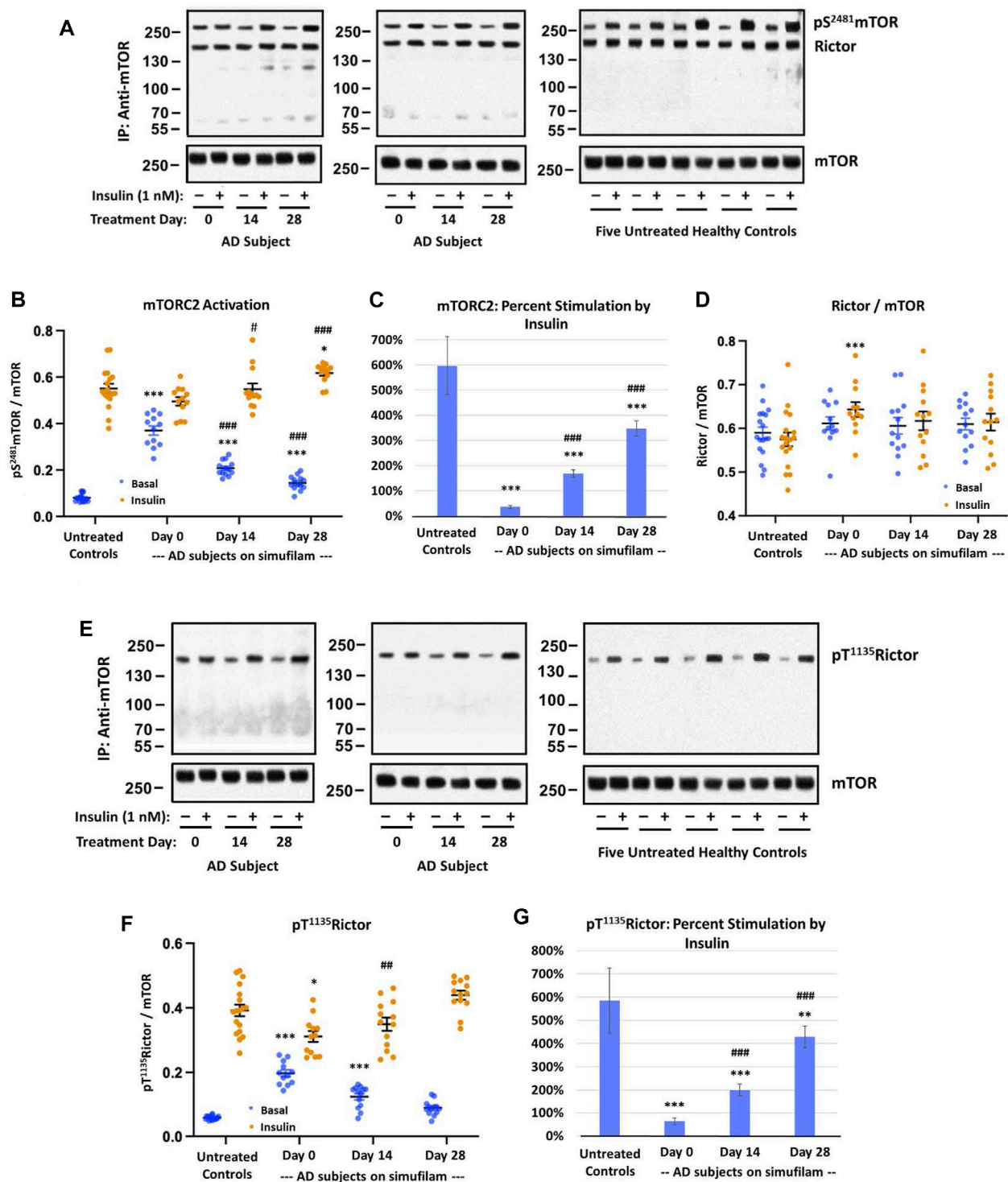


FIGURE 2

Simufilam treatment attenuated basal mTORC2 overactivation and restored its response to insulin in lymphocytes from AD subjects. Representative blot images from two AD and five healthy control subjects (A,E) show increased basal mTORC2 signaling by elevated levels of mTOR phosphorylation at S²⁴⁸¹ (A) and by increased phosphorylation of the mTORC2 component Rictor at T¹¹³⁵ (E) in AD subjects versus healthy controls. Blots were analyzed by densitometric quantitation (B,D,F). As with mTORC1 signaling, the heightened basal mTORC2 signaling in AD subjects left little room for insulin stimulation. The elevated levels of pT¹¹³⁵Rictor, still lower than insulin-stimulated control levels, again showed a weak response to insulin. Oral simufilam treatment decreased the elevated basal mTORC2 signaling and restored its response to insulin on both measures. Insulin-stimulated p S²⁴⁸¹mTOR was slightly higher on Day 28 than in untreated healthy controls. Percent stimulation of these mTORC2 signaling components by insulin improved dramatically after simufilam treatment (C,G). mTOR association with Rictor was unchanged in AD and unaffected by insulin or simufilam (D). Data are means \pm SEM. $N = 13$ for AD, 18 for control. * $p < 0.05$, ** $p < 0.01$, *** $p < 0.001$ vs. respective value in healthy control by two-sided two-sample t -test; # $p < 0.01$, ### $p < 0.001$ vs. respective AD value at Day 0 by two-sided paired t -test.

(Figure 1C; $p < 0.001$). Insulin responsiveness significantly improved on Day 14 and Day 28 of treatment ($p < 0.001$).

These changes in mTORC1 activation in AD subjects and improvements following simufilam treatment were not due to changes in mTOR or Raptor expression levels or association of mTOR with Raptor, a component of mTORC1. Interestingly however, mTOR—Raptor association was lower in healthy control than in AD subject lymphocytes (Figure 1D).

Additional confirmation of mTORC1 activation is provided by activation of p70S6K, a downstream kinase of mTORC1 by its phosphorylation at T¹³⁸⁹. Similar to mTORC1 activation, p70S6K basal activity, indicated by pT¹³⁸⁹p70S6K, was elevated in AD subjects relative to healthy controls (Figures 1E, F; $p < 0.001$). This elevated basal p70S6K activity was reduced on Day 14 and Day 28 compared to pre-treatment levels ($p < 0.001$). Insulin-stimulated activation of p70S6K was significantly lower than in healthy controls ($p < 0.001$) before treatment and at Day 14 but was slightly higher than in healthy controls after 28 days of simufilam ($p < 0.05$). Insulin responsiveness of p70S6K was significantly improved at Day 14 and Day 28 ($p < 0.001$). Percent stimulation by insulin was significantly lower in AD subjects before treatment and on Day 14 compared to healthy controls but significantly higher at Day 28 (Figure 1G; $p < 0.001$).

Simufilam reduced basal mTORC2 signaling and restored its insulin sensitivity

Similar to mTORC1, mTORC2 basal activation was elevated in AD subjects relative to healthy controls, as assessed by levels of pS²⁴⁸¹mTOR (Figures 2A, B; $p < 0.001$), and this high basal activity was significantly reduced by simufilam treatment ($p < 0.001$). Insulin-induced mTORC2 activation was elevated on Day 14 ($p < 0.05$) and Day 28 ($p < 0.001$) in AD subjects relative to Day 0. Similar to p70S6K, insulin-stimulated mTORC2 on Day 28 of simufilam treatment in AD subjects was slightly higher than in healthy controls ($p < 0.05$). Like mTORC1, percent stimulation by insulin for mTORC2 was markedly reduced in AD subjects at all treatment days relative to healthy controls but markedly increased following simufilam treatment (Figure 2C; $p < 0.001$).

There were no notable differences in mTOR and Rictor expression levels and mTOR—Rictor association between AD and healthy controls and no effects of insulin or simufilam on this interaction, despite a slight increase in insulin-stimulated mTORC2 levels in AD on Day 0 (Figure 2D).

Activation of the mTORC2 component Rictor is evidenced by its phosphorylation at T¹¹³⁵. Basal levels of pT¹¹³⁵Rictor were elevated in AD compared to healthy control lymphocytes (Figures 2E, F; $p < 0.001$). This heightened level of pT¹¹³⁵Rictor was reduced after 14 and 28 days of simufilam treatment ($p < 0.001$). Insulin-stimulated pT¹¹³⁵Rictor was slightly lower in untreated AD subjects than in healthy controls ($p = 0.05$) and was significantly increased following simufilam treatment ($p < 0.01$ at Day 14 and $p < 0.001$ at Day 28 vs. Day 0). The slight increase in insulin-stimulated pT¹¹³⁵Rictor in AD subjects on Day 28 versus healthy controls is not significant ($p = 0.07$). As with other mTORC1 and mTORC2 markers, percent stimulation by insulin of pT¹¹³⁵Rictor was dramatically reduced in AD versus healthy control lymphocytes (Figure 2G; $p < 0.001$) and significantly improved with simufilam treatment ($p < 0.001$).

Simufilam reduced basal Akt1 activation and restored its insulin sensitivity

Akt is activated by PI3K in the PI3K/Akt/mTORC1 pathway (indicated by pT³⁰⁸Akt) but also by mTORC2 in a positive feedback loop (indicated by pS⁴⁷³Akt). Activation of Akt is indicated by its phosphorylation at S⁴⁷³. Like the other mTORC1 and mTORC2 markers, basal pS⁴⁷³Akt1 was elevated in AD versus healthy control subjects (Figure 3, $p < 0.001$). The heightened basal Akt1 activity was reduced by simufilam treatment ($p < 0.001$) and not different from healthy controls by Day 28. Insulin-stimulated pS⁴⁷³Akt1 was also lower in AD than in healthy controls ($p < 0.001$) and improved with simufilam treatment ($p < 0.001$) to a level not different from control on Day 28. Percent stimulation by insulin was once again markedly reduced in AD compared to controls (Figure 3C; $p < 0.001$) and significantly improved with simufilam treatment ($p < 0.001$) to a level close to control on Day 28.

Simufilam improved dissociation of FLNA—IR β linkage by insulin

To investigate a potential mechanism of simufilam on insulin responsiveness, we examined interactions of simufilam's target protein, FLNA, with the insulin receptor. Levels of FLNA association with the IR β subunit of the insulin receptor were lower in healthy control lymphocytes than in AD lymphocytes (Figures 4A, B; $p < 0.001$), as seen by the very faint IR β bands in the immunoblots of the FLNA immunoprecipitates of healthy control lymphocytes. This linkage was further reduced in response to insulin in the healthy controls ($p < 0.001$), although the magnitude of reduction as calculated by densitometric quantitation of the already faint immunoblot bands may not be reliable. The much higher levels of FLNA linked to IR β in AD patient lymphocytes suggest it is a pathogenic interaction, perhaps preventing IR β from interacting with IRS-1. Insulin had very little effect on these much higher levels of FLNA—IR β association in lymphocytes of AD subjects prior to simufilam treatment ($p = 0.06$). After simufilam treatment, insulin's ability to reduce this FLNA—IR β linkage was partially restored on Day 14 and further improved by Day 28 ($p < 0.001$ for Day 14 or 28 vs. Day 0). Percent stimulation by insulin was significantly lower in untreated AD subjects than in healthy controls, and significantly improved with simufilam (Figure 4C; $p < 0.001$) to levels close to healthy control.

Simufilam reduced pS²¹⁵²FLNA and restored FLNA—PTEN linkage

To explore additional potential FLNA-mediated mechanisms of the mTOR overactivation and resistance to insulin, we examined FLNA phosphorylation and a critical protein interaction. Specifically, FLNA was hyperphosphorylated at S²¹⁵² in lymphocytes of AD subjects compared to lymphocytes from

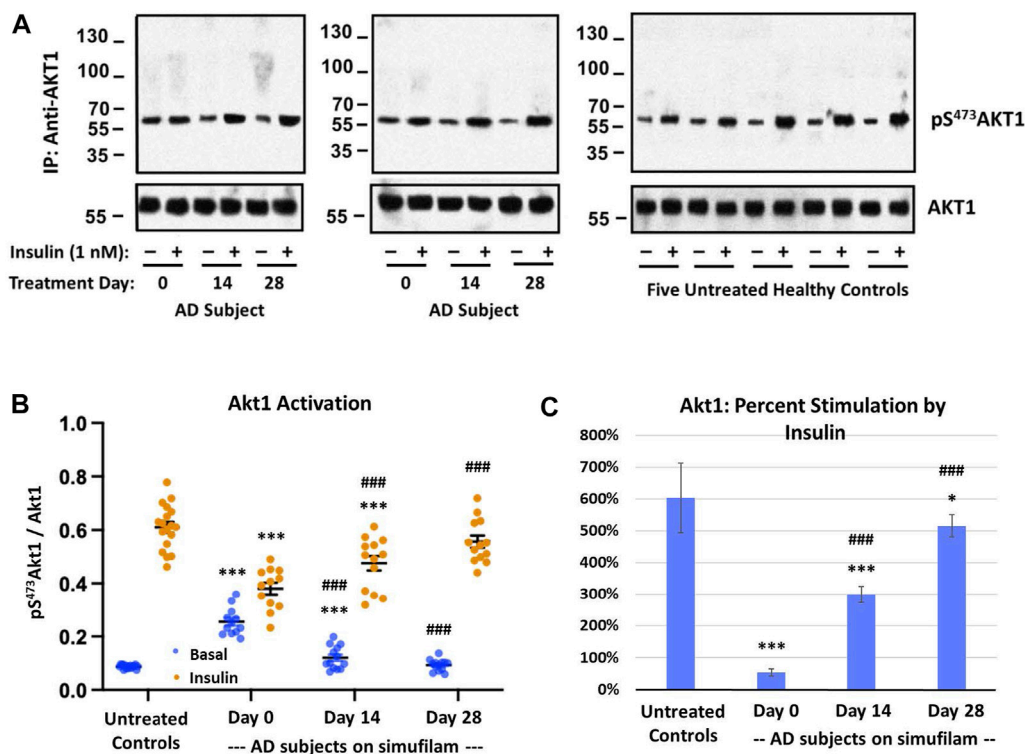


FIGURE 3

Simufilam treatment attenuates mTORC2-mediated Akt1 activation. Akt1 is activated by mTORC2 signaling by phosphorylation on S⁴⁷³ to further activate mTORC1. Representative blot images from two AD and five healthy control subjects (A) show increased basal Akt1 activation, as indicated by its phosphorylation at S⁴⁷³, in AD subjects versus healthy controls. Blots were analyzed by densitometric quantitation (B). Showing a similar pattern to downstream effectors p70S6K and pT¹³⁵Rictor, basal Akt1 activity was elevated in AD subjects without nearing insulin-stimulated control levels, and its response to insulin was still blunted. Oral simufilam treatment decreased the elevated Akt1 activation and restored its response to insulin to a level not different from healthy control. Percent stimulation of Akt1 by insulin improved dramatically after simufilam treatment (C). Data are means \pm SEM. $N = 13$ for AD, 18 for control. * $p < 0.05$, *** $p < 0.001$ vs. respective value in healthy control by two-sided two-sample t -test; # $p < 0.05$, ### $p < 0.001$ vs. respective AD value at Day 0 by two-sided paired t -test.

age-matched controls (Figures 5A, B; $p < 0.01$). Importantly, incubation of control lymphocytes with 0.1 μ M A β ₄₂ for 1 h increased pS²¹⁵²FLNA ($p < 0.01$) to a level comparable to pS²¹⁵²FLNA in AD lymphocytes, suggesting that this FLNA alteration is mediated by A β ₄₂. Correlating with the FLNA hyperphosphorylation, FLNA's interaction with the mTOR suppressor PTEN was reduced in AD versus control lymphocytes ($p < 0.01$). However, unlike the induction of pS²¹⁵²FLNA by exogenous A β ₄₂, incubation of control lymphocytes with A β ₄₂ did not reduce the FLNA–PTEN interaction to levels comparable to AD lymphocytes, suggesting that the time needed to dissociate PTEN tethering to FLNA may be longer than the time needed to hyperphosphorylate FLNA in response to A β ₄₂. Alternatively, the reduced FLNA–PTEN interaction in AD lymphocytes might have other influences. AD lymphocytes were also incubated with 0.1 μ M A β ₄₂ to maintain experimenter blinding and to show that FLNA hyperphosphorylation in AD lymphocytes is mediated by endogenous A β ₄₂. Oral simufilam given to AD subjects in the clinical trial reduced levels of pS²¹⁵²FLNA at Day 28 (Figures 5C, D; $p < 0.001$) and increased FLNA–PTEN linkage in lymphocytes at both Day 14 and Day 28 ($p < 0.01$).

Simufilam incubation reduced pS²¹⁵²FLNA in AD and amnesic MCI postmortem brain tissue

To explore whether simufilam's effects on lymphocytes may also occur in brain, we examined the FLNA hyperphosphorylation in six well-matched sets of postmortem brain tissue from healthy control, amnesic MCI, non-amnesic MCI and AD subjects. FLNA is hyperphosphorylated at S²¹⁵² in AD and amnesic MCI compared to control and non-amnesic MCI, as seen by increased levels of pS²¹⁵²FLNA in FLNA immunoprecipitates of solubilized synaptosomes from the brain tissue (Figure 6, $p < 0.01$). Incubation with 1 nM simufilam for 1 h reduced pS²¹⁵²FLNA in AD and amnesic MCI postmortem brain tissue ($p < 0.01$) but had no effect on the already low levels in non-amnesic MCI or control tissue. In reciprocal fashion, incubation of control and non-amnesic MCI tissue with 0.1 μ M A β ₄₂ increased pS²¹⁵²FLNA to levels comparable to AD and amnesic MCI ($p < 0.01$) but had no further effect on the already high levels in amnesic MCI and AD tissue. The increase in pS²¹⁵²FLNA by exogenous A β ₄₂ to levels resembling those in AD or amnesic MCI again suggests that this AD-related hyperphosphorylation of FLNA is A β ₄₂-dependent. In contrast to our observations in AD and control lymphocytes, levels

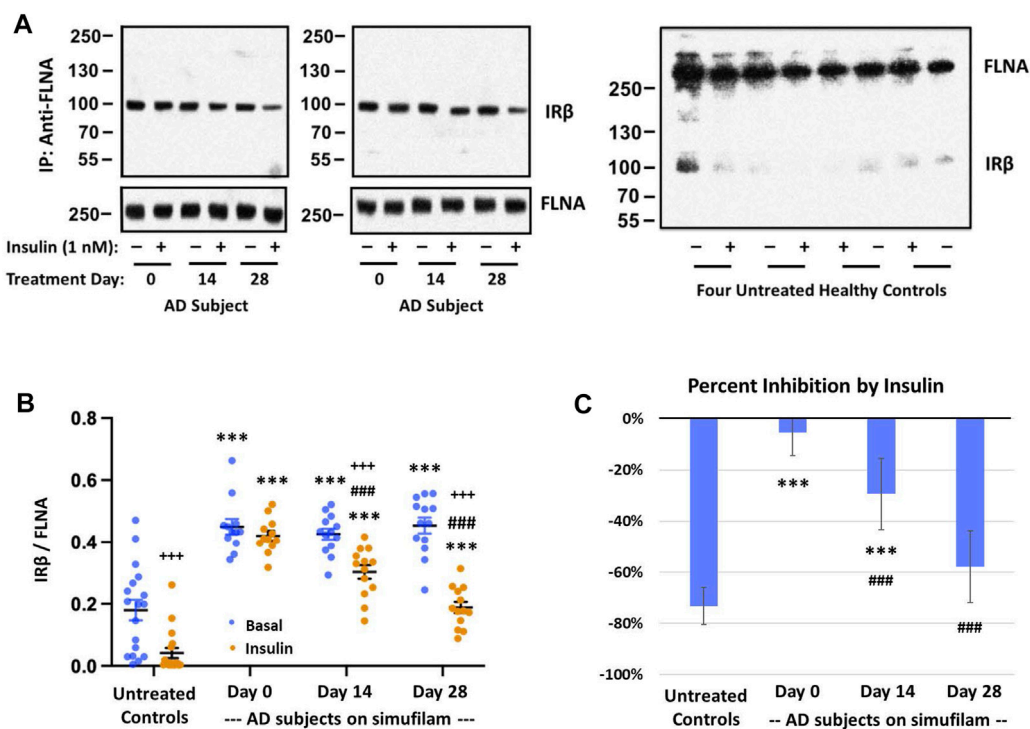


FIGURE 4

Simufilam treatment restores the insulin-stimulated reduction in FLNA linkage to insulin receptor beta (IR β). Representative blot images from two AD and four healthy control subjects (A) show higher levels of the FLNA–IR β interaction and impaired dissociation of this linkage upon insulin stimulation in AD subjects versus healthy controls. Simufilam treatment improved the insulin-stimulated dissociation of FLNA–IR β interaction. Blots were analyzed by densitometric quantitation (B). Percent inhibition by insulin in AD subjects improved dramatically with simufilam treatment (C). Data are means \pm SEM. $N = 13$ for AD, 18 for control. *** $p < 0.001$ vs. respective value in healthy control by two-sided two-sample t -test; ### $p < 0.001$ vs. respective AD value at Day 0 by two-sided paired t -test; +++ $p < 0.001$ insulin vs. basal value at respective timepoint by two-sided paired t -test.

of IR β linked to FLNA were not different between groups and were also not affected by simufilam or A β_{42} incubation.

Discussion

Simufilam is an AD drug candidate that disrupts an upstream pathogenic pathway that hyperphosphorylates tau, prior to the aggregation and deposition of tau or amyloid, as well as a separate neuroinflammatory pathway (Wang et al., 2012; Burns and Wang, 2017; Wang et al., 2017; Wang et al., 2020; Burns et al., 2023). We now show that oral simufilam reduces overactive mTOR signaling in AD lymphocytes, with stronger effects with longer treatment. We found that the interaction of simufilam's target, FLNA, with the IR β subunit of insulin receptors is elevated in AD lymphocytes. This interaction is reduced upon insulin stimulation, but this dissociation by insulin is impaired in AD lymphocytes. Although simufilam did not reduce the high levels of FLNA–IR β , it markedly improved insulin's ability to un-link FLNA from IR β , potentially allowing IR β to recruit IRS-1 to initiate signaling. Suggesting another possible mechanism, simufilam oral treatment restored FLNA's normal linkage to the mTOR suppressor PTEN in AD lymphocytes. We hypothesize that the effects of simufilam on multiple disease-associated signaling pathways are mediated by reversing an altered conformation of FLNA. We further

hypothesize that an altered conformation in AD leads to the hyperphosphorylation of FLNA at S²¹⁵² in AD lymphocytes, which was also reduced by simufilam. Implying translation to brain, *ex vivo* incubation with simufilam significantly reduced the high levels of pS²¹⁵²FLNA in postmortem AD and amnesic MCI brain tissue.

Overactive mTOR and its resistance to insulin stimulation are considered pathological features of AD that represent insulin resistance independent of type-2 diabetes (Oddo, 2012; Norambuena et al., 2017), along with impaired insulin receptor function in AD postmortem brain (Talbot et al., 2012). Simufilam's reduction of overactive mTOR and improvement to mTOR stimulation by insulin, detected across five mTORC1 and mTORC2 signaling components, is another mechanistic benefit of this therapeutic drug candidate. For mTORC1 and mTORC2 signaling, the elevated basal levels in AD lymphocytes prior to simufilam treatment were comparable to insulin-stimulated levels in healthy controls, leaving little room for further stimulation by insulin. The elevated basal activity of mTORC1's downstream kinase p70S6K, however, was markedly below the insulin-stimulated level of healthy control lymphocytes, and its weak stimulation by insulin did not approach that of healthy controls. Simufilam both suppressed p70S6K basal levels and improved its stimulation by insulin, in fact, to a level higher than insulin-stimulated healthy controls. Similar patterns were shown for pT¹¹³⁵Rictor and Akt1, both phosphorylated by

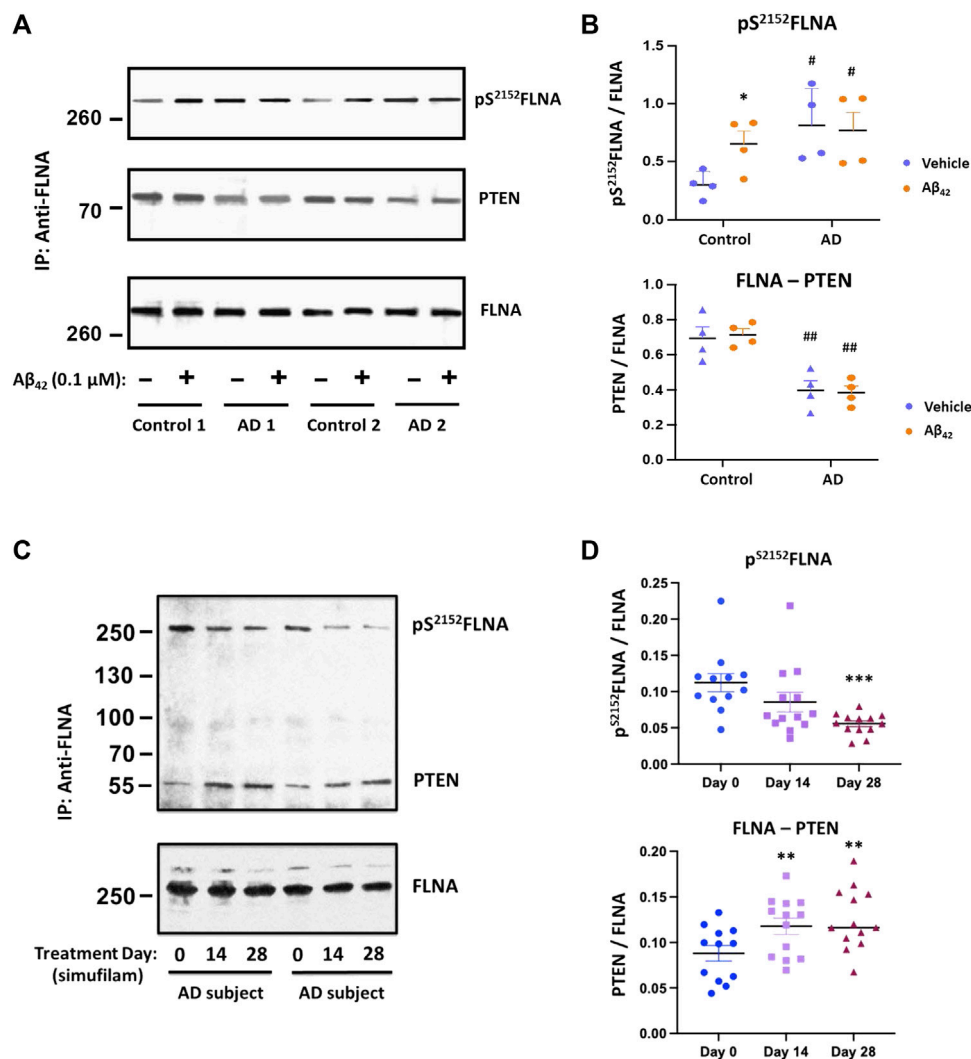


FIGURE 5

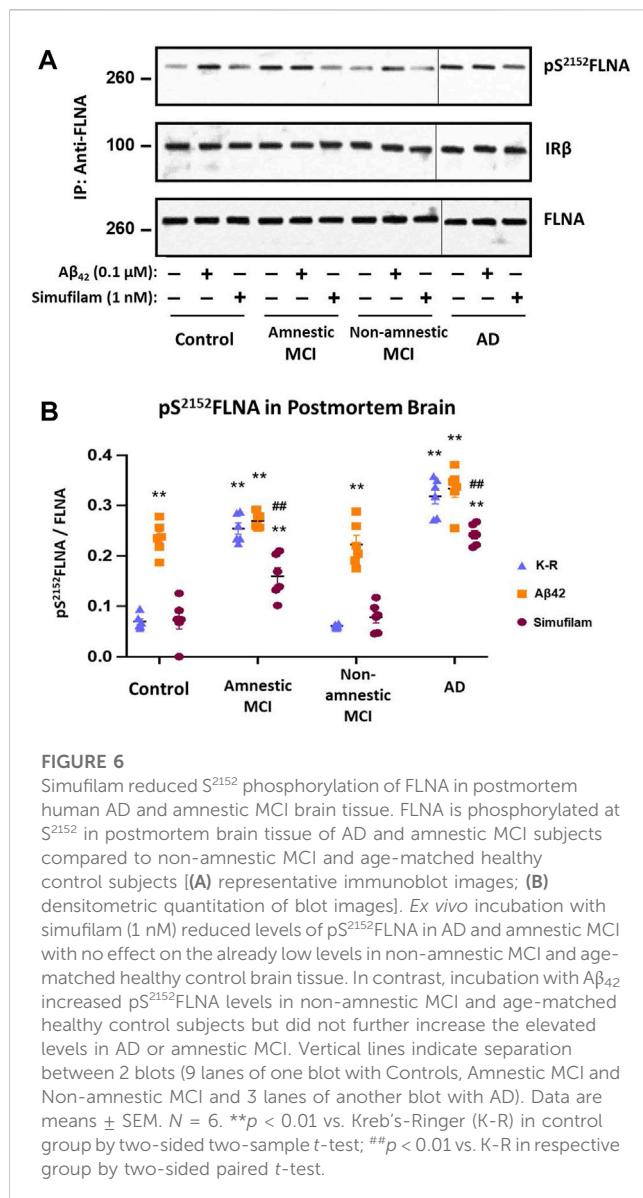
Elevated pS²¹⁵²FLNA and reduced FLNA–PTEN linkage in lymphocytes of AD subjects were improved by oral simufilam. Increased levels of FLNA phosphorylation at S²¹⁵² were coincident with a reduced FLNA–PTEN linkage in AD versus age-matched control lymphocytes. Exogenous Aβ₄₂ increased S²¹⁵²FLNA to AD-like levels but did not reduce the FLNA–PTEN linkage in control lymphocytes. Aβ₄₂ had no further effect on AD lymphocytes. [(A) representative blot images; (B) densitometric quantitation of blot images]. Oral simufilam to AD subjects reduced the high levels of S²¹⁵²FLNA and improved PTEN tethering to FLNA in their lymphocytes [(C) representative blot images; (D) densitometric quantitation of blot images]. Data are means ± SEM. *N* = 4 for AD and age-matched healthy control (A,B), and *N* = 13 for AD patients treated with simufilam (C,D). **p* < 0.05 vs. vehicle by two-sided paired *t*-test (B); #*p* < 0.05, ##*p* < 0.01 vs. control by two-sided two-sample *t*-test (B); ****p* < 0.001, ***p* < 0.01 vs. Day 0 by two-sided paired *t*-test (D).

mTORC2. These findings show that the effect of simufilam is not just a suppression of overactive basal levels but also includes a lessening of mTOR's insulin resistance. The effect of simufilam to reduce overactivation of both mTORC1 and mTORC2 signaling molecules and improve their stimulation by insulin suggests that simufilam may lessen mTOR's contribution to AD pathology. In addition to improving insulin resistance of these mTOR parameters, simufilam has improved insulin receptor signaling both in postmortem AD brain and in AD mouse models, although not to normal levels (Wang et al., 2012; Wang et al., 2017).

The differences in mTOR activity induced by simufilam or insulin were not due to changes in mTOR association with either Raptor in mTORC1 or Rictor in mTORC2, because neither insulin

nor simufilam treatment affected the levels of Raptor/Rictor association with mTOR. However, it is possible that the reduced Raptor (but not Rictor) association with mTOR in healthy control versus AD lymphocytes might indicate that different downstream signaling pathways for mTORC1 are prominent in the diseased versus normal lymphocytes, because differential binding of Raptor/Rictor to mTORC1/2 can affect substrate specificity for mTOR (Hay and Sonenberg, 2004; Su and Jacinto, 2011).

The absence of significant differences in mTOR parameters in lymphocytes of healthy control subjects in different age ranges, allowing for their combination into one control group, was unexpected, despite their small size (*n* = 6). However, the role of mTOR in aging has been demonstrated only in flies, worms and mice



without substantial variations in diet, exercise, epigenetics and other factors (Johnson et al., 2013). The within-group variability in each age range of healthy control subjects suggests that besides disease, other factors may more strongly influence mTOR signaling than age itself.

The higher levels of FLNA linkage to IRβ of the insulin receptor in AD versus healthy control lymphocytes and the impaired response to insulin in reducing that FLNA—IRβ linkage in AD lymphocytes may also reflect insulin receptor dysfunction, as occurs in AD brain (Talbot et al., 2012). A plausible explanation for the dissociation of IRβ from FLNA upon insulin stimulation is that it may free IRβ to initiate signaling by linking to IRS-1, the signaling adaptor molecule that integrates downstream insulin receptor signaling cascades (Shaw, 2011). In support of this possibility, our unpublished data show minimal linkage of FLNA with IRS-1 in postmortem control brain. Interestingly, in A7 cells that overexpress FLNA, blocking the FLNA—IR linkage by ectopic expression of a C-terminal FLNA fragment blocked the MAPK cascade of the insulin receptor (He et al., 2003). In contrast to

lymphocytes, there were no differences in FLNA—IRβ linkage in postmortem brain tissue between control, amnesic MCI, non-amnesic MCI and AD, nor was this linkage affected by exogenous Aβ₄₂. The fact that FLNA—IRβ levels are comparable in control and AD brain but strikingly different in AD and control lymphocytes illustrates that this protein interaction and its disease influence varies by cell type or tissue, as is the case with mTORC2 (Knudsen et al., 2020). In healthy control but not AD lymphocytes, insulin reduced this FLNA—IRβ linkage, and simufilam treatment improved insulin's ability to dissociate FLNA from IRβ in AD lymphocytes. The improved insulin-mediated FLNA—IRβ dissociation in AD lymphocytes by simufilam echoes simufilam's improvement in IR signaling in postmortem AD brain and in AD mouse models (Wang et al., 2012; Wang et al., 2017). Together, the restored insulin-stimulated FLNA—IRβ dissociation and the restored responsiveness of mTOR to insulin show a coordinated improvement in insulin sensitivity in AD patient lymphocytes following simufilam.

The beneficial effects on mTOR signaling may be related to simufilam's mechanism of action of reversing an altered conformation of FLNA that occurs in AD brain, implied by a shift in isoelectric focusing point (Wang et al., 2017; Wang et al., 2020). We previously demonstrated that FLNA in AD brain and lymphocytes aberrantly links to α7AChR and to TLR4, and these aberrant protein interactions (and resulting pathologies) are disrupted by simufilam and induced by Aβ₄₂ (Wang et al., 2012; Wang et al., 2017; Wang et al., 2020). Because the shift in isoelectric focusing point is unaffected by complete dephosphorylation, an altered conformation is the most likely explanation for this shift (Wang et al., 2017). FLNA's hyperphosphorylation at S²¹⁵² in AD brain and lymphocytes may be a consequence of the altered shape, especially as it was reduced by simufilam (*ex vivo* incubation of postmortem brain tissue or oral administration for lymphocytes). The fact that pS²¹⁵²FLNA levels are elevated by incubation with exogenous Aβ₄₂ indicates that soluble Aβ₄₂ in AD brain or lymphocytes (Meng et al., 2019) can activate kinase(s) such as mTOR (Shaw, 2011) to phosphorylate FLNA. Simufilam facilitates dephosphorylation of pS²¹⁵²FLNA and prevents further phosphorylation, perhaps by restoring FLNA's native shape.

The reduction in pS²¹⁵²FLNA by simufilam in lymphocytes following oral treatment and in postmortem brain tissue incubated *ex vivo* suggests that treatment effects in lymphocytes might mirror those in brains of AD subjects, but the significance of pS²¹⁵²FLNA is not fully clear. pS²¹⁵²FLNA has been implicated in FLNA—integrin interactions and their role in focal adhesion formation and cell migration of cancer cells (Sato et al., 2016). Phosphorylation of FLNA at S²¹⁵² was shown to occur by mTOR (Sato et al., 2016) and by IGF-1 in cancer cells (Ravid et al., 2008). Upon T cell receptor activation, the kinase Ndr2 phosphorylates FLNA at S²¹⁵², causing FLNA to dissociate from the inactive conformation of an integrin so that other proteins can stabilize this integrin's active conformation (Waltdt et al., 2018). pS²¹⁵²FLNA has also been shown to block the anti-tumoral signaling of the somatostatin subtype 2 receptor, thereby exacerbating pituitary cancer (Peverelli et al., 2018). Importantly, simufilam reduced pS²¹⁵²FLNA in human pituitary tumor cells and enhanced somatostatin subtype 2 receptor signaling (Marra et al., 2023). Elevated pS²¹⁵²FLNA is also associated with poor prognosis and

high-metastatic liver cancer (Xing et al., 2019). Overall, elevated pS²¹⁵²FLNA appears to be pathological, and we propose that it is related to an altered conformation and altered protein interactions of FLNA in AD.

The reduced PTEN—FLNA interaction in AD lymphocytes may be another consequence of altered FLNA. We hypothesize that the disruption of the FLNA—PTEN interaction in AD lymphocytes, and presumably also in brain, may impair PTEN's negative regulation of the mTOR pathway, contributing to the overactive mTOR signaling in AD. Simufilam's reduction of pS²¹⁵²FLNA and improved FLNA—PTEN linkage in lymphocytes of AD subjects supports this theory. AD-related changes to FLNA, both in conformation and phosphorylation (at S²¹⁵² and potentially other sites) may impact multiple protein interactions of FLNA, including the reduced interaction with PTEN shown here in AD brain and lymphocytes. Their reversal by simufilam, which shifts the majority of FLNA in AD back to its native state (Wang et al., 2017; Wang et al., 2020), also suggests the reduced PTEN tethering to FLNA and FLNA's hyperphosphorylation in AD are consequences of an altered conformation of FLNA. However, whether the restored PTEN tethering directly dephosphorylates pS²¹⁵²FLNA requires further research.

With important implications for AD, mTOR signaling is known to regulate synaptic plasticity and long-term potentiation (LTP), affecting memory formation (Lipton and Sahin, 2014; Bockaert and Marin, 2015). Long-term fear memory mediated by medial prefrontal cortex in rat has been shown to require mTOR activation, and LTP induction by high-frequency stimulation activates mTOR and p70S6K (Sui et al., 2008). Additionally, direct administration of PI3K inhibitors together with rapamycin into the medial prefrontal cortex suppressed both induced LTP and long-term fear memory (Sui et al., 2008). These findings imply that improved mTOR signaling may benefit synaptic plasticity and memory in AD patients.

Conclusion

The suppression of overactive mTOR signaling and its improved responsiveness to insulin represents a mechanistic benefit of simufilam beyond the disruption of pathogenic signaling pathways of soluble amyloid. These improvements in mTOR signaling may similarly result from reversing an altered conformation of FLNA, here allowing insulin to dissociate FLNA's linkage to the insulin receptor and initiate signaling. Further, restoring PTEN tethering to FLNA may allow PTEN to regulate mTOR. Although this work relied on lymphocytes from AD subjects before and after treatment with simufilam compared to healthy control lymphocytes, these treatment effects shown in lymphocytes likely translate to mTOR in brain and other tissues, as evidenced by simufilam's reduction of FLNA hyperphosphorylation in postmortem human AD brain. Because mTOR contributes to age-related cellular changes, simufilam's suppression of mTOR overactivation concurrent with improved insulin sensitivity may slow certain aging processes and attenuate this pathological feature of AD, potentially benefiting brain function and memory in AD and in aging.

Data availability statement

The datasets presented in this article are not readily available because the subject-level research data will not be shared. Requests to access the datasets should be directed to Eric Schoen, eschoen@cassavasciences.com.

Ethics statement

The studies involving human participants were reviewed and approved by the Advarra IRB and Quorum IRB (three separate protocols). The patients/participants provided their written informed consent to participate in this study.

Author contributions

H-YW and LB designed the experiments and wrote the manuscript. H-YW, ZP, and K-CL conducted experiments. NF oversaw clinical trial design. BN, TD, and JP were investigators in the clinical trial protocols. All authors contributed to the article and approved the submitted version.

Funding

The clinical trial in AD subjects was funded by NIA grant award AG060878.

Acknowledgments

We sincerely thank the National Institute on Aging (NIA) for their support of our work in AD. We thank the subjects and caregivers who participated in the clinical trial of simufilam and the healthy volunteers who provided blood samples.

Conflict of interest

This basic research was supported in part by supplies and funding from Cassava Sciences, Inc. LB is an employee and shareholder of Cassava Sciences, as was the late NF. H-YW is an employee of City University of New York School of Medicine, is a long-time consultant and scientific advisor to Cassava Sciences, owns an insignificant financial interest (less than ½ of 1%) in the equity of Cassava Sciences, and has consulted to various pharmaceutical companies over the past 20 years. LB and H-YW are inventors on simufilam patents. None of the authors are due patent royalties. This basic research was conducted in non-GCP compliant facilities. ZP and K-CL are employees of City University of New York School of Medicine. BN, TD, and JP are investigators in the clinical trial protocols. Author BN is employed by IMIC, Inc. Authors TD and JP are employed by Cognitive Clinical Trials.

Publisher's note

All claims expressed in this article are solely those of the authors and do not necessarily represent those of their affiliated

References

- Bloom, G., Lazod, J., and Norambuena, A. (2018). Reduced brain insulin signaling: A seminal process in Alzheimer's disease pathogenesis. *Neuropharmacology* 136, 192–195. doi:10.1016/j.neuropharm.2017.09.016
- Bockaert, J., and Marin, P. (2015). mTOR in brain physiology and pathologies. *Physiol. Rev.* 95, 1157–1187. doi:10.1152/physrev.00038.2014
- Burns, L. H., Pei, Z., and Wang, H. Y. (2023). Targeting $\alpha 7$ nicotinic acetylcholine receptors and their protein interactions in Alzheimer's disease drug development. *Drug Dev. Res.* 2023, 22085. doi:10.1002/ddr.22085
- Burns, L. H., and Wang, H.-Y. (2017). Altered filamin A enables amyloid beta-induced tau hyperphosphorylation and neuroinflammation in Alzheimer's disease. *Neuroimmunol. Neuroinflammation* 4, 263–271. doi:10.20517/2347-8659.2017.50
- Caccamo, A., Magri, A., Medina, D., Wisely, E., Lopez-Aranda, M., Silva, A., et al. (2013). mTOR regulates tau phosphorylation and degradation: implications for Alzheimer's disease and other tauopathies. *Aging Cell* 12, 370–380. doi:10.1111/accel.12057
- Caccamo, A., Majumder, S., Richardson, A., Strong, R., and Oddo, S. (2010). Molecular interplay between mammalian target of rapamycin (mTOR), amyloid-beta, and tau: Effects on cognitive impairments. *J. Biol. Chem.* 285, 13107–13120. doi:10.1074/jbc.M110.100420
- Caccamo, A., Maldonado, M., Majumder, S., Medina, D., Holbein, W., Magri, A., et al. (2011). Naturally secreted amyloid-beta increases mammalian target of rapamycin (mTOR) activity via a PRAS40-mediated mechanism. *J. Biol. Chem.* 286, 8924–8932. doi:10.1074/jbc.M110.180638
- Cai, Z., Chen, G., He, W., Xiao, M., and Yan, L.-J. (2015). Activation of mTOR: A culprit of Alzheimer's disease? *Neuropsychiatr. Dis. Treat.* 11, 1015–1030. doi:10.2147/NDT.S75717
- Cai, Z., Zhao, B., Li, K., Zhang, L., Li, C., Quazi, S., et al. (2012). Mammalian target of rapamycin: A valid therapeutic target through the autophagy pathway for alzheimer's disease? *J. Neurosci. Res.* 90, 1105–1118. doi:10.1002/jnr.23011
- Dineley, K., Bell, K., Bui, D., and Sweatt, J. (2002). Beta -Amyloid peptide activates alpha 7 nicotinic acetylcholine receptors expressed in *Xenopus* oocytes. *J. Biol. Chem.* 277, 25056–25061. doi:10.1074/jbc.M200066200
- Fingar, D., Richardson, C., Tee, A., Cheatham, L., Tsou, C., and Blenis, J. (2004). mTOR controls cell cycle progression through its cell growth effectors S6K1 and 4E-BP1/eukaryotic translation initiation factor 4E. *Mol. Cell Biol.* 24, 200–216. doi:10.1128/MCB.24.1.200-216.2004
- Georgescu, M. (2010). PTEN tumor suppressor network in PI3K-Akt pathway control. *Genes Cancer* 1, 1170–1177. doi:10.1177/1947601911407325
- Griffin, R. J., Moloney, A., Kelliher, M., Johnston, J. A., Ravid, R., Dockery, P., et al. (2005). Activation of Akt/PKB, increased phosphorylation of Akt substrates and loss and altered distribution of Akt and PTEN are features of Alzheimer's disease pathology. *J. Neurochem.* 93 (1), 105–117. doi:10.1111/j.1471-4159.2004.02949.x
- Guo, L., Tian, J., and Du, H. (2017). Mitochondrial dysfunction and synaptic transmission failure in Alzheimer's disease. *J. Alzheimers Dis.* 57, 1071–1086. doi:10.3233/JAD-160702
- Harrison, D., Strong, R., Sharp, Z., Nelson, J., Astle, C., Flurkey, K., et al. (2009). Rapamycin fed late in life extends lifespan in genetically heterogeneous mice. *Nature* 460, 392–395. doi:10.1038/nature08221
- Hay, N., and Sonenberg, N. (2004). Upstream and downstream of mTOR. *Genes Dev.* 18, 1926–1945. doi:10.1101/gad.1212704
- He, H. J., Kole, S., Kwon, Y. K., Crow, M. T., and Bernier, M. (2003). Interaction of filamin A with the insulin receptor alters insulin-dependent activation of the mitogen-activated protein kinase pathway. *J. Biol. Chem.* 278 (29), 27096–27104. doi:10.1074/jbc.M301003200
- Johnson, S. C., Rabinovitch, P. S., and Kaeblerlein, M. (2013). mTOR is a key modulator of ageing and age-related disease. *Nature* 493 (7432), 338–345. doi:10.1038/nature11861
- Julien, L.-A., Carriere, A., Moreau, J., and Roux, P. (2010). mTORC1-activated S6K1 phosphorylates Rictor on threonine 1135 and regulates mTORC2 signaling. *Mol. Cell Biol.* 30, 908–921. doi:10.1128/MCB.00601-09
- Khamzina, L., Veilleux, A., Bergeron, S., and Marette, A. (2005). Increased activation of the mammalian target of rapamycin pathway in liver and skeletal muscle of obese rats: Possible involvement in obesity-linked insulin resistance. *Endocrinology* 146 (3), 1473–1481. doi:10.1210/en.2004-0921
- Kim, Y. C., and Guan, K. L. (2015). mTOR: a pharmacologic target for autophagy regulation. *J. Clin. Invest.* 125 (1), 25–32. doi:10.1172/JCI73939
- Knudsen, J. R., Fritzen, A. M., James, D. E., Jensen, T. E., Kleinert, M., and Richter, E. A. (2020). Growth factor-dependent and-independent activation of mTORC2. *Trends Endocrinol. Metab.* 31 (1), 13–24. doi:10.1016/j.tem.2019.09.005
- Laplanche, M., and Sabatini, D. (2012). mTOR signaling in growth control and disease. *Cell* 149, 274–293. doi:10.1016/j.cell.2012.03.017
- Lipton, J., and Sahin, M. (2014). The neurology of mTOR. *Neuron* 84, 275–291. doi:10.1016/j.neuron.2014.09.034
- Liu, G., and Sabatini, D. (2020). mTOR at the nexus of nutrition, growth, ageing and disease. *Nat. Rev. Mol. Cell Biol.* 21, 183–203. doi:10.1038/s41580-019-0199-y
- Majd, S., and Power, J. H. T. (2018). Oxidative stress and decreased mitochondrial superoxide dismutase 2 and peroxiredoxins 1 and 4 based mechanism of concurrent activation of AMPK and mTOR in alzheimer's disease. *Curr. Alzheimer Res.* 15 (8), 764–776. doi:10.2174/1567205015666180223093020
- Majumder, S., Richardson, A., Strong, R., and Oddo, S. (2011). Inducing autophagy by rapamycin before, but not after, the formation of plaques and tangles ameliorates cognitive deficits. *PLoS One* 6, e25416. doi:10.1371/journal.pone.0025416
- Marra, G., Treppiedi, D., Di Muro, G., Mangili, F., Catalano, R., Esposito, E., et al. (2023). A novel filamin A-binding molecule may significantly enhance somatostatin receptor type 2 antitumoral actions in growth hormone-secreting PitNET cells. *25th European Congress of Endocrinology*. Istanbul, Turkey. doi:10.1530/endoabs.90.OC7.5
- Meng, X., Li, T., Wang, X., Lv, X., Sun, Z., Zhang, J., et al. (2019). Association between increased levels of amyloid- β oligomers in plasma and episodic memory loss in Alzheimer's disease. *Alzheimers Res. Ther.* 11 (1), 89. doi:10.1186/s13195-019-0535-7
- Miller, R., Harrison, D., Astle, C., Fernandez, E., Flurkey, K., Han, M., et al. (2014). Rapamycin-mediated lifespan increase in mice is dose and sex dependent and metabolically distinct from dietary restriction. *Aging Cell* 13, 468–477. doi:10.1111/accel.12194
- Nagele, R., D'Andrea, M., Anderson, W., and Wang, H.-Y. (2002). Intracellular accumulation of beta-amyloid(1-42) in neurons is facilitated by the alpha 7 nicotinic acetylcholine receptor in Alzheimer's disease. *Neuroscience* 110, 199–211. doi:10.1016/s0306-4522(01)00460-2
- Nakamura, F., Stossel, T., and Hartwig, J. (2011). The filamins: Organizers of cell structure and function. *Cell Adh. Migr.* 5, 160–169. doi:10.4161/cam.5.2.14401
- Norambuena, A., Wallrabe, H., McMahon, L., Silva, A., Swanson, E., Khan, S., et al. (2017). mTOR and neuronal cell cycle re-entry: How impaired brain insulin signaling promotes Alzheimer's disease. *Alzheimers Dement.* 13, 152–167. doi:10.1016/j.jalz.2016.08.015
- Oddo, S. (2012). The role of mTOR signaling in Alzheimer disease. *Front. Biosci. Sch. Ed.* 4, 941–952. doi:10.2741/s310
- Paccalin, M., Pain-Barc, S., Pluchon, C., Paul, C., Besson, M., Carret-Rebillat, A., et al. (2006). Activated mTOR and PKR kinases in lymphocytes correlate with memory and cognitive decline in Alzheimer's disease. *Dement. Geriatr. Cogn. Disord.* 22, 320–326. doi:10.1159/000095562
- Perluigi, M., Di Domenico, F., and Butterfield, D. (2015). mTOR signaling in aging and neurodegeneration: At the crossroad between metabolism dysfunction and impairment of autophagy. *Neurobiol. Dis.* 84, 39–49. doi:10.1016/j.nbd.2015.03.014
- Peeverelli, E., Giardino, E., Mangili, F., Treppiedi, D., Catalano, R., Ferrante, E., et al. (2018). cAMP/PKA-induced filamin A (FLNA) phosphorylation inhibits SST2 signal transduction in GH-secreting pituitary tumor cells. *Cancer Lett.* 435, 101–109. doi:10.1016/j.canlet.2018.08.002
- Ravid, D., Chuderland, D., Landsman, L., Lavie, Y., Reich, R., and Liscovitch, M. (2008). Filamin A is a novel caveolin-1-dependent target in IGF-I-stimulated cancer cell migration. *Exp. Cell Res.* 314 (15), 2762–2773. doi:10.1016/j.yexcr.2008.06.004
- Rosner, M., Hanneder, M., Siegel, N., Valli, A., Fuchs, C., and Hengstschläger, M. (2008). The mTOR pathway and its role in human genetic diseases. *Mutat. Res.* 659, 284–292. doi:10.1016/j.mmrrev.2008.06.001
- Sarbassov, D. D., Guertin, D. A., Ali, S. M., and Sabatini, D. M. (2005). Phosphorylation and regulation of Akt/PKB by the rictor-mTOR complex. *Science* 307 (5712), 1098–1101. doi:10.1126/science.1106148

- Sato, T., Ishii, J., Ota, Y., Sasaki, E., Shibagaki, Y., and Hattori, S. (2016). Mammalian target of rapamycin (mTOR) complex 2 regulates filamin A-dependent focal adhesion dynamics and cell migration. *Genes cells* 21 (6), 579–593. doi:10.1111/gtc.12366
- Saxton, R. A., and Sabatini, D. M. (2017). mTOR signaling in growth, metabolism, and disease. *Cell* 168 (6), 361–371. doi:10.1016/j.cell.2017.03.035
- Shaw, L. (2011). The insulin receptor substrate (IRS) proteins: At the intersection of metabolism and cancer. *Cell Cycle* 10, 1750–1756. doi:10.4161/cc.10.11.15824
- Su, B., and Jacinto, E. (2011). Mammalian TOR signaling to the AGC kinases. *Crit. Rev. Biochem. Mol. Biol.* 46, 527–547. doi:10.3109/10409238.2011.618113
- Sui, L., Wang, J., and Li, B. (2008). Role of the phosphoinositide 3 kinase-Akt-mammalian target of the rapamycin signaling pathway in long-term potentiation and trace fear conditioning memory in rat medial prefrontal cortex. *Learn Mem.* 15, 762–776. doi:10.1101/lm.1067808
- Switon, K., Kotulska, K., Janusz-Kaminska, A., Zmorzynska, J., and Jaworski, J. (2017). Molecular neurobiology of mTOR. *Neuroscience* 341, 112–153. doi:10.1016/j.neuroscience.2016.11.017
- Szwed, A., Kim, E., and Jacinto, E. (2021). Regulation and metabolic functions of mTORC1 and mTORC2. *Physiol. Rev.* 101 (3), 1371–1426. doi:10.1152/physrev.00026.2020
- Talbot, K., Wang, H., Kazi, H., Han, L., Bakshi, K., Stucky, A., et al. (2012). Demonstrated brain insulin resistance in Alzheimer's disease patients is associated with IGF-1 resistance, IRS-1 dysregulation, and cognitive decline. *J. Clin. Invest.* 122, 1316–1338. doi:10.1172/JCI59903
- Tang, Z., Ioja, E., Bereczki, E., Hultenby, K., Li, C., Guan, Z., et al. (2015). mTor mediates tau localization and secretion: Implication for Alzheimer's disease. *Biochim. Biophys. Acta* 1853 (7), 1646–1657. doi:10.1016/j.bbamcr.2015.03.003
- Waldt, N., Seifert, A., Demiray, Y. E., Devroe, E., Turk, B. E., Reichardt, P., et al. (2018). Filamin A phosphorylation at serine 2152 by the serine/threonine kinase Ndr2 controls TCR-induced LFA-1 activation in T cells. *Front. Immunol.* 9, 2852. doi:10.3389/fimmu.2018.02852
- Wang, H.-Y., Bakshi, K., Frankfurt, M., Stucky, A., Goberdhan, M., Shah, S., et al. (2012). Reducing amyloid-related Alzheimer's disease pathogenesis by a small molecule targeting filamin A. *J. Neurosci.* 32, 9773–9784. doi:10.1523/JNEUROSCI.0354-12.2012
- Wang, H.-Y., Lee, K.-C., Pei, Z., Khan, A., Bakshi, K., and Burns, L. (2017). PTI-125 binds and reverses an altered conformation of filamin A to reduce Alzheimer's disease pathogenesis. *Neurobiol. Aging* 55, 99–114. doi:10.1016/j.neurobiolaging.2017.03.016
- Wang, H.-Y., Li, W., Benedetti, N., and Lee, D. (2003). Alpha 7 nicotinic acetylcholine receptors mediate beta-amyloid peptide-induced tau protein phosphorylation. *J. Biol. Chem.* 278, 31547–31553. doi:10.1074/jbc.M212532200
- Wang, H.-Y., Pei, Z., Lee K.-C., K.-C., Lopez-Brignoni, E., Nikolov, B., Crowley, C., et al. (2020). PTI-125 reduces biomarkers of Alzheimer's disease in patients. *J. Prev. Alzheimer's Dis.* 7, 256–264. doi:10.14283/jpad.2020.6
- Xie, J., and Proud, C. G. (2013). Crosstalk between mTOR complexes. *Nat. Cell Biol.* 15 (11), 1263–1265. doi:10.1038/ncb2877
- Xing, X., Yuan, H., Sun, Y., Ke, K., Dong, X., Chen, H., et al. (2019). ANXA2(Tyr23) and FLNA(Ser2152) phosphorylation associate with poor prognosis in hepatic carcinoma revealed by quantitative phosphoproteomics analysis. *J. Proteomics* 200, 111–122. doi:10.1016/j.jprot.2019.03.017
- Yoon, M. S. (2017). The role of mammalian target of rapamycin (mTOR) in insulin signaling. *Nutrients* 9 (11), 1176. doi:10.3390/nu9111176



OPEN ACCESS

APPROVED BY
Frontiers Editorial Office,
Frontiers Media SA, Switzerland

*CORRESPONDENCE
Frontiers Editorial Office,
✉ research.integrity@frontiersin.org

RECEIVED 19 August 2024
ACCEPTED 19 August 2024
PUBLISHED 22 August 2024

CITATION

Frontiers Editorial Office (2024) Expression of concern: Simufilam suppresses overactive mTOR and restores its sensitivity to insulin in Alzheimer's disease patient lymphocytes. *Front. Aging* 5:1483030. doi: 10.3389/fragi.2024.1483030

COPYRIGHT

© 2024 Frontiers Editorial Office. This is an open-access article distributed under the terms of the [Creative Commons Attribution License \(CC BY\)](#). The use, distribution or reproduction in other forums is permitted, provided the original author(s) and the copyright owner(s) are credited and that the original publication in this journal is cited, in accordance with accepted academic practice. No use, distribution or reproduction is permitted which does not comply with these terms.

Expression of concern: Simufilam suppresses overactive mTOR and restores its sensitivity to insulin in Alzheimer's disease patient lymphocytes

Frontiers Editorial Office*

An Expression of Concern on

Simufilam suppresses overactive mTOR and restores its sensitivity to insulin in Alzheimer's disease patient lymphocytes

by Wang H-Y, Pei Z, Lee K-C, Nikolov B, Doehtner T, Puente J, Friedmann N and Burns LH (2023). *Front. Aging* 4:1175601. doi: [10.3389/fragi.2023.1175601](https://doi.org/10.3389/fragi.2023.1175601)

With this notice, Frontiers states its awareness of concerns regarding the images for “Simufilam suppresses overactive mTOR and restores its sensitivity to insulin in Alzheimer's disease patient lymphocytes” published on the 29th of June 2023. An investigation is currently being conducted in accordance with COPE guidelines. This notice will be updated as soon as the investigation is complete.



OPEN ACCESS

EDITED BY

Andréa Cristina Paula-Lima,
University of Chile, Chile

REVIEWED BY

Felipe Salech,
University of Chile, Chile
Cristal M. Hill,
University of Southern California,
United States

*CORRESPONDENCE

Katherine A. Collins,
✉ katherine.collins791@duke.edu

RECEIVED 27 April 2023

ACCEPTED 20 June 2023

PUBLISHED 30 June 2023

CITATION

Collins KA, Ambrosio F, Rogers RJ,
Lang W, Schelbert EB, Davis KK and
Jakicic JM (2023), Change in circulating
klotho in response to weight loss, with
and without exercise, in adults with
overweight or obesity.
Front. Aging 4:1213228.
doi: 10.3389/fragi.2023.1213228

COPYRIGHT

© 2023 Collins, Ambrosio, Rogers, Lang,
Schelbert, Davis and Jakicic. This is an
open-access article distributed under the
terms of the [Creative Commons
Attribution License \(CC BY\)](#). The use,
distribution or reproduction in other
forums is permitted, provided the original
author(s) and the copyright owner(s) are
credited and that the original publication
in this journal is cited, in accordance with
accepted academic practice. No use,
distribution or reproduction is permitted
which does not comply with these terms.

Change in circulating klotho in response to weight loss, with and without exercise, in adults with overweight or obesity

Katherine A. Collins^{1*}, Fabrisia Ambrosio^{2,3}, Renee J. Rogers⁴,
Wei Lang⁵, Eric B. Schelbert^{6,7}, Kelliann K. Davis⁸ and
John M. Jakicic⁴

¹Duke Molecular Physiology Institute, Duke University School of Medicine, Durham, NC, United States, ²Discovery Center for Musculoskeletal Recovery, Schoen Adams Research Institute at Spaulding, Boston, MA, United States, ³Department of Physical Medicine and Rehabilitation, Harvard Medical School, Boston, MA, United States, ⁴Department of Internal Medicine, University of Kansas Medical Center, Kansas City, KS, United States, ⁵Department of Aging Medicine and Center on Aging and Mobility, University Hospital Zurich and University of Zurich, Zurich, Switzerland, ⁶School of Medicine, University of Pittsburgh, Pittsburgh, PA, United States, ⁷Minneapolis Heart Institute East, Saint Paul, MN, United States, ⁸Department of Health and Human Development, University of Pittsburgh, Pittsburgh, PA, United States

Introduction: Klotho is a protein associated with protection from aging-related diseases and health conditions. Obesity is associated with lower Klotho concentrations. Thus, this secondary analysis of adults with obesity examined 1) the change in serum Klotho concentration in response to a behavioral weight loss intervention by the magnitude of weight loss achieved; and 2) the association among serum Klotho concentration and weight, body composition, and cardiorespiratory fitness.

Methods: Participants were randomized to either diet alone (DIET), diet plus 150 min of physical activity per week (DIET + PA150), or diet plus 250 min of physical activity per week (DIET + PA250). Participants [$n = 152$; age: 45.0 ± 7.9 years; body mass index (BMI): 32.4 ± 3.8 kg/m²] included in this secondary analysis provided blood samples at baseline, 6-, and 12 months, and were classified by weight loss response (Responder: achieved $\geq 10\%$ weight loss at 6 or 12 months; Non-responder: achieved $< 5\%$ weight loss at both 6 and 12 months). Serum Klotho was measured using a solid-phase sandwich enzyme-linked immunosorbent assay (ELISA). Analyses of covariance (ANCOVA's) were used to examine changes in weight, body composition, cardiorespiratory fitness, and Klotho concentration by weight loss response across the 12-month weight loss intervention.

Results: Responders had a greater reduction in measures of weight and body composition, and a greater increase in cardiorespiratory fitness, compared to Non-Responders ($p < 0.05$). Change in Klotho concentration differed between Responders and Non-Responders ($p < 0.05$), with the increase in Klotho concentration from baseline to 6 months for Responders being statistically significant. The 6-month change in Klotho concentration was inversely associated with the 6-month change in weight ($r_s = -0.195$), BMI ($r_s = -0.196$), fat mass ($r_s = -0.184$), and waist circumference ($r_s = -0.218$) (p -values < 0.05).

Discussion: Findings provide evidence within the context of a behavioral intervention, with and without exercise, that change in Klotho concentration is

significantly different between adults with weight loss $\geq 10\%$ compared to $< 5\%$ across 12 months. These findings suggest that weight loss and reduction in fat mass may be favorably associated with the change in Klotho concentration. This may reduce the risk of negative health consequences associated with accelerated aging in middle-aged adults.

KEYWORDS

aging, klotho, obesity, physical activity, weight loss

Introduction

Overweight and obesity are associated with major health risks and increased risk for premature death (Van Gaal et al., 2006; Hales et al., 2017). The current prevalence of obesity in the United States is approximately 41.9% (Stierman et al., 2021). Due to obesity's association with many chronic diseases such as cardiovascular disease, diabetes, and certain cancers, among others, the increased prevalence of obesity is of significant public health concern (Must et al., 1999; Vgontzas et al., 2000; Field et al., 2001; Mokdad et al., 2003; Wolk et al., 2003; Poirier et al., 2006). These health-related concerns of obesity may be a result of excess body weight affecting aging mechanisms through the maturation of adipose tissue, influencing inflammation and glucose homeostasis, oxidative stress, DNA damage, telomere dysfunction, and increased vasomotor tone and sympathetic drive (Seidell et al., 1992; Steinberg et al., 1996; Weinsier et al., 1998; He et al., 2001; Woo et al., 2004; Poirier et al., 2006; Ahima, 2009; Consitt et al., 2009; Galgani and Ravussin, 2009; Barton, 2010; Flegal et al., 2012; Hales et al., 2017). The accelerated aging processes that result from overweight and obesity may serve as a mechanistic pathway leading to the development of chronic diseases.

One biomarker, among others, that may provide insight into the accelerated aging process and accompany obesity is Klotho (Orces, 2022a; Orces, 2022b). Klotho is a protein shown to promote longevity and provide cardiovascular and neuroprotective effects (Arking et al., 2003; Wang and Sun, 2009; Semba et al., 2011; Razzaque, 2012; Semba et al., 2012; Drüeke and Massy, 2013; Avin et al., 2014; Di Bona et al., 2014; Semba et al., 2015; Xu and Sun, 2015; Hui et al., 2017). Circulating Klotho results from either direct secretion by the cell or from cleavage of the intracellular domain of the full-length protein by secretases (Drüeke and Massy, 2013). Cleavage of the intracellular domain of the full-length protein is performed by secretases—more specifically by α - β -secretase. Klotho is cleaved by α -secretases ADAM10 and 17 (A Disintegrin and Metalloprotease), as well as β -secretase BACE1 (Beta-Secretase 1). The remaining membrane-bound fragment is a substrate for regulated intramembrane proteolysis by γ -secretase (Bloch et al., 2009). Both of these processes lead to “soluble” or circulating Klotho, which is found in blood, urine, and cerebrospinal fluid (Matsumura et al., 1998; Wang and Sun, 2009; Drüeke and Massy, 2013). Higher concentrations of Klotho are associated with a slower aging process and fewer negative-health outcomes (Kuro-o et al., 1997; Kurosu et al., 2005; Xu and Sun, 2015). Evidence has shown Klotho to be lower in adults with obesity compared to their normal-weight counterparts (Amitani et al., 2013). This may suggest that treatment of overweight and obesity through weight loss may increase Klotho concentration, potentially counteracting the

accelerated aging effects of obesity. However, the influence of intentional weight loss on Klotho concentration among adults with overweight or obesity has not been well characterized.

Behavioral interventions—the use of principles and techniques to change a participant's behavior and habits (Wadden and Stunkard, 2002; Lang and Froelicher, 2006)—for weight loss are effective strategies for the treatment of overweight and obesity, with the majority of weight loss resulting from dietary changes via reduced energy intake (Dietary Guidelines Advisory Committee, 2015; Physical Activity Guidelines Advisory Committee, 2018; Heinicke and Halle, 2020). However, the addition of physical activity to dietary changes can enhance weight loss and result in additional health benefits compared to diet-induced weight loss alone (Webb and Wadden, 2017; Jakicic et al., 2018). The addition of physical activity to diet for weight loss may also have effects on Klotho concentration, as prior studies have shown an independent effect of physical activity increasing concentrations of Klotho (Avin et al., 2014). However, the effects of weight loss resulting from dietary changes alone or dietary changes in combination with physical activity have not been reported, warranting investigation.

The Heart Health Study aimed to examine the effect of a reduced calorie diet alone compared to diet in conjunction with one of two prescribed doses of physical activity on weight loss, measures of cardiac structure, and other cardiometabolic risk factors among adults with overweight or obesity (Jakicic et al., 2022). The Heart Health Study collected fasting blood samples, cardiorespiratory fitness, and body composition measures at baseline, 6 months, and 12 months during the weight loss intervention period. These data and blood samples were used to conduct this secondary analysis in a subsample of participants to examine: 1) the change in Klotho concentration in response a behavioral weight loss intervention by magnitude of weight loss achieved; and 2) the association among Klotho concentration and body weight, waist circumference, measures of body composition, and cardiorespiratory fitness.

Materials and methods

Study Design. In the Heart Health Study (ClinicalTrials.gov NCT01500356, recruitment occurred between December 2011 and June 2015), participants completed assessments prior to (baseline), during (6 months), and at the end of a 12-month behavioral weight loss intervention. Participants were randomized to one of three intervention groups: 1) DIET—diet alone; 2) DIET + PA150—diet combined with progression to 150 min per week of prescribed moderate-to-vigorous intensity physical activity (MVPA), or 3) DIET + PA250—diet combined with progression to 250 min per week of prescribed MVPA. As previously reported, randomization

was stratified by sex and race (white or nonwhite) in randomly selected block sizes (Jakicic et al., 2022). The Heart Health Study protocol was approved by the institutional review board at the University of Pittsburgh.

Participants. The protocol for participant recruitment has been previously reported (Jakicic et al., 2022). Eligibility criteria have previously been reported and included an age between 18 and 55 years and body mass index between 25 and $<40 \text{ kg/m}^2$ (Rogers et al., 2020). Exclusion criteria included 1) self-reporting $\geq 60 \text{ min/week}$ of structured MVPA 2) weight loss of $\geq 5\%$ within the prior 6 months or a history of bariatric surgery; 3) history of cardiometabolic disease, diabetes mellitus, or cancer; 4) taking medication that could affect heart rate or blood pressure; 5) taking medication that could influence body weight; 6) treatment for psychological conditions that included medication or counseling; 7) currently pregnant, pregnant within the prior 6 months, or planning a pregnancy within the next 12 months; 8) planning on geographical relocation outside of the region within 12 months; 9) inability to comply with the components of the interventions; or (10) had a contraindication that would prohibit cardiac magnetic resonance imaging scanning. Participants provided written informed consent and medical clearance from their physician prior to enrolling in this study.

Because Klotho is a blood biomarker, to be eligible for this secondary analysis the participant needed to have blood samples available for analysis from the baseline, 6-month, and 12-month assessment periods, along with other outcome measures of interest for these secondary analyses. Moreover, because the secondary analysis focused on examining potential differences for change in Klotho concentration at lower and higher magnitudes of weight loss, an *a priori* decision was made to only include participants in these secondary analyses if they achieved $\geq 10\%$ weight loss at both 6 months and 12 months (classified as a “responder”) or achieved $< 5\%$ weight loss at both 6 months and 12 months (classified as a “non-responder”).

Intervention. As previously described, participants were randomized into DIET, DIET + PA150, and DIET + PA250 intervention groups for a period of 12 months (Jakicic et al., 2022). Participants in all intervention groups were instructed to attend weekly weight loss group sessions for weeks 1–24. For weeks 25–52 participants were instructed to attend in-person intervention sessions approximately every other week and to also receive an individual brief telephone intervention approximately every other week. If a participant missed a group session, a brief individual make-up session was offered to allow the content to be shared with the participant.

DIET, DIET + PA150, and DIET + PA250 were prescribed the same diet to reduce energy intake to be between 1,200 and 1,800 kcal/day based on baseline body weight, and to reduce dietary fat intake to be between 20% and 30% of total daily energy intake (Jakicic et al., 2022). The intervention staff reviewed self-monitoring records of dietary intake and provided written feedback to the participants.

Randomization groups differed in their prescribed physical activity (Jakicic et al., 2022). DIET was instructed to maintain their current level of physical activity and was not provided a prescription to increase their physical activity. DIET + PA150 was prescribed a progression to 150 min/week of

unsupervised MVPA, whereas DIET + PA250 was prescribed a progression to 250 min/week of unsupervised MVPA.

Demographic Characteristics. Information on sex, race, and ethnicity were collected via questionnaire. Age was confirmed from the birth date listed on a government issued identification card (e.g., driver’s license or passport).

Height, Weight, and Body Mass Index. Weight and height were collected at baseline, 6 months, and 12 months (Rogers et al., 2020; Jakicic et al., 2022). Participants were clothed in a lightweight hospital gown and their shoes removed. Weight was assessed to the nearest 0.1 kg with duplicate measures differing by $\leq 0.2 \text{ kg}$ using a calibrated digital scale. Height was assessed to the nearest 0.1 cm with duplicate measures differing by $\leq 0.5 \text{ cm}$ using a wall-mounted stadiometer. Weight and height were used to calculate body mass index (BMI, kg/m^2).

Body Composition. Body composition measures were assessed prior to the start of the intervention, 6 months, and 12 months (Jakicic et al., 2022). Participants were clothed in a lightweight hospital gown and their shoes removed. Women completed a urine pregnancy test to confirm non-pregnancy prior to the measurement. Total body composition, including measures of fat mass, lean mass, and percent body fat, were measured using dual-energy x-ray absorptiometry (DXA, GE Lunar iDXA, Madison, WI). Waist circumference was measured horizontally in duplicate at the iliac crest.

Cardiorespiratory Fitness. Submaximal cardiopulmonary exercise tests were conducted on all participants prior to the start of the intervention period, 6 months, and 12 months (Jakicic et al., 2022). All tests were performed using a motorized treadmill, with oxygen consumption measured using a calibrated metabolic cart. The test was terminated when the participant first achieved or exceeded 85% of their age-predicted maximal heart rate ($\text{HR}_{\text{max}} = 220 - \text{age}$). Cardiorespiratory fitness is expressed in absolute (L/min) and relative terms (mL/kg/min). Change in cardiorespiratory fitness was computed as the difference between these values on the baseline test and on the subsequent 6-month and 12-month tests. Time to termination was measured as the time the cardiopulmonary exercise test was stopped in minutes.

Blood Collection and Klotho Concentration. Blood samples were collected at baseline, 6 months, and 12 months. Samples were collected in the morning with participants instructed to fast with the exception of water, abstain from exercise, and abstain from alcohol and smoking for at least 12 h. Blood samples were collected into evacuated tubes, processed in a refrigerated centrifuge, and stored at -80°C . For this secondary analysis, stored serum blood samples were used to measure Klotho concentration. Klotho was measured in duplicate by a solid-phase sandwich enzyme-linked immunosorbent assay (ELISA) (Yamazaki et al., 2010), with intra- and inter-assay coefficients of variation determined for the specific Klotho assays. The measurement procedure was performed as follows.

- 1) Test sample blank wells were determined, and 100 μL of EIA buffer was placed into the wells.
- 2) 100 μL of prepared test samples and 100 μL of prepared standard were placed into appropriate wells.
- 3) An incubation period of 60 min with the plate lid was performed at room temperature.

TABLE 1 Baseline characteristics by sample.

Variable	Total sample (N = 383)	Sample with complete blood samples for klotho analysis (N = 152)
Age (years)	45.0 ± 7.9	45.4 ± 8.0
Weight (kg)	90.9 ± 13.7	90.4 ± 13.1
Body Mass Index (kg/m ²)	32.4 ± 3.8	32.1 ± 3.7
Lean Mass (kg)	48.6 ± 8.7	48.1 ± 8.7
Fat Mass (kg)	39.2 ± 8.2	39.1 ± 7.8
Tissue Percent Body Fat (%)	44.5 ± 5.6	44.8 ± 5.6
Region Percent Body Fat (%)	43.2 ± 5.5	43.5 ± 5.6
Waist Circumference (cm)	106.4 ± 9.9	106.6 ± 9.6
Cardiorespiratory Fitness (mL/kg/min)	22.6 ± 4.4	22.9 ± 4.5
Cardiorespiratory Fitness (Termination Time - minutes)	7.7 ± 3.0	8.0 ± 3.0
Female (N, %)	304, 79.4%	118, 77.6%
Non-White (N, %)	104, 27.2%	36, 23.7%

Values are mean ± standard deviation unless indicated otherwise.

- 4) The plate was washed with the prepared wash buffer four times, with all liquid completely removed following the fourth wash.
- 5) 100 µL of the prepared labeled antibody was added into the wells.
- 6) An incubation period of 30 min with the plate lid was performed at room temperature.
- 7) The plate was washed with the prepared wash buffer five times, with all liquid completely removed follow the fifth wash.
- 8) 100 µL of Chromogen—TMB solution was added into the wells.
- 9) An incubation period of 30 min in the dark was performed at room temperature.
- 10) 100 µL of the Stop solution was added to the wells.
- 11) Removal of dirt and drops of water on the bottom of the plate was done, as well as confirmation that no bubbles were on the surface of the liquid. Then the optical density of the standard and the test samples were measured against a test sample blank, with the measurement wavelength at 450 nm. The minimum level of detectability of the assay was 6.15 pg/mL.

Statistical Analysis. Statistical analyses were performed using Statistical Package for the Social Sciences (SPSS) software, version 27. Repeated measures analyses of covariance (ANCOVA's) modeled as *weight loss response category × time* were conducted to 1) assess the effect of the 12-month behavioral weight loss intervention by weight loss response (“responder” vs “non-responder”) on key variables of body weight, waist circumference, body composition, and cardiorespiratory fitness; and 2) to examine the change in Klotho across the 12-month behavioral weight loss intervention by weight loss response (“responder” vs “non-responder”). ANCOVA's controlled for race and sex, which were randomization stratification variables for the parent study, intervention group, intervention group × time interaction, and baseline value of the variable being analyzed. Association between baseline Klotho concentration and baseline weight, waist circumference, body composition, and

cardiorespiratory fitness, as well as changes from baseline to 6 months and 12 months were examined using the Spearman's rho controlled for race and sex. The analyses assessing the association between the change in Klotho concentration at 6 or 12 months and the corresponding change in variables for weight, waist circumference, body composition, and cardiorespiratory fitness controlled for race, sex, intervention group, baseline Klotho concentration, and baseline value of the other corresponding variable. Statistical significance was defined at $p \leq 0.05$. Because the outcome variable in the present study was not the primary outcome variable for the Heart Health Study, there were no *a priori* power calculations for this secondary analysis.

Results

The parent study recruited and randomized 383 participants. As described above, a subsample of 152 participants (39.7% of the full sample) were classified as a Responder or Non-Responder, as well as provided blood samples at baseline, 6 months, and 12 months were included in these secondary analyses. Descriptive characteristics of the sample from the parent study and the subsample used for these analyses are shown in Table 1. Overall, participants included in this secondary analysis were 45.4 ± 8.0 years of age, women (77.6%), and White/Caucasian (76.3%). The distribution by intervention group is shown in Table 2.

In this subsample of participants, the 12-month behavioral weight loss intervention resulted in significantly greater reductions in body weight, BMI, lean mass, fat mass, percent body fat, and waist circumference ($p < 0.0001$) in Responders compared to Non-Responders. Moreover, the improvement in cardiorespiratory fitness ($p < 0.0001$) was significantly greater in Responders vs Non-Responders (Table 3).

Baseline Klotho concentration for Responders was 936.2 pg/mL (95% Confidence Interval (CI): 870.6, 1006.5) and 926.1 pg/mL

TABLE 2 Number of participants by randomized intervention group by weight loss response.

Classification	Intervention group		
	DIET	DIET + PA150	DIET+250
N = 182			
Responder	43	44	44
Non-Responder	20	15	16
N = 152*			
Responder	37	35	39
Non-Responder	15	13	13

*Indicates that blood samples were available for Klotho analysis at 0, 6, and 12 months. Responder: $\geq 10\%$ weight loss at both 6 months and 12 months. Non-responder: $< 5\%$ weight loss at both 6 months and 12 months.

(95% CI: 800.4, 1077.0) for Non-Responders. There was a significant difference for the change in Klotho from baseline between Responders and Non-Responders (Baseline to 6-month change: 74.1 (95% CI: 30.5, 117.7) pg/mL vs. -10.6 (95% CI: -84.1 , 62.9) pg/mL; Baseline to 12-month change: 25.9 (95% CI: -16.7 , 68.5) pg/mL vs. -44.7 (95% CI: -116.6 , 27.1) pg/mL; $p = 0.047$) (Table 3; Figure 1). Klotho concentration significantly increased from baseline to 6 months in Responders; however, while Klotho remained above baseline levels at 12 months, the change from baseline to 12 months was not statistically significant. The change in Klotho concentration from baseline to both 6 and 12 months for Non-Responders was not statistically significant. Of potential importance, when intervention group (DIET, DIET + PA150, and DIET + PA250) was entered into the ANCOVA, intervention group as a covariate was not statistically significant.

Correlation analysis, controlling for covariates described above, showed baseline Klotho concentration was not significantly associated with measures of weight, body composition, waist circumference, or cardiorespiratory fitness (Table 4). The change in Klotho concentration from baseline to 6 months was inversely associated with change in weight ($r_s = -0.195$, $p = 0.019$), BMI ($r_s = -0.196$, $p = 0.016$), fat mass ($r_s = -0.184$, $p = 0.026$), and waist circumference ($r_s = -0.218$, $p = 0.008$) but not significantly associated with the change in other measures of body composition or cardiorespiratory fitness. The change in Klotho from baseline to 12 months was not significantly associated with the change in measures of weight, body composition, waist circumference, or cardiorespiratory fitness.

Discussion

The purpose of this secondary analysis was to investigate the potential association between obesity, weight loss, and Klotho concentration. Obesity is associated with many chronic conditions and promotion of advanced aging activity (Ahima, 2009; Barton, 2010), with Klotho being a biomarker of premature aging processes (Kuro-o et al., 1997; Xu and Sun, 2015). We found Klotho concentration significantly increased from baseline to 6 months in participants with weight loss $\geq 10\%$ (Responders), but the increase observed at 12 months was no longer statistically

significant. The Non-Responders had no significant change in Klotho concentration at either 6 or 12 months.

Baseline Klotho concentration for the middle-aged adults with overweight or obesity included in this secondary analysis was approximately 930 pg/mL. However, there is variability surrounding the concentration of circulating Klotho dependent upon age and BMI. Amitani et al. (2013), investigated Klotho's role in human metabolism by examining the association between plasma Klotho concentration and BMI. Participants ($n = 34$) either with normal weight (mean BMI: 21.8 kg/m²), underweight or diagnosed with anorexia nervosa (mean BMI: 13.1 kg/m²), or with obesity (mean BMI: 35.7 kg/m²) and a mean age of 21 years old. Findings show mean Klotho concentration for participants with normal weight to be 1391.6 pg/mL, underweight or diagnosed with anorexia nervosa to be 764.6 pg/mL, and for participants with obesity to be 847.1 pg/mL (Amitani et al., 2013). When studying children and adolescents of ranging BMI's, Klotho concentrations continue in this variable trend. Children and adolescents with obesity had a significantly higher Klotho concentration (median: 168.6 pg/mL) compared to individuals with overweight (median: 131.3 pg/mL) and normal weight status (median: 116.6 pg/mL) (Socha-Banasiak et al., 2020). The change in Klotho concentration, to the best of our knowledge, has not been reported for healthy young and middle-aged adults with overweight or obesity undergoing a behavioral weight loss intervention. The findings presented in this report suggest that weight loss, of sufficient magnitude, may have a favorable influence on this biomarker of aging, which may be of clinical importance. This may also suggest that in adults with excess weight or obesity, intentional weight loss may have a favorable influence of reducing the risk for premature deleterious health effects of aging. There is evidence that Klotho, specifically β -Klotho, acts as an essential component in endocrine fibroblast growth factor receptor complexes. β -Klotho is required for high-affinity binding of endocrine fibroblast growth factors to induce a signaling cascade (Kuro-o, 2019). This cascade is actively involved in homeostatic maintenance of glucose metabolism,—which is largely dependent on adipose tissue—energy expenditure, and cardiovascular complications in abdominal obesity and obesity-related diseases (Chen et al., 2007; Ornitz and Itoh, 2015; Scheja and Heeren, 2016; Meex and Watt, 2017; Ghadge et al., 2018). Potentially

TABLE 3 Change in Klotho (pg/mL), body weight (kg), lean mass (kg), fat mass (kg), and relative cardiorespiratory fitness (mL/kg/min) by weight loss response category (responder vs non-responder) across the 12-month intervention.

Variable	Category	Baseline mean (95% CI)	Change from baseline*		<i>p</i> -values		
			6 Month	12 Month	Category	Time***	Category X time***
Body Weight (kg)	Responder (N = 111)	91.0 (88.6, 93.4)	−14.1 (−14.8, −13.5)**	−16.8 (−17.8, −15.8)**	<0.001	0.236	<0.001
	Non-Responder (N = 41)	88.7 (84.8, 92.6)	−2.0 (−3.1, −0.9)**	−0.4 (−1.9, 1.1)			
Body Mass Index (kg/m ²)	Responder (N = 111)	91.0 (88.6, 93.4)	−5.0 (−5.2, −4.8)**	−5.9 (−6.3, −5.6)**	<0.001	0.079	<0.001
	Non-Responder (N = 41)	88.7 (84.8, 92.6)	−0.7 (−1.0, −0.3)**	−0.1 (−0.7, 0.4)			
Lean Mass (kg)	Responder (N = 111)	48.4 (46.8, 49.9)	−2.2 (−2.1, −1.9)**	−2.3 (−2.6, −1.9)**	<0.001	0.205	0.762
	Non-Responder (N = 41)	47.2 (44.7, 49.8)	−0.1 (−0.5, 0.4)	−0.2 (−0.7, 0.4)			
Fat Mass (kg)	Responder (N = 111)	39.3 (37.9, 40.9)	−11.6 (−12.1, −11.0)**	−14.0 (−14.8, −13.2)**	<0.001	0.472	<0.001
	Non-Responder (N = 41)	38.4 (36.2, 40.7)	−2.0 (−2.8, −1.1)**	−0.3 (−1.7, 1.0)			
Percent Body Fat (%)	Responder (N = 111)	44.8 (43.7, 45.8)	−7.5 (−7.9, −7.0)**	−9.6 (−10.3, −8.9)**	<0.001	0.688	<0.001
	Non-Responder (N = 41)	45.0 (43.1, 46.4)	−1.2 (−2.0, −0.5)**	−0.1 (−1.3, 1.0)			
Waist Circumference (cm)	Responder (N = 111)	107.3 (105.4, 109.2)	−12.6 (−13.5, −11.6)**	−15.2 (−16.3, −14.1)**	<0.001	0.185	0.010
	Non-Responder (N = 41)	104.5 (101.7, 107.3)	−2.0 (−3.6, −0.3)**	−2.2 (−4.1, −0.3)**			
Cardiorespiratory Fitness (mL/kg/min)	Responder (N = 110)	23.0 (22.3, 23.8)	3.9 (3.3, 4.5)**	4.7 (4.1, 5.3)**	<0.001	0.154	<0.001
	Non-Responder (N = 37)	22.6 (21.2, 24.2)	0.8 (−0.1, 1.8)	−0.5 (−1.6, 0.6)			
Cardiorespiratory Fitness (minute to termination)	Responder (N = 111)	8.0 (7.5, 8.6)	2.9 (2.5, 3.3)**	2.9 (2.5, 3.3)**	<0.001	0.556	0.099
	Non-Responder (N = 40)	7.9 (7.0, 8.8)	0.8 (0.1, 1.5)**	0.0 (−0.7, 0.7)			
Klotho (pg/mL)	Responder (N = 111)	936.2 (870.6, 1006.5)	74.1 (30.5, 117.7)**	25.9 (−16.7, 68.5)	0.047	0.547	0.727
	Non-Responder (N = 41)	926.1 (800.4, 1077.0)	−10.6 (−84.1, 62.9)	−44.7 (−116.6, 27.1)			

*LS Means (95% confidence interval); analysis adjusted for race, sex, intervention group, and baseline value.

***p* < 0.05 for change from baseline.

***Time effect represents the comparison of change scores at 6 and 12 months.

Bolded values indicate statistical significance (*p* < 0.05).

signifying Klotho concentrations may serve as a predictor for prediabetes, type 2 diabetes, cardiovascular disease, and obesity, however more work needs to be done in this area of research.

Abdominal obesity, or visceral obesity, is independently linked to several pathological conditions including impaired glucose and lipid metabolism, insulin resistance, increased predisposition to cancers of the colon, breast, and prostate, prolonged hospital stays, increased incidence of infections and non-infectious

complications, and increased mortality in the hospital (Schapira et al., 1994; Von Hafe et al., 2004; Fox et al., 2007; Ritchie and Connell, 2007; Oh et al., 2008; Tsujinaka et al., 2008). The similar pathological pathways affected by visceral adiposity and Klotho suggest a possible relationship. A cross-sectional analysis aimed to evaluate the association between visceral adiposity index and serum Klotho among 6,252 adults (Cui et al., 2023). The visceral adiposity index represents the waist circumference relative to the

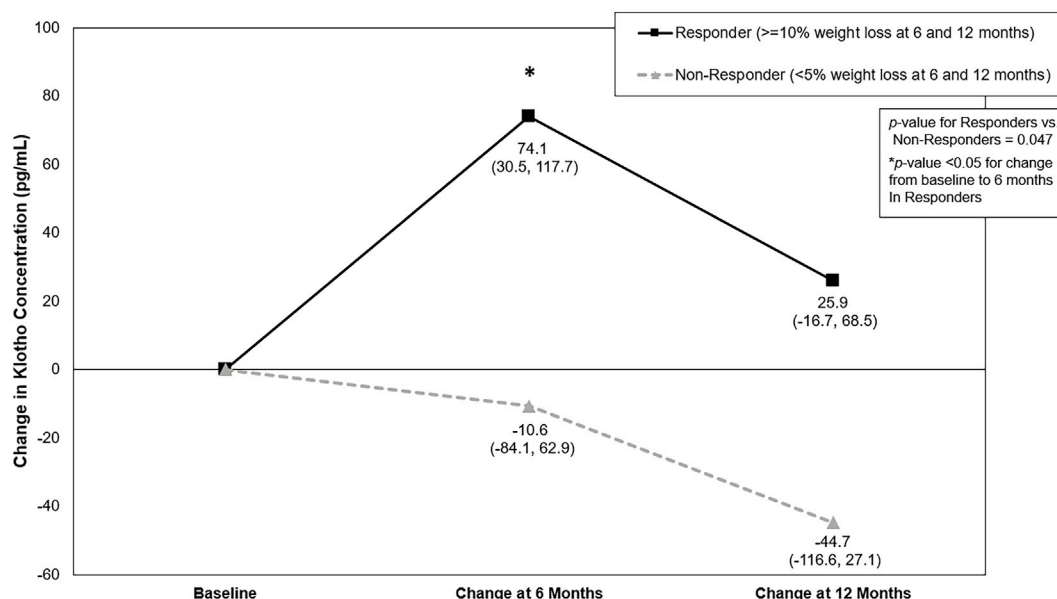


FIGURE 1

Change in Klotho concentration (pg/mL) by weight loss response category across the 12-month behavioral weight loss intervention. Results based on analysis of covariance adjusted for race, sex, intervention group, and baseline Klotho concentration. Values represent LS means (95% confidence interval).

combination of BMI, triglycerides, and high-density lipoprotein. A multivariable regression analysis found serum Klotho concentration was lower in participants with a high visceral adiposity index. A segmented regression analyses showed that this relationship was non-linear, only being observed when the visceral adiposity index score was less than 3.21. These findings may suggest that a lower level of adiposity may have anti-aging and health benefits by increasing Klotho concentrations (Cui et al., 2023). However, this analysis is limited in its cross-sectional nature and suggests the need for prospective studies to confirm a causal relationship and mechanistic pathway. The current study demonstrated a significant association between reduction in waist circumference at 6 months and the change in Klotho, suggesting that reduced abdominal adiposity may contribute to beneficial changes in biomarkers reflective of healthy aging.

While Klotho concentration did significantly increase at 6 months in Responders—defined as reducing weight by at least 10%—the increase in Klotho concentration from baseline to 12 months in these participants was no longer statistically significant despite weight loss being sustained. This may suggest that Klotho begins to regress toward baseline levels during periods of weight loss maintenance. Of interest, the regression of health benefits observed with weight loss has been shown in response to other weight loss treatments. A randomized clinical trial from Courcoulas and others (Courcoulas et al., 2015), observed significant weight loss among individuals who underwent bariatric surgery, which was maintained up to 3 years following the intervention (Courcoulas et al., 2015). Moreover, 60% individuals who underwent Roux-en-Y Gastric Bypass (RYGB) surgery and 45% of individuals who underwent laparoscopic adjustable gastric band (LAGB) surgery had complete or partial remission of type 2 diabetes at year one following surgery. However, 3 years following surgery only 29% of the RYGB and 40% of

the LAGB participants remained in remission (Courcoulas et al., 2015). Thus, the pattern of change in Klotho concentration observed in the current study may not be a unique phenomenon, but rather the body's potential desire to return to baseline levels despite weight loss maintenance and this warrants further investigation.

There is evidence to support performing exercise may lead to improvements in Klotho concentration in both human and animal models (Avin et al., 2014; Dalise et al., 2017); potentially indicating reducing sedentary time and increasing muscle activity through exercise may provide either improvements or maintenance in Klotho concentration. In a 16-week exercise training program (Avin et al., 2014) among individuals with obesity, participants showed a substantial increase in Klotho concentration in response to an acute exercise bout performed post-intervention compared to an acute exercise bout performed pre-intervention (Avin et al., 2014). Further, in mice models (Dalise et al., 2017), a 30-min bout of exercise resulted in a significant upregulation of Klotho in mice from pre-to post-exercise bout (Dalise et al., 2017). However, when adults with overweight or obesity undergo a behavioral weight loss intervention using dietary restriction and two intervention groups including physical activity, the association between change in Klotho concentration and weight loss was not altered. Moreover, change in Klotho concentration was not significantly associated with change in cardiorespiratory fitness. This may suggest that the effects of physical activity, or physical activity that increases cardiorespiratory fitness, on Klotho concentration may be influenced by whether physical activity is accompanied with dietary restriction that results in weight loss. This potential difference in response warrants further investigation.

Strengths include that the parent study included a 12-month behavioral weight loss intervention, with measures collected prior to, during, and post-intervention. This intervention resulted in variability in weight loss, that allowed the present analysis to

TABLE 4 Spearman's rho between Klotho concentration at baseline and change at 6- and 12 months with corresponding measures of body weight, body mass index, body composition, and cardiorespiratory fitness.

Variable	Assessment period	Klotho concentration (pg/mL)		
		Baseline*	Change [#] : Baseline to 6 months**	Change [#] : Baseline to 12 months**
Body Weight (kg) [N = 152]	Baseline	$r_s = -0.076$ ($p = 0.361$)	-----	-----
	Change [#] : baseline to 6 months	-----	$r = -0.223$ ($p = 0.007$)	-----
	Change [#] : baseline to 12 months	-----	-----	$r = -0.070$ ($p = 0.399$)
Body Mass Index (kg/m ²) [N = 152]	Baseline	$r_s = -0.100$ ($p = 0.226$)	-----	-----
	Change [#] : baseline to 6 months	-----	$r = -0.205$ ($p = 0.013$)	-----
	Change [#] : baseline to 12 months	-----	-----	$r = -0.068$ ($p = 0.412$)
Lean Mass (kg) [N = 152]	Baseline	$r_s = -0.148$ ($p = 0.073$)	-----	-----
	Change [#] : baseline to 6 months	-----	$r = -0.108$ ($p = 0.195$)	-----
	Change [#] : baseline to 12 months	-----	-----	$r = -0.122$ ($p = 0.143$)
Fat Mass (kg) [N = 152]	Baseline	$r_s = 0.005$ ($p = 0.952$)	-----	-----
	Change [#] : baseline to 6 months	-----	$r = -0.192$ ($p = 0.020$)	-----
	Change [#] : baseline to 12 months	-----	-----	$r = -0.042$ ($p = 0.615$)
Percent Body Fat (%) [N = 152]	Baseline	$r_s = 0.067$ ($p = 0.421$)	-----	-----
	Change [#] : baseline to 6 months	-----	$r = -0.188$ ($p = 0.023$)	-----
	Change [#] : baseline to 12 months	-----	-----	$r = -0.061$ ($p = 0.464$)
Waist Circumference (cm) [N = 152]	Baseline	$r_s = -0.079$ ($p = 0.340$)	-----	-----
	Change [#] : baseline to 6 months	-----	$r_s = -0.218$ ($p = 0.008$)	-----
	Change [#] : baseline to 12 months	-----	-----	$r_s = -0.026$ ($p = 0.752$)
Cardiorespiratory Fitness (mL/kg/min) [N = 147]	Baseline	$r_s = 0.015$ ($p = 0.856$)	-----	-----
	Change [#] : baseline to 6 months	-----	$r = 0.042$ ($p = 0.620$)	-----
	Change [#] : baseline to 12 months	-----	-----	$r = 0.067$ ($p = 0.424$)

(Continued on following page)

TABLE 4 (Continued) Spearman's rho between Klotho concentration at baseline and change at 6- and 12 months with corresponding measures of body weight, body mass index, body composition, and cardiorespiratory fitness.

Variable	Assessment period	Klotho concentration (pg/mL)		
		Baseline*	Change [#] : Baseline to 6 months**	Change [#] : Baseline to 12 months**
Cardiorespiratory Fitness (Termination Time, minutes) [N = 151]	Baseline	$r_s = 0.036$ ($p = 0.660$)	-----	-----
	Change [#] : baseline to 6 months	-----	$r = 0.020$ ($p = 0.814$)	-----
	Change [#] : baseline to 12 months	-----	-----	$r = 0.102$ ($p = 0.221$)

*Analysis controlled for race and sex.

**Analysis controlled for race, sex, intervention condition, baseline Klotho concentration, and baseline of other corresponding variable.

[#]6-month change = 6-month value minus baseline value; 12-month change = 12-month value minus baseline

Bolded values indicate statistical significance ($p < 0.05$).

investigate change in Klotho concentration in participants with at least 10% weight loss (Responders) compared to participants with less than 5% weight loss (Non-Responders).

Despite these strengths, the present analysis is not without limitations that could impact the interpretation of the observed results. The study sample included individuals with overweight or obesity but otherwise relatively healthy individuals, therefore functional impairments needed to observe associations with Klotho concentrations may not have been detected. This analysis contains a subsample of the original 383 participants recruited for the parent Heart Health Study, with only 152 participants included and stratified into category of weight loss response classification to the weight loss intervention. Though weight loss of $\geq 10\%$ is clinically meaningful, whether Klotho concentration changes differently with other magnitudes of weight loss may warrant future research. Also, the average age of this population was 45 years, representing a slightly younger population than what has been typically reported within the Klotho literature. Thus, future research should consider assessing the impact of intentional weight loss on Klotho concentration among older adults, where Klotho concentration has been predominantly studied, and where excess body weight and adiposity are also present. Although Klotho is primarily produced and released into circulation by the kidney (Kim et al., 2018; Cheikhi et al., 2019), this study did not measure or estimate renal function. Klotho levels are strongly correlated with chronic kidney disease and renal failure, and individuals with obesity are at a greater risk for developing these conditions (Kim et al., 2018; Lakkis and Weir, 2018; Nehus, 2018; Cheikhi et al., 2019; Chen et al., 2021). Therefore, future research should consider including a measure of renal function in their screening criteria.

In conclusion, this secondary analysis of the Heart Health Study provides evidence within the context of a behavioral weight loss intervention, that Klotho concentration significantly increases with weight loss of $\geq 10\%$. This may suggest that weight loss in middle-aged adults with overweight or obesity may have a favorable effect on biomarkers associated with aging, and this warrants additional investigation. Moreover, future studies should examine whether similar findings are present in older adults with overweight or obesity and whether weight loss has a similar effect as what was observed in this current study. There is also a need for future studies to disentangle the potential effects of variations in macro-nutrient composition. These findings may have clinical importance

for understanding the effects of excess weight and adiposity, along with reductions in these factors, on health outcomes.

Data availability statement

The raw data supporting the conclusion of this article will be made available by the authors, without undue reservation, upon reasonable request.

Ethics statement

The studies involving human participants were reviewed and approved by Institutional Review Board at the University of Pittsburgh. The patients/participants provided their written informed consent to participate in this study.

Author contributions

JJ, RR, ES, and WL contributed to the parent study conception and design. KC, JJ, RR, KD, and FA contributed to the secondary analysis conception and design. KC, JJ, and WL contributed to the secondary data analysis. The first draft of the manuscript was written by KC and all authors commented on previous versions of the manuscript. All authors contributed to the article and approved the submitted version.

Funding

Support for the parent project was provided by R01 HL103646 and UL1 TR001857. KC is supported by the National Human Genome Research Institute—1 T32 HG008955-01.

Acknowledgments

We recognize the contribution of the staff and graduate students at the Physical Activity and Weight Management Research Center at the University of Pittsburgh who contributed to this project.

We would also like to acknowledge and thank all Heart Health Study participants.

Conflict of interest

JJ currently receives compensation for serving on the Scientific Advisory Board for Wondr Health, Inc., is the Principal Investigator on a research contract awarded to the University of Kansas Medical Center by Epitome Medical Inc., and previously received compensation for serving on the Scientific Advisory Board for WW International, Inc. and as a consultant for Educational Initiatives, Inc., has received remuneration for professional presentations, and serves as a volunteer in a professional leadership role to the American College of Sports Medicine. RR is a consultant and instructor for Wondr Health, Inc., has received remuneration for

professional presentations, and serves as a volunteer in a professional leadership role to the American College of Sports Medicine. ES serves on the Scientific Advisory Board for Hay Therapeutics.

The remaining authors declare that the research was conducted in the absence of any commercial or financial relationships that could be construed as a potential conflict of interest.

Publisher's note

All claims expressed in this article are solely those of the authors and do not necessarily represent those of their affiliated organizations, or those of the publisher, the editors and the reviewers. Any product that may be evaluated in this article, or claim that may be made by its manufacturer, is not guaranteed or endorsed by the publisher.

References

- Ahima, R. S. (2009). Connecting obesity, aging and diabetes. *Nat. Med.* 15, 996–997. doi:10.1038/nm0909-996
- Amitani, M., Asakawa, A., Amitani, H., Kaimoto, K., Sameshima, N., Koyama, K. I., et al. (2013). Plasma klotho levels decrease in both anorexia nervosa and obesity. *Nutrition* 29, 1106–1109. doi:10.1016/j.nut.2013.02.005
- Arking, D. E., Becker, D. M., Yanek, L. R., Fallin, D., Judge, D. P., Moy, T. F., et al. (2003). KLOTHO allele status and the risk of early-onset occult coronary artery disease. *Am. J. Hum. Genet.* 72, 1154–1161. doi:10.1086/375035
- Avin, K. G., Coen, P. M., Huang, W., Stolz, D. B., Sowa, G. A., Dubé, J. J., et al. (2014). Skeletal muscle as a regulator of the longevity protein, Klotho. *Front. Physiology* 5, 189. doi:10.3389/fphys.2014.00189
- Barton, M. (2010). Obesity and aging: Determinants of endothelial cell dysfunction and atherosclerosis. *Pflügers Archiv-European J. Physiology* 460, 825–837. doi:10.1007/s00424-010-0860-y
- Bloch, L., Sineschekova, O., Reichenbach, D., Reiss, K., Saftig, P., Kuro-O, M., et al. (2009). Klotho is a substrate for alpha-beta- and gamma-secretase. *FEBS Lett.* 583, 3221–3224. doi:10.1016/j.febslet.2009.09.009
- Cheikhi, A., Barchowsky, A., Sahu, A., Shinde, S. N., Pius, A., Clemens, Z. J., et al. (2019). Klotho: An elephant in aging research. *J. Gerontol. A Biol. Sci. Med. Sci.* 74, 1031–1042. doi:10.1093/gerona/glz061
- Chen, C.-D., Podvin, S., Gillespie, E., Leeman, S. E., and Abraham, C. R. (2007). Insulin stimulates the cleavage and release of the extracellular domain of Klotho by ADAM10 and ADAM17. *Proc. Natl. Acad. Sci.* 104, 19796–19801. doi:10.1073/pnas.0709805104
- Chen, Y., Dabbas, W., Gangemi, A., Benedetti, E., Lash, J., Finn, P. W., et al. (2021). Obesity management and chronic kidney disease. *Semin. Nephrol.* 41, 392–402. doi:10.1016/j.semnephrol.2021.06.010
- Consitt, L. A., Bell, J. A., and Houmard, J. A. (2009). Intramuscular lipid metabolism, insulin action, and obesity. *IUBMB Life* 61, 47–55. doi:10.1002/iub.142
- Courcoulas, A. P., Belle, S. H., Neiberg, R. H., Pierson, S. K., Eagleton, J. K., Kalarchian, M. A., et al. (2015). Three-year outcomes of bariatric surgery vs lifestyle intervention for type 2 diabetes mellitus treatment: A randomized clinical trial. *J. Am. Med. Assoc. Surg.* 150, 931–940. doi:10.1001/jamasurg.2015.1534
- Cui, J., Yang, Z., Wang, J., Yin, S., Xiao, Y., Bai, Y., et al. (2023). A cross-sectional analysis of association between visceral adiposity index and serum anti-aging protein Klotho in adults. *Front. Endocrinol.* 14, 1082504. doi:10.3389/fendo.2023.1082504
- Dalise, S., Cavalli, L., Ghuman, H., Wahlberg, B., Gerwig, M., Chisari, C., et al. (2017). Biological effects of dosing aerobic exercise and neuromuscular electrical stimulation in rats. *Sci. Rep.* 7, 10830. doi:10.1038/s41598-017-11260-7
- Di Bona, D., Accardi, G., Virruso, C., Candore, G., and Caruso, C. (2014). Association of klotho polymorphisms with healthy aging: A systematic review and meta-analysis. *Rejuvenation Res.* 17, 212–216. doi:10.1089/rej.2013.1523
- DIETARY GUIDELINES ADVISORY COMMITTEE (2015). “2015–2020 dietary Guidelines for Americans,” in *AGRICULTURE, U. S. D. O. H. A. H. S. A. U. S. D. O. (ed.)* (Washington D.C.).
- Drücke, T. B., and Massy, Z. A. (2013). Circulating klotho levels: Clinical relevance and relationship with tissue klotho expression. *Kidney Int.* 83, 13–15. doi:10.1038/ki.2012.370
- Field, A. E., Coakley, E. H., Must, A., Spadano, J. L., Laird, N., Dietz, W. H., et al. (2001). Impact of overweight on the risk of developing common chronic diseases during a 10-year period. *Archives Intern. Med.* 161, 1581–1586. doi:10.1001/archinte.161.13.1581
- Flegal, K. M., Carroll, M. D., Kit, B. K., and Ogden, C. L. (2012). Prevalence of obesity and trends in the distribution of body mass index among US adults, 1999–2010. *J. Am. Med. Assoc.* 307, 491–497. doi:10.1001/jama.2012.39
- Fox, C. S., Massaro, J. M., Hoffmann, U., Pou, K. M., Maurovich-Horvat, P., Liu, C.-Y., et al. (2007). Abdominal visceral and subcutaneous adipose tissue compartments: Association with metabolic risk factors in the framingham heart study. *Circulation* 116, 39–48. doi:10.1161/CIRCULATIONAHA.106.675355
- Galgani, J., and Ravussin, E. (2009). Energy metabolism, fuel selection and body weight regulation. *Int. J. Obes.* 32, S109–S119. doi:10.1038/ijo.2008.246
- Ghadge, A. A., Khaire, A. A., and Kuvalekar, A. A. (2018). Adiponectin: A potential therapeutic target for metabolic syndrome. *Cytokine Growth Factor Rev.* 39, 151–158. doi:10.1016/j.cytogfr.2018.01.004
- Hales, C. M., Carroll, M. D., Fryar, C. D., and Ogden, C. L. (2017). *Prevalence of obesity among adults and youth: United States, 2015–2016, US department of health and human services, centers for disease control and prevention.* National Center for Health Statistics.
- He, J., Watkins, S., and Kelley, D. E. (2001). Skeletal muscle lipid content and oxidative enzyme activity in relation to muscle fiber type in type 2 diabetes and obesity. *Diabetes* 50, 817–823. doi:10.2337/diabetes.50.4.817
- Heinicke, V., and Halle, M. (2020). Lifestyle intervention in the primary prevention of cardiovascular diseases. *Herz* 45, 30–38. doi:10.1007/s00059-019-04886-y
- Hui, H., Zhai, Y., Ao, L., Cleveland, J. R. J. C., Liu, H., Fullerton, D. A., et al. (2017). Klotho suppresses the inflammatory responses and ameliorates cardiac dysfunction in aging endotoxemic mice. *Oncotarget* 8, 15663–15676. doi:10.18632/oncotarget.14933
- Jakicic, J. M., Rogers, R. J., Davis, K. K., and Collins, K. A. (2018). Role of physical activity and exercise in treating patients with overweight and obesity. *Clin. Chem.* 64, 99–107. doi:10.1373/clinchem.2017.272443
- Jakicic, J. M., Rogers, R. J., Lang, W., Gibbs, B. B., Yuan, N., Fridman, Y., et al. (2022). Impact of weight loss with diet or diet plus physical activity on cardiac magnetic resonance imaging and cardiovascular disease risk factors: Heart Health Study randomized trial. *Obesity* 30, 1039–1056. doi:10.1002/oby.23412
- Kim, H. J., Kang, E., Oh, Y. K., Kim, Y. H., Han, S. H., Yoo, T. H., et al. (2018). The association between soluble klotho and cardiovascular parameters in chronic kidney disease: Results from the KNOW-ckd study. *BMC Nephrol.* 19, 51. doi:10.1186/s12882-018-0851-3
- Kuro-O, M., Matsumura, Y., Aizawa, H., Kawaguchi, H., Suga, T., Utsugi, T., et al. (1997). Mutation of the mouse klotho gene leads to a syndrome resembling ageing. *Nature* 390, 45–51. doi:10.1038/36285
- Kuro-O, M. (2019). The Klotho proteins in health and disease. *Nat. Rev. Nephrol.* 15, 27–44. doi:10.1038/s41581-018-0078-3

- Kurosu, H., Yamamoto, M., Clark, J. D., Pastor, J. V., Nandi, A., Gurnani, P., et al. (2005). Suppression of aging in mice by the hormone Klotho. *Science* 309, 1829–1833. doi:10.1126/science.1112766
- Lakkis, J. I., and Weir, M. R. (2018). Obesity and kidney disease. *Prog. Cardiovasc. Dis.* 61, 157–167. doi:10.1016/j.pcad.2018.07.005
- Lang, A., and Froelicher, E. S. (2006). Management of overweight and obesity in adults: Behavioral intervention for long-term weight loss and maintenance. *Eur. J. Cardiovasc. Nurs.* 5, 102–114. doi:10.1016/j.ejcnurse.2005.11.002
- Matsumura, Y., Aizawa, H., Shiraki-Iida, T., Nagai, R., Kuro-O, M., and Nabeshima, Y.-I. (1998). Identification of the human klotho gene and its two transcripts encoding membrane and secreted klotho protein. *Biochem. Biophys. Res. Commun.* 242, 626–630. doi:10.1006/bbrc.1997.8019
- Meex, R. C. R., and Watt, M. J. (2017). Hepatokines: Linking nonalcoholic fatty liver disease and insulin resistance. *Nat. Rev. Endocrinol.* 13, 509–520. doi:10.1038/nrendo.2017.56
- Mokdad, A. H., Ford, E. S., Bowman, B. A., Dietz, W. H., Vinicor, F., Bales, V. S., et al. (2003). Prevalence of obesity, diabetes, and obesity-related health risk factors, 2001. *J. Am. Med. Assoc.* 289, 76–79. doi:10.1001/jama.289.1.76
- Must, A., Spadano, J., Coakley, E. H., Field, A. E., Colditz, G., and Dietz, W. H. (1999). The disease burden associated with overweight and obesity. *J. Am. Med. Assoc.* 282, 1523–1529. doi:10.1001/jama.282.16.1523
- Nehus, E. (2018). Obesity and chronic kidney disease. *Curr. Opin. Pediatr.* 30, 241–246. doi:10.1097/MOP.0000000000000586
- Oh, T.-H., Byeon, J.-S., Myung, S.-J., Yang, S.-K., Choi, K.-S., Chung, J.-W., et al. (2008). Visceral obesity as a risk factor for colorectal neoplasm. *J. Gastroenterology Hepatology* 23, 411–417. doi:10.1111/j.1440-1746.2007.05125.x
- Orces, C. H. (2022a). The association between metabolic syndrome and the anti-aging humoral factor klotho in middle-aged and older adults. *Diabetes Metab. Syndr.* 16, 102522. doi:10.1016/j.dsx.2022.102522
- Orces, C. H. (2022b). The association of obesity and the antiaging humoral factor klotho in middle-aged and older adults. *ScientificWorldJournal* 2022, 7274858. doi:10.1155/2022/7274858
- Ornitz, D. M., and Itoh, N. (2015). The fibroblast growth factor signaling pathway. *WIREs Dev. Biol.* 4, 215–266. doi:10.1002/wdev.176
- PHYSICAL ACTIVITY GUIDELINES ADVISORY COMMITTEE (2018). “2018 physical activity guidelines advisory committee scientific report,” in *SERVICES*, U. S. D. O. H. A. H. (Washington, D.C.).
- Poirier, P., Giles, T. D., Bray, G. A., Hong, Y., Stern, J. S., Pi-Sunyer, F. X., et al. (2006). Obesity and cardiovascular disease: Pathophysiology, evaluation, and effect of weight loss: An update of the 1997 American heart association scientific statement on obesity and heart disease from the obesity committee of the council on nutrition, physical activity, and metabolism. *Circulation* 113, 898–918. doi:10.1161/CIRCULATIONAHA.106.171016
- Razzaque, M. S. (2012). The role of Klotho in energy metabolism. *Nat. Rev. Endocrinol.* 8, 579–587. doi:10.1038/nrendo.2012.75
- Ritchie, S. A., and Connell, J. M. (2007). The link between abdominal obesity, metabolic syndrome and cardiovascular disease. *Nutr. Metabolism, Cardiovasc. Dis.* 17, 319–326. doi:10.1016/j.numecd.2006.07.005
- Rogers, R. J., Schelbert, E. B., Lang, W., Fridman, Y., Yuan, N., and Jakicic, J. M. (2020). Association of fitness and body fatness with left ventricular mass: The heart health study. *Obes. Sci. Pract.* 6, 19–27. doi:10.1002/osp4.380
- Schapira, D. V., Clark, R. A., Wolff, P. A., Jarrett, A. R., Kumar, N. B., and Aziz, N. M. (1994). Visceral obesity and breast cancer risk. *Cancer* 74, 632–639. doi:10.1002/1097-0142(19940715)74:2<632::aid-cnrcr2820740215>3.0.co;2-t
- Scheja, L., and Heeren, J. (2016). Metabolic interplay between white, beige, Brown adipocytes and the liver. *J. Hepatology* 64, 1176–1186. doi:10.1016/j.jhep.2016.01.025
- Seidell, J., Muller, D., Sorkin, J., and Andres, R. (1992). Fasting respiratory exchange ratio and resting metabolic rate as predictors of weight gain: The Baltimore longitudinal study on aging. *Int. J. Obes. Relat. Metabolic Disord.* 16, 667–674.
- Semba, R. D., Cappola, A. R., Sun, K., Bandinelli, S., Dalal, M., Crasto, C., et al. (2011). Plasma klotho and cardiovascular disease in adults. *J. Am. Geriatrics Soc.* 59, 1596–1601. doi:10.1111/j.1532-5415.2011.03558.x
- Semba, R. D., Cappola, A. R., Sun, K., Bandinelli, S., Dalal, M., Crasto, C., et al. (2012). Relationship of low plasma klotho with poor grip strength in older community-dwelling adults: The InCHIANTI study. *Eur. J. Appl. Physiology* 112, 1215–1220. doi:10.1007/s00421-011-2072-3
- Semba, R. D., Ferrucci, L., Sun, K., Simonsick, E., Turner, R., Miljkovic, I., et al. (2015). Low plasma klotho concentrations and decline of knee strength in older adults. *Journals Gerontology Ser. A Biomed. Sci. Med. Sci.* 71, 103–108. doi:10.1093/gerona/glv077
- Socha-Banasia, A., Michalak, A., Paczes, K., Gaj, Z., Fendler, W., Socha, A., et al. (2020). Klotho and fibroblast growth factors 19 and 21 serum concentrations in children and adolescents with normal body weight and obesity and their associations with metabolic parameters. *BMC Pediatr.* 20, 294. doi:10.1186/s12887-020-02199-2
- Steinberg, H. O., Chaker, H., Leaming, R., Johnson, A., Brechtel, G., and Baron, A. D. (1996). Obesity/insulin resistance is associated with endothelial dysfunction. Implications for the syndrome of insulin resistance. *J. Clin. Investigation* 97, 2601–2610. doi:10.1172/JCI118709
- Stierman, B., Afful, J., Carroll, M. D., Chen, T.-C., Davy, O., Fink, S., et al. (2021). “National health and nutrition examination survey 2017–March 2020 prepandemic data files development of files and prevalence estimates for selected health outcomes,” in *National Health Statistics Reports*. Editor National Center for Health, S. (Hyattsville, MD). doi:10.15620/cdc:106273
- Tsujioka, S., Konishi, F., Kawamura, Y. J., Saito, M., Tajima, N., Tanaka, O., et al. (2008). Visceral obesity predicts surgical outcomes after laparoscopic colectomy for sigmoid colon cancer. *Dis. Colon and Rectum* 51, 1757–1765. doi:10.1007/s10350-008-9395-0
- Van Gaal, L. F., Mertens, I. L., and Christophe, E. (2006). Mechanisms linking obesity with cardiovascular disease. *Nature* 444, 875–880. doi:10.1038/nature05487
- Vgontzas, A. N., Papanicolaou, D. A., Bixler, E. O., Hopper, K., Lotsikas, A., Lin, H.-M., et al. (2000). Sleep apnea and daytime sleepiness and fatigue: Relation to visceral obesity, insulin resistance, and hypercytokinemia. *J. Clin. Endocrinol. Metabolism* 85, 1151–1158. doi:10.1210/jcem.85.3.6484
- Von Hafe, P., Pina, F., Pérez, A., Tavares, M., and Barros, H. (2004). Visceral fat accumulation as a risk factor for prostate cancer. *Obes. Res.* 12, 1930–1935. doi:10.1038/oby.2004.242
- Wadden, T. A., and Stunkard, A. J. (2002). *Handbook of obesity treatment*. Guilford Press.
- Wang, Y., and Sun, Z. (2009). Current understanding of klotho. *Ageing Res. Rev.* 8, 43–51. doi:10.1016/j.arr.2008.10.002
- Webb, V. L., and Wadden, T. A. (2017). Intensive lifestyle intervention for obesity: Principles, practices, and results. *Gastroenterology* 152, 1752–1764. doi:10.1053/j.gastro.2017.01.045
- Weinsier, R. L., Hunter, G. R., Heini, A. F., Goran, M. I., and Sell, S. M. (1998). The etiology of obesity: Relative contribution of metabolic factors, diet, and physical activity. *Am. J. Med.* 105, 145–150. doi:10.1016/s0002-9343(98)00190-9
- Wolk, R., Shamsuzzaman, A. S., and Somers, V. K. (2003). Obesity, sleep apnea, and hypertension. *Hypertension* 42, 1067–1074. doi:10.1161/01.HYP.0000101686.98973.A3
- Woo, K., Chook, P., Yu, C., Sung, R., Qiao, M., Leung, S., et al. (2004). Overweight in children is associated with arterial endothelial dysfunction and intima-media thickening. *Int. J. Obes.* 28, 852–857. doi:10.1038/sj.ijo.0802539
- Xu, Y., and Sun, Z. (2015). Molecular basis of klotho: From gene to function in aging. *Endocr. Rev.* 36, 174–193. doi:10.1210/er.2013-1079
- Yamazaki, Y., Imura, A., Urakawa, I., Shimada, T., Murakami, J., Aono, Y., et al. (2010). Establishment of sandwich ELISA for soluble alpha-Klotho measurement: Age-dependent change of soluble alpha-Klotho levels in healthy subjects. *Biochem. Biophysical Res. Commun.* 398, 513–518. doi:10.1016/j.bbrc.2010.06.110

Frontiers in Aging

Explores the biological processes of human aging

Advances our understanding of human aging and the fundamental link with age-related diseases, ultimately leading to improved healthspans.

Discover the latest Research Topics

[See more →](#)

Frontiers

Avenue du Tribunal-Fédéral 34
1005 Lausanne, Switzerland
frontiersin.org

Contact us

+41 (0)21 510 17 00
frontiersin.org/about/contact



Frontiers in Aging

